DISSERTATION

# EXPLORING MODEL CHEMICAL SYSTEMS THROUGH A NEW LENS: COMBINING NOVEL MICROFLUIDIC TECHNOLOGY WITH INFRARED ANALYSIS TECHNIQUES

Submitted by

Michael Barich

Department of Chemistry

In partial fulfillment of the requirements

For the Degree of Doctor of Philosophy

Colorado State University

Fort Collins, Colorado

Summer 2016

Doctoral Committee

Advisor: Amber T. Krummel

Nancy Levinger
Steve Strauss
Matt Kipper
Randy Bartels

# ABSTRACT

## EXPLORING MODEL CHEMICAL SYSTEMS THROUGH A NEW LENS: COMBINING NOVEL MICROFLUIDIC TECHNOLOGY WITH INFRARED ANALYSIS TECHNIQUES

Multiple designer peptides, such as RADA-16, have been used as model systems to investigate the chemical parameters that influence protein folding and self-assembly processes. As such, the cause and effect relationship between folding outcomes and folding environmental factors have been extensively investigated. However, the mechanism of the folding process is largely unexplained due to the lack of an analysis technique that can capture structural changes on the time scale of the folding process. This thesis is the first step towards the ability to monitor the protein folding process with atomic structural resolution in real time. In this work, the sample handling capabilities of microfluidic devices are used to expand the experimental range of both infrared (IR) and two dimensional infrared (2D IR) measurement techniques. This includes the development of novel channel designs, overcoming IR compatibility issues, and setting precedent in monitoring chemical processes within microfluidic devices. Microfluidic channel geometries that perform microsecond mixing were developed to allow access to early reaction kinetics. A novel fabrication technique was developed to afford IR analysis methods to be utilized in microfluidic detection schemes. Lastly, model chemical reactions were studied in both Fourier transform IR microspectroscopy (FTIR microspectroscopy) and 2D IR spectroscopy experiments to highlight the applicability of the technology towards a broad range of chemical and biological systems, including the protein folding and self assembly processes.

# ACKNOWLEDGEMENTS

My journey through graduate school has been analogous to a marathon. I started off in 2011 with so much enthusiasm and hope for what would come, fully knowing that it was going to be a long and arduous experience. As with any race, although my success has been personal, it would not have been possible without the unwavering support from a great many people.

I would like to thank Amber for her mentorship, and truly understanding what it took to bring the best out of me. Amber created the perfect lab environment for my talents to both develop and flourish, and I would not have been the person I am today without you. Thank you for believing in me, even if you wouldn't admit it for the first few years.

I would also like to acknowledge the support from the other faculty within the chemistry department, especially Chuck Henry, Nancy Levinger, and Melissa Reynolds. Chuck opened both his lab and expertise to me as if I were one of his students. Thank you for helping me grow into a more professional researcher. Nancy provided me guidance and support, and always addressed my issues with a level head and sound advice. Melissa Reynolds was incredible with maintaining my direction and timeliness for every degree milestone. I would also like to thank the Department of Chemistry support staff for taking most of the stress out of the process.

I especially would like to thank Julie Denham. Your patience and selfless actions throughout these past years have significantly improved my state of being, both professionally and personally. I would not be half the person that I am today without you

I would thank my family for their love and support. My parents have always encouraged me to strive for bigger and better things while maintaining a clear view of the bigger picture, and my sister for constantly reminding me that there are more important issues than failed experiments.

Lastly, I would like to thank to all of my friends and co-workers that I have met during my time here. Without your support, outdoor excursions, and shenanigans, I would not have maintained the sanity required for this process.

TABLE OF CONTENTS

LIST OF FIGURES

# Chapter 1

# Introduction

## 1.1 Specific Aims

The objective of this work was to utilize the sample handling capabilities of microfluidic devices to expand the experimental range for infrared spectroscopy (IR) and two dimensional infrared (2D IR) spectroscopy techniques. This included the development of novel channel designs, overcoming IR compatibility issues with current microchip fabrication methods, and to set precedent for monitoring biological folding processes in microfluidic devices. Specifically, this thesis will cover the fabrication techniques developed, which afforded IR analysis within a microfluidic chip. Once the advantages of microfluidic sample manipulation were available, channel designs were developed to generate chemical environments previously unattainable via IR sampling methods. Lastly, the benefits of the technologies developed, were highlighted using model chemical reactions in both Fourier transform infrared microspectroscopy (FTIR microspectroscopy) and 2DIR spectroscopy experiments.

## 1.2 Protein Folding

Proteins perform many of the essential functions in cells, and are a necessary component to all life on Earth. The function of a protein is largely dictated by its shape, since the shape determines what other molecules can interact with that protein.[1] The process of folding and assembling into functional form is ubiquitous in nature. The entire process occurs through non-covalent interactions under thermodynamic equilibrium conditions to form well-defined arrangements. All protein structure starts with chains of amino acids, known as the primary

structure, then through a series of electrostatic interactions and solvation effects, fold into secondary and tertiary structures. Hydrogen bonding of the peptide backbone creates stabilization in the secondary structures, creating common arrangements such as α-helices or ß-sheets. Functional forms for many proteins require multiple tertiary structures, assembling into larger arrangements, or quaternary structures. The entire process utilizes its folding environment, composed of chemical factors such as pH, temperature, hydration, salt concentration, enzymatic assistance, and solvation environment.[2–7] The folding environment helps facilitate the change from primary and secondary to tertiary and quaternary structure, and has a direct impact on both the rate and outcome of the folding process.[8,9] Consequently, if the folding environment is altered, the proteins can misfold, creating structurally abnormal proteins. Structurally abnormal proteins can be harmless, however, others can be toxic, or lead to diseases. For example, proteopathy is a class of diseases that are caused by structurally abnormal proteins. Proteopathic diseases include Alzheimer's disease, Parkinson's disease, Huntington's disease, Amyotrophic Lateral Sclerosis, and prion diseases, to name a few.[10] A better understanding of the influence that environmental factors have on the folding and the self-assembly process for proteins, linked with proteomic knowledge for each of these diseases could allow for improved prevention or treatment.

Investigations using simple protein or peptide model systems are of particular interest due to the ubiquitous nature of protein folding and self-assembly. As a result, many simple systems of self-assembling peptides have been designed by cross-disciplinary fields ranging from chemical synthesis, polymer science, biotechnology, nanotechnology, molecular electronics, biomedical applications, and surface engineering.[11–17] The model system that inspired the work performed in this thesis is ideal for studying the folding and self-assembly process and is known as RADA.[18–20]

RADA-16 is a sixteen residue amino acid sequence, with a block of arginine (R), alanine (A), aspartic acid (D), and alanine (A) repeating four times, as seen in Figure 1.1. This creates a short strand with alternating hydrophilic and hydrophobic residues, where the hydrophilic residues alternate between positive and negative charges. This systematic pattern of alternating charges on hydrophilic residues creates complementary ionic bonds, aided by hydrophobic interactions that enhance the assembly process. Alternating positive and negative side chains was proposed to create antiparallel ß-sheets that would pair up into ß-strands, and further self-assemble into nanofibrils; the general scheme for this process is illustrated in Figure 1.1. More importantly, the well-ordered secondary, tertiary, and quaternary structures of RADA-16 are both initiated and influenced by specific changes in the folding environment. Understanding the influence that folding environment has on the formation of the RADA nanofibrils affords the opportunity to initiate and observe the folding process through controlled experimental design.

Different environment parameters for folding that have been studied with the RADA-16 self-assembly process are pH, temperature, hydration, salt concentration, and solvation environment.[2–7] In 2008, Zhaoyang Ye et al. used both circular dichroism (CD) and atomic force microscopy (AFM) to observe biophysical and morphological properties of the ß-sheet and self-assembled nanofibers under low pH and heat denatured conditions for RADA-16.[2] Under such extreme conditions, RADA was able to assemble into ß-sheets and nanofibers, however, ß-sheet content dramatically decreased from less extreme conditions. More importantly, they found that other physical or chemical factors such as peptide concentration, solvents, and solvation environment influence the nanofiber formation. In 2012, using AFM, CD, and Fourier Transform Infrared Spectroscopy (FTIR), Paolo Arosio et al. confirmed the stability of these

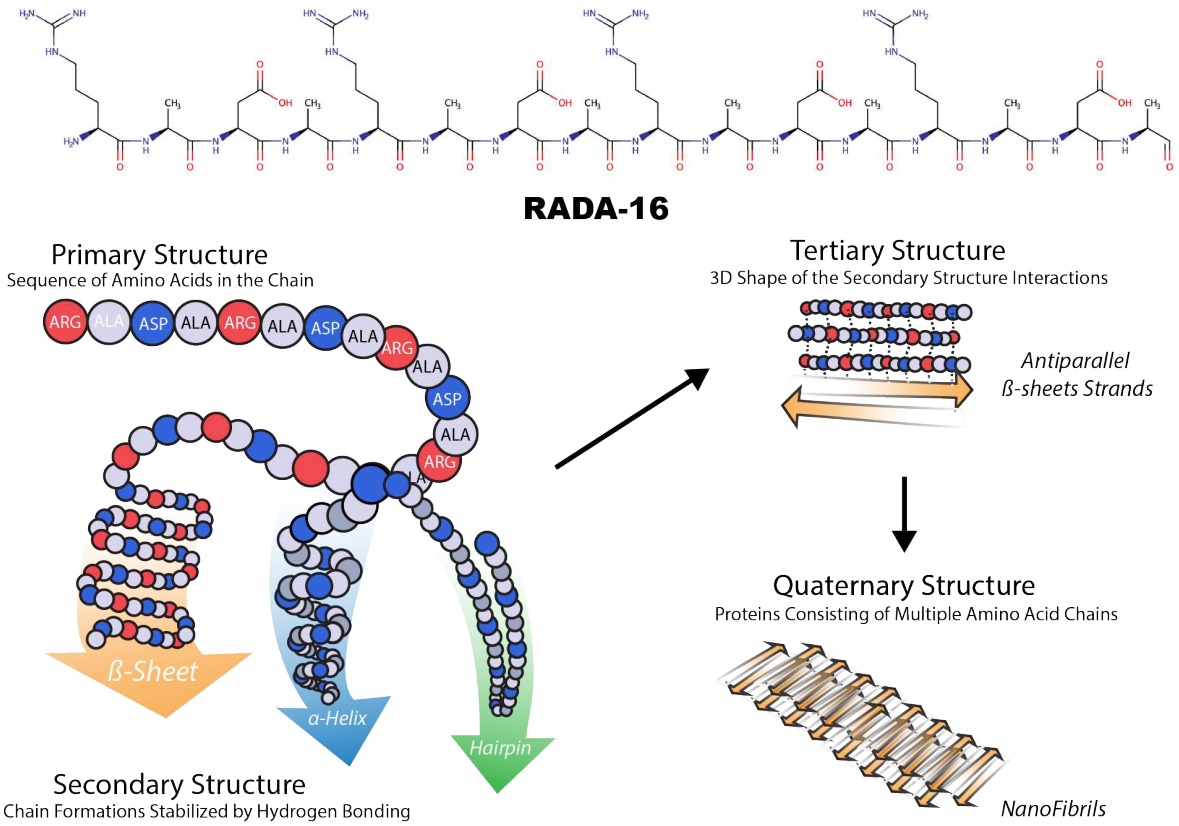


**Figure 1.1 RADA-16 Structure and Assembly Scheme**

The Molecular structure and suggested assembly scheme of RADA-16. RADA sequences of amino acids pair up into ß-sheets, that then align with other ß-sheets to form ß-Strands. The ß-strands then assemble into nanofibrils.

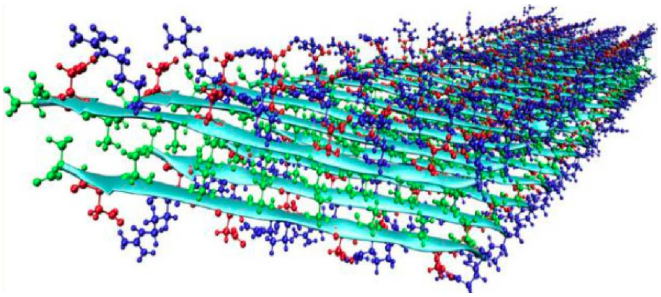

**Figure 1.2 RADA-16 Simulated Structure of a Nanofibril**

The simulated structure of a shift registered anti-parallel RADA-16 nanofibril. Reprinted with permission from Analytical Chemistry, **2013,** 7, 9, 7562-7572. Copyright 2013 American Chemical Society.[5]

nanofibers at low pH with varying conjugate bases.[3] Arosio, also found that the slow aggregation kinetics is dependent on both pH and anion type, observed through elongation of the fibrils without changing diameter. Using nuclear magnetic resonance (NMR), wide-angle x-ray diffraction (WAXD), and FTIR Ashley Cormier et al. explored the effects that temperature and hydration had on molecular structure and organization of the secondary structure of RADA-16.[4] Both factors, increased peptide storage temperature as well as the addition of water, caused changes to occur on faster time scales (measured over weeks), observed by monitoring secondary structure and long-range order. Further NMR studies in 2013, on isotopically labeled RADA-16 in combination with molecular modeling, led to the discovery of a molecular structure model for the nanofiber matrices.[5,6] Contrary to previously proposed anti-parallel ß-sheet structure, NMR established that the nanofibers were composed of shift-registered parallel ß-strands, consisting of two stacked ß-sheets with a hydrophobic core consisting of the alanine residues, shown as a simulated molecular structure in Figure 1.2. This hydrophobic core was supported by a study using AFM performed in 2013 by Maryam Kabiri et al.[7] Hydrophobic interactions were identified as the driving force behind self-assembly by using amino acids with different hydration potential added to the terminal amino acid of RADA.

By early 2014, the combined research had firmly established the structural response of RADA-16 to pH, temperature, hydration, salt concentration, and solvation environment. Still, very limited information existed regarding the step-by-step mechanisms behind the self-assembly and folding process itself. This lack of knowledge is due to the either limitations of the measurement techniques used, or difference in intention within the investigations performed. In order to measure the folding process itself, a measurement technique will require multiple experimental characteristics. These will include the structural sensitivity necessary to distinguish

between the protein conformations, and the time resolution that is faster than the folding process. Typically, folding and self-assembly timescales for proteins occurs on the microsecond to second time scales.[21] The measurement process will also require the ability to sample over a large number of experimental parameters, both effectively and efficiently and to initiate the folding process on command. Previous studies used structurally sensitive techniques such as AFM, NMR, WAXD, CD, and FTIR to identify the differences in secondary or quaternary structure caused by a change in one of the environmental conditions. AFM, NMR, and WAXD have the structural sensitivity necessary, but do not have the required time resolution. Both CD and IR spectroscopy can have both the time resolution and structural specificity necessary to observe the folding process, but were used to analyze the secondary structure content of assembled peptide because they lack the sample handling characteristics necessary to accomplish these measurements. The work performed in this thesis addressed these shortcomings by utilizing microfluidic sample handling procedures with IR analysis methods to move towards monitoring the structure of RADA-16 as it is undergoing the assembly process.

### 1.3 Infrared Spectroscopy

IR has been used extensively in the study of proteins.[22,23] Using IR, protein structure and function can be observed by two separate characteristics of the peptide chains: the normal modes of the amide group and the amino acid side chains.[24–26] The normal modes of the amide group include the amide I, amide II, amide III, and N-H stretching vibrations. The amide I and amide II vibrational modes are centered around 1650 $cm^{-1}$ and 1550 $cm^{-1}$ respectively. Both modes are sensitive to the hydrogen bonding environment and are used to report on the secondary structure of the protein backbone. The amino acid side chains have characteristic absorptions and are often directly involved in the molecular mechanism of protein folding. As such, observing

changes in the spectrum can provide insight into the local conditions the side chain is experiencing, yielding information regarding the mechanism of folding.

Multidimensional IR spectroscopies have also been used to explore protein structure and the folding process. Multidimensional IR spectroscopies are techniques that utilize ultrafast lasers to offer chemically specific information about solvent dynamics, molecular structure and conformational dynamics, and reaction kinetics. These tools have been used to examine a range of systems including solute-solvent interactions, protein conformational studies, and chemical exchange kinetics studies.[27–29] Further detail on the atomic level structure of proteins has been achieved through combining multidimensional spectroscopies with isotope labeling.[30] Isotope labeling affords site-specific investigation, even in complex and full-length proteins.[31–35] One of important capabilities that multidimensional spectroscopies provide is time resolution, achieving femtosecond (fs) time resolution. As a result, the time resolution is not limited by the measurement technique, but by the kinetic processes being observed. This introduces one of the challenges in using linear and multidimensional IR spectroscopy in monitoring the folding process: initiating the folding process.

Linear and multidimensional IR experiments have historically been performed on bulk samples, where a solution is created and then introduced into a sample cell, encased between two calcium fluoride ($CaF_2$) plates. The sample is inserted into the beam path and measurements are taken. The process from sample creation to measurement spans the course of minutes, generally longer, creating two distinct limitations. First, chemical kinetics are unable to be observed because at the time of first measurement, some form of chemical equilibrium has been achieved (steady state) due to the delay between sample preparation and measurement. Second, adequately sampling a large reaction space for one or two variables will take a considerably long

time since the time from sample preparation to measurement spans minutes. Several methods have been developed to overcome this limitation. Optical triggers were developed to initiate conformational changes in molecules or release hydronium ions in solution. In 2003, Jens Bredenbeck et al. used different frequencies of light to reversibly switch between cis and trans conformations in a cyclic octapeptide with azobenzene photoswitch embedded in the backbone.[36] The resulting conformational change was observed using both transient infrared spectroscopy and transient 2D IR spectroscopy.[37,38] The timescale of the conformational change occurred on the order of picoseconds, and the effects of homogeneous and inhomogeneous broadening were discussed in terms of the conformational distribution and dynamics. Angela Ramajo et al. performed temperature jump measurements by focusing nanosecond laser pulses into small sample volumes, aided by a small amount of heat-transducing dye.[39] The temperature jump experiments were used to trigger the fast folding/unfolding kinetics of an alanine based α-helical model peptide and reinforced the significant effect that ionic effects and pH have on folding. Further exploration of α-helical model peptides were performed using multiple laser-induced pH-jump experiments by the photoexcitative release of a proton.[40–44] Optical triggers are useful but have a limited time range with which to observe the folding process. Chemical triggers have been employed via stop flow technologies with limited success, however, only millisecond timescales and longer can be accessed.[45–47] A sample handling technique that could continuously chemically trigger a reaction on the microsecond time scales which folding and self-assembly processes occur would be ideal. We will utilize the sample handling capabilities of microfluidics to both initiate the chemical reactions and provide chemical environments capable of multiplexed measurements. Prior to the work performed in this thesis, chemical mixing in combination with 2D IR measurement techniques had not been accomplished.

## 1.4 Microfluidics

The field of microfluidics explores the flow of fluids through channels on the micrometer scale.[48] Microfluidic devices share the ability to precisely control nanoscale to microscale volumes of sample in order to perform a specific function. Precision control is performed using a microchannel, or series of microchannels, tailored to the particular experiment being performed. Functional difference between microfluidic channels arise due to both active and passive components, using fluid dynamic properties to manipulate the fluid within the channel.[49] Both channel type and functional components were previously developed for microfluidic devices and are covered extensively in the literature.[50]

A microfluidic device designed for monitoring protein folding would initiate the folding process on the microsecond to millisecond time scale by chemically changing the folding environment around the sample. This type of device is categorized as a fast or ultrafast mixer. Fast and ultrafast mixers have been demonstrated through a variety of techniques, such as lamination devices, droplet generators, turbulent flow devices, and other passive device geometries.[53–58] The focus herein will be on the passive geometry known as flow focusing devices due to the passive fast mixing process that it employs and its prior application to protein folding. Flow focusing devices use side channels to apply hydraulic pressure on a center inlet fluid into a thin stream, reducing the distance with which molecules have to diffuse. James Knight et al. introduced flow focusing devices in 1998 (Figure 1.3) where the control and function of the center fluid stream was an alternative approach to the fast mixing schemes at the time.[51,59] Mixing times were determined to be less than 10 $\mu$s, and stream widths as small as 50 nm were generated. This prompted further investigation and optimization into the form and function of device geometry.[60–63] For example, the simulated concentration map and mixing time

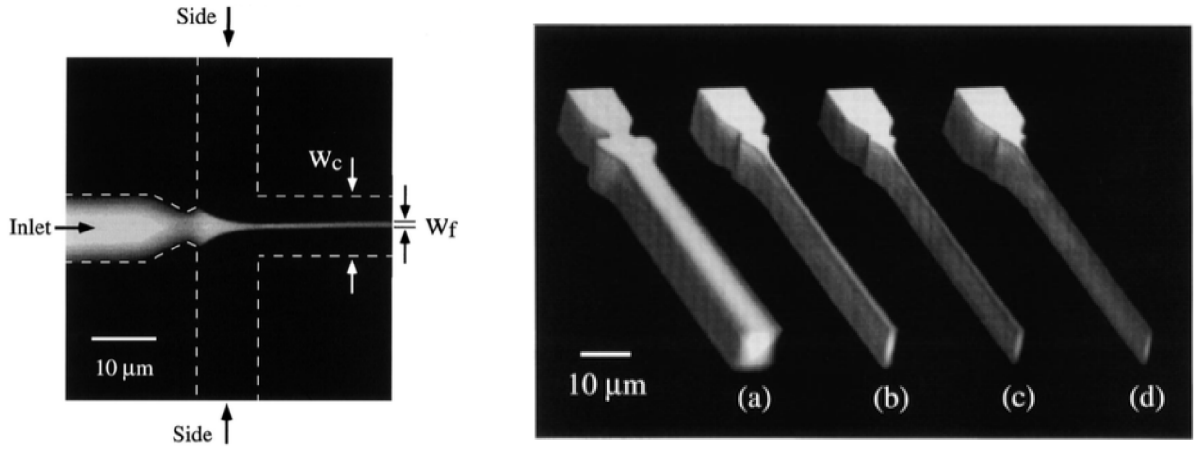


**Figure 1.3 Flow Focusing Geometry**

The general flow focusing layout and examples of the center streams achieved by varying the flow rate. Reprinted from Phys. Rev. Lett. **1998,** 80, 17, 3863-3866 with permission from The American Physical Society.[51]

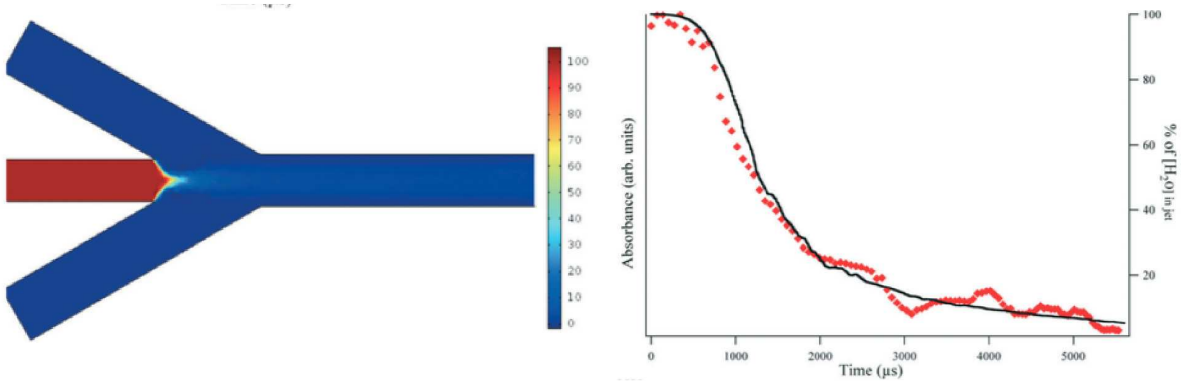


**Figure 1.4 Experimental Mixing Times Observed by the Flow Focusing Device**

A simulated flow focusing device focusing $H_2O$ with $D_2O$ and the plot of mixing with respect to time. Reproduced from Lab. Chip. **2014,** 14, 584-591 with permission from The Royal Society of Chemistry.[52]

results are shown Figure 1.4 of a flow focusing device used to focus $H_2O$ with $D_2O$. Hertzog et al. was the first application of flow focusing devices to observe the kinetics of protein folding.[62,64] Using a flow focusing device, 8 $\mu$s mixing time was achieved on single stranded DNA and acyl-CoA binding protein. Since then, further studies on the dynamics of proteins helped define the flow focusing device geometry as a reliable fast mixer.[52,65]

Another attribute that a device design tailored towards protein folding would have is the ability to sample multiple experimental parameters in a single measurement (multiplexed experiments). By employing multiplexing to the protein folding process, a range of different environmental conditions could be observed quickly. Multiplexed experiments are well established in the microfluidic and chemical biology literature, and are most commonlyperformed through the use of gradients.[66] Development of gradients in microfluidic devices first appeared in 2000 by Noo Jeon et al. with the introduction of a pyramidal microfluidic network, depicted in Figure 1.5.[67] Fluidic streams were repeatedly combined, mixed, and split to create different branches within the device with distinct mixture compositions. All branches were recombined to establish a gradient across the outlet channel. Similar modular microfluidic gradients were explored using larger numbers of branches to manipulate the shape of the gradient within the output channel.[69–72] Daniel Irimia et al. developed a different type of gradient generator in 2006, utilizing parallel dividers between adjacent streams in a microchannel, shown in figure 1.6.[68] The position and length of the dividers restricted the diffusion between the two streams to allow control over the mixing process, and therefore allowed a controlled gradient to be established. Jeon et al. is representative of the need and application of gradients in chemical biology in 2002, through a study monitoring the

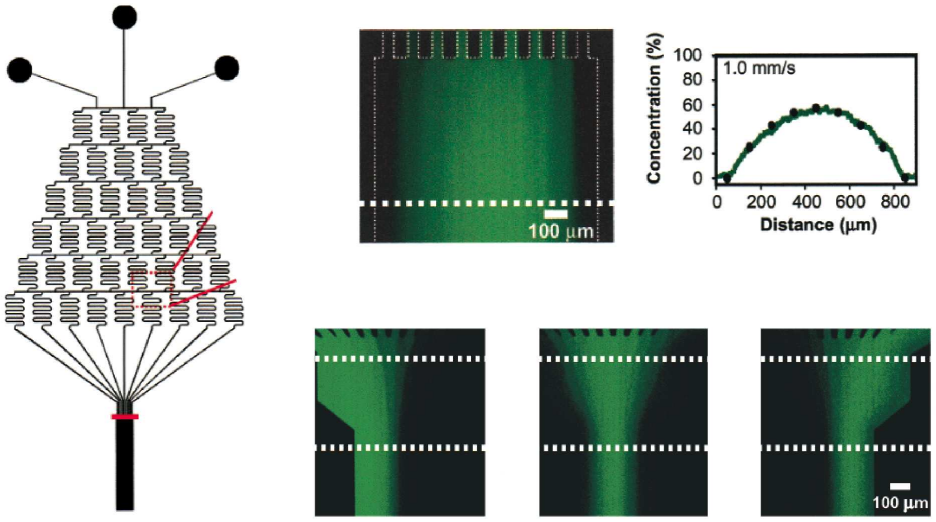


**Figure 1.5 Example of Piramidal Gradient Generation**

An example channel design for a piramidal gradient generation device. Examples of the gradients formed are also shown, exhibiting the control provided by this method. Adapted and reprinted with permission from Langmuir **2000,** 16, 8311-8316. Copyright 2000 American Chemical Society. [67]

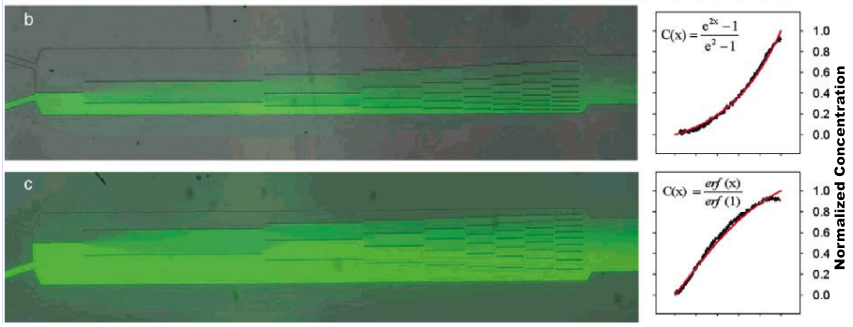


**Figure 1.6 Alternative Approach to Gradient Generation**

Two examples gradient generatiors designed to recreate target functions with the concentration gradient output. Adapted and reprinted with permission from Analytical Chemistry, **2006,** 78, 3472-3477. Copyright 2006 American Chemical Society. [68]

migration of human neutrophils in a interleukin-8 linear gradient.[73] By 2008, control over the gradient forming process and usefulness in chemical biology had been thoroughly established.

The microfluidic device ideally suited for monitoring protein folding would include attributes from both fast mixing and multiplexing devices. Fast mixing devices afford time resolution required to do kinetic studies. Multiplexed devices afford large numbers of experimental parameters to be measured simultaneously. However, prior to the work performed in this thesis, there have been no documented device designs that combine both fast mixing and multiplexing. Furthermore, the need to combine these capabilities has been overlooked. The work performed herein has created a bridge between both device families.

### 1.5 Infrared Analysis in Microfluidic Devices

Infrared analysis techniques coupled with microfluidic systems has become more prominent in the last decade. Prior to the rapid development of microfluidic devices in the early 2000's, minimal use of microfluidic devices for IR analysis had been performed. At that point, many microfluidic devices were fabricated through standard techniques.[74–79] Standard fabrication techniques consist of replica molding or hot embossing using silicon master mold, and are not compatible with any type of infrared analysis methods due to the high IR absorption of the fabrication materials. Many attempts at interfacing microfluidics with IR explored fabricating devices out of materials that are inherently IR transparent, or coupling on-line IR detection cells into current fluidic systems.[80–83] In 2004, Pan et al. fabricated a microfluidic device into a $CaF_2$ window.[80] Devices were crafted using a photolithographic patterning followed by etching with a bath of aqueous $Fe(NH_4)(SO_4)_2$ solution. Etching rates were determined to be 18 $\mu$m per day, and resulted in broadening of the desired channel widths, and could not reliably fabricate vertical walls as depicted in Figure 1.7. Also, developing a procedure for bonding the $CaF_2$ substrates

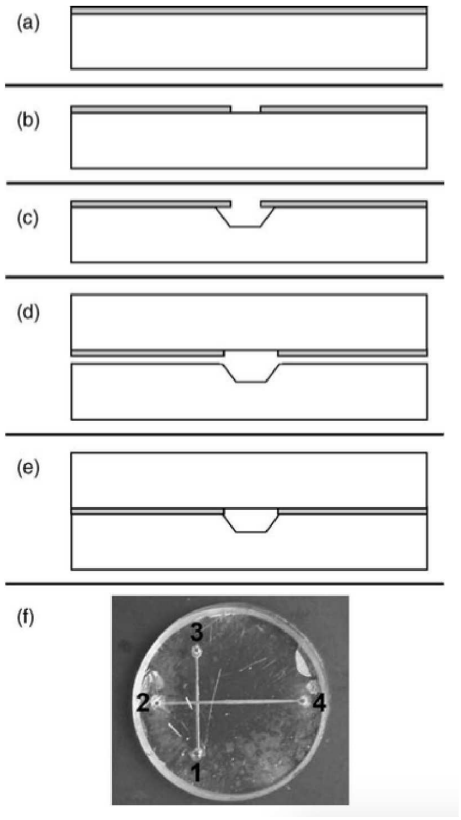


**Figure 1.7 Etched Calcium Fluoride Microfluidic Device**

Fabrication scheme for etched calcium fluoride microfluidic devices and an image of the final product. Reproduced from J. Chromatogr. A. **2004,** 231-235 with permission from Elsevier.

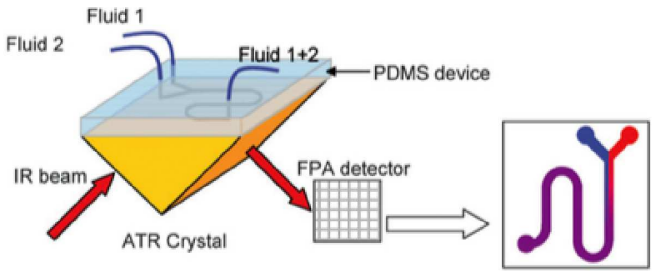


**Figure 1.8 ATR-FTIR Microfluidic Imagin System**

Schematic diagram for the ATR-FTIR imaging system. Reproduced from Lab. Chip. **2009,** 9, 2909-2913 with permission from The Royal Society of Chemistry.[93]

together was quite difficult. Birarda et al. had similar findings in 2010, using X-ARP 3100/10 photoresist, achieving etching rates of 100 nm/hr.[84] Further investigation into etching was performed by Brynson Lehmkuhl et al. in 2015 using a poly(dimethlsiloxane) (PDMS) channel with nitric acid, but was still plagued with slow etch rates. In 2002 and 2006 (respectively), Malin Kölhed et al. and S. Kulka et al. coupled capillary electrophoretic system to a FTIR detection scheme through insertion of a $CaF_2$ flow cell. The IR flow cell was created by using SU-8 polymer to pattern the channels onto one of the $CaF_2$ disks, and then sealed by the second $CaF_2$ disk. [81,83] Many similar methods using a thin layer of silicon or wax were explored, however, devices fabricated using this method result in channel walls with different wettability.[85–91] Similar approaches used thin layers of silicon in place of the SU-8 polymer. In 2007, Sergei Kazarian successfully implemented a different approach utilizing attenuated total reflectance FTIR spectroscpy (ATR-FTIR) as the detection scheme, illustrated in Figure 1.8.[92,93] Microfluidic channels were fabricated into PDMS or other polymers and then secured through self-adhesion or compression to the ATR crystal surface.[94,95] Using ATR allowed the application of polymer microfluidic devices, however, ATR detection is limited by the short penetration depth into the fluidic channels. In review, slow fabrication rates, mixed wettability issues, or surface detection methods limited the capabilities of microfluidic devices compatible with IR analysis techniques.

Prior to the work performed in this thesis, microchips comparable to the standard fabrication method that also allow transmission IR analysis techniques to be applied did not exist. Transmission capabilities affords analysis of microfluidic systems by more specialized IR techniques, such as FTIR imaging and multidimensional IR analysis. Application of these

techniques would greatly expand the experimental capabilities available to both IR and microfluidic disciplines.

### 1.6 Model Chemical Systems

Model chemical systems were used in this thesis to showcase the utility of the developed technology. Each model chemical system was derived from RADA-16 in order to simulate a potential parameter to be measured. Figure 1.9 indicates the component of RADA from which each model chemical system originated. N-methylacetamide (NMA) served as a prototype molecule for the peptide backbone.[96–102] Using the shift in vibrational frequency as an indicator of hydrogen bonding environment is analogous to using the shift in the Amide I to indicate secondary structure. Acetic acid was chosen for protonation and deprotonation experiments, and has been used as a model system for carboxylic acids.[103] Both the C-terminus and amino acid residue aspartic acid contain the carboxylic acid functional group. Their protonation state is an essential part in secondary, tertiary, and quaternary structure formation. Picolinic acid was chosen as a model system for a kinetic reaction due to the presence of a carboxylic acid side chain.[104–107] Picolinic acid is an essential chelation agent in the body, and the kinetic rates for the binding of iron (II) have never before been determined. Determining reaction kinetics is one of the major motivations behind the work performed in this thesis. Lastly, potassium cyanate (KOCN) was chosen as a representative molecular tag.[108–110] Although KOCN does not directly originate from RADA, vibrational tags are used as site specific probes to report on solvation dynamics. The KOCN experiments were also used to establish the feasibility of performing multidimensional IR spectroscopy on-chip. These model systems were chosen to represent significant stepping-stones towards experiments on a peptide-folding event and were used to validate the technology being developed.

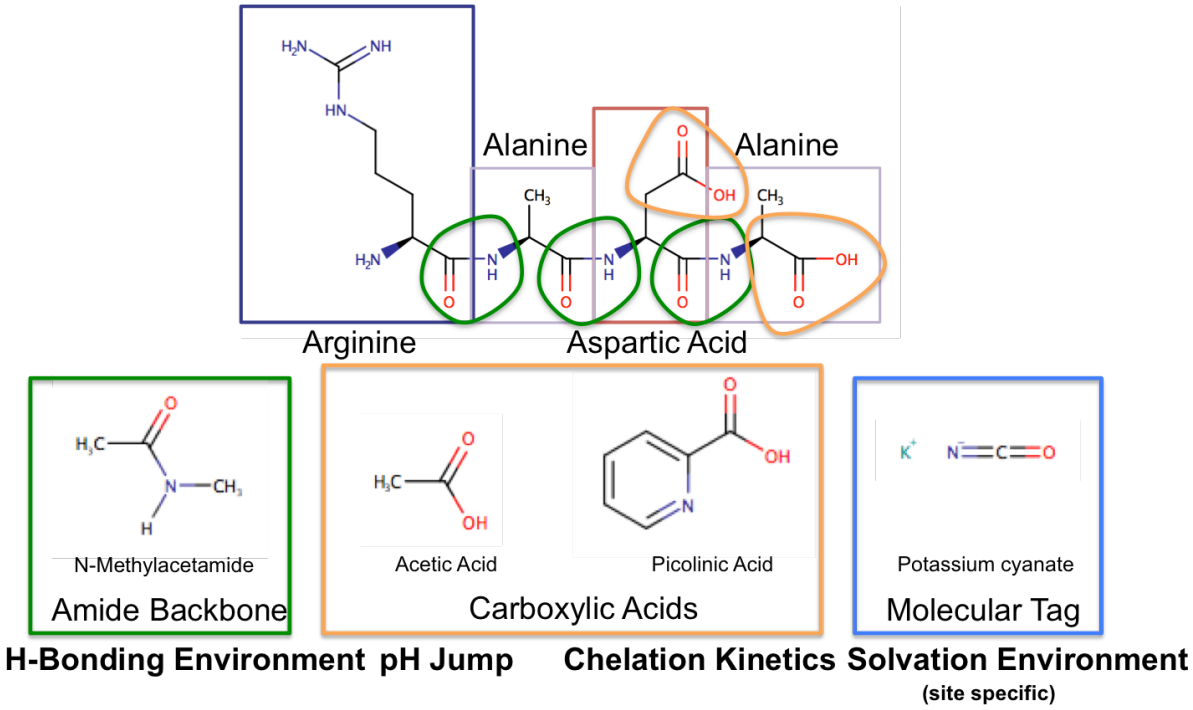


**Figure 1.9 Origin of the Chemical Model Systems**

The specific components of the peptide chain RADA with which the model chemical systems used in this thesis originate.

## 1.7 Outline of Thesis

This thesis details the efforts in developing a microfluidic platform that expanded the experimental range of both IR and 2DIR spectroscopy techniques. We aim to develop an experimental method that has the capability to characterize the fundamental interactions that drive protein folding and the self-assembly processes. This will include, structural sensitivity, time resolution, the ability to sample over a large number of sampling parameters, and the ability to initiate the assembly process.

Chapter 2 details all techniques performed in this work, which includes the methods and procedures required for fabrication, data collection, and data analysis. Examples of the Matlab and Labview code corresponding to the analysis are available in the appendices.

Chapter 3 describes the method used to integrate the structurally sensitive IR analysis techniques with microfluidic sample handling. This includes the techniques used to fabricate the IR compatible PDMS microfluidic devices used extensively in this thesis. IR compatible PDMS microfluidic devices afford low background absorption values in many wavelength regions of interest despite being fabricated in polymers that heavily absorb in the mid-IR.

Chapter 4 details design of a novel device geometry that allows the initiation of chemical reactions on a chip, the fast gradient generator. Interesting phenomenon occur away from chemical equilibrium, yet, current IR and 2DIR techniques make observing these phenomenon prohibitively challenging. The microfluidic design described in this chapter allows access to the early reaction kinetics.

In Chapter 5, all device architectures developed in this thesis are exhibited. Each geometry was specifically designed to create a unique experimental condition previously inaccessible to traditional infrared analysis techniques. Using FTIR microspectroscopy, model reactions were

used to highlight the utility and experimental value of each device design and provide examples of the new chemical insight available to each device style. This includes analysis on a pH jump experiment, solvation dynamics, and determination of the rate of a reaction.

Chapter 6 details the first successful implementation of 2DIR collected in a microfluidic device to quantify the spectral response of a model vibrational tag. A solvent gradient of methanol and DMF was generated in a serpentine device design, allowing the complete solvation response of potassium cyanate to be measured using 2DIR.

Chapter 7 concludes this thesis with a discussion of what was accomplished and the future direction for this technology.

## References


(1) Berg, J. M.; Tymoczko, J. L.; Stryer, L.; Berg, J. M.; Tymoczko, J. L.; Stryer, L. *Biochemistry*, 5th ed.; W H Freeman, 2002.

(2) Ye, Z.; Zhang, H.; Luo, H.; Wang, S.; Zhou, Q.; Du, X.; Tang, C.; Chen, L.; Liu, J.; Shi, Y.-K.; Zhang, E.-Y.; Ellis-Behnke, R.; Zhao, X. *J. Pept. Sci.* **2008**, *14* (2), 152.

(3) Arosio, P.; Owczarz, M.; Wu, H.; Butté, A.; Morbidelli, M. *Biophys. J.* **2012**, *102* (7), 1617.

(4) Cormier, A. R.; Ruiz-Orta, C.; Alamo, R. G.; Paravastu, A. K. *Biomacromolecules* **2012**, *13* (6), 1794.

(5) Cormier, A. R.; Pang, X.; Zimmerman, M. I.; Zhou, H.-X.; Paravastu, A. K. *ACS Nano* **2013**, *7* (9), 7562.

(6) Cormier, A. R.; Lopez-Majada, J. M.; Alamo, R. G.; Paravastu, A. K. *J. Pept. Sci.* **2013**, *19* (8), 477.

(7) Kabiri, M.; Bushnak, I.; McDermot, M. T.; Unsworth, L. D. *Biomacromolecules* **2013**, *14* (11), 3943.

(8) Kamp, M. W. van der; Daggett, V. *Biophysical Journal* **2010**, *99* (7), 2289.

(9) Herczenik, E.; Gebbink, M. F. B. G. *FASEB J* **2008**, *22* (7), 2115.

(10) Liang, C.; Ni, R.; Smith, J. E.; Childers, W. S.; Mehta, A. K.; Lynn, D. G. *J. Am. Chem. Soc.* **2014**, *136* (43), 15146.

(11) Leon, E. J.; Verma, N.; Zhang, S.; Lauffenburger, D. A.; Kamm, R. D. *J Biomater Sci Polym Ed* **1998**, *9* (3), 297.

(12) Zhu, J.; Marchant, R. E. *Expert Rev Med Devices* **2011**, *8* (5), 607.

(13) Zhang, S. *Biotechnology Advances* **2002**, *20* (5–6), 321.

(14) Jonker, A. M.; Löwik, D. W. P. M.; van Hest, J. C. M. *Chem. Mater.* **2012**, *24* (5), 759.

(15) Rajagopal, K.; Schneider, J. P. *Current Opinion in Structural Biology* **2004**, *14* (4), 480.

(16) Fichman, G.; Gazit, E. *Acta Biomaterialia* **2014**, *10* (4), 1671.

(17) Zhang, S.; Altman, M. *Reactive and Functional Polymers* **1999**, *41* (1–3), 91.

(18) Paradís-Bas, M.; Tulla-Puche, J.; Zompra, A. A.; Albericio, F. *Eur. J. Org. Chem.* **2013**, *2013* (26), 5871.

(19) Zhang, S.; Holmes, T. C.; DiPersio, C. M.; Hynes, R. O.; Su, X.; Rich, A. *Biomaterials* **1995**, *16* (18), 1385.

(20) Yokoi, H.; Kinoshita, T.; Zhang, S. *PNAS* **2005**, *102* (24), 8414.

(21) Naganathan, A. N.; Muñoz, V. *J. Am. Chem. Soc.* **2005**, *127* (2), 480.

(22) Barth, A.; Zscherp, C. *Q. Rev. Biophys.* **2002**, *35* (4), 369.

(23) Barth, A. Biochimica et Biophysica Acta (BBA) - Bioenergetics **2007**, 1767 (9), 1073.

(24) Wolpert, M.; Hellwig, P. Spectrochimica Acta Part A: Molecular and Biomolecular Spectroscopy **2006**, 64 (4), 987.

(25) Barth, A. Progress in Biophysics and Molecular Biology **2000**, 74 (3–5), 141.

(26) Byler, D. M.; Susi, H. *Biopolymers* **1986**, *25* (3), 469.

(27) Fayer, M. D. Annual Review Of Physical Chemistry **2009**, 60, 21.

(28) Hochstrasser, R. M. *PNAS* **2007**, *104* (36), 14190.

(29) Woutersen, S.; Hamm, P. *J. Phys.: Condens. Matter* **2002**, *14* (39), R1035.

(30) Kim, Y. S.; Wang, J.; Hochstrasser, R. M. *J. Phys. Chem. B* **2005**, *109* (15), 7511.

(31) Middleton, C. T.; Woys, A. M.; Mukherjee, S. S.; Zanni, M. T. *Methods* **2010**, *52* (1), 12.

(32) Thielges, M. C.; Axup, J. Y.; Wong, D.; Lee, H. S.; Chung, J. K.; Schultz, P. G.; Fayer, M. D. *Journal Of Physical Chemistry B* **2011**, *115* (38), 11294.

(33) Middleton, C. T.; Marek, P.; Cao, P.; Chiu, C.; Singh, S.; Woys, A. M.; de Pablo, J. J.; Raleigh, D. P.; Zanni, M. T. *Nat Chem* **2012**, *4* (5), 355.

(34) Buchanan, L. E.; Dunkelberger, E. B.; Tran, H. Q.; Cheng, P.-N.; Chiu, C.-C.; Cao, P.; Raleigh, D. P.; Pablo, J. J. de; Nowick, J. S.; Zanni, M. T. *PNAS* **2013**, *110* (48), 19285.

(35) Moran, S. D.; Zanni, M. T. *J. Phys. Chem. Lett.* **2014**, *5* (11), 1984.

(36) Bredenbeck, J.; Helbing, J.; Sieg, A.; Schrader, T.; Zinth, W.; Renner, C.; Behrendt, R.; Moroder, L.; Wachtveitl, J.; Hamm, P. *Proceedings of the National Academy of Sciences of the United States of America* **2003**, *100* (11), 6452.

(37) Bredenbeck, J.; Helbing, J.; Behrendt, R.; Renner, C.; Moroder, L.; Wachtveitl, J.; Hamm, P. *J. Phys. Chem. B* **2003**, *107* (33), 8654.

(38) Bredenbeck, J.; Helbing, J.; Hamm, P. *J. Am. Chem. Soc.* **2004**, *126* (4), 990.

(39) Pozo Ramajo, A.; Petty, S. A.; Volk, M. *Chemical Physics* **2006**, *323* (1), 11.

(40) Causgrove, T. P.; Dyer, R. B. *Chemical Physics* **2006**, *323* (1), 2.

(41) Kolano, C.; Helbing, J.; Bucher, G.; Sander, W.; Hamm, P. *The Journal of Physical Chemistry. B* **2007**, *111* (38), 11297.

(42) Baiz, C. R.; McRobbie, P. L.; Anna, J. M.; Geva, E.; Kubarych, K. J. *Acc. Chem. Res.* **2009**, *42* (9), 1395.

(43) Gooding, E. A.; Sharma, S.; Petty, S. A.; Fouts, E. A.; Palmer, C. J.; Nolan, B. E.; Volk, M. *Chem. Phys.* **2013**, *422*, 115.

(44) Donten, M. L.; Hamm, P. *Chem. Phys.* **2013**, *422*, 124.

(45) Kimura, T.; Takahashi, S.; Akiyama, S.; Uzawa, T.; Ishimori, K.; Morishima, I. *J. Am. Chem. Soc.* **2002**, *124* (39), 11596.

(46) Schleeger, M.; Wagner, C.; Vellekoop, M. J.; Lendl, B.; Heberle, J. *Anal Bioanal Chem* **2009**, *394* (7), 1869.

(47) Hinsmann, P.; Frank, J.; Svasek, P.; Harasek, M.; Lendl, B. *Lab Chip* **2001**, *1* (1), 16.

(48) Beebe, D. J.; Mensing, G. a; Walker, G. M. *Annual Review of Biomedical Engineering* **2002**, *4*, 261.

(49) Stone, H. A. In *CMOS Biotechnology*; Lee, H., Westervelt, R. M., Ham, D., Eds.; Series on Integrated Circuits and Systems; Springer US, 2007; pp 5–30.

(50) Squires, T. *Rev. Mod. Phys.* **2005**, *77* (3), 977.

(51) Knight, J. B.; Vishwanath, A.; Brody, J. P.; Austin, R. H. *Phys. Rev. Lett.* **1998**, *80* (17), 3863.

(52) Kise, D. P.; Magana, D.; Reddish, M. J.; Dyer, R. B. *Lab Chip* **2013**, *14* (3), 584.

(53) Gleeson, J. P. *Physics of Fluids (1994-present)* **2005**, *17* (10), 100614.

(54) You, J. B.; Kang, K.; Tran, T. T.; Park, H.; Hwang, W. R.; Kim, J. M.; Im, S. G. *Lab Chip* **2015**.

(55) Lu, Z.; McMahon, J.; Mohamed, H.; Barnard, D.; Shaikh, T. R.; Mannella, C. A.; Wagenknecht, T.; Lu, T.-M. *Sensors and Actuators B: Chemical* **2010**, *144* (1), 301.

(56) Hossain, S.; Ansari, M. a.; Husain, A.; Kim, K.-Y. *Chemical Engineering Journal* **2010**, *158* (2), 305.

(57) Bessoth, F. G.; DeMello, A. J.; Manz, A. *Anal. Commun.* **1999**, *36* (6), 213.

(58) Jeon, W.; Shin, C. B. *Chemical Engineering Journal* **2009**, *152* (2–3), 575.

(59) Brody, J. P.; Yager, P.; Goldstein, R. E.; Austin, R. H. *Biophys J* **1996**, *71* (6), 3430.

(60) Lee, G.-B.; Chang, C.-C.; Huang, S.-B.; Yang, R.-J. *J. Micromech. Microeng.* **2006**, *16* (5), 1024.

(61) Park, H. Y.; Qiu, X.; Rhoades, E.; Korlach, J.; Kwok, L. W.; Zipfel, W. R.; Webb, W. W.; Pollack, L. *Anal. Chem.* **2006**, *78* (13), 4465.

(62) Hertzog, D. E.; Ivorra, B.; Mohammadi, B.; Bakajin, O.; Santiago, J. G. *Anal. Chem.* **2006**, *78* (13), 4299.

(63) Gambin, Y.; Simonnet, C.; VanDelinder, V.; Deniz, A.; Groisman, A. *Lab on a Chip* **2010**, *10* (5), 598.

(64) Hertzog, D. E.; Michalet, X.; Jäger, M.; Kong, X.; Santiago, J. G.; Weiss, S.; Bakajin, O. *Anal. Chem.* **2004**, *76* (24), 7169.

(65) Burke, K. S.; Parul, D.; Reddish, M. J.; Dyer, R. B. *Lab Chip* **2013**, *13* (15), 2912.

(66) Weibel, D. B.; Whitesides, G. M. *Current Opinion in Chemical Biology* **2006**, *10* (6), 584.

(67) Jeon, N. L.; Dertinger, S. K. W.; Chiu, D. T.; Choi, I. S.; Stroock, A. D.; Whitesides, G. M. *Langmuir* **2000**, *16* (22), 8311.

(68) Irimia, D.; Geba, D. a; Toner, M. *Anal. Chem.* **2006**, *78* (10), 3472.

(69) Dertinger, S. K. W.; Chiu, D. T.; Jeon, N. L.; Whitesides, G. M. *Anal. Chem.* **2001**, *73* (6), 1240.

(70) Lin, F.; Saadi, W.; Rhee, S. W.; Wang, S.-J.; Mittal, S.; Jeon, N. L. *Lab Chip* **2004**, *4* (3), 164.

(71) Sun, K.; Wang, Z.; Jiang, X. *Lab Chip* **2008**, *8* (9), 1536.

(72) Mao, H.; Yang, T.; Cremer, P. S. *J. Am. Chem. Soc.* **2002**, *124* (16), 4432.

(73) Li Jeon, N.; Baskaran, H.; Dertinger, S. K. W.; Whitesides, G. M.; Van De Water, L.; Toner, M. *Nat Biotech* **2002**, *20* (8), 826.

(74) Anderson, J. R.; Chiu, D. T.; Jackman, R. J.; Cherniavskaya, O.; McDonald, J. C.; Wu, H.; Whitesides, S. H.; Whitesides, G. M. *Anal. Chem.* **2000**, *72* (14), 3158.

(75) Duffy, D. C.; McDonald, J. C.; Schueller, O. J.; Whitesides, G. M. *Anal. Chem.* **1998**, *70* (23), 4974.

(76) McDonald, J. C.; Whitesides, G. M. *Acc. Chem. Res.* **2002**, *35* (7), 491.

(77) Miserere, S.; Mottet, G.; Taniga, V.; Descroix, S.; Viovy, J.-L.; Malaquin, L. *Lab Chip* **2012**, *12* (10), 1849.

(78) Jo, B.; Lerberghe, L. M. V.; Motsegood, K. M.; Beebe, D. J. *Journal of Microelectromechanical Systems* **2000**, *9* (1), 76.

(79) Becker, H.; Gärtner, C. *Anal Bioanal Chem* **2007**, *390* (1), 89.

(80) Pan, T.; Kelly, R. T.; Asplund, M. C.; Woolley, A. T. *Journal of Chromatography A* **2004**, *1027* (1-2), 231.

(81) Kölhed, M.; Hinsmann, P.; Svasek, P.; Frank, J.; Karlberg, B.; Lendl, B. *Anal. Chem.* **2002**, *74* (15), 3843.

(82) Floyd, T. M.; Schmidt, M. a.; Jensen, K. F. *Industrial & Engineering Chemistry Research* **2005**, *44* (8), 2351.

(83) Kulka, S.; Quintás, G.; Lendl, B. *Vibrational Spectroscopy* **2006**, *42* (2), 392.

(84) Birarda, G.; Grenci, G.; Businaro, L.; Marmiroli, B.; Pacor, S.; Vaccari, L. *Microelectronic Engineering* **2010**, *87* (5-8), 806.

(85) Grenci, G.; Birarda, G.; Mitri, E.; Businaro, L.; Pacor, S.; Vaccari, L.; Tormen, M. *Microelectronic Engineering* **2012**, *98*, 698.

(86) Mitri, E.; Birarda, G.; Vaccari, L.; Kenig, S.; Tormen, M.; Grenci, G. *Lab Chip* **2014**, *14* (1), 210.

(87) Mitri, E.; Pozzato, a.; Coceano, G.; Cojoc, D.; Vaccari, L.; Tormen, M.; Grenci, G. *Microelectronic Engineering* **2013**, *107*, 6.

(88) Wagner, C.; Buchegger, W.; Vellekoop, M.; Kraft, M.; Lendl, B. *Anal Bioanal Chem* **2011**, *400*, 2487.

(89) Chan, K. L. A.; Kazarian, S. G. *Anal. Chem.* **2012**, *84* (9), 4052.

(90) Chan, K. L. A.; Niu, X.; de Mello, A. J.; Kazarian, S. G. *Lab Chip* **2010**, *10* (16), 2170.

(91) Chan, K. L. A.; Niu, X.; deMello, A. J.; Kazarian, S. G. *Anal. Chem.* **2011**, *83* (9), 3606.

(92) Kazarian, S. G. *Anal Bioanal Chem* **2007**, *388* (3), 529.

(93) Chan, K. L. A.; Gulati, S.; Edel, J. B.; Mello, A. J. de; Kazarian, S. G. *Lab Chip* **2009**, *9* (20), 2909.

(94) Greener, J.; Abbasi, B.; Kumacheva, E. *Lab Chip* **2010**, *10* (12), 1561.

(95) Karabudak, E. *ELECTROPHORESIS* **2014**, *35* (2-3), 236.

(96) Ham, S.; Kim, J.-H.; Lee, H.; Cho, M. *J. Chem. Phys.* **2003**, *118* (8), 3491.

(97) Eaton, G.; Symons, M. C. R.; Rastogi, P. P. *J. Chem. Soc., Faraday Trans. 1* **1989**, *85* (10), 3257.

(98) Guo, H.; Karplus, M. *J. Phys. Chem.* **1992**, *96* (18), 7273.

(99) Woutersen, S.; Mu, Y.; Stock, G.; Hamm, P. *Chem. Phys.* **2001**, *266* (2–3), 137.

(100) Woutersen, S.; Pfister, R.; Hamm, P.; Mu, Y.; Kosov, D. S.; Stock, G. *J. Chem. Phys.* **2002**, *117* (14), 6833.

(101) Zanni, M. T.; Asplund, M. C.; Hochstrasser, R. M. *J. Chem. Phys.* **2001**, *114* (10), 4579.

(102) Kwac, K.; Cho, M. *J. Raman Spectrosc.* **2005**, *36* (4), 326.

(103) Emmeluth, C.; Suhm, M. A.; Luckhaus, D. *The Journal of Chemical Physics* **2003**, *118* (5), 2242.

(104) Gary W. Evans. *Life Chemistry Reports* **1982**, *1*, 57.

(105) Boyd, S. A.; Kohrman, R. E.; West, D. X. *Journal of Inorganic and Nuclear Chemistry* **1976**, *38* (3), 607.

(106) Freiser, H. *Acc. Chem. Res.* **1984**, *17* (4), 126.

(107) Fife, T. H.; Przystas, T. J. *J. Am. Chem. Soc.* **1985**, *107* (4), 1041.

(108) Son, H.; Jin, H.; Choi, S. R.; Jung, H. W.; Park, S. *J. Phys. Chem. B* **2012**, *116* (30), 9152.

(109) Lenchenkov, V.; She, C.; Lian, T. *J. Phys. Chem. B* **2006**, *110* (40), 19990.

(110) Wilderen, L. J. G. W. van; Kern-Michler, D.; Müller-Werkmeister, H. M.; Bredenbeck, J. *Phys. Chem. Chem. Phys.* **2014**, *16* (36), 19643.

# Chapter 2

## Methods and Materials

### 2.1 Introduction

The work described in this chapter explains the steps required to create microfluidic devices compatible with mid-IR light and quantifies the chemical environments created on-chip for IR and 2D IR experiments. Each experiment involving microfluidic devices consisted of the same general layout, as summarized in section 2.2. Further detail regarding the microfluidic experimental methods follow. These methods include fabrication, flow control, fluid delivery, and device integration. Section 2.3 describes experimental detection methods used in this thesis, and the experimental parameters used. The chapter concludes with the approach to processing and interpretation of the data collected from each method of detection.

### 2.2 General Microfluidic Experimental Setup

Every experiment performed in this thesis involving a microfluidic device follows the same general experimental design, as seen in Figure 2.1. Following the flow of the fluidic control, a custom Labview VI was developed, controlling the syringe pumps used to deliver a constant flow of fluids to the chip. Fluids were then, either collected for further analysis or as a waste by-product upon exiting the microfluidic chip. Detection and imaging methods varied, however, all methods of detection utilized an illumination source and a detector. All methods were performed in transmission mode with the exception of fluorescent microscopy. Fluorescent microscopy was performed with excitation illumination from the same direction as the device was being imaged, such that the excitation light was not detected.

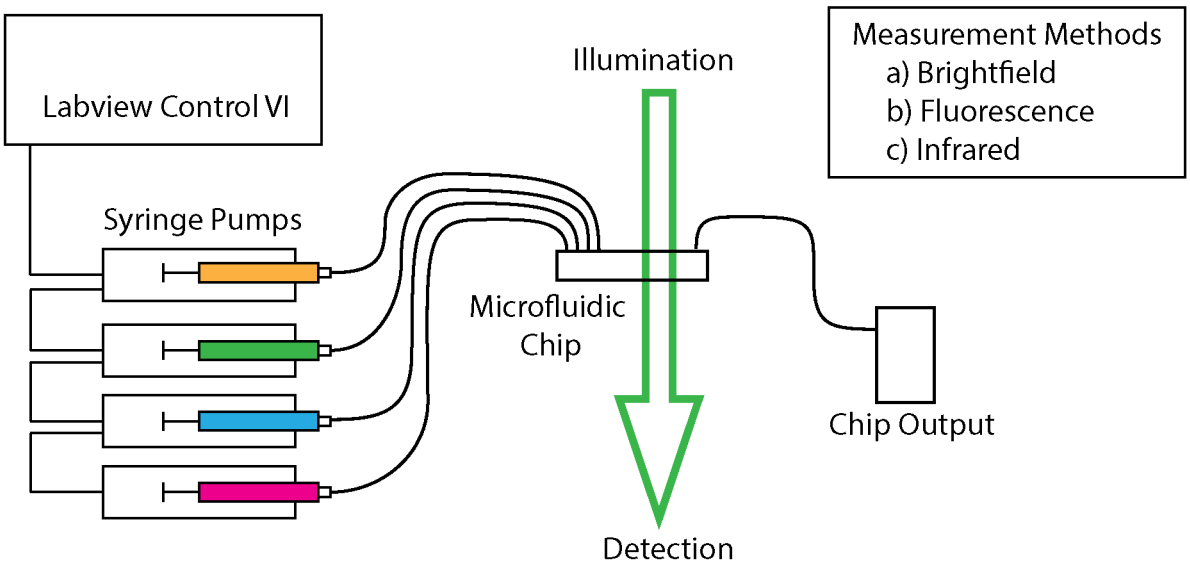


**Figure 2.1 Overview of the Microfluidic Experimental Design**

The figure can be followed from upper left to right. Briefly, a laptop with a customized Labview VI controls an appropriate number of syringe pumps. The syringe pumps deliver the fluidic solutions to the microfluidic chip. The microfluidic chip then performs the desired fluidic handling, and dispenses the output. Detection and imaging was performed normal to the device by the appropriate illumination source and detection method.

### 2.2.1 Fabrication of Microfluidic Devices

Multiple types of microfluidic devices were necessary in this project due to the broad range of detection methods applied. For example, microfluidic devices used in IR microscopy experiments required more than the standard microfluidic fabrication methods. In this section, the fabrication method used in this project will be described in detail. This will include, fabrication of the master mold, standard poly(dimethylsiloxane) (PDMS), the IR compatible PDMS, and IR compatible cyclo-olefin copolymer (COC) microfluidic chips.

Each device ultimately started from a custom channel design crafted in Adobe Illustrator. From here, negatives of the channel designs were printed at 20K DPI, emulsion side down, by CAD/Art Services, and used as photomasks. Photolithography was used to transfer the designs on the photomasks into 3D molds. Polished 76.2 mm diameter silicon wafers (Silicon Valley Microelectronics, Inc.) were cleaned using a combination of solvent rinses of acetone, methanol, and DI water, and then air plasma. Using a Laurell Tech Corp. (WS-6500Mz-23NPP/Lite) spin-coater, SU-8 2025 (MicroChem) was evenly distributed across the silicon wafer. SU-8 2025 is specifically designed for use in the fabrication of microfluidic molds between 20 $\mu$m and 80 $\mu$m tall. Fabrication of each mold followed the recommended protocol provided by MicroChem to the desired channel depth.[1] The mold making process is summarized in Figure 2.2. The height of the SU-8 2025 channels on the mold were appropriate to both the channel design and the intended experiment. Once the molds were fabricated, further modifications were needed to allow for IR compatibility. Hexamethyldisilazane (HMDS, Sigma Aldrich) was added dropwise to the master molds to modify the surface. Surface modification of the microfluidic molds facilitated the transfer of the microchannel layers more effectively.

Standard PDMS devices were fabricated using standard soft lithography techniques, also known as replica molding.[2,3] The lower part of Figure 2.2 displays the brief steps involved in replica molding. Each SU-8 2025 mold was placed into a 100 mm diameter petri dish. The petri dish was then filled with de-gassed, premixed Sylgard 184 Silicon Elastomer (Dow Corning) and heated in a 95 ºC oven for at least 1 hour. Tubing access into the microchannel system was accomplished using 1 mm biopsy punch and punching through the PDMS. Elastomeric sections of PDMS, one containing the microchannel and a blank section, were sealed in a Harrick Plasma Cleaner/Sterilizer PDC-32G by exposing each section to air plasma for 20 seconds, and then applying a constant pressure. Each face of the microfluidic chip was covered with Scotch Tape for protection from dust until use.

Fabrication of IR compatible PDMS microfluidic chips was accomplished by first creating every component required, then assembling them together, into a microchip.[4] An overview of this process is outlined in Figure 2.3. IR compatible microfluidic chips leveraged thinner areas of PDMS in strategic locations, or 'viewing areas', on the chip. This reduced the background absorption of the device during measurement. Assembly of the chips consisted of sealing each of the three different pieces together: the microchannel layer, the support layer, and the IR transparent backbone with an adhesion layer. The microchannel layer was fabricated by placing a small amount of PDMS onto a surface-modified SU-8 2025 mold, encompassed by 3M Scotchpak Release liner. The specific Scotchpak release liner was chosen because its resistance to the heat required to cure PDMS and the specific adhesion to cured PDMS allowing both heat and pressure to be applied with a Hydraulic Unit (Model 3912, Carver Inc.). A thin layer of PDMS was cured onto the mold and attached to the release liner. The mold was then disengaged leaving a thin PDMS layer attached to the release liner with the channels embedded into it, the

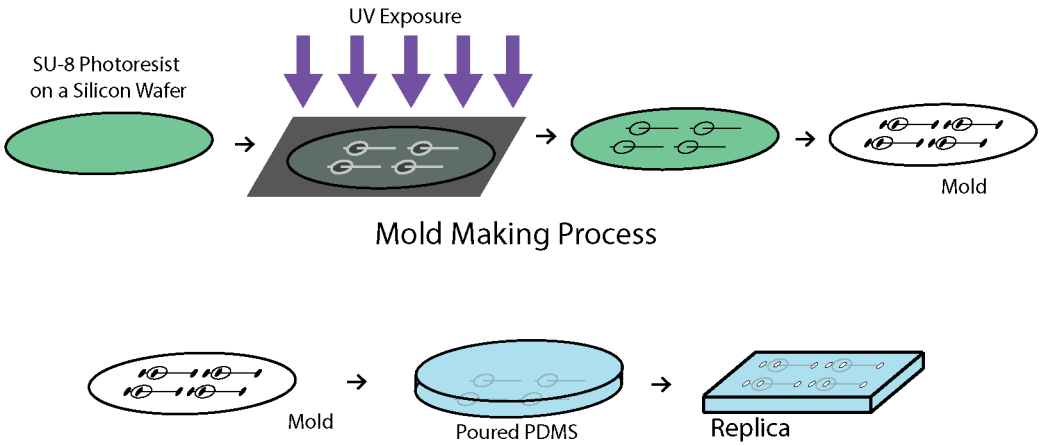


**Figure 2.2 Mold and Traditional Microfluidic Device Fabrication**

Master molds were made through photolithography (Top). Traditonal fabrication undergoes replica molding for the fabrication of PDMS microfluidic devices (Bottom).

microchannel layer. The support layer consisted of a thick PDMS slab and was responsible for interfacing the microchannels with the tubing. Fabrication occurred through the method used for standard PDMS devices, using a photomask of only the tubing access points and a 'viewing area'. The viewing area consisted of a section of PDMS removed right above the channel in the region of interest for measurement. The IR transparent backbone and adhesion layer were required to provide rigid structure to the chip and seal the backside of the microfluidic channels. $CaF_2$ was chosen as the material for the backbone due to the IR transparency of the material. An adhesion layer of PDMS was spun across the surface of the $CaF_2$ window using the Laurell Tech Corp. spin coater. The PDMS adhesion layer ranged in height between 8 $\mu$m and 20 $\mu$m, and was cured in a 95 ºC oven for minimum of 1 hour. This layer allows for the microchannel layer to be sealed to the $CaF_2$ surface and provides uniform wettability for all channel walls once the chip is assembled. Assembly of the complete microfluidic chip was accomplished through rapid PDMS-PDMS bonding using air plasma, first bonding the microchannel layer to the adhesion layer on the IR transparent backbone. Once secure, the release liner was carefully removed and any PDMS extending past the edges of the $CaF_2$ was trimmed. The support layer was then sealed to the top of the microchannel layer. Scotch tape was used for protection of the support layer and viewing area until use.

IR compatible COC microfluidic chips were fabricated using a combination of hot embossing and lamination as shown in Figure 2.4. Thin COC and cyclo-olefin polymer (COP) are commercially available through the Microfluidic ChipShop. Zeonor COP sheets of 40 $\mu$m, 50 $\mu$m, and 100 $\mu$m thick were aquired, as well as 140 $\mu$m and 240 $\mu$m thick Topaz COC for microchip fabrication. Squares of the COP were cut to match the size of the microchannels on the surface-modified SU-8 2025 molds. Using a hydraulic heated press, the COP squares were

pressed into the master mold, similar to hot embossing.[5] After the squares were removed and adequately cooled, fluid access holes to the channels were punched out via 1 mm biopsy punch. Using an Apache AL13P laminator, the COP square with embedded microchannels was laminated onto a similarly sized square of Topaz COC.[6] Using an 8" ULINE impulse sealer, the edges of the laminated squares were permanently sealed together, and then secured onto a ¼" acrylic plate. IDEX Nanoport assemblies were used to interface the fluidic tubing with the channels, followed by sealing the nanoports to the device with epoxy.

### 2.2.2 Microfluidic Interfacing and Flow Control

Accurate and stable flow conditions are necessary to apply the assumptions of steady state fluid mechanics. To achieve steady-state fluid mechanics, a consistent and unwavering environment for every part of the microfluidic system must be provided. Undisturbed tubing delivering the fluids to the device, consistent pressure being provided by the pumps, and a controlled environment for the microfluidic devices are all necessary to afford steady state flow conditions. Every microfluidic device used in this project took advantage of these conditions to provide the precision and accuracy appropriate for the experiments performed. In this section, the precautions and procedures used to assure steady state flow will be discussed.

Active flow pumping was utilized to provide the pressure drop required for fluid flow in every experiment performed. Consistent fluid flow was accomplished using NE-500 Programmable OEM syringe pumps controlled through a custom Labview VI, found in Appendix A2.1. The programmable syringe pumps allowed for flow parameters to be controlled through a computer interface, limiting the required adjustment for the syringe pumps themselves. By minimizing any external contact with the syringe pumps and tubing connecting the pumps to

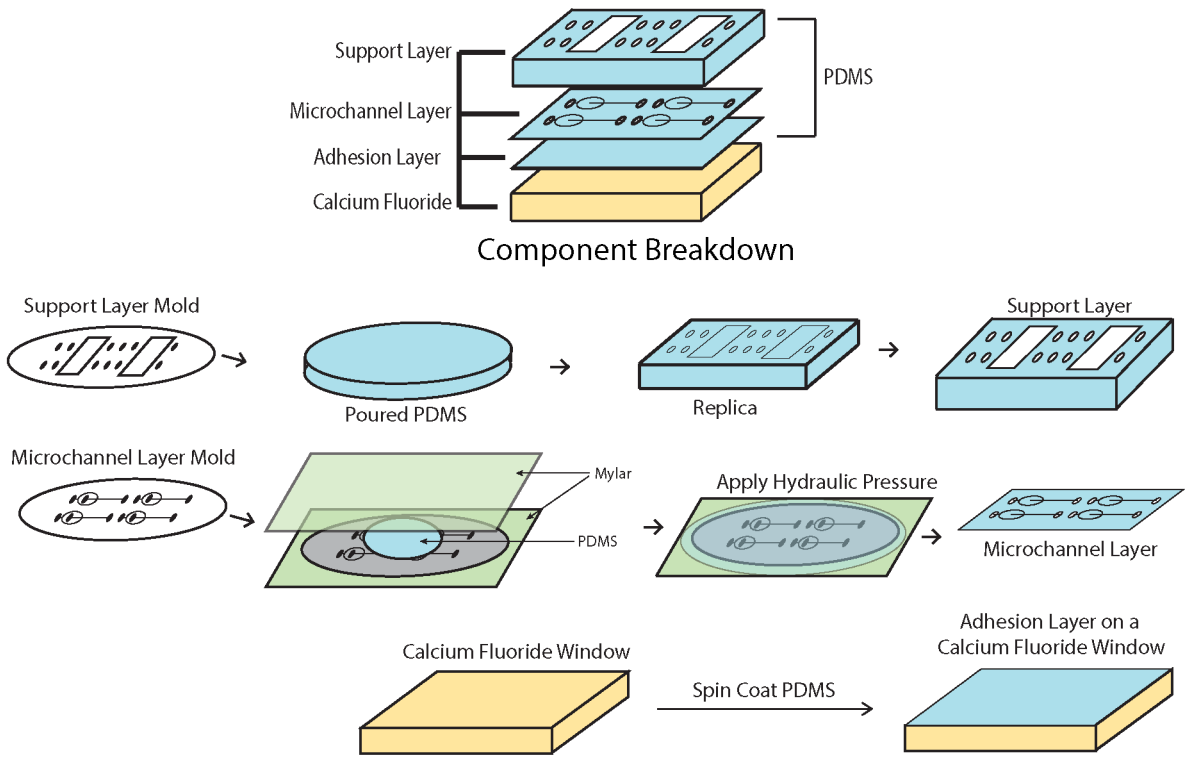


**Figure 2.3 IR Compatible PDMS Fabrication**

IR Compatible PDMS devices consist of four components (top). An overview of the fabrication of each component is then listed in order from the top most layer, the support layer, to the adhesion layer on the Calcium Fluoride backbone.

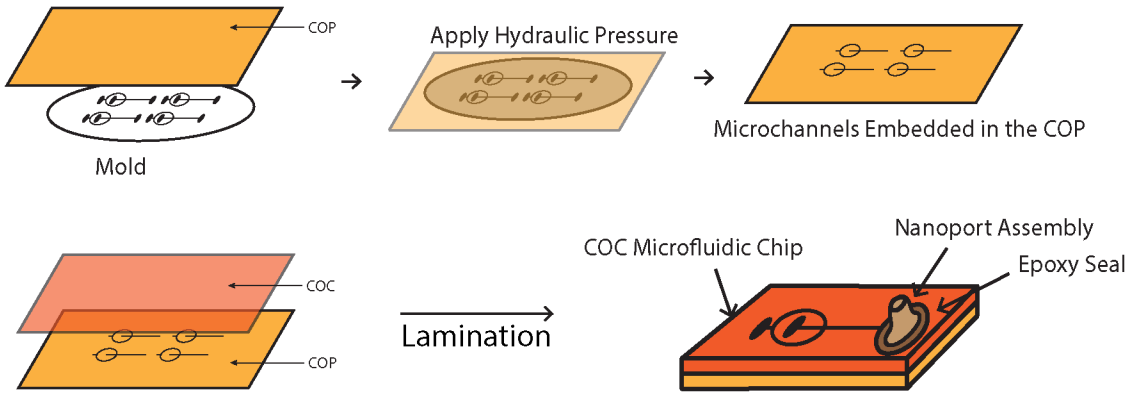


**Figure 2.4 IR Compatible COC Fabrication**

Fabrication of IR compatible COC devies is accomplished through hot embossing, followed by lamination, both outlined above.

the chip, a more stable fluidic environment could be achieved. The specific parameters of the setup varied depending on the necessary flow conditions. Syringes, between 1 mL to 10 mL, were connected through IDEX Luer Lock adaptors to the Teflon tubing that interfaced with the microfluidic device. The tubing was then connected to the microfluidic device through either the tubing access holes or the IDEX Nanoport assemblies. The entire setup can be observed in Figure 2.5.

Extra stability for the microfluidic device was provided by an acrylic case forming a controlled environment. Ideally, such a case would also provide a universal interface between the microfluidic chips and every instrument used for measurement or detection. The goal was to create a 'plug–and-play' style microfluidic chip casing. Theoretically, the case would allow any microfluidic chip to be quickly inserted in the IR microscope, custom built time-space mapping fluorescent microscope, and 2DIR spectrometer. Each chip casing would also provide stabilization for the chip-tubing interface, support for the seals between chip components, protect the $CaF_2$ backbone layer, and maintain rigid support for the COC microfluidic chips. Lastly, the ideal casing must not interfere with any of the measurements performed by the instruments listed above.

Developing a universal case was done using a Zing Epilog laser cutter and Adobe Illustrator. Each case consisted of three separate individually designed layers cut out of ¼" clear acrylic and held together by four or six screws. A schematic for the case is shown in Figure 2.6 on the left side of the figure. Two of the acrylic layers were more generic, providing unobstructed access from the lower side of the microfluidic device and a rigid base to mount the microfluidic chip. Two layers were required to reinforce the ¼" acrylic and provide the necessary rigidity. The last acrylic layer, the top of the case, was designed to provide small amounts of compression by

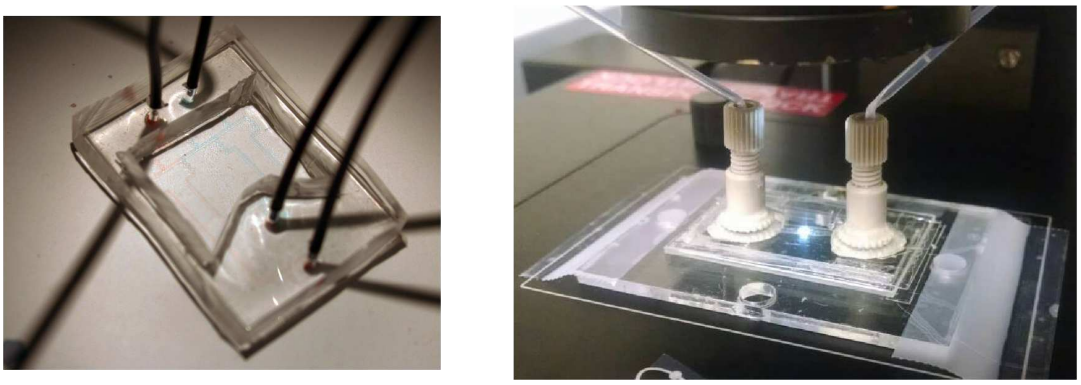

**Figure 2.5 Tubing Coupled to Microfluidic Devices**

PDMS (Left) and COC (Right) Microfluidic devices interfaced with the syringes that provide the fluids into the channels.

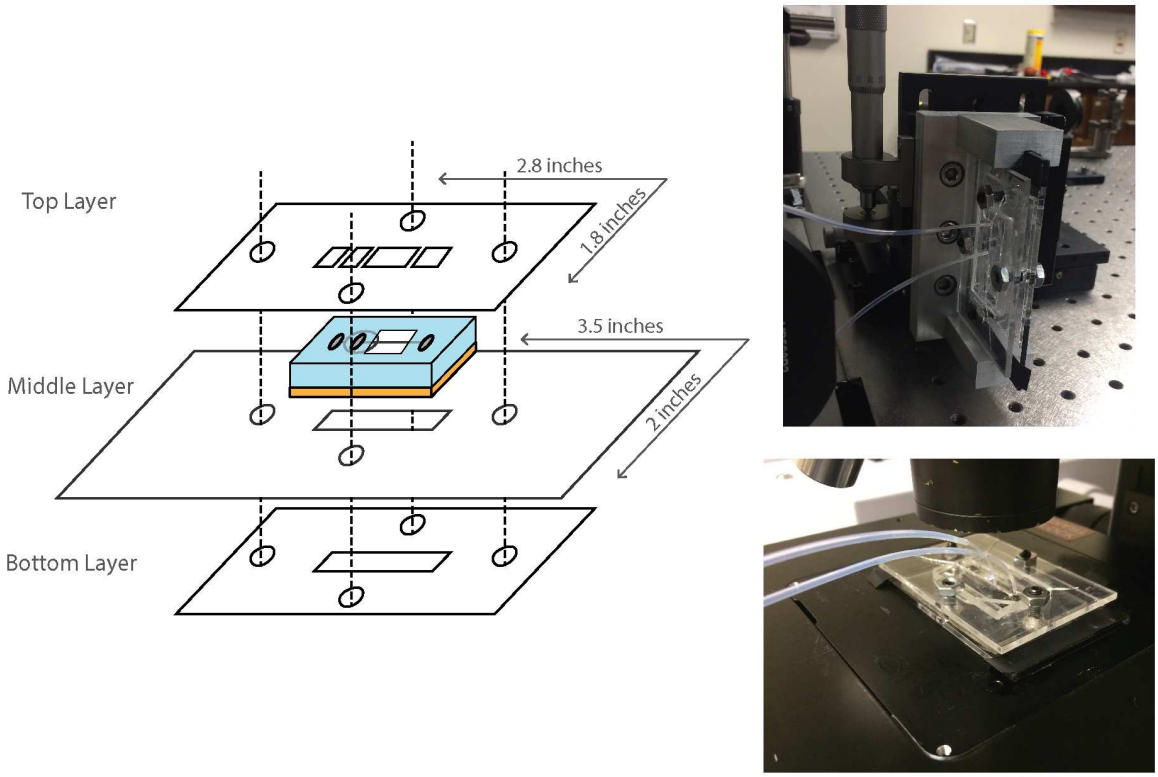


**Figure 2.6 Microfluidic Device Case Schematic**

The schematic for the microfluidic case designed for easy integration with all detection methods is displayed on the left. Images of the case in use on the 2DIR spectrometer (top right) and the FTIR microspectroscope (lower right).

using the assembly screws to press the microfluidic chip into the rigid base layers. The compression was necessary to reinforce the seams between the layers of the PDMS IR compatible microfluidic device. Top layers were customized to each channel design, incorporating openings in the acrylic specifically for the viewing area of interest, and tubing access into the microfluidic chip.

The dimensions for the case mimicked the standard $CaF_2$ sample cell used for static FTIR spectroscopy. The specific components of the standard sample cell will be discussed further in section 2.3.2. The $CaF_2$ sample cell was chosen as a model since it was designed to transfer between both the FTIR and 2D IR spectrometers; therefore the universality was already a benefit. Specifically, the interfacing mechanism of the standard sample cell consisted of a 3.5" by 2" steel plate that slotted in place and then into the spectrometers. The middle layer of the microfluidic case was cut to match the dimensions of the steel plate. By design, the middle layer would fit securely into the sample holders on the spectrometers. However, the IR microscope did not share a common sample holder, therefore, the lowest layer of the microfluidic case was tasked to interface with the IR microscope. The microscope stage was designed to have several exchangeable sample stage interfaces, each with a specific purpose. One of these attachments was originally intended to house microscope slides, and therefore had a section open that was 2.8" x 1.8". The lowest layer of the acrylic was then cut to match this opening, fitting snuggly within the case to prevent any possible side-to-side movement or drift of the case. By matching the hole exactly, the microfluidic case had the option to fit securely into the stage insert without the need for any extra fastening devices. Lastly, the time-space mapping fluorescence microscope was designed in the final stages of this project. At that time, the cases for the microfluidic devices had been extensively developed. Therefore, it was much simpler to adjust

the sample holder on the spectrometers to match the case for the microfluidic devices. Using a Lulzbot 3D Printer (Aleph Objects Inc.), a sample holder identical to the one printed for the FTIR spectrometer was created and mounted onto a XYZ stage. This allowed for the cases to be secured, while maintaining the translation required for the images.

### 2.3 Detection Instrumentation Methods

The analysis performed in this thesis required many different detection methods to be applied. For example, a single chemical kinetics study requires the collection and interpretation of four different brightfield and fluorescent images, multiple FTIR spectra, a time-space fluorescent image map, and an IR microscope image. This section will describe in detail, the instrumentation and experimental parameters used during the collection of all data.

#### 2.3.1 Brightfield and Fluorescence Microscopy

A microscope with both brightfield and fluorescence capabilities was utilized for examining the flow profiles for the microfluidic devices in this study. Both brightfield and fluorescence microscopy have the advantage of high spatial resolution, allowing the devices to be imaged in great detail. The contributions of individual fluid streams were identified using a combination of brightfield and fluorescence microscopy on microfluidic devices flowing sodium fluorescein solutions and water. All images were collected using a Nikon Eclipse TE2000 microscope, supplied with a Photometrics CoolSNAP HQ2 Scientific CCD Camera. The microscope is equipped with a 4x, 10x, and 40x microscope objectives, as well as a variety of different filters. The appropriate magnification and filter combination was used to supply the spatial resolution and uniform illumination intensity for all images collected. The fluorescent source available for fluorescein excitation was an X-Cite 120 Series UV-Vis excitation lamp that provided uniform

illumination across the sample. Images were collected using the CoolSNAP HQ2 through a MicroManager add-on to ImageJ and saved as 12 bit grayscale tiff images.

### 2.3.2 Fourier Transform Infrared Spectroscopy

FTIR spectroscopy was used to verify the absorption spectrum of each sample solution prior to further IR experimentation. All measurements were performed on a Bruker Vertex 70. The FTIR sample compartment chamber was fitted with a 3D printed sample holder to provide a common sample cell interface between all spectrometers. The standard IR sample cells consisted of a metal back plate, sample housing, two O-rings, two $CaF_2$ windows, and a Teflon spacer. Samples were encompassed by the Teflon spacer of specific width, and compressed between the two $CaF_2$ windows. The sample cells were then sandwiched between the O-rings and inserted into the metal sample housing. Spacer widths were appropriate to the sample being analyzed. Each component was cleaned between samples using Thermo Scientific Softcide soap and warm water. After which, each component was rinsed with acetone, methanol, and distilled water.

All FTIR sample scans were performed using the same experimental parameters. Each measurement was taken between 1000 $cm^{-1}$ to 4000 $cm^{-1}$ with 1 $cm^{-1}$ spectral resolution. Reducing water absorption was accomplished through two different methods. First, atmospheric compensation was performed on each sample through the Bruker Opus software. Second, each section of the spectrometer was purged with dry air. A 120 second delay prior to measurement was programed into the collection method to allow adequate time for the sample chamber to purge. All spectra taken used a 0.5 mm aperture setting. Each measurement consisted of an air background averaged over 64 scans, and a sample measurement averaged for 32 scans. Each spectrum was individually exported to data point table files and processed using a custom Matlab plotting routine.

### 2.3.3 Fourier Transform Infrared Microscopy

Fourier Transform Infrared Microscopy was used to map chemical species within the microfluidic channels. All FTIR microscope image were collected using a Bruker Hyperion 3000 microscope attachment to the Bruker Vertex 70. The FTIR microscope is equipped with a 64 x 64 element liquid nitrogen cooled FPA detector and 15x IR objective, allowing images to be taken of 170 x 170 $\mu$m areas with 2.7 $\mu$m spatial resolution. The specific parameters of each experiment varied.

For miscible fluids, all images were taken in transmission mode covering 1000 $cm^{-1}$ to 4000 $cm^{-1}$ with either 4 $cm^{-1}$ or 1 $cm^{-1}$ spectral resolution. Both the background and sample spectra were averaged over 32 scans. During image acquisition, similar techniques were used as mentioned previously in the section 2.3.2 for removing water absorption. Briefly, the IR source and all internal compartments of the microscope were purged with dry air, and the OPUS software applied atmospheric compensation during processing. The data collected was then exported into data point table files and processed with custom Matlab routines.

Immiscible fluidic experiments required specific parameters to accommodate the rate with which the droplets were moving. Specifically, the parameters were optimized for the shortest acquisition times possible. This is due to the complication that the droplet formation rate was not synced with the repetition rate of the sample scans, therefore, only a single scan was acquired for every measurement. Multiple single scans were collected consecutively to adequately capture droplet movement. The bandwidth that each image was scanned over was reduced depending on the chemical species being analyzed to minimize the collection time for each frame. For each measurement, only the sample interferrogram were collected and saved. Converting the interferrogram data into absorption images was performed using the OPUS software post

collection of the data. Absorption images were then exported into data point table format for processing in Matlab.

### 2.3.4 Time-Space Mapping Fluorescent Microscopy

The purpose of the custom built fluorescent microscope was to provide a specific area of excitation within the microfluidic channels.[7] On the right side of Figure 2.7 is a schematic for the time-space mapping fluorescent microscope. First, the excitation light must be selectively focused into the chip. Second, the channel must be then imaged into the camera in parallel with a brightfield source. The system starts from an Opotek Inc. Opolette 355 LD tunable laser, where the 7 ns 355 nm pump beam for the OPO system is emitted. The 355 nm excitation beam then travels into a dogleg for alignment purposes before passing through a Thor Labs adjustable mechanical slit. The slit was imaged onto the microfluidic channel by a lens, causing an area the width of the slit to be illuminated by the excitation beam. The microfluidic chip was placed on a 3-axis sample stage to allow for adjustment of the location of the excitation area in reference to the channel being imaged. The channel is then imaged onto a Retiga R1 Scientific CCD camera using a 20x Nikon microscope objective. Both the camera and the microscope lens were placed upon another stage, allowing for imaging of any portion of the channel independent of the excitation area. An optical filter was placed in front of the camera to filter out as much of the excitation light as possible. Images were collected using the native Occular software of the Retiga R1 camera.

The left side of Figure 2.7 is the schematic of the instrument used to standardize the fluorescent lifetimes. Standard determination of the fluorescent lifetimes was performed using the same excitation source. The 355 nm excitation beam was diverted prior to entering the Time-Space Mapping Fluorescent Microscope and directed through a 1-cm quartz cuvette.

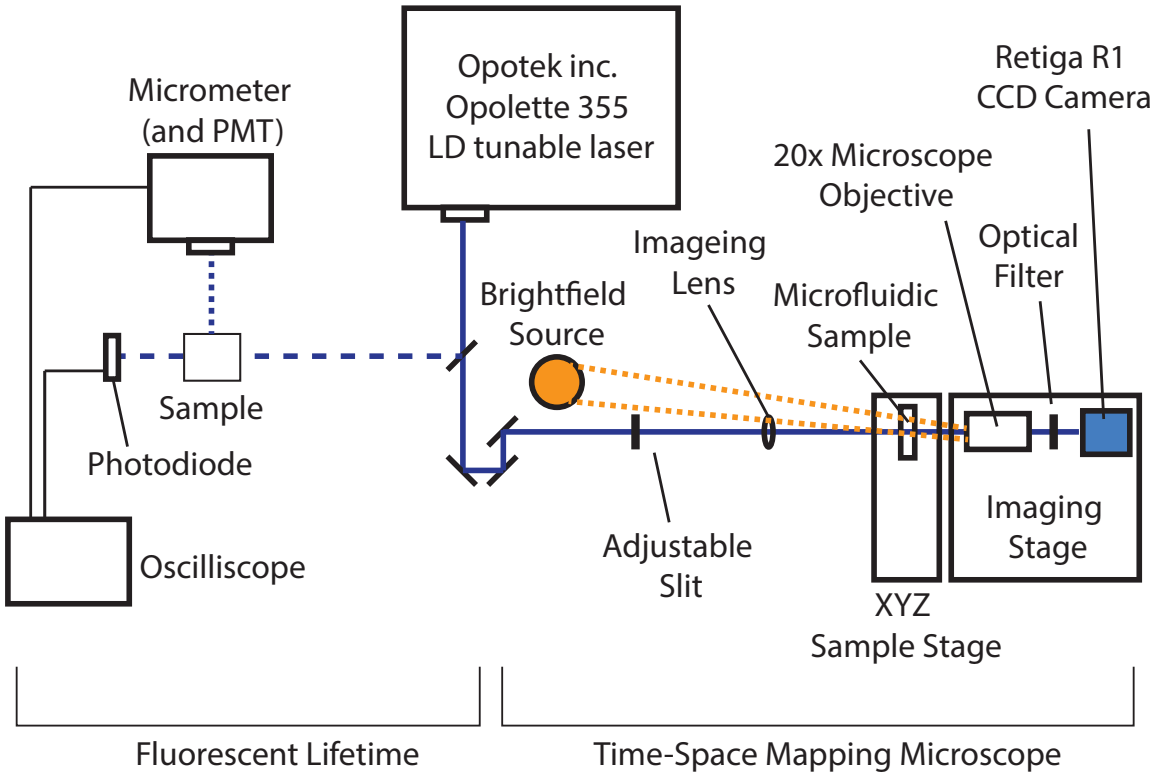


**Figure 2.7 Time-Space Fluorescent Microscope**

The schematic for the Time-Space Mapping Fluorescent Microscope (right) and the schematic for the time resolved fluorescence instrument (left)

Fluorescent intensity was measured perpendicular to the incident beam and focused into a Thermo Jarrell Ash (Model 82-410) 0.25 Meter Monochrometer Spectrograph with attached photomultiplier tube. The excitation beam was collected on a photodiode and used to trigger the oscilloscope. Excitation with respect to time was collected and fit to a standard exponential decay to determine the fluorescent lifetime of the sample.

### 2.3.5 Two Dimensional Infrared Spectroscopy

Two-dimensional infrared spectroscopy was performed on a homebuilt optical parametric chirped pulse amplification (OPCPA) 2D IR spectrometer.[8] The specifics of the laser system will not be discussed in detail, however the methods with which microfluidics were interfaced with the spectrometer will be reviewed.

The interface between the microfluidic device and the 2D IR spectrometer have been previously discussed in section 2.2. Interfacing the microfluidic devices simply required encasing each chip into the custom acrylic cases. In doing so, the microfluidic device being sampled was easily inserted into the spectrometer of choice in place of the traditional $CaF_2$ windows used for bulk samples.

The IR microscope was used to verify the fluidic behavior through IR imaging prior to insertion into the 2D IR spectrometer. To better increase the continuity of this process, an extension cord was added to the fluidic pump power strip increasing the range of travel for the cart to include both the IR microscope and the 2D IR spectrometer. IR images were acquired of the area of interest using the methods discussed in section 2.3.3 to verify the fluidic parameters of interest. The microfluidic chip was then removed from the IR microscope and placed upon a breadboard, already holding the fluidic pumps, for transport to the 2D IR spectrometer. Transport was done from the IR microscope to the 2D IR spectrometer with extreme care as to

not disturb the tubing connections or add too much stress the setup as to maintain constant conditions between the two experiments. The entire cart with the pumps, microfluidic chip, and controlling computer was then to the 2D IR spectrometer where the breadboard and pump control computer were transferred onto the laser table. Using the breadboard as a transport vehicle, the microfluidic chip and both pumps were pushed along the table to the 2D IR sample holder. The microfluidic chip was carefully inserted into the sample holder.

2D IR measurements require multiple pulses of IR light to interact with the sample at specific time increments. Experimentally, the OPCPA 2D IR spectrometer uses a pump beam and a probe beam overlapped in both space and time within the sample to accomplish this, and is shown in the top portion of Figure 2.8. Alignment of the optical portion of the 2D IR setup was performed on a static sample. Realignment of the sample stage was required for measurements taken in microfluidic devices such that the beam overlap was occurring within the channel and was performed by mapping the channel with respect to each beam. The microfluidic channel was oriented normal to the table, such that fluids travelled from top to bottom. Specific mapping of the channel with respect to the incoming beams was accomplished by monitoring the signal observed on the array detector as the microfluidic channel was scanned in the horizontal plane of the incoming beam. The channel walls of the microfluidic device scattered a distinguishable amount of light from any incoming beam. Therefore, by mapping the X and Z locations of the scattered light for both the right and left edge of the channel, the beam paths relative to the channel walls located. Fitting each edge location to a line allowed the intersection of each beam to be calculated in 2D space with respect to the microfluidic channel. Overlap was then fine-tuned by making small iterative adjustments in the X and Y dimensions till the signal was

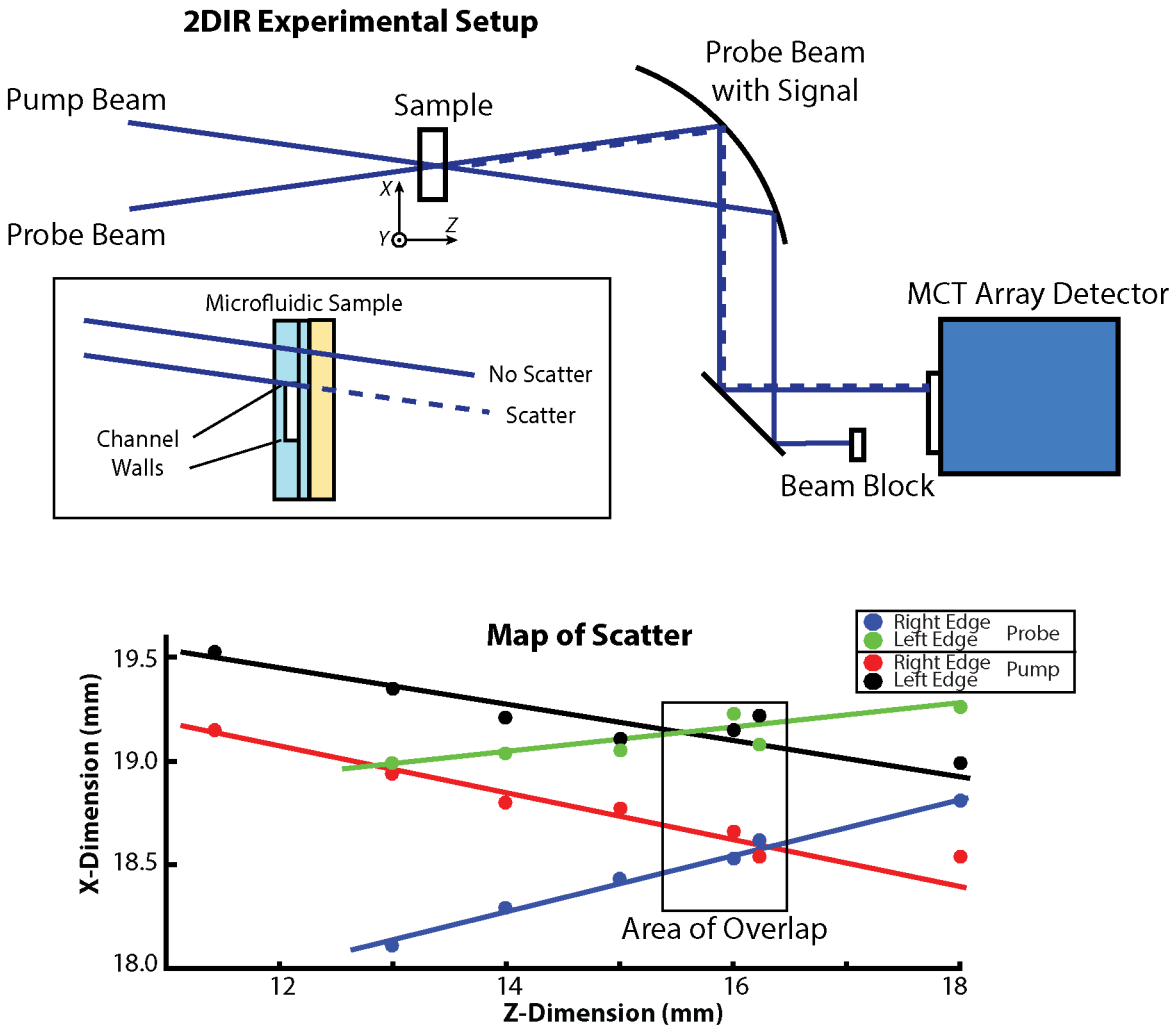


**Figure 2.8 Overview of 2D IR and Microfluidic Setup**

The general experimental layout of the 2D IR optical geometry for the experiments performed on the OPCPA 2D IR. (top) The inset depicts the incoming beams response to different portions of the channel. (inset) The mapped locations for the sample stage while observing scatter off of the channel walls from both the pump and probe beam.

maximized. 2D IR spectra were collected at all desired locations within the channel and processed with a plotting code, developed by Kathryn Tracy and Dr. Brad Luther.

### 2.4 Sample Preparation

All fabrication materials, solvents, and analytes used in this thesis were commercially available. Fabrication materials consisted of PDMS, COC, COP, Acrylic, Aquapel, and HMDS. PDMS was purchased from Dow Corning as a Sylgard 184 Elastomer Kit. Both Zeonor COP and Topaz COC were purchased from the microfluidic ChipShop at the appropriate thicknesses. Acrylic was purchased in town from Fort Collins Plastics in large sheets and then divided into pieces appropriate for the Zing Laser cutter. Aquapel was acquired in applicator form from Pittsburgh Glass Works LLC, and disassembled for the Aquapel fluid inside. HMDS was acquired from Alfa Aesar.

Many different solutions and solvents were used in this thesis. Deuterated solvents were used for all IR mapping experiments. Deuterated water ($D_2O$) was purchased from Sigma-Aldrich. DCl and NaOD were acquired from Acros Organics. Gradients were formed using methanol (Fisher), dimethylformamide (DMF, Sigma Aldrich), dimethylsulfoxide (DMSO, EMD), and $D_2O$. Droplets were formed using Novec HFE-7500 Engineering fluid (3M) and a Krytox 157 FSL surfactant (DuPont) as the non-aqueous phase. Distilled water was used as the aqueous phase.

Multiple analytes were observed in this thesis using each of the detection techniques previously described. Sodium azide ($NaN_3$, Fisher) and N-methyl acetamide (NMA, Sigma-Aldrich) were used as strong oscillators for the original IR compatible microchip work. The protonation and deprotonation of acetic acid (Sigma-Aldrich) using dueterated hydrochloric acid (DCl) and deuterated sodium hydroxide (NaOD) were used as an easily monitored model

reaction occurring in a device. Picolinic acid (Aldrich) and iron (II) chloride ($FeCl_2$ Sigma-Aldrich) were used as model systems to study chemical kinetics. Sodium fluorescein (Fluka) in combination with distilled water was used as a marker for flow profiles using the fluorescent microscope. By exchanging the distilled water with potassium iodide (KI, Fisher) quenching experiments were performed. Time-space mapping was accomplished using europium nanospheres acquired from Life technologies. 2D IR was taken on samples of potassium thiocyanate (KOCN) in the solvents N,N-dimethylformimide (DMF, HPLC grade) and methanol (MeOH, HPLC grade), all purchased from Sigma-Aldrich.

### 2.5 Data Analysis and Interpretation

The resulting data from each experiment typically consisted of either images or spectra of some system of interest. In order to extrapolate more useful information, the raw data from each instrument was imported into Matlab for the appropriate processing. Matlab 2015 for mac was used in all of the processing, with the included image processing toolbox. In this section, the actions performed by the code for processing each experiment will be discussed in detail. All code discussed in this section can be found in the appendices.

#### 2.5.1 Brightfield and Fluorescent Image Processing

Brightfield and fluorescent images were taken using a Nikon Eclipse TE2000 microscope. These images were used for multiple purposes. First, the images were used in quantifying the gradient and its behavior relative to different modifications of either the fluid flow or the channel geometry. Images processed yielded characterization parameters such as the width of the gradient, the location of the streamlines outlining the gradient, and the streamlines included in the center stream. A second purpose behind processing visible images was to use fluorescent

images to calibrate concentrations for each input fluid at every position within the channel. Lastly, visible images were used to visualize fluidic behavior by capturing the trajectory and velocity of polystyrene beads flowed through the channel. Processing of all brightfield and fluorescent images was done in Matlab through customized processing codes and can be found in Appendix A1.4.

The raw output saved from the fluorescent microscope is in a tiff format. The data for both characterization of the gradient and concentration calibration experiments required a set of four images to be processed. The four images required were two combination brightfield-fluorescence images and the two pure fluorescent images for fluorescein, for both fluorescein as the inner and outer streams. The specific code can be found in Appendix A1.4. In this code, the two combination brightfield-fluorescence images are outlined using the edge function. All features are traced providing points of reference for image cross correlation using the 'imregister' function in the image processing toolbox. The transform applied during the cross correlation was applied to the raw pure fluorescent images, effectively aligning those images as well. Next, the relative orientation and dimensional scaling for the images was performed. A rectangle was drawn across the width of the channel, with the top left corner ending on the intersection with a vertical channel wall, and the outer fluids channel supplying fluid to the nozzle. The left edge of the channel and the vertical position for the second nozzle are registered as the 0 positions of both the horizontal and vertical axis. By boxing the width of the channel, the ratio of the width in pixels of the rectangle to the known channel width in $\mu$m gives the accurate scaling factor required for converting pixels to $\mu$m. The correlated pure fluorescent images are plotted using each image, as a single color of an RGB image, with the axis correctly converted to $\mu$m.

The parameters of the gradient were determined by first splitting each image into slices, where each slice consisted of every pixel in the row perpendicular to the primary flow within the channel. Each slice was then baseline corrected, normalized, and dissected with iterative loops. The loop scanned across a slice for a maximum and minimum threshold value in the fluorescent intensity. A line was drawn between the encompassing pixels and the exact location for the threshold values were calculated for both sides of the symmetric gradient. Other points, such as the point of maximum value were identified. All points of interest were saved into an output matrix and identified on the original gradient image. Gradient widths were calculated by taking the difference between the maximum and minimum threshold pixel locations on each side of the gradient.

Visible images were also used in conjunction with polystyrene beads for rudimentary particle tracking experiments. The primary use in these images was to follow the trajectory of the beads to visualize the streamlines within the channels. The most useful particle images taken were of the droplet formation process. Droplets consisting of a 50-50 ratio of 10x diluted polystyrene beads and DI water were formed in HFE-7500 oil with added Krytox surfactant. Images were captured using the Nikon Eclipse TE2000 microscope, however, the native camera was replaced with a Mightex 1.2 MP Global Shutter CMOS camera (SMN-B012-U). The camera was chosen for the faster frame rate with which it captures images, adding to the definition seen in the particle tracking experiments. Images were captured at 100 frames per second as still frame images, combined using ImageJ to form short gifs during analysis for the means of visual streamline pattern recognition.

### 2.5.2 Fourier Transform Infrared Spectroscopy

FTIR spectroscopy data files were exported into the data point table file format. Each file consisted of a two-column matrix with wavelengths in the first column and absorbance values in the second. An example MatLab code for processing linear IR data can be found in Appendix A1.1. In general, multiple IR spectra for the samples, reference spectra, and controls were imported into Matlab at the same time. Absorbance spectra for each sample were obtained by subtracting the absorbance values from the correct proportion of the reference spectra. In the case where the analyte absorption could not be deconvolved, baseline correction was performed on the analyte peaks of interest. The bounds of the wavelength peak of interest were identified and a line between each point on the absorbance spectrum was calculated. The values at each point in the baseline are then subtracted from the absorbance spectrum, effectively removing any non-peak absorbance values. Baseline correction was used only when the baseline being subtracted was due to a rolling solvent background or other large contributions where a linear baseline is appropriate.

Molar absorptivities for analytes with known concentration were calculated using background subtracted linear spectra. The area underneath independent analyte peaks was calculated for a range of wavelengths using the mathematical integral equation for a discrete data set. The molar absorptivity constant for the range of wavelengths under the peaks was calculated using Beers Law. The path length of the sample cell is determined by the width of the spacer used in data collection. The concentration of the solution was known. Using the area underneath the absorbance peak, the path length and concentration, the molar absorptivity constant for the range of wavelengths under the peaks was calculated. Using the molar absorptivity values and

the area under the absorbance spectra for multiple samples, the equilibrium constants could be calculated for various reactions.

### 2.5.3 Fourier Transform Infrared Microscopy

FTIR microscopy data was exported as data point tables from the Bruker OPUS software. The OPUS software prior to post-processing the images was used to background subtract the microfluidic chip or appropriate solvent contributions. Background subtraction was performed by isolating the average spectrum of an area containing only the background component and subtracting it from the entire image. Background subtraction was performed within the OPUS software rather than in the post processing Matlab code due to the large file sizes associated with the IR microscopy images. Every opportunity to reduce the file size was taken prior to exporting the data. Smaller file sizes were successfully accomplished by reduction of the wavelength range, encompassing all of the desired peaks of interest and eliminating all data outside of those limits. For most of the experiments performed, the data ranges were reduced from ranges 3000 $cm^{-1}$ wide to 300 - 500 $cm^{-1}$. In doing so, the files exported were reduced in size from 6-8 GB to 1-2 GB. The output file of the acquisition process is a data point table with the wavelengths listed in the first column and the IR spectrum data for each individual pixel of the 64 x 64 element array detector listed in the following rows. Further processing was necessary because the matrices are not immediately translatable to images, and is found in Appendix A1.2. Translation to images requires each column of data to be condensed into a single value. The area under a specific absorption peak was the value chosen to represent the component being imaged, as it relates through Beer's law directly to the concentration of the analyte. The area under the absorption peak was calculated by first identifying the frequency bounds of the absorption peak of interest. From here, the integral under the curve was calculated using the formula for a

discrete data set. The calculated area under the curve was either directly reported, or baseline subtracted. Baselines were calculated by plotting the integral underneath a line connecting the absorbance value at both bounds of the absorption peak of interest. The value was then subtracted from the integral of the area of the absorption peak itself, effectively background subtracting the integrated area value. The background subtraction method was necessary for calculating the relative area of shoulders on known solvent or chip material absorbance. The background subtraction method was repeated in a loop to perform the background subtraction to every single column within the sample data. The next step was rearranging the 1 x 4096 pixel matrix filled with integrated absorbance values into a 64 x 64 pixel matrix. The values at each pixel of the integrated absorbance value between the wavelength bounds for the absorbance peak of interest, and can be expressed as a 64 x 64 pixel image. The image extraction method was performed for every species of interest, using the background subtraction method when appropriate. Concentration values were calculated using the area of the absorbance peak, height of the channel (path length), and the molar absorptivity constants calculated from linear spectra.

### 2.5.4 Chemical Kinetics Measurements

Measuring the chemical kinetics of a reaction can be performed in the microfluidic devices that have been developed in our lab. These measurements are contingent upon the necessary calibration steps, cross-referencing data from multiple techniques previously mentioned. Determining the rate of reaction requires the concentrations of reactants, concentrations of products, and the rate of travel for fluids in their respective streamlines to be known. Reactant concentrations were determined using the data collected from the fluorescent microscope. Product concentrations of the reaction were determined using the FTIR Microscope images. The time-space mapping of the device using the custom built fluorescent microscope supplied the

rate of travel for the fluids. The data from each of these experiments follow the appropriate techniques described in the previous sections of this chapter. As an example, the following data will be specific to the dual nozzle fast gradient generating device developed in our lab. The MatLab code used for processing can be found in Appendix A1.5.

Reactant concentration calibration was performed using a fluorescent microscope to map the fluorescence intensity of sodium fluorescein solutions as they are flowed through the different input channels of the device. The combination of both fluorescence and brightfield images acquired from the microscope provided spatial references for the data processing and image correlation. This allowed for accurate mapping of the fluids within the device and the relative concentrations for the inner and outer fluids at each point to be determined. The specific experiments involved taking a pair of images, one with fluorescein as the inner fluid and water as the outer fluid, and a second image with the fluids switched. Using fluorescein as the indicator of the relative abundance of each fluid. Image processing was performed using the same techniques covered in section 2.3.1. Briefly, brightfield and fluorescent images were imported into Matlab. The brightfield images were traced using the edge function and cross correlated. Using the transformation calculated in the cross correlation, the fluorescent images were transformed and overlaid as individual components of an RGB image. Image profiles were taken representing the relative abundance of the inner and outer fluids within the gradient device. The concentrations of the inner and outer fluids observed in the image overlay are directly relatable to the reactant fluids.

Measuring the concentration of the products requires processing of the IR images collected of the desired reaction. The specific data is collected using the technique described in section 2.3.3 for the collection of IR microscope images for miscible liquid systems. A detailed

description of the IR image processing is discussed in detail in section 2.5.3. Briefly, the output file of the acquisition process is a data point table. Shrinking the amount of data to process was done prior to the exportation, accomplished by limiting the wavelength range to a window of interest. Once a manageable size, translation of each pixel's spectrum to a single area-under-the-curve value was performed using the integral equation for a discrete data set with a background correction applied when appropriate. The 1 x 4096 pixel matrix was then rearranged into a 64 x 64 pixel matrix that can be expressed as an image. The value at each pixel is the area under the absorption spectrum. Concentration values were calculated using the area of the absorbance peak, height of the channel, and the molar absorptivity constants calculated from linear spectra.

Concentration formation rates per pixels were determined by fitting the concentration of product versus the pixel number along each of the streamlines. The pixels associated with each streamline were identified similar to the method used to identify the gradient width in visible images discussed in section 2.5.1, and is shown in the top of Figure 2.9. The IR concentration map of the chemical species found in the center stream was imported into the Matlab code, then immediately separated into slices perpendicular to the direction of primary flow in the analysis channel. Each slice was then scanned, identifying the maximum and minimum threshold values outlining the gradient region. The pixel number for these values were then recorded and visually confirmed on the reactant concentration image before being projected onto the product concentration image. Identification of the gradient region for both the product and reactant concentration images are shown in the middle section of Figure 2.9. The pixel values between the identified locations of the maximum and minimum threshold values with a 5 pixel buffer were then extracted and centered into a new matrix. The extracted matrix consists of the streamlines associated with the gradient generated, and has been reoriented such that each

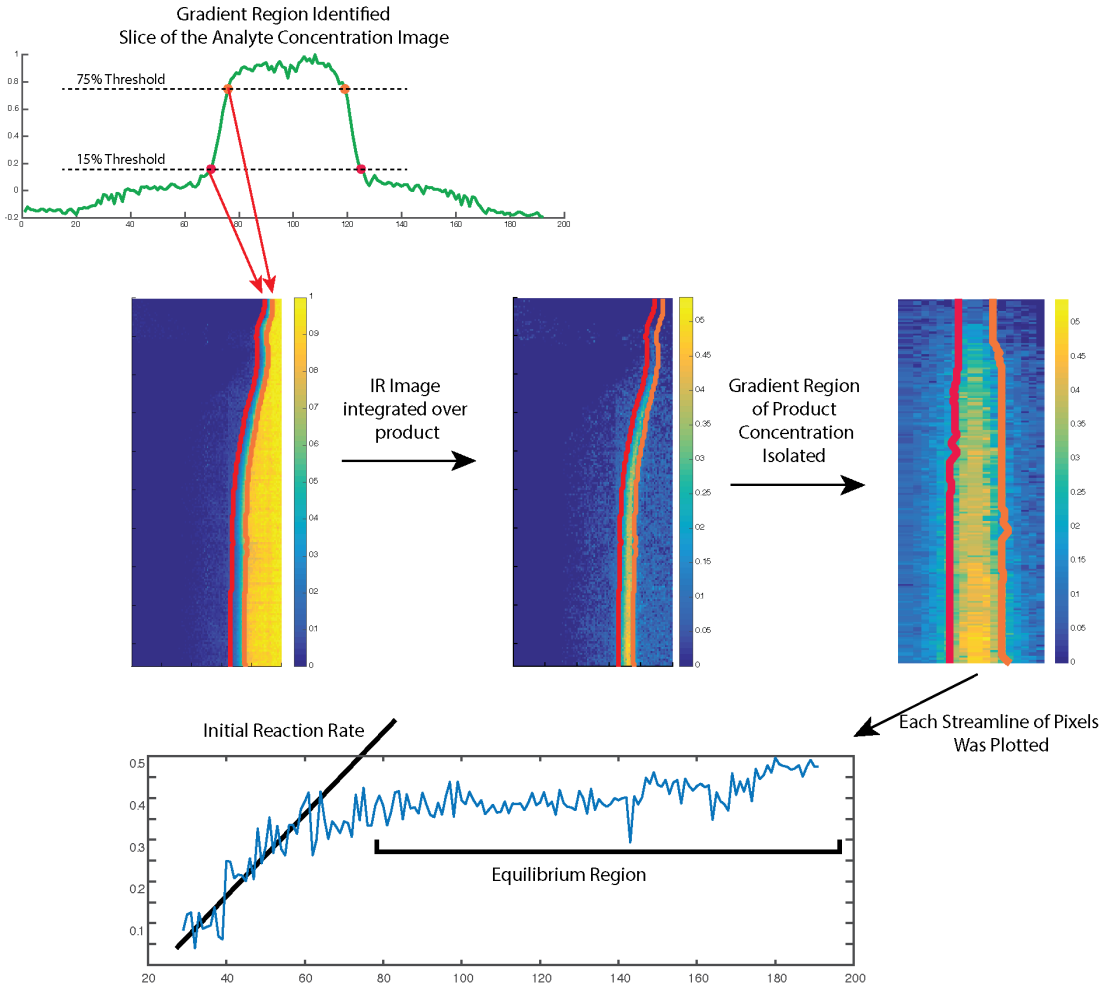


**Figure 2.9 Rate of Product Formation per Pixel Determination**

The determination of rate of concentration per pixel formation per pixel for each streamline. (top) Identification of the gradient region was identified from the reactant concentration IR image. (middle) the gradient region was projected onto the product concentration map and isolated. (bottom) the colums of pixels from the gradient region were plotted as individual streamlines displaying the product concentration as a function of pixel down the channel.

streamline now travels vertically in a linear fashion. These values were then exported into Microsoft Excel. Each individual column within the excel table represented an individual streamline within the gradient region. Plotting each streamline versus the pixel number down the channel allowed for each region prior to the product concentration reaching equilibrium to be identified, as shown in the lower portion of Figure 2.9. The slope of the pre-equilibrium region is the rate of the appearance of product concentration per pixel, which was converted to the rate of appearance of product per $\mu$m.

Theoretical concentration values of the product and reactants were calculated based off of the gradient region identified using the IR image of center fluid concentration. The code used for calculating the theoretical concentrations can be found in Appendix A1.5. The initial reactant concentrations determined through the brightfield and fluorescence images processed previously in this section suggest an approximately linear gradient at the inner and outer fluidic interface. Using the threshold points determined in identifying the gradient region, a linear gradient was calculated. The slope of the concentration gradient was mathematically determined using the concentration and pixel values of each threshold point. Boundary conditions for the inner fluid concentration gradient were set to 0% and 100% of the maximum concentration value. Outer fluidic concentration was determined by taking the complementary percentage to the inner fluid component. Theoretical product concentrations were calculated for each pixel using the reactant gradient contributions and an equilibrium reaction constant determined from the linear IR absorption spectra. Theoretical product concentrations were compared to the experimental values observed above to provide guidelines for the identification of the regions of equilibrium and pre-equilibrium.

Accurate measurements of the rate of travel for the fluids are necessary for any type of chemical kinetic measurement. Calibration of each device design was discussed in section 2.3.4, using a custom built fluorescence microscope in combination with a fluidic medium with a known fluorescent decay lifetime. The raw data consisted of 14 bit tiff images collected from the Retiga R1 Scientific CCD camera. Each image was imported into MatLab, and basic analysis was performed. The exact MatLab code is found in Appendix A1.6. A background subtraction was performed, the image was rotated, and the scaling factor and origin point were identified. Using the decay equation and the previously determined fluorescent lifetimes, the fluorescent intensity of each pixel was converted into time values. The calculated time values represent the time in between the fluorescent particles leaving the specified area of excitation and arriving at the measured pixel location. For example, the calculated time values for the fast gradient generating devices are the amount of time elapsed since the fluid at that particular pixel has exited the second nozzle. This was accomplished by choosing the excitation area to include the entire section of outer and inner fluid channels immediately prior to the second nozzle. The region of the gradient determined in the IR concentration maps could be projected into the time-space image maps by direct comparison, in $\mu$m space, to the IR concentration maps. In doing so, the appropriate streamlines could be identified. By plotting the time values for each streamline, the time travelled per pixel, converted to time travelled per $\mu$m, by the fluid was determined for each streamline within the gradient region.

The kinetics of the reaction was calculated using the combination of the IR product concentration map and the time-space fluorescent map. The rate of product concentration per $\mu$m was divided by the $\mu$s per $\mu$m obtained from the time mapping. The resulting value is the rate of reaction, in molarity per $\mu$s, of the rate of the reaction pre equilibrium. Rate was plotted

against the position within the gradient to observe any possible trends caused by the changing reactant concentrations. Due to the extent of symmetry of the rate's response to the varying inner and outer fluid concentrations, conclusions were drawn relating to the relative order of the individual reactants.

## References


(1) MICROCHEM: SU-8 2000 PROCESSING GUIDELINES; 2000; pp 1–5.

(2) McDonald, J. C.; Whitesides, G. M. Acc. Chem. Res. **2002**, 35 (7), 491.

(3) Duffy, D. C.; McDonald, J. C.; Schueller, O. J.; Whitesides, G. M. Anal. Chem. **1998**, 70 (23), 4974.

(4) Barich, M. V.; Krummel, A. T. Anal. Chem. **2013**, 85 (21), 10000.

(5) Becker, H.; Gärtner, C. Anal Bioanal Chem **2007**, 390 (1), 89.

(6) Miserere, S.; Mottet, G.; Taniga, V.; Descroix, S.; Viovy, J.-L.; Malaquin, L. Lab Chip **2012**, 12 (10), 1849.

(7) Burke, K. S.; Parul, D.; Reddish, M. J.; Dyer, R. B. Lab Chip **2013**, 13 (15), 2912.

(8) Luther, B. M.; Tracy, K. M.; Gerrity, M.; Brown, S.; Krummel, A. T. Opt Express **2016**, 24 (4), 4117.

# Chapter 3

## Polymeric Infrared Compatible Microfluidic Devices for Spectrochemical Analysis

This chapter is a publication from 2013 and is published in Analytical Chemistry[1]. This work focuses on the innovative fabrication method that affords combination of PDMS microfluidic technology with vibrational spectroscopy. PDMS devices were produced with uniform thicknesses ranging from 25 μm to 400 μm. The optical characteristics of the microfluidic devices in the mid-infrared are reported. The broad utility of this approach is demonstrated through IR imaging of flows in functional gradient generators and flow-focusing devices.

## 3.1 Introduction

Microfluidic device technology has been broadly applied to drive developments in many biological and chemical arenas including diagnostics,[2–4] chemical dynamics,[5] polymer and nanomaterial synthesis,[6–9] and reaction monitoring,[10,11] to name a few. While the advancement of microfluidic device technology has been rapid, the combination of microfluidic device technology with a chemical selective read out such as Raman or infrared (IR) spectroscopy has been limited.[12] Linear and nonlinear IR spectroscopies are ideal for monitoring reaction kinetics,[13] molecular conformational dynamics,[14,15] and solvent dynamics[16,17] with chemical specificity. In order to take advantage of these spectroscopies for on-chip measurements, an IR transmissive microfluidic platform is required. This is a challenging problem because standard materials used for microfluidics strongly absorb mid-IR light.

Infrared compatible microfluidic devices have previously been reported. Devices have been produced via etching IR transparent calcium fluoride ($CaF_2$) windows,[18,19] by patterning photoresist onto $CaF_2$ windows,[18,20–22] and by printing parafin wax on $CaF_2$ windows to pattern the microchannels.[23] These approaches are unfortunately limited in their use due to the difficulties in fabrication, limited device functionality, and higher fabrication costs. Recently, polymer based devices have also been developed for interfacing with IR light, but these approaches are generally restricted to attenuated total reflection (ATR) geometries rather than transmission geometries.[23,24] Thus, the overall utility of microfluidic devices to the vibrational spectroscopy community is diminished.

Herein we report a robust fabrication approach to polymeric IR compatible microfluidic devices using standard soft lithography that, for the first time, allow for transmission IR spectroscopy and IR microscopy experiments to be performed. The optical density of a device is directly related to the amount of material the IR light must travel through, therefore by precisely controlling the thickness of material for each device, optical densities at a level similar to typical solvents used in IR absorption spectroscopy are readily achieved. In addition to fabrication details, the optical characteristics of the devices in the mid-IR and a demonstration of the utility of these devices for IR spectrochemical analysis are provided.

### 3.2 Device Construction

The IR compatible microfluidic devices, shown in Figure 3.1a, combine four separate layers, each prepared prior to the assembly of the complete microchip. In Figure 3.1b, the four layers necessary for construction are shown: a top support layer, a microchannel layer, an adhesion layer, and an IR transparent backbone such as $CaF_2$ used here.

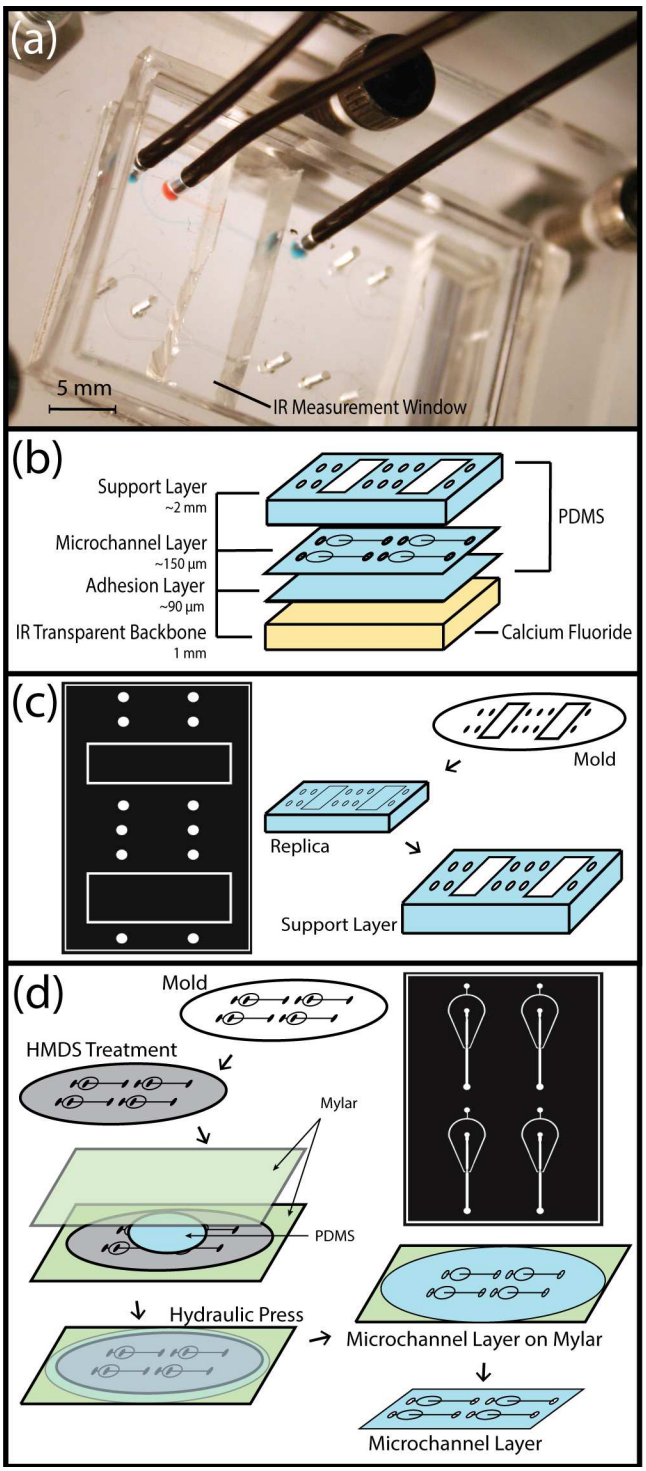


**Figure 3.1 Fabrication Summary of IR Compatible PDMS Devices**

(a) Complete IR compatible microchip. (b) Overview of complete microchip assembly. (c) The mask and fabrication method for support layer (d) and for microchannel layer.

The support layer is created via standard soft lithography replica molding,[25–27] as is illustrated in Figure 3.1c. The mold is designed to guide the placement of fluid ports. PDMS is removed from this layer to produce direct fluid ports to the microfluidic channels and the desired IR measurement window. The second layer is the microchannel layer, an optically thin layer containing the microfluidic features. The features in the microchannel layer are molded using a technique similar to exclusion molding (Figure 3.1d).[28,29] Hexamethyldisilazane (HMDS Sigma Aldrich) is used to modify the surface of the mold in order to facilitate the transfer of the microchannel layer. The microchannel feature heights define the optical path length used in IR transmission experiments. Path lengths ranging from 20 to 150 $\mu$m were fabricated, and exhibited identical characteristics to traditionally fabricated microchannels; most notably, the microchannels were measured to be uniform across each chip and experience no measurable deformation under flow conditions. Channel deformation is a concern due to the overall thickness of the PDMS; however, pressures measured at constant flow rates exhibited no fluctuations. Therefore no local chip deformations are apparent. The examples shown contain an adhesion layer of PDMS, applied to a calcium fluoride ($CaF_2$) window. The layers are plasma sealed to facilitate PDMS-PDMS covalent bonding in the order presented, from bottom to top, in Figure 3.1b. PDMS-PDMS bonding affords homogeneous wetting properties in the device channels and allows for surface modification within the chip.

### 3.3 Absorption Characteristics

In Figure 3.2a, the IR absorption spectrum of a traditionally fabricated PDMS chip (red ~2mm thick) is compared to two IR transparent PDMS chips that are 240 μm (blue) and 125 μm (magenta) thick, respectively. In addition, two IR absorption spectra of bulk $^2H_2O$ in $CaF_2$ sample cells with Teflon spacers of 50 μm (green) and 25 μm (cyan) are provided for reference.

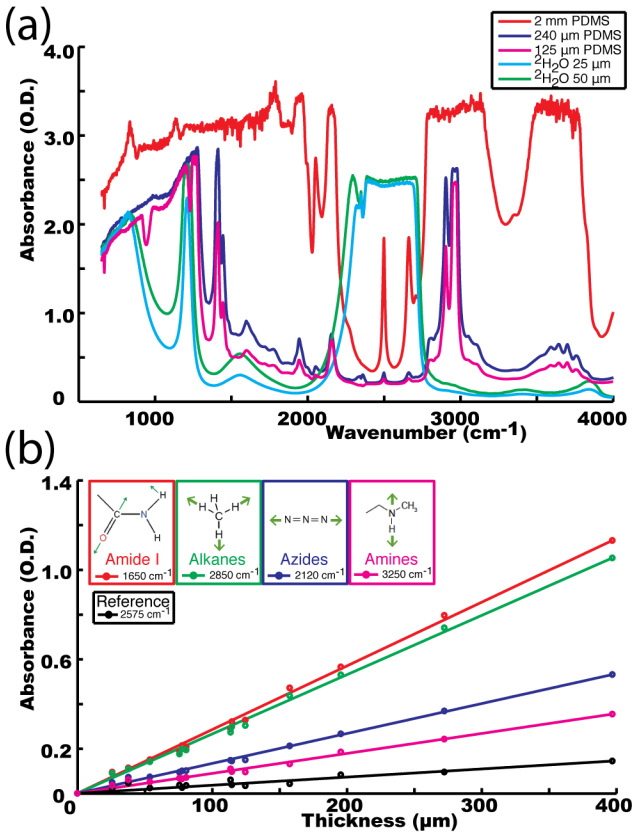


**Figure 3.2 Infrared Absorption Response of PDMS**

Comparison IR spectra of PDMS and $^2H_2O$ (a). Optical density of PDMS as a function of thickness at five vibrational frequencies of interest (b).

The background optical density of the IR transparent microfluidic devices is similar to that of $^2H_2O$ in the spectral range of 1450 $cm^{-1}$ to 2800 $cm^{-1}$, a frequency range applicable to chemical and biological systems. For example, nitriles, azides, and metal carbonyls all have characteristic vibrational frequencies that lie between 2000 $cm^{-1}$ and 2800 $cm^{-1}$. These particular molecular species are important due to their recent use as site-specific vibrational labels.[30–34]

The optical density of IR compatible microchips on $CaF_2$ as a function of the total chip thickness is presented in Figure 3.b. Total chip thickness is the combined thickness of the PDMS microchannel and adhesion layers. This relationship is plotted for five different frequencies often utilized in linear and nonlinear IR spectroscopy. Each frequency is associated with a vibrational mode of chemical interest. For example, the red data corresponds to 1650 $cm^{-1}$; natural vibrational frequencies of nucleic acids, peptides, and lipids exist in the frequency range of 1500 $cm^{-1}$ to 1800 $cm^{-1}$. Structure and dynamics of these biomolecules are routinely probed using their natural vibrational modes. Thus, it is imperative that microfluidic devices can be transmissive in this region. The blue data correspond to the vibrational frequencies of azido groups found between 2000-2100 $cm^{-1}$. Azido groups are common reactive moieties in chemical synthesis and can be a good vibrational marker for monitoring the completion of a chemical reaction. The black data correspond to 2575 $cm^{-1}$ and is a good reference wavelength for these devices. This wavelength lies at the midpoint of a uniform absorption feature in the spectrum of the device. The optical densities of these devices at 2575 $cm^{-1}$ correlates strongly to the total thickness of the devices as measured by optical profilometry. In general, a total chip thickness less than 200 μm is sufficient to attain IR compatibility for important carbonyl, azide, and nitrile vibrational modes; each of these chemical moieities have oscillator strengths that allow detection at low optical densities.

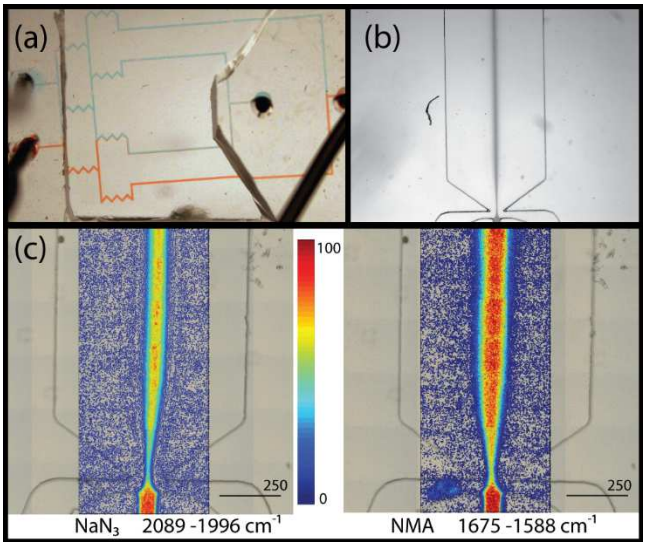


**Figure 3.3 Spectrochemical Mapping in a IR Compatible Microfluidic Device**

a) Photograph of an IR compatible gradient generator.(b) Bright-field image of an IR compatible flow-focusing device. (c) IR chemical map of focused streams of 50 mM $NaN_3$ in $^2H_2O$ (left) and 100 mM NMA in $^2H_2O$ (right).

### 3.4 Spectrochemical Mapping

Functioning IR compatible gradient generators (Figure 3.3a) and flow-focusing devices (Figure 3.3b) were fabricated in order to demonstrate the broad applicability of this fabrication approach. The flow-focusing devices double as drop-makers if two immiscible fluids are chosen. Each of these chips has a uniform channel height of 33.4 μm measured with an optical profilometer. In Figure 3.3c, IR images[35,36] of flow-focusing devices with 82 $\mu$m uniform channel heights are shown. The IR images were collected under a 15x objective on a Bruker Hyperion 3000 IR microscope outfitted with a 64x64 element focal plane array detector. The device on the left focuses an inner stream of 50 mM sodium azide ($NaN_3$) in $^2H_2O$ with an outer stream of pure $^2H_2O$. On the right, an inner stream of 100 mM N-methylacetamide (NMA) in $^2H_2O$ is focused with an outer stream of pure $^2H_2O$. The relative flow rates control the focused width of the inner stream. A flow rate ratio of 8:1 was employed in the azide experiment (left) and a ratio of 6:1 was used in the NMA experiment (right). Chemical maps are produced from the IR images; the intensities in the chemical maps are generated from integrating the total area under the peak in the IR spectra associated with the azide antisymmetric stretch centered at 2040 $cm^{-1}$ (left) and the amide I vibration in NMA centered at 1625 $cm^{-1}$ (right). The ΔOD in the center of the azide and NMA focused streams are 0.4 and 0.8 OD, respectively. The intermediate intensities represent ΔOD equal to 0.25 and 0.4 OD for the azide and NMA experiments, respectively. The intensities of each chemical map fall to zero at the outer edge of the focused stream. Infrared peak intensities scale with the path length and the square of the oscillator strength of the vibrational mode of interest. The path length tunability of these devices is discussed above. The model compounds $NaN_3$ and NMA are used here for demonstration purposes; $NaN_3$ is representative of site-specific vibrational labels and NMA is representative of the amide I mode

monitored during protein investigations. Typical concentrations of site-specific vibrational labels are 5 mM to 10 mM in the label.[34,37–39] Based on the ΔOD detected in the $NaN_3$ experiment, we fully expect these devices to perform well with $NaN_3$ concentrations in the range typically used in labeling experiments. Typical protein concentrations used in infrared spectroscopy studies range from 0.5 mM to 10 mM often depending on the size of the protein. For example, several linear IR and 2D IR absorption experiments have been performed on ubiquitin, a protein with 76 amino acids, at concentrations ranging from 1 mM to 6 mM ubiquitin in buffer which thus corresponds to 76 mM to 456 mM in peptide backbone carbonyls.[4,40–42] The concentration of NMA used in the experiments reported here is well within this range. Therefore the IR compatible devices described here will be useful for probing peptide and protein conformational dynamics and kinetics with precision control over reagent mixing and reaction initiations in kinetics experiments. The IR images are collected in transmission mode—a capability only made possible by the IR translucence of these devices.

The polymeric IR compatible microfluidic platform presented here affords the advantages of PDMS microfluidic technology to be combined with vibrational spectroscopy and microscopy techniques. In addition, the rapid fabrication and flexibility of these devices allows the channels to be designed to accommodate specific laser beam diameters and geometries. This technology will be particularly important when tailoring microfluidic devices that can be interfaced with pulsed, ultrafast IR laser experiments in a straightforward manner.

### 3.5 Additional Notes

Reprinted with permission from Analytical Chemistry **2013,** 85, 21, 10000. Copyright 2013 American Chemical Society. A. T. Krummel is grateful for generous funding from Colorado State University. M. V. Barich acknowledges the generous support of the NSF IGERT

Fellowship Program: Multidisciplinary Approaches to Sustainable Bioenergy (NSF grant, 0801707). The authors thank Professor Charles Henry for allowing us open access to the fabrication laboratory.

## References


(1) Barich, M. V.; Krummel, A. T. *Anal. Chem.* **2013**, *85* (21), 10000.

(2) Seong, G. H.; Heo, J.; Crooks, R. M. *Analytical Chemistry* **2003**, *75* (13), 3161.

(3) Chen, D.; Love, K. T.; Chen, Y.; Eltoukhy, A. a; Kastrup, C.; Sahay, G.; Jeon, A.; Dong, Y.; Whitehead, K. a; Anderson, D. G. *J. Am. Chem. Soc.* **2012**, *134* (16), 6948.

(4) Toepke, M. W.; Brewer, S. H.; Vu, D. M.; Rector, K. D.; Morgan, J. E.; Gennis, R. B.; Kenis, P. J. A.; Dyer, R. B. *Anal. Chem.* **2007**, *79* (1), 122.

(5) Nichols, K. P.; Pompano, R. R.; Li, L.; Gelis, A. V.; Ismagilov, R. F. *J. Am. Chem. Soc.* **2011**, *133* (39), 15721.

(6) Wu, T.; Mei, Y.; Cabral, J. T.; Xu, C.; Beers, K. L. *J. Am. Chem. Soc.* **2004**, *126* (32), 9880.

(7) Li, W.; Greener, J.; Voicu, D.; Kumacheva, E. *Lab Chip* **2009**, *9* (18), 2715.

(8) Puigmartí-Luis, J.; Rubio-Martínez, M.; Hartfelder, U.; Imaz, I.; Maspoch, D.; Dittrich, P. S. *J. Am. Chem. Soc.* **2011**, *133* (12), 4216.

(9) Martínez Arias, E. L.; Fazzio Martins, P.; Jardini Munhoz, A. L.; Gutierrez-Rivera, L.; Maciel Filho, R. *Industrial & Engineering Chemistry Research* **2012**, *51* (33), 10755.

(10) Yue, J.; Schouten, J. C.; Nijhuis, T. A. *Industrial & Engineering Chemistry Research* **2012**, *51* (45), 14583.

(11) Lubbeck, J. L.; Dean, K. M.; Ma, H.; Palmer, A. E.; Jimenez, R. *Analytical Chemistry* **2012**, *84* (9), 3929.

(12) George, P. A.; Hui, W.; Rana, F.; Hawkins, B. G.; Smith, A. E.; Kirby, B. J. *Opt. Express* **2008**, *16* (3), 1577.

(13) Anna, J. M.; Baiz, C. R.; Ross, M. R.; McCanne, R.; Kubarych, K. J. *International Reviews in Physical Chemistry* **2012**, *31* (3), 367.

(14) Kolano, C.; Helbing, J.; Bucher, G.; Sander, W.; Hamm, P. *The Journal of Physical Chemistry. B* **2007**, *111* (38), 11297.

(15) Bredenbeck, J.; Helbing, J.; Sieg, A.; Schrader, T.; Zinth, W.; Renner, C.; Behrendt, R.; Moroder, L.; Wachtveitl, J.; Hamm, P. *Proceedings of the National Academy of Sciences of the United States of America* **2003**, *100* (11), 6452.

(16) Fayer, M. D. Annual Review Of Physical Chemistry **2009**, 60, 21.

(17) Fenn, E. E.; Wong, D. B.; Fayer, M. D. *Journal Of Chemical Physics* **2011**, *134* (5), 54512.

(18) Birarda, G.; Grenci, G.; Businaro, L.; Marmiroli, B.; Pacor, S.; Vaccari, L. *Microelectronic Engineering* **2010**, *87* (5-8), 806.

(19) Pan, T.; Kelly, R. T.; Asplund, M. C.; Woolley, A. T. *Journal of Chromatography A* **2004**, *1027* (1-2), 231.

(20) Hinsmann, P.; Frank, J.; Svasek, P.; Harasek, M.; Lendl, B. *Lab Chip* **2001**, *1* (1), 16.

(21) Grenci, G.; Birarda, G.; Mitri, E.; Businaro, L.; Pacor, S.; Vaccari, L.; Tormen, M. *Microelectronic Engineering* **2012**, *98*, 698.

(22) Kölhed, M.; Hinsmann, P.; Svasek, P.; Frank, J.; Karlberg, B.; Lendl, B. *Anal. Chem.* **2002**, *74* (15), 3843.

(23) Chan, K. L. A.; Kazarian, S. G. *Anal. Chem.* **2012**, *84* (9), 4052.

(24) Chan, K. L. A.; Gulati, S.; Edel, J. B.; Mello, A. J. de; Kazarian, S. G. *Lab Chip* **2009**, *9* (20), 2909.

(25) Duffy, D. C.; McDonald, J. C.; Schueller, O. J.; Whitesides, G. M. *Anal. Chem.* **1998**, *70* (23), 4974.

(26) McDonald, J. C.; Duffy, D. C.; Anderson, J. R.; Chiu, D. T.; Wu, H.; Schueller, O. J. A.; Whitesides, G. M. *ELECTROPHORESIS* **2000**, *21* (1), 27.

(27) McDonald, J. C.; Whitesides, G. M. *Acc. Chem. Res.* **2002**, *35* (7), 491.

(28) Jo, B.-H.; Beebe, D. J. SPIE Conference on Microfluidic Devices and Systems II **1999**, 3877, 222.

(29) Folch, a; Jo, B. H.; Hurtado, O.; Beebe, D. J.; Toner, M. *Journal of Biomedical Materials Research* **2000**, *52* (2), 346.

(30) King, J. T.; Kubarych, K. J. *J. Am. Chem. Soc.* **2012**, *134* (45), 18705.

(31) Urbanek, D. C.; Vorobyev, D. Y.; Serrano, A. L.; Gai, F.; Hochstrasser, R. M. *J Phys Chem Lett* **2010**, *1*, 3311.

(32) Getahun, Z.; Huang, C.-Y.; Wang, T.; De León, B.; DeGrado, W. F.; Gai, F. *J. Am. Chem. Soc.* **2003**, *125* (2), 405.

(33) Krummel, A. T.; Zanni, M. T. *J Phys Chem B* **2008**, *112* (5), 1336.

(34) Dutta, S.; Cook, R. J.; Houtman, J. C. D.; Kohen, A.; Cheatum, C. M. *Analytical Biochemistry* **2010**, *407* (2), 241.

(35) Koenig, J. L.; Wang, S. Q.; Bhargava, R. *Anal. Chem.* **2001**, *73* (13), 360A.

(36) Lewis, E. N.; Treado, P. J.; Reeder, R. C.; Story, G. M.; Dowrey, A. E.; Marcott, C.; Levin, I. W. *Anal. Chem.* **1995**, *67* (19), 3377.

(37) Watson, M. D.; Gai, X. S.; Gillies, A. T.; Brewer, S. H.; Fenlon, E. E. *J. Phys. Chem. B* **2008**, *112* (42), 13188.

(38) Tucker, M. J.; Gai, X. S.; Fenlon, E. E.; Brewer, S. H.; Hochstrasser, R. M. *Phys. Chem. Chem. Phys.* **2011**, *13* (6), 2237.

(39) Londergan, C. H.; Wang, J.; Axelsen, P. H.; Hochstrasser, R. M. *Biophysical Journal* **2006**, *90* (12), 4672.

(40) Wagner, C.; Buchegger, W.; Vellekoop, M.; Kraft, M.; Lendl, B. *Anal Bioanal Chem* **2011**, *400*, 2487.

(41) Kakuta, M.; Hinsmann, P.; Manz, A.; Lendl, B. *Lab Chip* **2003**, *3* (2), 82.

(42) Chung, H. S.; Ganim, Z.; Jones, K. C.; Tokmakoff, A. *PNAS* **2007**, *104* (36), 14237.

# Chapter 4

## Fast Microfluidic Gradient Generation Coupled with Infrared Microspectroscopy for Chemical Imaging

This chapter is a publication submitted to the journal Analytical Chemistry in 2016. This work focuses on the development and characterization of a microfluidic fast gradient generator. A second nozzle was incorporated into a flow focusing device, creating a contraction/expansion region within the device resulting in the curvature of streamlines. The resulting flow profile enables probing molecular interactions at early times in a multiplexed fashion.

### 4.1 Introduction

Microfluidic devices have now gained wide acceptance and utility in a variety of settings ranging from point-of-care environments to centralized laboratories. In centralized laboratories, microfluidics have found growing acceptance because the two- and three-dimensional channels enable better fluidic control than many traditional fluidic systems. As a result, they have found application in areas ranging from single cell analysis to protein crystallization to chemical synthesis. The keys to success in each of these examples are control of fluid flow, reagent concentrations via gradient generation, mixing, and interfacing with detection modalities that provide the appropriate compromise between sensitivity and chemical selectivity. For example, if one is performing chemical synthesis on-chip, the microfluidic technology employed should afford interfacing with spectroscopic techniques that can report on chemical transformations such as nuclear magnetic resonance spectroscopy or vibrational spectroscopies, including linear infrared spectroscopy or Raman spectroscopy.

Development of gradient generation and fast mixing in microfluidic devices have been subjects of intense investigation for decades.[1–11] Both are critical tools for high throughput investigations of chemical and biological systems—fast mixing on-chip delivers the ability to monitor the time progression of molecular interactions or kinetics and gradient generation on-chip offers the ability to monitor chemical interactions under multiple reaction conditions simultaneously.[12–19] Microfluidic devices capable of fast mixing or gradient generation have been interfaced with spectroscopic techniques that provide chemical sensitivity, independently. [7,20] However, the integration of such microfluidic tools coupled with vibrational spectroscopy for experiments on a single chip has yet to be reported.

Several approaches to access early time scales during chemical interactions have been demonstrated. Flow-focusing devices, T-junction mixing devices, and droplet generator devices are three specific examples that have been broadly used to capture chemical interactions. [14,18,21–25] However, the development of these tools to operate in a parallelized fashion to afford multiplexing measurements has been limited. Creating a gradient generator that affords access to interactions at early times is important in order to open the potential for multiplexing measurements of chemical and biological interactions across multiple time scales.

Expansion/contraction regions can be utilized to generate curved streamlines at low Reynolds numbers. Remaining in a low Reynolds number regime on-chip has the added advantage of maintaining tunability in the output flows. Development of a tunable gradient laterally in the device is a natural product of the streamline curvature. Moreover, an added benefit of this approach is the inherent fast mixing that takes place in the device. In this work, we present a dual nozzle device geometry that exploits flow behavior accessible in the simple contraction/expansion geometry. Curvatures in the fluid streamlines are present and can be

tuned by device geometry and flow conditions. In doing so, a stable concentration gradient is generated on millisecond timescales. The effect of total flow rate, relative flow rates, and nozzle geometry are discussed herein. The results are juxtaposed to a traditional hydrodynamic flow-focusing device, because the operation of flow-focusing devices is governed by diffusion and the tunability of such devices are controlled by flow conditions. The fast gradient generated is produced by the addition of an expansion/contraction region to a cross junction, or alternatively, by simply adding a second nozzle to a traditional flow focusing device.

Many different detection motifs have been described for microfluidics but vibrational spectroscopy has been among the least utilized because common substrate materials are not transparent in the IR regime.[26] Raman spectroscopy has been utilized for a number of applications in a range of microfluidic devices. [27,28] Infrared spectroscopy has been described less frequently despite its power for characterizing a variety of chemical and biological systems. Recently, fast-mixing, flow-focusing devices have been coupled to IR microspectroscopy to follow structural dynamics of proteins and nucleic acids.[18] We recently reported an IR transparent poly(dimethylsiloxane) (PDMS) system that enables use of common soft lithography to create final channels in devices for IR spectroscopy.[29] Here, we demonstrate a gradient generation system enabled by the PDMS microfluidic thin chip technology. The gradient generator affords mixing in under 2 μs and a stable gradient produced in 1.1 ms. We first describe the gradient generator and then demonstrate its use with infrared microspectroscopy for studying chemical reactions and solute-solvent interactions.

## 4.2 Methods

### 4.2.1 Device Fabrication

All microfluidic devices were fabricated in polydimethyl siloxane (PDMS, Sylgard 184) using standard soft photolithography techniques. Briefly, SU-8 2025 was applied to clean silicon wafers, then spun to a thickness of 45 $\mu$m. Channel designs were imprinted using UV-photolithography, and the unexposed SU-8 was removed. A 10:1 PDMS to cross-linker liquid mixture was then poured on the molds and cured. Optical profilometer measurements confirmed the channel heights in PDMS were the same as the SU-8 photoresist molds. With a biopsy tool, tubing ports were punched out of the cured PDMS. The PDMS channels were then plasma sealed to a flat piece of PDMS. Fluid was pumped out of 10 mL syringes using two NE-500 Programmable OEM syringe pumps.

IR compatible microfluidic chips were made using PDMS to house the fluidic channels. The fabrication of the PDMS IR compatible microfluidic chips has been described previously.[29] Briefly, each microfluidic chip consists of four layers: a support layer, microchannel layer, adhesion layer, and calcium fluoride backbone. Each layer is prepared independently and then assembled into the complete microchip. The microchannel layer is prepared by placing PDMS on a SU-8 mold that is then compressed using a hydraulic press to achieve specific thicknesses required by the experiment. The adhesion layer was prepared by spin coating clean calcium fluoride windows with PDMS to the desired thickness. All assembly was done via PDMS sealing with oxygen plasma.

### 4.2.2 Fluid Characterization Methods

Fluid flow was imaged using brightfield and fluorescence microscopy. For all fluorescence images used to characterize the behavior of the gradients generated, deionized water and a

solution of 0.15 mM sodium fluorescein in deionized water were flowed through the device in either the inner or outer channels. All flow rates were within the range of 1 to 95 $\mu$L/min in order to produce specific flow rate ratios, and total flow rates, for each experiment. Duplicate images were taken, one a purely fluorescent image and the second, with the addition of a low backlight as to also capture the channel features. All images were collected under steady-state flow conditions using a Nikon Eclipse TE2000 microscope supplied with a 1392 x 1040 imaging CCD camera. Camera settings were optimized to incorporate a 35-millisecond exposure time and binning of 4 to visualize mixing by fluorescence.

The travel time at each position within the channel was determined by observing the fluorescence decay of europium microspheres (FluoSphere, Invitrogen). Fluorescent intensity images were taken at multiple points down the channel while the europium bead solution was flowing through the device. Fluorescent lifetime images of the beads *in situ* were used to correlate fluid velocity to position in the devices. The fluorescent lifetime of the europium microspheres was determined using standard methods. Briefly, the europium microspheres were placed in a 1-cm pathlength quarts cuvette and excited with a 355 nm 7 ns pulsed pump beam tuned to 355 nm (Opotek inc Opolette 355 LD tunable laser). Fluorescence intensity measurements were collected perpendicular to the incident beam and focused onto a Thermo Jarrell Ash (Model 82-410) 0.25 Meter Monochromator Spectrograph with attached photomultiplier tube. The fluorescence lifetime of the beads was determined to be 540 $\mu$s and is in good agreement with the literature.[18] For the measurements taken inside the channel, the 355 nm pulsed pump beam from the Opolette 355 LD was centered onto an adjustable mechanical slit (Thor Labs). Using a lens, the slit was imaged onto the microfluidic channel. Images were collected collinear to the excitation beam, using a filter to remove the residual pump beam prior

to imaging. The channel was imaged using a 20x Nikon microscope objective onto a Mightex monochrome 1.2MP Global Shutter CMOS Camera (SMN-B012-U). Images were collected through the Mightex application software prior to custom Matlab processing. In combination with volumetric flow rate calculations, the time taken for the fluid passing through the second nozzle at each pixel was calculated. Mixing times were computed from this data and the results are discussed below. Details regarding the time-to-pixel calibration and the mechanism of gradient formation are provided in the supplemental information.

In order to investigate the mixing characteristics of the devices, fluorescence-quenching experiments were performed. Fluorescence images for each flow rate were collected using aqueous solutions of sodium fluorescein (1.29 mM) and deionized water. These images were compared to images collected during fluorescence quenching experiments in which aqueous solutions of sodium fluorescein (1.29 mM) and 0.5 M potassium iodide served as the inner and outer fluids, respectively. In-house Matlab routines were used to compare the fluorescence distribution in each image set. By doing so, the presence and relative intensity of quenching was determined for each point in the channel.

Chemical mixing was further confirmed using FTIR microscopy. All infrared microscope images were acquired using a Bruker Hyperion 3000 FTIR microscope. The FTIR microscope is equipped with a 64 x 64 element FPA detector and a 15x objective producing 2.7 $\mu$m spatial resolution. All images were taken in transmission mode, and were processed using the OPUS software (Bruker Optics). Chemical maps were generated by integrating the signal under the absorption peaks for the species of interest. Intensities depicted are the integrated area under the absorbance spectrum between two specified frequencies. More advanced data analysis was accomplished using in-house Matlab routines.

In this work, an acid-base reaction and solvent-solute interactions were used to demonstrate the utility of the gradient generators for chemical applications. For the acid-base reaction, the protonation state of the carboxylic acid group in acetic acid was monitored. Deprotonation was accomplished with solutions of 100 mM acetic acid in $D_2O$ mixing with 1.0 M NaOD (Acros). Solvent-solute interactions were observed by monitoring the 2150 $cm^{-1}$ absorbance peak of a 30 mM KOCN solution. Methanol was flowed as the inner fluid and dimethylformamide was flowed as the outer fluid. The utility of the gradients generated are discussed below.

### 4.3 Device Characterization

Two distinct devices were compared, a traditional flow-focusing device and a dual nozzle gradient generator device. Both designs are illustrated in Figure 4.1. Each design is symmetric around the vertical axis thus only half of the design is shown for ease of comparison. In each design, the outer fluid focuses the inner fluid. The orifice at which the two fluids first interact ranges from 28 $\mu$m to 84 $\mu$m wide and is designated as the first nozzle. In the traditional flow focusing devices, the outer fluid flows into the main channel via channels that are 170 $\mu$m wide. The center focused fluid flows unobstructed down the length of the outlet channel that is 350 $\mu$m wide and 8500 $\mu$m long. In the dual nozzle gradient generators, the inner fluid is hydrodynamically focused into a stream and passes through a second nozzle. In the device shown in Figure 4.1a, the second nozzle is situated 42 $\mu$m down stream of the first nozzle, and is produced with 36° notch that extends into the 350 $\mu$m wide channel from each side. The widths of the first and second nozzles in this device are 42 $\mu$m. Fluorescence images of the resulting flow for each device are analyzed in order to provide a full characterization of the dual nozzle

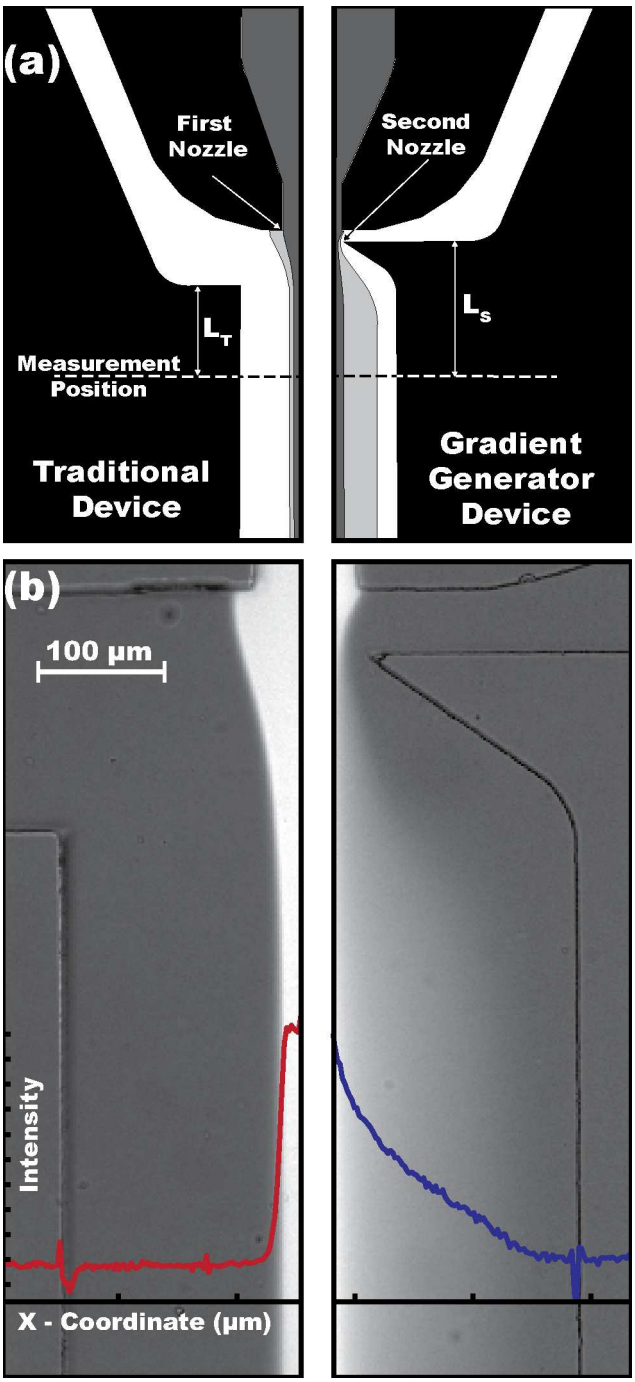


**Figure 4.1 Sumarized Comparison of a Traditional and Gradient Generator Device**

(a) Summarized channel illustrations for the layouts of the traditional flow focusing (left) and the dual nozzle gradient generator device (right) (b) brightfield images of the devices in use. The modification to the flow profile is highlighted by the changes in distribution of sodium fluorescein, illustrated by the fluorescence intensity profile on the lower portion of both images.

gradient generator in context of a traditional flow-focusing device in which no gradients are formed. Individual intensity profiles perpendicular to the channel were observed at distances, L, from the second nozzle down the channel. A quantitative description of the behavior of each flow experiment could be obtained by plotting parameters of the profiles as a function of distance down the channel.

Dimensionless numbers are often used in the microfluidics literature in order to assess the relative contributions of different aspects of flows that contribute to the observed flow characteristics within the device. The Reynolds number compares the relative strength of inertial forces to viscous forces within a given geometry according to the equation,

$$\mathrm{Re} = \frac{\rho L_0 U_0}{\eta}$$

where, $\rho$ is the density of the fluid, $L_0$ is the typical length scale, $U_0$ is the fluidic velocity, and $\eta$ is the shear viscosity. The largest gradient widths are observed at the largest Reynolds number examined in these experiments, Re = 42.6, which occurs within the second nozzle. In addition, Re = 42.6 generates the mixing required to form the gradient as observed by 3 $\mu$m after exiting the second nozzle, corresponding to a mixing time of 2 $\mu$s. The gradient produced in the dual nozzle design at Re = 42.6 expands to 250 $\mu$m wide at a distance 175 $\mu$m beyond the second nozzle, seen in Figure 4.1b; thus, the desired gradient is established in 1.1 ms. Mixing in the dual nozzle gradient device occurs in a two-step process in which advection induced mixing occurs immediately out of the second nozzle and mixing at longer timescales is due to diffusion. Moreover, we find the gradient formed in the dual nozzle gradient generator design is broadly tunable with total flow rate, as well as the ratio of outer flow rate to inner flow rate. Complete characterization of the gradient response is reported in the supplemental information.

The affect a dual nozzle design has in the formation of gradients when added to traditional flow focusing devices can be explained through comparison of the flow profiles between both device styles. Characterization was accomplished using in-house Matlab routines to analyze the gray scale intensity in the purely fluorescent images. The captured images covered a range flow rate ratios, $\alpha$, over a span of total flow rates, $Q_T$. $\alpha$ is defined as the ratio of the total outer flow rate to the inner flow rate, and total flow rate, $Q_T$, is the sum of the two outer and inner flow rates. The profiles of the dual nozzle gradient generator device were compared to the profiles of a traditional flow-focusing device under the same flow conditions. Figure 4.2 is a direct comparison between traditional flow focusing device and gradient generator devices. In Figure 4.2a and 4.2b the fluorescence images are shown of a traditional flow focusing and a dual nozzle gradient generator at a total flow rate of 100 $\mu$L/min and $\alpha$ equal to 9. From these images, the intensity profiles were obtained using the gray scale values of each pixel along selected rows of the image. Examples of the intensity profiles from each image are plotted as intensity of the fluorescein versus position across the channel, shown in Figure 4.2c and 4.2d. The respective positions of each profile are denoted in 4.2a and 4.2b by the correspondingly colored bars. Each intensity profile is individually sampled to find the intensity values corresponding to 95% and 5% of the maximum intensity of that profile. The distance between the two 95% values in each profile is referred to as the center width or center stream; the average distance between 95% and 5% intensity values in each profile is referred to as the gradient width. Figure 4.2c and 4.2d depict the flow profiles at six points down the channel by plotting the intensity of the fluorescence at each point across the channel, and are offset for clarity. For both device designs, the inner fluid has a higher local pressure than the outer fluid at the first nozzle, leading to an immediate expansion of the center stream out of the nozzle, which is observed in the uppermost

flow profiles. In a traditional device, the center stream width comes to a constant value as the channel transitions out of the channel junction and into the output channel. In the gradient generator device, the center stream immediately shrinks to the narrowest point as the fluids pass through the constriction of the second nozzle. Upon exiting the second nozzle, the center stream expands to a constant width as it travels out of the nozzle and into the output channel. Plots of the width of the center stream relative to the distance from the first nozzle for both the traditional and dual nozzle gradient generator channel designs are shown in Figure 4.2e and 4.2f, respectively. For both styles of devices, the majority of the center stream width change occurs within the first 100 $\mu$m from the first nozzle, directly caused by the merging of the three channels and equilibrating once entering the output channel. The equilibrium center stream width is constant and is inversely proportional to $\alpha$, confirming that beyond the second nozzle, the established center flow profiles of the gradient generator devices reflect similar behavior to the traditional flow-focusing devices, with the added benefit of a gradient region on either side of the center stream. Under the flow conditions and nozzle geometries explored in this work the smallest center stream width achieved in the traditional flow-focusing devices was 5 $\mu$m. This is similar to focused stream widths achieved previously.[21,30–33]

One specific parameter that sets our gradient generator apart is the time required to form the gradient. Faster formation time values are important because chemical reactions can only occur when each reactant comes into contact with the other. We have calibrated the gradient produced in the dual nozzle gradient generator device and confirmed the mechanism by which the gradient is formed using three different methods. First, the concentration profiles for the outer and inner fluids were verified ensuring that there are regions of mixed solutions. Second, the regions of mixed solutions were confirmed to be mixed, rather than layered, using fluorescence quenching

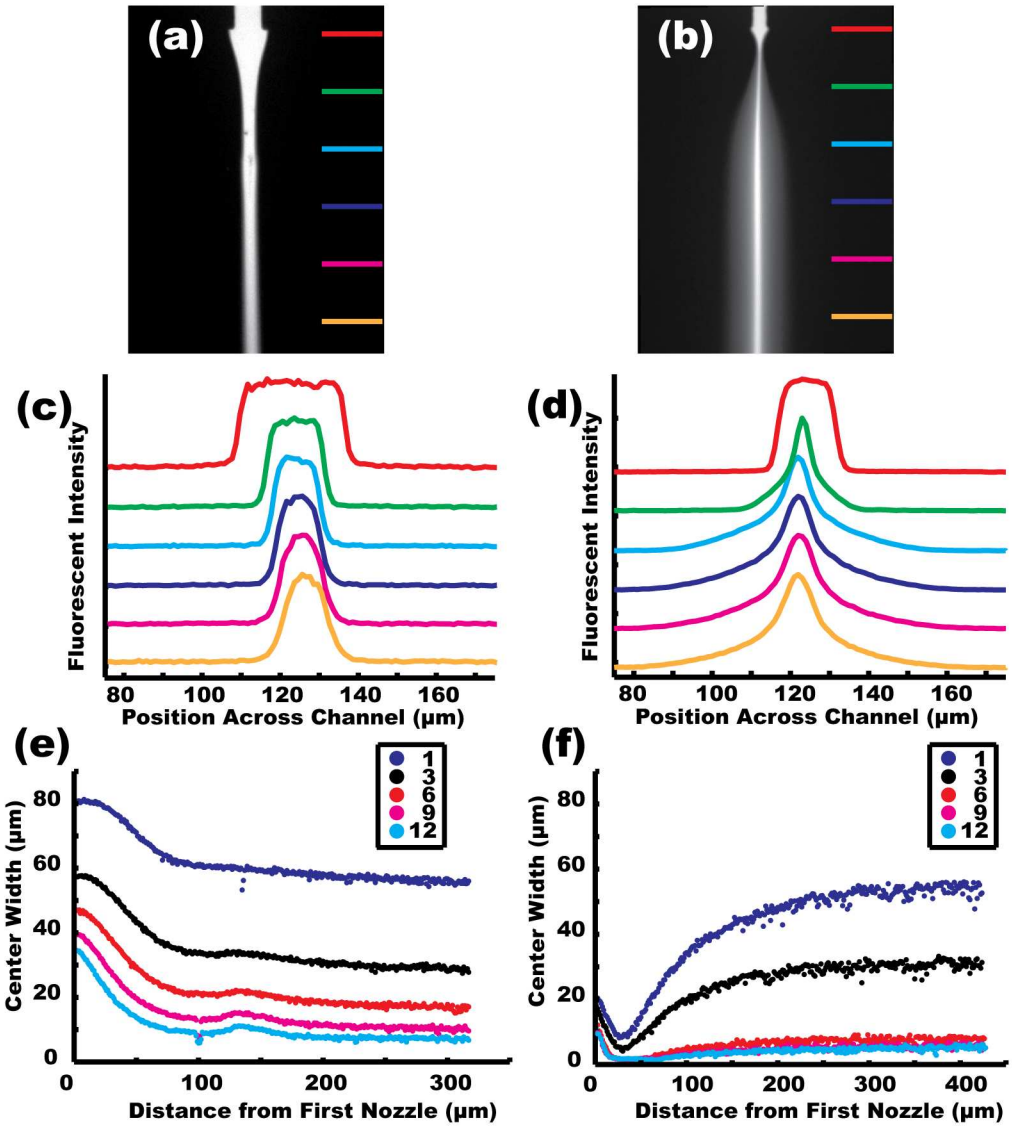


**Figure 4.2 Quantitative Comparison Between the Two Device Designs**

(Left) Traditional flow focusing device and (Right) gradient devices. (a, b) fluorescence images of sodium fluorescein focused by water (c,d) a representative sample of intensity profiles measured from the the fluorescence images. The color of each line corresponds to the measurements positions indicated by the matching color bars in (a,b) for each device design. (e,f) The width of the focused stream in each design, measured from the intensity profiles, plotted against the distance from the first nozzle.

experiments. The expansion contraction region was confirmed to be the source of the gradient generation through experiments decoupling the first and second nozzles. Lastly, time-to-pixel values for the device were determined using europium bead fluorescence. These time values were then compared to calculated values based on channel dimensions and the total flow rate for the dual nozzle gradient generator devices. The full details of these experiments and their results are provided in the supplemental information. In brief, all calibration experiments reveal that mixing in the devices results from the second nozzle and is accomplished in 2 μs at a total flow rate of 100 μL/min and α value equal to 12. Under these flow conditions the gradient across the channel is established in 1.1 ms and is 75 μm in width from the center of the channel.

Each of the total flow rates explored in this work establish the gradient in the device many magnitudes faster than diffusion due to the advection produced by the contraction/expansion region in the device defined by the dual nozzle design. For perspective, a small molecule such as fluorescein diffusing in water, would take approximately 1.5 seconds and require a 19000 mm long channel to establish the 40 $\mu$m gradient that the 12 $\mu$L/min flow rate generates in this dual nozzle gradient generator device described in this work. Moreover, in a traditional flow-focusing device an inner sheath would need to be produced at nanometer length scales in order to achieve mixing in 1.0 $\mu$s. For example, sodium fluorescein, which has a diffusion coefficient equal to 5.4 x$10^{-6}$ cm$^2$/sec in water, will travel 32 nm in 1.0 $\mu$s under these flow conditions.

### 4.4 Infrared Microspectroscopy

Applications of the gradients generated using the dual nozzle device design were performed through chemical mapping using IR microscopy. Traditionally, gradients have been used to perform experiments such as pH jumps or a solvent-solute interaction experiment. Discussed

below, we have demonstrated one of each type of experiment using the gradient generator devices.

Figure 4.3a is an image taken via IR microscopy of a solution of 100 mM acetic acid in $D_2O$ being focused by an outer solution of 1.0 M NaOD at a total flow rate of 20 $\mu$L/min and alpha value of 1. The color map illustrates the integrated intensity of the 1700 $cm^{-1}$ acetic acid carbonyl absorption, representative of the presence and relative concentration of protonated acetic acid. The focused stream is easily identified by the drastic color change from blue to red, indicating that the center stream has had little to no mixing with the outer fluid. Mixing within the center stream is governed by the diffusion of the outer fluid into the inner fluid and the reverse. The total flow used when acquiring the data affords the outer fluid to diffuse 8.2 $\mu$m into the inner fluid in the length of the channel shown in the image, therefore, we do not expect to see a great deal of change in the center stream along the distance of the channel. Figure 4.3b is an intensity map for the integrated intensity under the 1560 $cm^{-1}$ acetate absorption peak. Acetate forms when the acetic acid is mixed with the solution of NaOD, therefore any intensity observed in this image is a direct result of the inner and outer fluids mixing. Intensity for the peak appears at the boundary between the inner and outer fluids prior to the second nozzle. As the fluids pass through the second nozzle, the gradient generated is observed by an increase in the intensity of the integrated area. However, at this point, the gradient is so narrow that intensity of the peak is still quite small. The spatial resolution of the IR portion of the microscope is 7.29 $\mu m^2$, therefore the signal that is measured covers more area than the gradient itself, thus reducing the signal. Once the gradient has increased to a width distinguishable by the detector, the intensity increases. At 175 $\mu$m beyond the second nozzle, the gradient maintains a constant width,

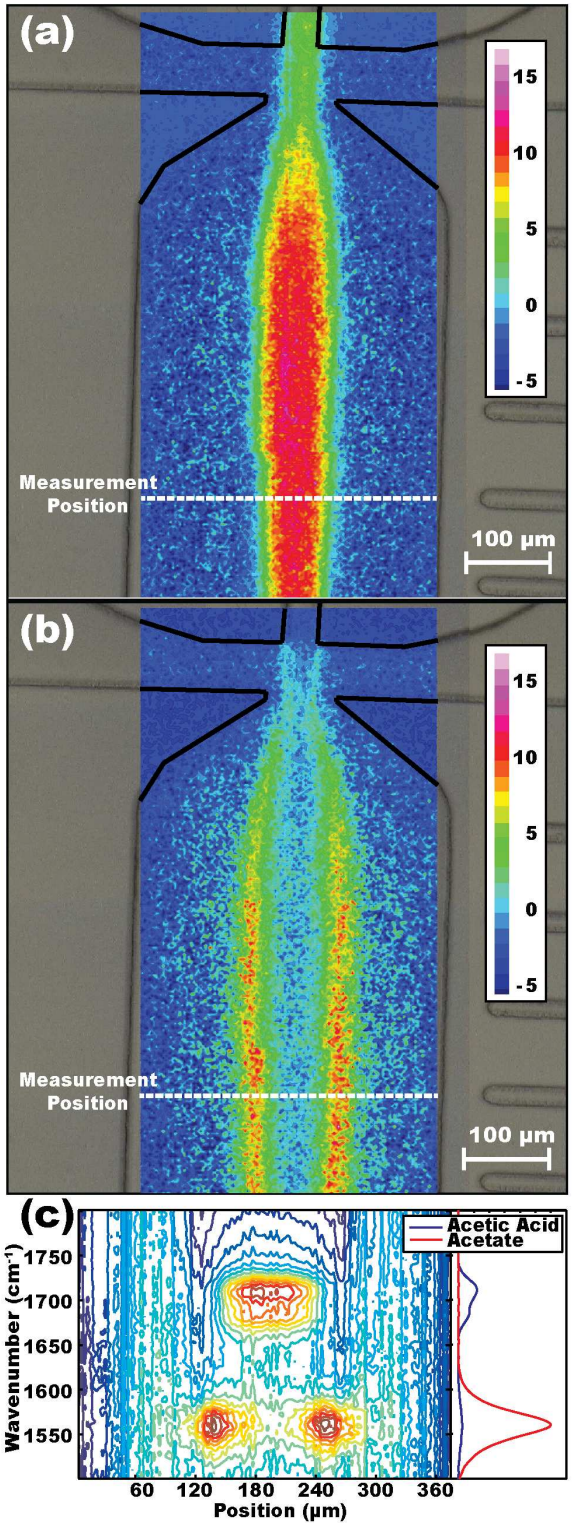


**Figure 4.3 Spectrochemical Mapping in the Dual Nozzle Gradient Generator Geometry**

FTIR micro-spectroscopy mapping the integrated peak intensity of (a) protonated acetic acid and (b) unprotonated conjugate base. (c) A graph plotting the measured spectrum at each point across the microchannel.

indicating that diffusion plays a limited roll within the field of view of the image collected. Secondly, the stability of the gradient reinforces the conclusion that we are in the laminar flow regime. Laminar flow assures steady state flow dynamics and affords the ability to observe multiple reaction conditions in the same measurement. Both IR intensity maps depicted in Figure 4.3a and 4.3b provide a simple representation for tracking individual species in each image. Figure 4.3c is a plot of wavelength on the y-axis as a function of position across the channel on the x-axis, and absorbance in the z-axis. By scanning in the vertical direction from any point on the x direction, we can obtain an idea of what spectral features are present at that specific point. In this example, we are able to identify the presence of the acetic acid species by identifying the peak at 1700 $cm^{-1}$ and the acetate species at 1560 $cm^{-1}$. Since the peaks for each species are not overlapping, we can easily distinguish which points across the channel slice contain each species, and where the two are both present.

The fast gradient generator is also a powerful tool for exploring solvation dynamics in a multiplexed measurement. We demonstrate this by monitoring potassium cyanate (KOCN) in a gradient of cosolvent conditions produced in the device. The absorption peak in the 2100 $cm^{-1}$ to 2200 $cm^{-1}$ region of 30 mM KOCN was monitored in a solvent gradient. The gradient was generated with methanol and DMF as the inner and outer fluids, respectively, using a total flow rate of 20 $\mu$L/min and an alpha of 1. Figure 4a shows a chemical map split vertically to show the contributions from each solvent, Methanol (top) and DMF (bottom). Within this image, IR spectra from specified spatial coordinates, marked with different colored circles, were extracted. Those spectra were plotted in figure 4b, below the chemical map and in the same color as the circle marking its location. As the measurement positions track across the gradient, the absorbance peak for KOCN, centered at 2164 $cm^{-1}$ in methanol, shifts to the lower frequency

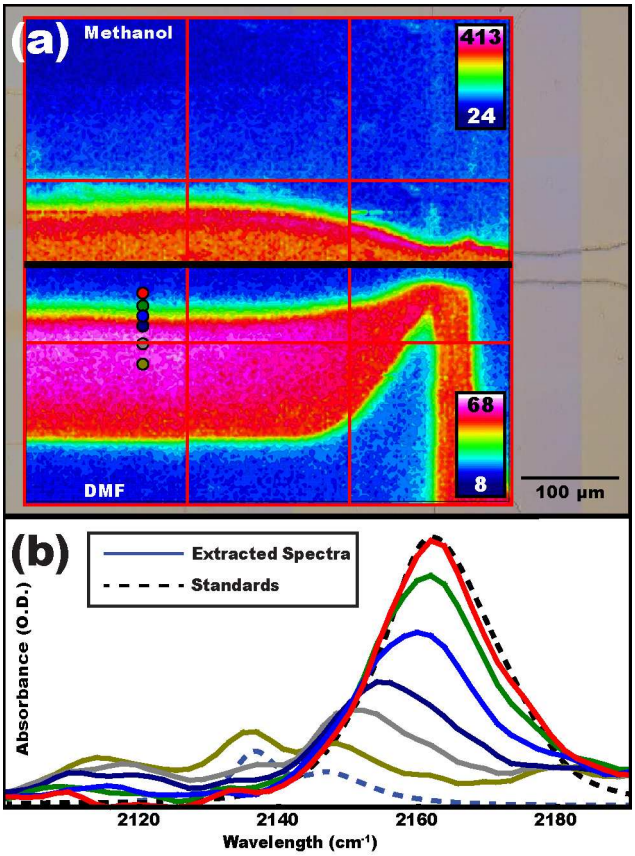


**Figure 4.4 A Solvent-Solute Gradient Experiment.**

(a) IR chemical map of the solvents Methanol (top) and DMF (bottom) mapped on each half of the device. Within this image are six points, indicated by the colored circles, with which the (b) individual spectra are plotted. Control spectra taken in traditional sample cells are also plotted, noted with the dashed lines.

absorption peak pair centered at 2136 $cm^{-1}$ and 2144 $cm^{-1}$. The cyanate oscillator is sensitive to the solvent environment with which it is exposed, thus, the shift in the absorption peak is indicative of a changing solvent environment and changes in the solvation shell surrounding the KOCN contact ion pair. The two spectra plotted with dotted lines were taken as control spectra, and are of 30 mM KOCN in pure solvent collected in wet demountable $CaF_2$ sample cells. The spectra of the controls show good agreement in direct comparison between points taken in the channel of the end points of the gradient. More importantly, from the image, the complete series of solvents can be gathered from taking small steps in between those endpoints. Using this method, the IR absorption behavior for KOCN in solvent mixtures of methanol and DMF was observed completely.

### 4.5 Conclusions

In this work, we have demonstrated the utility of a dual nozzle gradient generator device for chemical applications. We produce a stable gradient useful for incorporating multiplexed measurements of molecular interactions by exploiting the streamline curvature generated by a contraction/expansion region incorporated into a flow-focusing geometry. Moreover, the gradient is established within milliseconds of the fluids passing through the second nozzle in the device. Upon characterizing the response of the center stream width and gradient width to changes in flow conditions, we find the center stream width to behave similarly to traditional hydrodynamically focused inner sheaths and the gradient width to be broadly tunable. Thus, this technology will is useful in probing molecular systems across multiple timescales and in multiple environments within a single chip.

## 4.6 Additional Notes

The authors thank Professor Charles Henry for allowing us open access to the fabrication laboratory and providing important feedback regarding this manuscript. A. T. Krummel appreciates the generous funding for this work from BP Exploration Operating Company Ltd. and the National Science Foundation (Grant No. CHE-1255658).

The contents of supporting information follow the experiments used to validate the gradient that is formed and calibrate the time taken to form it. Experiments that confirm both the tunability of the gradient using flow parameters and that the gradient is dependent on the second nozzle are reported. The results of component concentration calibration experiments are discussed, ensuring that there are regions of both solutions and that they are mixing rather than being layered. Lastly, time calibration experiments are reported, confirming the gradient generation time in the device.

## References


(1) Li, Y.; Liu, C.; Feng, X.; Xu, Y.; Liu, B.-F. *Anal. Chem.* **2014**, *86* (9), 4333.

(2) Jeon, W.; Shin, C. B. *Chemical Engineering Journal* **2009**, *152* (2–3), 575.

(3) Lu, Z.; McMahon, J.; Mohamed, H.; Barnard, D.; Shaikh, T. R.; Mannella, C. A.; Wagenknecht, T.; Lu, T.-M. *Sensors and Actuators B: Chemical* **2010**, *144* (1), 301.

(4) Pakdel, P.; McKinley, G. H. *Phys. Rev. Lett.* **1996**, *77* (12), 2459.

(5) You, J. B.; Kang, K.; Tran, T. T.; Park, H.; Hwang, W. R.; Kim, J. M.; Im, S. G. *Lab Chip* **2015**.

(6) Gleeson, J. P. *Physics of Fluids (1994-present)* **2005**, *17* (10), 100614.

(7) Hinsmann, P.; Frank, J.; Svasek, P.; Harasek, M.; Lendl, B. *Lab on a Chip* **2001**, *1* (1), 16.

(8) Bessoth, F. G.; DeMello, A. J.; Manz, A. *Anal. Commun.* **1999**, *36* (6), 213.

(9) Johnson, M.; Kamm, R. *J. Fluid Mech.* **1986**, *172*, 329.

(10) Sudarsan, A. P.; Ugaz, V. M. *PNAS* **2006**, *103* (19), 7228.

(11) Afzal, A.; Kim, K.-Y. *J. Chem. Eng. Jpn.* **2013**, *46* (3), 230.

(12) Jiang, L.; Zeng, Y.; Sun, Q.; Sun, Y.; Guo, Z.; Qu, J. Y.; Yao, S. *Anal. Chem.* **2015**, *87* (11), 5589.

(13) Hertzog, D. E.; Michalet, X.; Jäger, M.; Kong, X.; Santiago, J. G.; Weiss, S.; Bakajin, O. *Anal. Chem.* **2004**, *76* (24), 7169.

(14) Gambin, Y.; Simonnet, C.; VanDelinder, V.; Deniz, A.; Groisman, A. *Lab on a Chip* **2010**, *10* (5), 598.

(15) Lee, K.; Kim, C.; Kim, Y.; Jung, K.; Ahn, B.; Kang, J. Y.; Oh, K. W. *Biomed Microdevices* **2010**, *12* (2), 297.

(16) Lin, F.; Saadi, W.; Rhee, S. W.; Wang, S.-J.; Mittal, S.; Jeon, N. L. *Lab Chip* **2004**, *4* (3), 164.

(17) Irimia, D.; Geba, D. A.; Toner, M. *Anal. Chem.* **2006**, *78* (10), 3472.

(18) Burke, K. S.; Parul, D.; Reddish, M. J.; Dyer, R. B. *Lab Chip* **2013**, *13* (15), 2912.

(19) Hertzog, D. E.; Ivorra, B.; Mohammadi, B.; Bakajin, O.; Santiago, J. G. *Anal. Chem.* **2006**, *78* (13), 4299.

(20) Hinsmann, P.; Haberkorn, M.; Frank, J.; Svasek, P.; Harasek, M.; Lendl, B. *Appl. Spectrosc.* **2001**, *55* (3), 241.

(21) Kise, D. P.; Magana, D.; Reddish, M. J.; Dyer, R. B. *Lab Chip* **2013**, *14* (3), 584.

(22) Song, H.; Ismagilov, R. F. *J. Am. Chem. Soc.* **2003**, *125* (47), 14613.

(23) Tice, J. D.; Song, H.; Lyon, A. D.; Ismagilov, R. F. *Langmuir* **2003**, *19* (22), 9127.

(24) Chan, K. L. A.; Kazarian, S. G. *Anal. Chem.* **2012**, *84* (9), 4052.

(25) Chan, K. L. A.; Gulati, S.; Edel, J. B.; Mello, A. J. de; Kazarian, S. G. *Lab Chip* **2009**, *9* (20), 2909.

(26) Fiorini, G. S.; Chiu, D. T. *BioTechniques* **2005**, *38* (3), 429.

(27) Sarrazin, F.; Salmon, J.; Bordeaux, R.; Schweitzer, D.; Pessac, F.-; Talaga, D.; Servant, L. *Analytical Chemistry* **2008**, *80* (5), 1689.

(28) Ashok, P. C.; Singh, G. P.; Rendall, H. A.; Krauss, T. F.; Dholakia, K. *Lab Chip* **2011**, *11*, 1262.

(29) Barich, M. V.; Krummel, A. T. *Anal. Chem.* **2013**, *85* (21), 10000.

30) Knight, J. B.; Vishwanath, A.; Brody, J. P.; Austin, R. H. *Phys. Rev. Lett.* **1998**, *80* (17), 3863.

(31) Park, H. Y.; Qiu, X.; Rhoades, E.; Korlach, J.; Kwok, L. W.; Zipfel, W. R.; Webb, W. W.; Pollack, L. *Anal. Chem.* **2006**, *78* (13), 4465.

(32) Simonnet, C.; Groisman, A. *Appl. Phys. Lett.* **2005**, *87* (11), 114104.

(33) Lee, G.-B.; Chang, C.-C.; Huang, S.-B.; Yang, R.-J. *J. Micromech. Microeng.* **2006**, *16* (5), 1024.

(34) Gan, H. Y.; Lam, Y. C.; Nguyen, N. T.; Tam, K. C.; Yang, C. *Microfluid Nanofluid* **2006**, *3* (1), 101.

(35) Gan, H. Y.; Lam, Y. C.; Nguyen, N.-T. *Appl. Phys. Lett.* **2006**, *88* (22), 224103.

(36) Rodd, L. E.; Scott, T. P.; Boger, D. V.; Cooper-white, J. J.; Mckinley, G. H. *J. Non-Newton. Fluid Mech* **2005**, *129*, 1.

(37) Lam, Y. C.; Gan, H. Y.; Nguyen, N. T.; Lie, H. *Biomicrofluidics* **2009**, *3* (1), 014106.

## Chapter 4 Supplemental Information

### S4.1 Supplementary Introduction

There are many components that set this gradient generator apart from current technology for use in chemical imaging. Having the ability to tune the size of the gradient with the flow parameters while maintaining fast gradient formation time values is useful when designing an experiment with a chemical reaction occurring on-chip. We used five different experiments to calibrate the fast gradient generator design to ensure that certain fluidic characteristics were met. First, the flow parameters governing the tunability of the gradient were explored. Second, the expansion contraction region was confirmed to be the source of the gradient generation through experiments decoupling the first and second nozzles. Third, the concentration profiles for the outer and inner fluids were verified ensuring that, at least two dimensionally, there are regions of mixed solutions. Next, the regions of mixed solutions were confirmed to be mixed, rather than layered, using fluorescence quenching experiments. Lastly, time calibration of the device was performed in two different ways. Mapping time-from-second-nozzle values for the device was performed using Europium bead fluorescence. These time values were then compared to calculated values based on channel dimensions and the total flow rate for the dual nozzle gradient generator devices at every combination of total flow rate and $\alpha$.

### S4.2 Calibration Section

The gradient flow profile was found to respond to changes in the flow rates of the inner and outer fluids. We found that the gradient width was most influenced by two flow parameters specifically: flow rate ratio, $\alpha$ and the total flow rate, $Q_T$. Figure S4.1 depicts the relationship

between the gradient width and these two variables. Three separate total flow rates were examined, 100, 60, and 12 $\mu$L/min, each at five flow rate ratios. Values of $\alpha$ equal to 1, 3, 6, 9, and 12 were used to illustrate the behaviour of the device across a range of possible flow rate ratios. By varying these parameters, we were able to characterize the response of the gradient width to changes in the flow conditions.

Changes in the total flow rate were found to affect the width of the gradient generated. Gradient widths increased when the total flow rate increased for equal alpha values. For example, the gradient width generated with $Q_T$ = 12 $\mu$L/min and $\alpha$ = 3, is 37 $\mu$m based on measurements taken after the gradient equilibrated 175 $\mu$m beyond the second nozzle (Figure S4.1c). At the same $\alpha$ value and location in the device, the gradient widths were 53 $\mu$m and 87 $\mu$m at $Q_T$ = 60 $\mu$L/min and $Q_T$ = 100 $\mu$L/min, respectively (Figure S4.1b and S4.1a). The increase in gradient width follows across all alpha values examined. However, the flow rate ratio, $\alpha$, offers an additional point of tunability in this system.

Figure S4.1a depicts the gradient width at a total flow rate of 100 $\mu$L/min for five alpha values. At 100 $\mu$L/min, the gradient width appears to behave independently from the flow rate ratio based on the similar gradient widths observed at all $\alpha$ values. Starting from the second nozzle at 18 $\mu$m wide, the gradient rapidly increases in width to 70 $\mu$m wide until the channel comes to constant width 175 $\mu$m down the channel. A similar independence of alpha is also seen at the lowest total flow rate, 12 $\mu$L/min, depicted in Figure S4.1c; the gradient widths for all alphas start at the second nozzle at 12 $\mu$m wide and expand to an average of 30 $\mu$m wide. At 60 $\mu$L/min, the gradient width is most dependent on the alpha value. The equilibrium gradient width increases from 40 to 65 $\mu$m wide as alpha decreases from 12 to 1, respectively. In this flow rate regime, the gradient widths are most easily tuned to fit potential applications of multiplexed

measurements. It is likely that at or slightly below a total flow rate of 60 $\mu$L/min, the gradient exhibits the most tunability in width with respect to changing $\alpha$ values.

The influence of alpha on the gradient width is also prominent in Figure S4.1. For both of the lower flow rates, when the alpha value decreases, the gradient width produced increases. Figure S4.1b and S4.1c both have the alpha values of 1, denoted by the purple lines, being slightly higher than the alpha value of three, denoted by the black. The trend can be continued to describe all of the alpha values, 1, 3, 6, 9, and 12. The influence of alpha on the gradient width is not constant for all flow rates, demonstrated by a total flow rate of 100 $\mu$L/min having a narrower distribution of gradient widths, 10 $\mu$m, as compared to the 30, and 25 $\mu$m spread for the 60 and 12 $\mu$L/min respectively. Figure S4.1 summarizes the relationship between total flow rate, alpha, and the gradient width. Larger gradient widths are beneficial because they create a more gradual change in concentration laterally in the device. Therefore, controlling the total flow rate and alpha affords the ability to tune the gradient width for specific applications.

The addition of the second nozzle was confirmed to be the critical component in the gradient generation mechanism through a series of experiments altering the contraction/expansion region created by the interaction between the two nozzles. We examined the interaction between the two nozzles by extending X, the distance between the first and second nozzles. The original design for the dual nozzle gradient generator device has a separation distance of X = 48 $\mu$m. A larger value of X corresponding to a larger separation distance between the first and second nozzle in the dual nozzle design reduces the gradient width, thereby decoupling the two nozzles. In order to illustrate this affect, six channel configurations were used to characterize the decoupling of the two nozzles. The X values were extended from the initial 48 $\mu$m to lengths of 68, 88, 148, 168, and 268 $\mu$m. Figure S4.2a displays the change in configuration of the extended

devices from the original dual nozzle gradient generator device with 48 $\mu$m separation. Figure S4.2b displays the instantaneous derivative of the gradient width. As with the original devices, the gradient shows the largest expansion within the first 100 $\mu$m after the point of the second nozzle. In this section, the width of the gradient increases by 1.2 $\mu$m and 1.0 $\mu$m for every $\mu$m step down the channel in the devices with 48 $\mu$m and 68 $\mu$m nozzle separation distances, respectively. Extending the second nozzle separation further to 88 $\mu$m exhibits a significantly smaller growth rate, 0.2 $\mu$m per $\mu$m down the channel. Extension distances longer than 88 $\mu$m did not show any gradient generation. Therefore, the proximity of the second nozzle to the first nozzle directly affects generation of the gradient; this result is consistent with previous work related to expansion/contraction geometries in viscoelastic flows.[34–37]

Concentration mapping of the gradient device was accomplished by fluorescent imaging. Figure S4.3b depicts the concentration map of the outer fluid, in blue, and the inner fluid, in red. Each fluid was imaged in independent experiments using the same microfluidic device. Sodium fluorescein was imaged while flowed through as the outer fluid, with DI water as the inner fluid at appropriate flow rates. Then, the fluids were switched and another set of images were taken at identical flow rates. The corresponding images were mapping of the inner and outer fluids with a total flow rate of100 $\mu$L/min, and an alpha value of 1. The intensity profile across the channel is displayed, in Figure S4.3a, above the image of associated components with each color. Within the areas on either side of the inner fluid are regions with which both fluids are present, indicating the previously noted gradient regions, however, due to the two dimensional nature of this measurement, further tests were required to distinguish mixed from layered solutions.

Fluorescence quenching was used to confirm that fluids are indeed mixing, as seen in Figure S4.4. The Figure S4.4b shows a normalized intensity map of the gradient generator device when

0.5 M potassium iodide is flowed as the outer fluid. An experiment with a total flow rate of 60 $\mu$L./min and an alpha value of 12 is displayed. The fluorescence intensity of the gradient is completely quenched and the center steam is reduced to roughly 30% of its initial value immediately as it passes through the second nozzle. The comparison of the quenched image to the non-quenched image, Figure S4.4a, in the same channel with identical flow rates emphasizes both that the inner and outer fluids are being mixed within the gradient, and the rate at which a gradient is formed at the second nozzle.

Lastly, fluorescence lifetime images were used to calibrate the gradient generation time component of the gradient generator. Figure S4.5 is an image of the time mapped nozzle section of a gradient generator device. Europium microspheres were flowed through a gradient generator device as both the inner and outer fluids, with Figure S4.5 specifically being taken with a total flow rate of 100 $\mu$L/min and an alpha of 1. Using a custom build fluorescence microscope, certain parts of the channel were illuminated with the 355 nm excitation light. The measured fluorescent intensity could then be directly related through the decay of the microspheres to the time travelled since being within the selective excitation area. The dark blue band across the top portion of the image is the area with which the beads were being excited. Note, the beads from the center stream were within the excitation area for a short amount of time, therefore, did not achieve equal initial fluorescence intensity as the Europium in the outer fluid channel. This phenomenon was confirmed by comparing the channel. Figure S4.5 is calculated using an initial fluorescent intensity for the decay calculations as an average value from one half of the excitation area for the outer fluidic channel. The intensity map shows that the outer fluid has travelled out of the nozzle portion of the channel in under 0.5 ms and has entered the output channel.

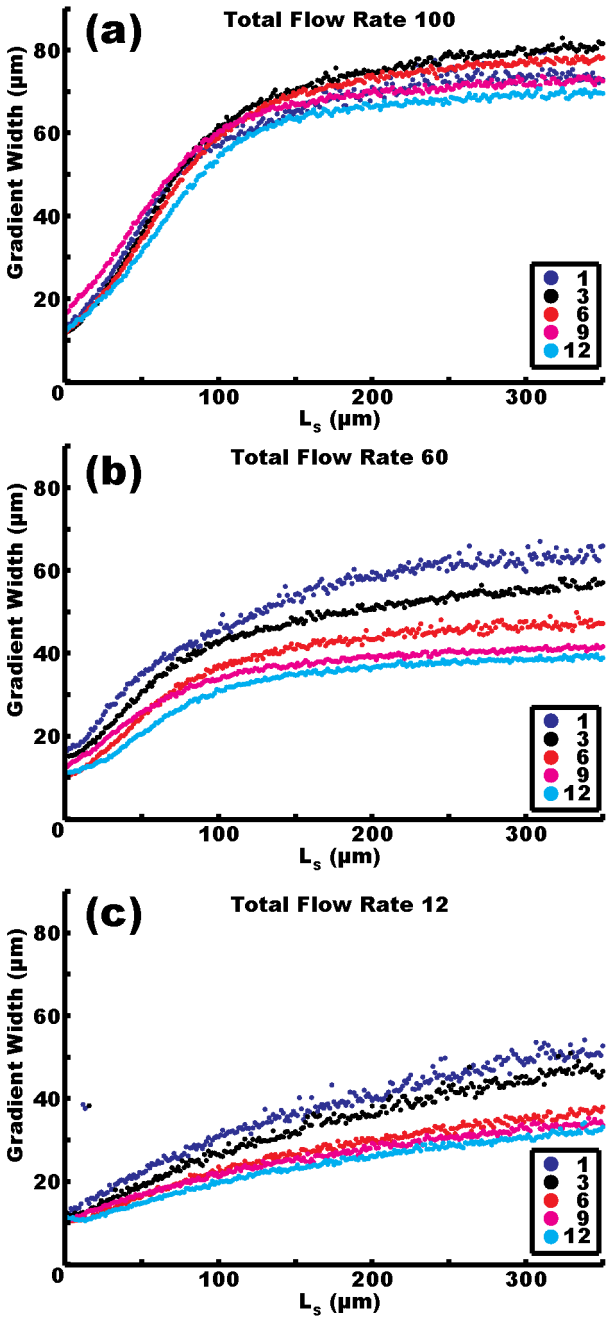


**Figure S4.1 Gradient Response to Total Flow Rate and Inner and Outer Flow Rate Ratio**

For three total flow rates, (a) 100 $\mu$L/min, (b) 60 $\mu$L/min, and (c) 12 $\mu$L/min, the measured width of the gradient generated by the device is plotted versus distance down the channel. Each plot compares the gradient width at five individual alpha values

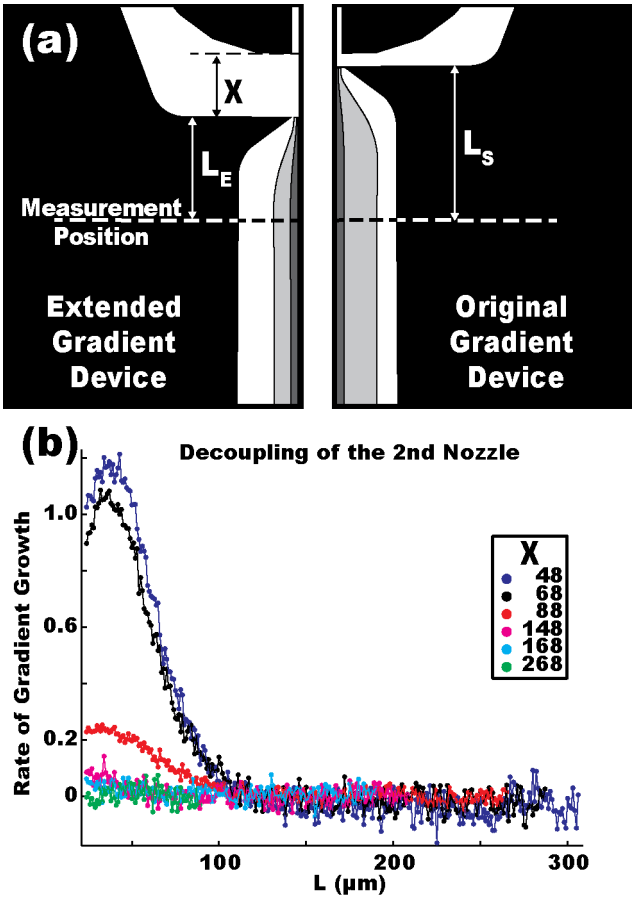


**Figure S4.2 Decoupling of the First and Second Nozzles**

(a) Illustrates the modifications to the channel design to decouple the gradient generation affect. X is the distance between the first and second nozzles, where X = 48 $\mu$m for the original gradient generator device design; $L_E$ and $L_S$ denote the distance from the point of measurement to the second nozzle for the extended and original gradient generator devices respectively. (b) The instantaneous change in the gradient width plotted against the location down the channel across or six different nozzle extension distances.

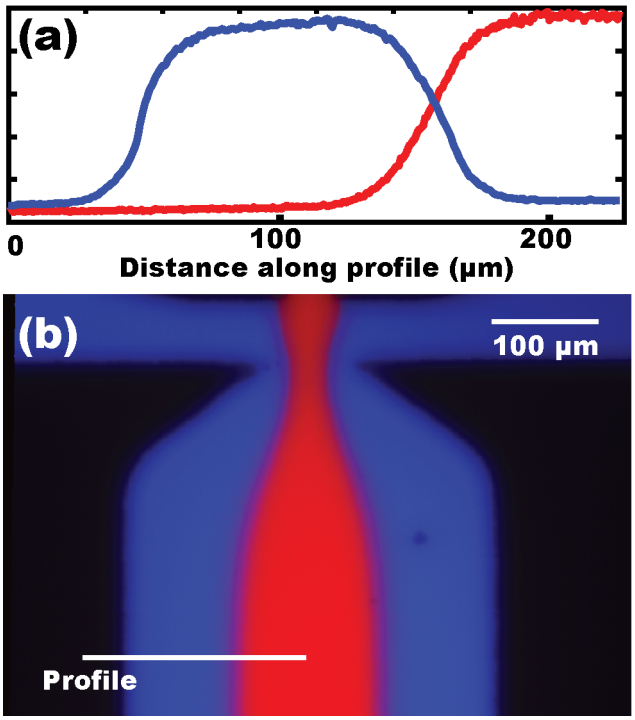


**Figure S4.3 Concentration Calibration of the Gradient Generatior Device**

(a) Concentration profile of the inner and outer fluids within the gradient generated within the device (b) Composite image of fluorescent experiments with fluorescein on as the inner and outer fluids that were cross correlated and overlaid as components of an RGB image.

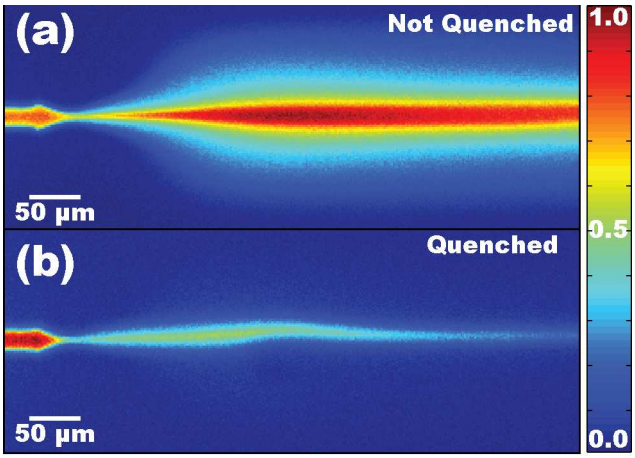


**Figure S4.4 Fluorescence Quenching Experiment in the Gradient Generator Device**

(a) an intensity image of the control gradient for the quenched experiment. (b) the gradient generated with KI as the quenching agent.

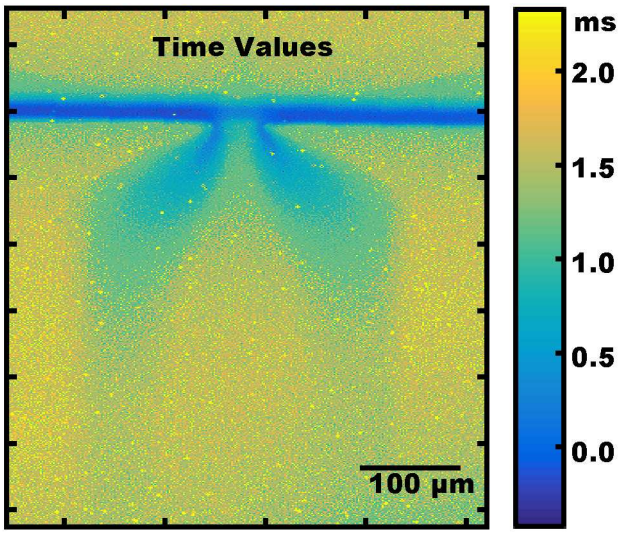


**Figure S4.5 Time-Space Mapping of the Gradient Generator Device**

Fluorescence lifetime images of Europium microspheres selectively excited within a gradient generator device. This experiment had a total flow rate of 100 $\mu$L/min and an alpha of 1.

# Chapter 5

## Infrared Compatible Microfluidics Tailored Towards Monitoring Chemical Interactions & Kinetics with Vibrational Spectroscopy

This chapter is a publication submitted to the Journal of Physical Chemistry B in 2016. This work focuses on a platform of microfluidic tools capable of interfacing with vibrational spectroscopy in order to probe chemical interactions and reaction kinetics on-chip. These microchips passively create specific chemical environments, only accessible by microfluidics, and make those environments available for use in vibrational spectroscopies. We have explored three different designs: a diffusive mixer for co-solvation experiments, a droplet generator for monitoring reactions in femtoliter vessels, and a fast gradient generation device for multiplexed reaction kinetic measurements. For each device design, complete characterization of the flow profile was performed and the unique utility was explicitly demonstrated through experiments using model systems. In doing so, we provided a template for vibrational spectroscopists to easily access stable chemical environments and reaction kinetics at early times with precision control.

### 5.1 Introduction

Chemoselective optical spectroscopy techniques including femtosecond stimulated Raman spectroscopy, linear infrared (IR) absorption spectroscopy, two-dimensional electronic spectroscopy (2D ES), and two-dimensional infrared (2D IR) spectroscopy, have developed into powerful tools to investigate chemical and biological systems.[1–4] These spectroscopic tools have made large impacts in our knowledge of chemical systems including protein conformational

dynamics, protein-lipid interactions, nucleic acid tautomerization, proton transfer processes, chemical exchange kinetics, and solute-solvent interactions, to name a few.[5–9] A common feature of these spectroscopic techniques is chemical selectivity combined with structural resolution. These spectroscopic approaches are suitable for probing dynamic systems far from equilibrium with high time resolution such that dynamics occurring on sub-picosecond timescales and longer can be measured; however, their use has been largely limited to optically triggered perturbations including laser-induced temperature jumps and laser-triggered photoswitches.[6,10–13] Optically triggered perturbations have the advantages of having precise knowledge of time zero, however, the trigger occurs on similar timescales as the spectroscopic measurements.[14] Alternatively, stopped-flow kinetics experiments are extensively used, but only millisecond timescales and longer can be accessed.[15] Chemical triggers combined with microfluidic platforms are used to access the tens of microseconds timescale and longer with the addition of precision sample control.[16,17] Unfortunately, challenges have prevented widespread implementation of microfluidic technology in vibrational spectroscopy measurements.

Microfluidic platforms offer the potential for capturing kinetics at early times and investigating chemical and biological systems away from equilibrium with a chemical perturbation.[18–24] The precision control over fluids in micro- and millifluidic platforms allowed by low Reynolds number flow is particularly useful. However, challenges with mixing on microsecond timescales and fabricating devices in materials that are compatible with a broad range of spectroscopic tools have limited the extent to which microfluidic platforms have been employed. In this work, we present three microfluidic device architectures that allow access to chemical interactions or early time kinetics with the important characteristic of being compatible with optical spectroscopies that range from UV to infrared excitation sources. Each device

employed in this work takes advantage of precision control of fluids to provide a specified chemical environment. In addition, previously developed thin-chip technology affords compatibility with a variety of optical spectroscopies.[25] Herein, chemical imaging by infrared microspectroscopy is utilized to demonstrate the utility of these microfluidic devices for integration with vibrational spectroscopy techniques.

**T**here are three specific benefits from microfluidic platforms that augment optical spectroscopy techniques: the possibility of performing multiplexed measurements, sample conservation, and fast chemical mixing.[26–28] Microfluidic technology originally developed in order to passively mix on-chip can be modified to accentuate these benefits. Figure 5.1 depicts the general form and function of three microfluidic platforms that are employed in this work. Figure 5.1a is a fluorescence image of a diffusion-based, single-phase mixer, consisting of a simple Y-junction connected to a long serpentine channel. The serpentine channel utilizes secondary flows to enhance lamination between the fluids, decreasing the time required for mixing.[29–32] In addition, this device can be used to probe solvation dynamics under different solvent conditions in a multiplexed fashion. Multiplexing reduces the number of measurements required to sample a given parameter, and in this instance, reduces the number of prepared solutions. Figure 5.1b is a fluorescence image of droplet generation. Two miscible fluids, A and B, are combined in a simple Y junction and after coming into contact with each other, the aqueous stream immediately arrives at a T-junction with an immiscible, carrier fluid. The shear force applied by the carrier fluid causes droplet pinch-off.[33,34] Figure 5.1b contains 4 frames of a single droplet being formed, to help visualize the droplet formation and mixing processes. Advection dramatically improves the mixing time of reagents encapsulated in the drops.[35,36] Figure 5.1c is a fluorescent image of a dual nozzle gradient generator developed recently and

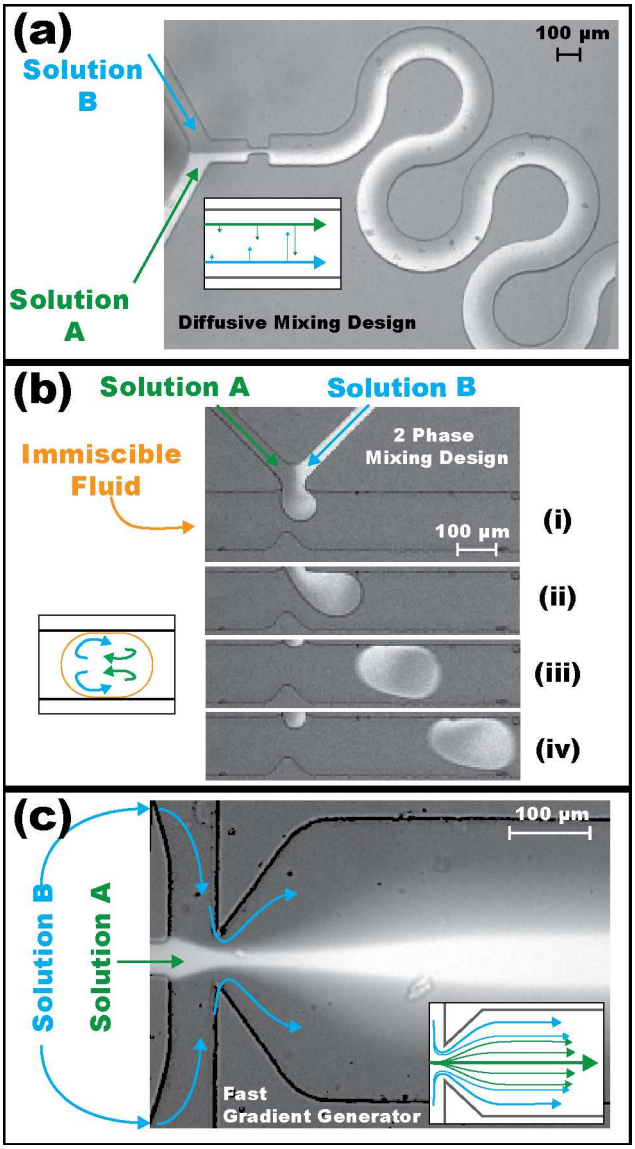


**Figure 5.1 General Form and Function for the Microfluidic Platforms**

(a) A single-phase diffusive mixer with serpentine channel. (b) Two-phase droplet mixers depicting the pinch-off and chaotic advection. (c) Dual nozzle gradient generator design utilizing the curvature of streamlines for fast production of a gradient.

detailed in our recent work.[37] The outer fluid focuses the inner fluid, which travels through a second nozzle generating a gradient pattern down stream. Mixing is achieved in under 2 μs in this device and a tunable gradient isestablished in 1 ms. In this architecture, gradient generation is achieved quickly in a single device by taking advantage of the curvature of streamlines that are accessible in microscale devices.[38–41] Below the details of fabrication of each microfluidic tool are provided and the performance of each device is quantified. We demonstrate broad applicability of these devices by following model chemical interactions and reaction kinetics that highlight the advantages each device provides using FTIR microspectroscopy.

## 5.2 Materials and Methods

### 5.2.1 Device Fabrication

All microfluidic devices for fluorescence experiments were fabricated through standard photolithography techniques.[42,43] Polished silicon wafers were spincoated with Microchem SU-8 2025 to a thickness of 30 $\mu$m. The wafers were then covered with a photomask outlining the channels and exposed to collimated UV radiation. Unexposed SU-8 was then removed leaving a mold containing the channels. Sylgard 184 Polydimethyl Siloxane (PDMS) was mixed at a 10:1 ratio, applied to the molds, and cured in an oven for one hour. The cured PDMS was removed and fluid port holes were punched. Devices were completed by sealing the cured PDMS with an oxygen plasma. For the droplet devices, channels were treated with Aquapel (PPG Industries) for 30 seconds before being flushed with air and placed in a 65 ˚C oven overnight.

IR compatible microfluidic chips were made by two separate methods. The first method was using PDMS to house the fluidic channels. The fabrication of the PDMS IR compatible microfluidic chips has been described previously.[25] Briefly, each microfluidic chip consists of

four layers: a support layer, microchannel layer, adhesion layer, and calcium fluoride backbone. Each layer is prepared independently and then assembled into the complete microchip. The microchannel layer is prepared by placing PDMS on a mold and then using a hydraulic press to achieve specific thicknesses required by the experiment. The adhesion layer was prepared by spin coating clean calcium fluoride windows with PDMS to the desired thickness. All assembly was done via PDMS sealing with oxygen plasma. The second method for fabricating IR compatible microfluidic chips utilizes commercially available thin Zeneor cyclo-olefin polymer (COP, Microfluidic Chip Shop, Germany) and Topaz cyclo-olefin copolymer (COC, Microfluidic Chip Shop, Germany). Fabrication was achieved through a modified lamination based technique.[44] Briefly, 40 $\mu$m thick COP was placed onto a SU-8 channel mold. Both heat and pressure were applied using a hydraulic heated press set to 315 ˚F. After 8 minutes, the pressure was released and the COP removed from the mold. The COP was then matched with an equal size piece of COC, and run through an Apache AL13P professional lamination device. The edges were then sealed using an 8 inch impulse sealer. IDEX microtubing ports were attached via epoxy.

### 5.2.2 Solution Chemistry

Fluorescence microscopy experiments were performed with the inner and outer fluids being aqueous solutions of 0.15 mM sodium fluorescein in deionized water, and deionized water respectively. Mixing was confirmed with quenching experiments by using 0.5 M potassium iodide, mixing with 1.25 mM sodium fluorescein in deionized water.[20,45]

Solvent-solute interactions and model chemical reactions were used to demonstrate the broad applicability of the microfluidic devices when paired with chemoselective FTIR microspectroscopy. The influence solvent environment has on the IR spectrum of NMA was

monitored on-chip via FTIR microspectroscopy. An analyte solution of 100 mM NMA in DMSO was mixed into $D_2O$ (Aldrich) on chip. An acid-base reaction was monitored using droplets as reaction vessels. Water-in-oil emulsion droplets were generated using a fluorocarbon oil continuous phase and encapsulating aqueous solutions containing the reactants through a T-junction dropmaker. The non-aqueous solution was a mixture of HFE-7500 fluorocarbon oil and Krytox surfactant.[46] Briefly, to prepare the fluorocarbon oil-krytox fluid a solution of 11.1 % by weight Krytox 157 FSL in methanol was created. Ammonium hydroxide was added drop-wise until the solution cleared, then the sample was left to evaporate the excess methanol. The Krytox mixture was then added to the HFE-7500 at 1.75% by weight. Aqueous solutions were chosen to model an acid-base reaction; the protonation state of the carboxylic acid group in acetic acid was monitored. Protonation experiments were performed by reacting a 0.21M acetic acid in 0.225 M NaOD aqueous solution with a 0.4 M DCl (Acros) aqueous solution in droplets. A chelation reaction was used to model a chemical kinetic system monitored in the fast gradient generator. The binding state of picolinic acid and iron (II) chloride was monitored. Binding was accomplished with 1.1 and 0.11 M solutions of picolinic acid, and 1.1 and 0.12 M concentrations of $FeCl_2$, respectively. All solutions were made in bulk then transferred into an appropriate syringe, either 1 mL or 10 mL, to be pumped using NE-500 Programmable OEM syringe pumps controlled through an in-house Labview program.

### 5.2.3 Fluorescence, and Infrared Microspectroscopy

Brightfield and fluorescence microscope images for the fast gradient generator and diffusion-based mixers were collected under steady-state flow conditions. Fluorescence, brightfield, and quenching experiment images were acquired using a Nikon Eclipse TE2000 microscope with 1392 x1040 imaging array. Bright-field images were taken of the fluorescence

fluids with low backlighting to highlight the channel features without overwhelming the fluorescence signal, where as the fluorescent images were taken in absence of any backlighting. All images were processed using a combination of in-house Matlab routines and ImageJ.

All infrared microscope images were acquired using a Bruker Hyperion 3000 FTIR microscope. The FTIR microscope is equipped with a 64 x 64 element FPA detector and a 15x objective producing 2.7 $\mu$m spatial resolution. All images were taken in transmission mode. All IR microscope images shown are processed using the OPUS software (Bruker Optics). Absorbance intensities are measured as the integrated area under the absorbance spectrum between two specified frequencies. The concentration map shown was calculated with more advanced data analysis, accomplished using in-house Matlab routines.

Time calibration of the fast gradient generation device was accomplished by monitoring the decay of europium nanospheres (FluoSphere, Invitrogen) being flowed through the device. The fluorescent lifetime of the europium microspheres was determined using a time-resolved fluorescence instrument. Briefly, the Europium microspheres were placed in a 1-cm pathlength quartz cuvette and excited with a 7 ns pulsed pump beam tuned to 355 nm (Opotek inc Opolette 355 LD tunable laser). Fluorescence intensity measurements were collected perpendicular to the incident beam and focused onto a Thermo Jarrell Ash (Model 82-410) 0.25 Meter Monochromator Spectrograph with attached photomultiplier tube. The fluorescence lifetime of the beads was determined to be 540 $\mu$s and is in good agreement with the literature[47]. For the measurements taken inside the channel, the 355 nm pulsed pump beam from the Opolette 355 LD was centered onto an adjustable mechanical slit (Thor Labs). Using a lens, the slit was imaged onto the microfluidic channel. Images were collected collinear to the excitation beam, using a filter to remove the residual pump beam prior to imaging. The channel was imaged using

a 20x Nikon microscope objective onto a Retiga R1 Scientific CCD Camera (QImaging). Images were collected through the Occular application software prior to custom Matlab processing. Experimental values for the time taken for the fluid passing through the second nozzle and at each pixel were calculated. Every time value was in good agreement with values calculated from the volumetric flow rate.

## 5.3 Results and Discussion

### 5.3.1 Single Phase Diffusive Mixing Device

The benefits of multiplexing in a vibrational spectroscopy experiment were explored using a single phase mixer to establish a solvent gradient across the device. The single-phase mixers create a gradient based upon diffusion of solvents and analytes laterally within the channel. We incorporated a serpentine geometry to promote secondary flows and improve mixing and form the gradient quickly. In Figure 5.2a, the composite brightfield and IR mapping experiment acquired from the IR microscope are shown. Two sections of the channel were captured with IR imaging. The color map represents the integrated area under the peak due to the carbonyl stretch in NMA, that is centered at 1630 $cm^{-1}$ when in $D_2O$ and 1668 $cm^{-1}$ when in DMSO. NMA in DMSO flows into the Y junction from the top channel, while $D_2O$ flows from the opposite arm. In the first section, the two solutions have distinct separation, illustrated by the sharp color change in the chemical intensity map. As the solutions travel further down the serpentine channel, the two solutions begin to diffuse into each other assisted by secondary flows. The lamination and mixing decreases the color jump at the interface between the two solutions. The extent of mixing is more evident in the second section of the chemical map. A magnified section of the IR image is shown in Figure 5.2b. By this point in the channel, the two separate sides have begun to mix, indicated by the more gradual color change. To be more specific, the

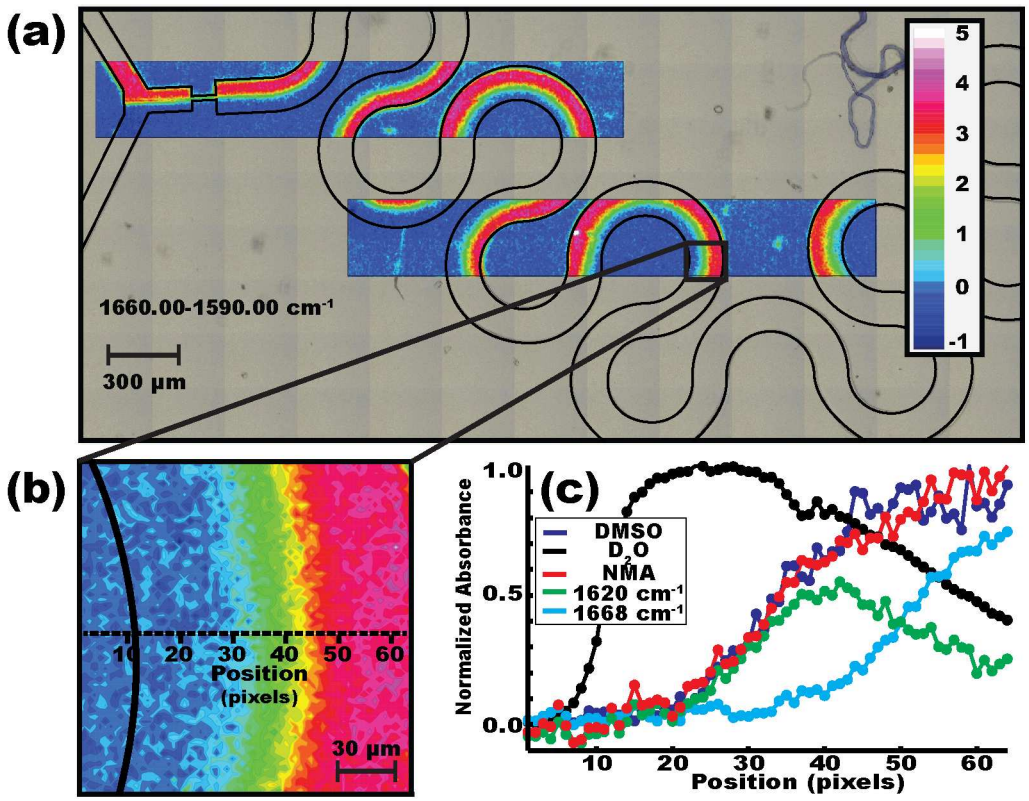


**Figure 5.2 IR Imaging of a Single Phase Diffusive Mixer**

(a) FTIR integrated intensity map of a concentration gradient of NMA being formed. (b) A zoomed in portion of the channel emphasizing the gradient produced. (c) A graph of normalized absorbance versus pixel position across the channel for the species present within the channel.

concentration profile for each chemical in the gradient was mapped by extracting the normalized absorbance values of independent absorption frequencies at every individual pixel.

The rate of mixing for the single-phase diffusion based mixers is based upon two specific properties. First, the diffusion coefficient of the chemical species present determines the rate of diffusion across the channel. Diffusion is considered the main form of mixing due to being in the laminar flow regime, dictated by the Reynolds number. The Reynolds number is a ratio of the inertial forces to viscous forces and is calculated according to the equation,

$$\mathrm{Re} = \frac{\rho L_0 U_0}{\eta}$$

where, $\rho$ is the density of the fluid, $L_0$ is the characteristic length scale, $U_0$ is the fluid velocity, and $\eta$ is the shear viscosity of the fluid. The experiment shown in Figure 5.2 has a Reynolds number calculated to be 0.45 placing us well within the laminar flow regime causing diffusion to be the main form of mixing. Using the diffusion constant and the fluidic velocity, the distance down the channel in which complete diffusion across the channel was accurately predicted. The second property that influences the rate of mixing is the geometry of the channel. Since the mixture is traveling through a serpentine channel, low magnitude secondary flows will be generated in each turn. A good metric to assess the strength of these secondary flows is the Deans number.[31] The Deans number, K, compares the relative magnitudes of the inertial and centrifugal forces, to the viscous force and can be calculated according to the equation,

$$K = \mathrm{Re}\sqrt{\frac{D_H}{R}}$$

where, Re is the Reynolds number, $D_H$ is the hydrodynamic radius, and R is the radius of curvature for the arc. A higher Deans number is indicative of stronger secondary flows. For the experiment shown in Figure 2, the Dean's number was calculated to be 0.19, creating a small to

moderate amount of lamination in the center stream of the channel and increasing the rate mixing is achieved. An increased lamination by secondary flows is important in this instance because mixing dominated by diffusion is a very slow process. By adding the secondary flows, the length of the channel between fluids meeting and where the mixing was achieved was reduced by over 4 mm. Thus demonstrating the potential for conserving costly samples in a continuous flow device.

The IR compatible single-phase diffusive mixing device presented here can be used to probe solute-solvent interactions in cosolvent conditions. We demonstrate this utility by monitoring the carbonyl vibrational mode of NMA in $D_2O$ and DMSO; highly controlled cosolvent conditions are produced by taking advantage of the gradient produced in the device. In Figure 5.2c, plots of the self-normalized absorbance of the chemical species present in the device as a function of the distance across the channel are shown. The data points are extracted at the position indicated by the dotted line in Figure 5.2b. The solvent profile is determined by observing the relative amounts of $D_2O$ and DMSO at each point, where the integrated absorbance values for both $D_2O$ and DMSO are shown self normalized. Note the DMSO was normalized to values calculated at a position within the gradient, such that its normalized value is not equal to the proportion of DMSO in the gradient. As the position number increases, the concentration of $D_2O$, plotted in black, decreases, meanwhile, the concentration of DMSO increases denoted by the rise of the dark blue line. Further evidence supporting the change in solvent environment across the channel can be seen by monitoring NMA. The green and light blue measurement points are taken at 1620 and 1668 $cm^{-1}$ respectively, and are a good representation of the solvent environment surrounding NMA. The red data points are a summation of the blue and green data points, representing the concentration of NMA at each position along the channel. The increase

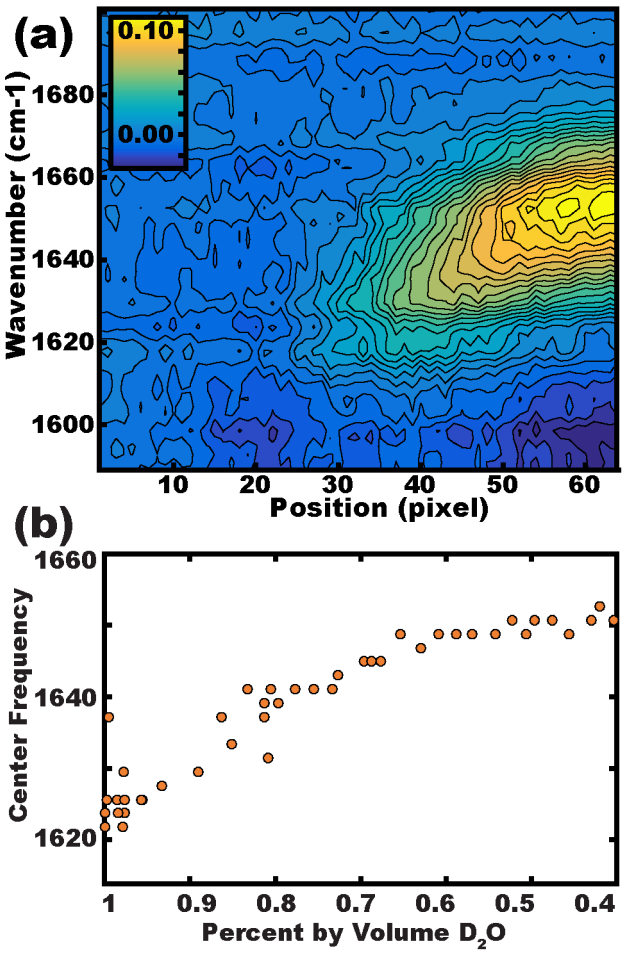


**Figure 5.3 Absorption Response of NMA Tracked in the Microfluidic Device.**

(a) The IR absorption spectrum mapped versus the position across the channel. (b) The center peak frequency of NMA plotted as a function of cosolvent environment.

in concentration of NMA follows that of DMSO, which is to be expected since both will diffuse across the channel at similar rates.

The carbonyl stretching vibrational mode is known to be sensitive to the local hydrogen-bonding environment surrounding the oscillator. In Figure 5.3a, the frequency of the carbonyl vibrational mode is correlated to the position across the channel at the positions noted in Figure 5.2b. Furthermore, the center frequency extracted from the spectra comprising the images in Figure 5.2b and the correlation plot in Figure 5.3a, can be plotted as a function of solvent composition which is shown in Figure 5.3b. As expected, when NMA is exposed to more hydrogen bonding across the gradient of solvent conditions, the frequency of the carbonyl vibrational mode shifts from 1668 $cm^{-1}$ to 1620 $cm^{-1}$. Linear and nonlinear IR spectroscopy measurements have been performed on NMA in water, methanol, and aprotic solvents such as DMSO to characterize the hydrogen bonding species present in solution. Although there has been intense work, both experimental and theoretical, to elucidate the hydrogen bonding dynamics of NMA and the structural dynamics associated with intermolecular hydrogen bonding among NMA molecules in protic and aprotic solvents these questions continue to be debated.[48–54] In part, because it is difficult to produce the appropriate cosolvent conditions to capture hydrogen bonding species of interest. In Figure 5.3b, the center frequency of the NMA carbonyl vibrational mode is plotted as a function of solvent environment accessed in this device. This data clearly demonstrates the utility of this device to access multiple local solvent environments in a well-controlled fashion. Albeit the IR microspectroscopy measurements presented here are inadequate to address and quantify the hydrogen-bonding dynamics of NMA in $D_2O$-DMSO cosolvents, we note that the technology demonstrated here can be easily implemented in

nonlinear IR spectroscopy techniques including 2D IR spectroscopy due to the capability of the devices to be used in a transmissive sample geometry.

### 5.3.2 Two Phase Droplet Mixers

Droplets were utilized for encapsulation of two miscible fluids. Droplets create ideal environments for containing specific quantities of reactants, and each droplet is easily assigned a time correlated to how long the reactants have been in contact with each other. A T-Junction drop maker design, shown as the black overlays in Figure 4a and 4b was specifically chosen and adapted for our chemical IR analysis application for the purpose of producing femtoliter-reaction vessels. One limiting factor for the device architecture is the ability to accommodate the slower frame rate of a typical IR FPA detector.[55–57] T-Junction dropmakers have greater stability at lower flow rates than other passive droplet generators, affording decreased speeds at which the droplet travels.[46] By incorporating larger channels, further speed reductions of the droplet were possible in our IR microspectroscopy experiments. Figure 5.4a and Figure 5.4b are IR maps of droplets being formed and moving down the channel, mapping the acetate peak centered at 1550 $cm^{-1}$ and the acetic acid peak centered at 1700 $cm^{-1}$, respectively. The red grid depicts the individual IR map acquisitions that were stitched together. Out of the six half-frames covering the channel, only two captured droplets. Figure 5.4a depicts the integrated area of the unreacted acetate peak, and four points marking different phases of the drop making process. Spectra for each point distinguished in Figure 5.4a are plotted in Figure 5.4c. Labeled in green and red, are the two initial fluids. The green spectrum contains a clear, distinct peak, centered at 1560 $cm^{-1}$ which indicates the presence of the acetate ion. The acidic DCl solution does not contain any distinguishing features in this region of the IR spectrum. Once mixed, the acetate becomes protonated forming acetic acid. The protonation shifts the observed peak into a peak centered at

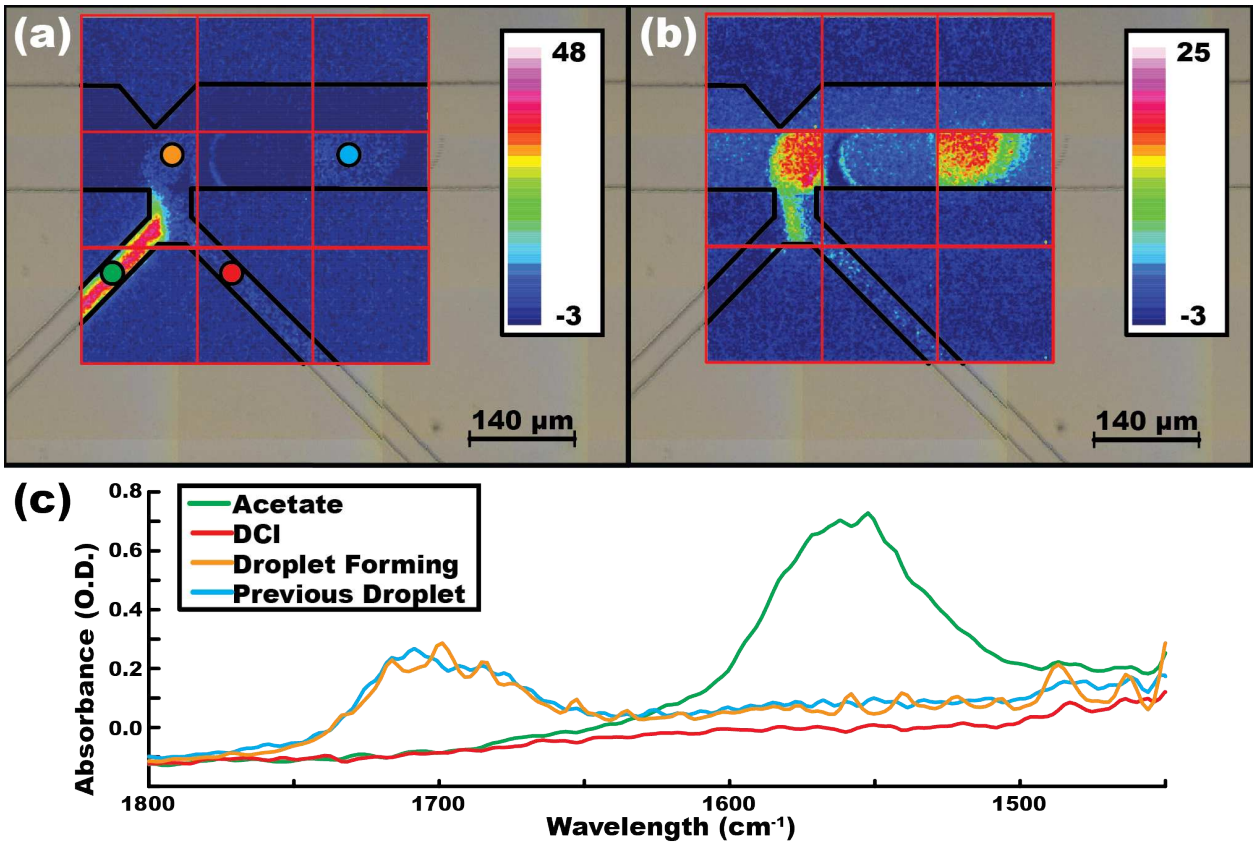


**Figure 5.4 IR Imaging for Two Phase Droplet Mixers**

(a) and (b) consist of brightfield images overlaid with nine FTIR microscope images, taken of the formation of droplets. The intensity corresponds to the integrated peak intensity for the protonated and unprotonated acetic acid peaks centered at 1700 $cm^{-1}$ (a) and 1555 $cm^{-1}$ (b), respectively. (c) Plotted infrared absorption spectra for four locations identified by the colored circles in (a).

1710 $cm^{-1}$ with a shoulder centered just below 1700 $cm^{-1}$. By mapping the 1560 $cm^{-1}$ peak intensity in comparison to the 1710 $cm^{-1}$ peak intensity, we can map the protonation state at each point in the channel. Figure 5.4a contains no trace of the acetate species in the droplets captured, indicating that the reaction has gone to completion within the droplets. Figure 5.4b maps the acetic acid peak, the product of the reaction. Within this figure each droplet is distinguished by the large values of the acetic acid integration, and can be found in the outer frames in the middle row. The presence and strength of the acetic acid peak, and lack of presence of the acetate peak provide strong evidence that the two solutions are mixing instantaneously at the formation of the droplet. This is confirmed with fluorescence quenching experiments, which can be visualized in a three-dimensional map shown in Figure 5.5. Figure 5.5a and Figure 5.5b contain fluorescence images, and the corresponding 3D surface plot, taken of the droplet forming process for an unquenched and quenched fluorescent experiment, respectively. The droplets observed in the fluorescence images for the unquenched and quenched situations exhibit drastically different fluorescence levels. To clearly depict these differences in intensity, surface plots of the intensity using a false color scheme are also displayed. In each experiment, the fluorescein solution exhibits high fluorescence intensity prior to coming in contact with the second aqueous fluid. During the fluorescein with water experiment depicted in Figure 5.5a, each droplet maintains a similar high level of fluorescence. In the presence of a quenching agent, the fluorescence intensity immediately drops during the early stages of droplet formation, even prior to pinch-off of the droplet, as evident in Figure 5.5b. Movies of the fluorescence quenching are provided in the supplementary material. The combination of the IR chemical mapping and quenching experiments support the conclusion that at droplet formation, the two aqueous solutions are being instantaneously mixed, establishing a definite point of time zero for reactants mixing within the

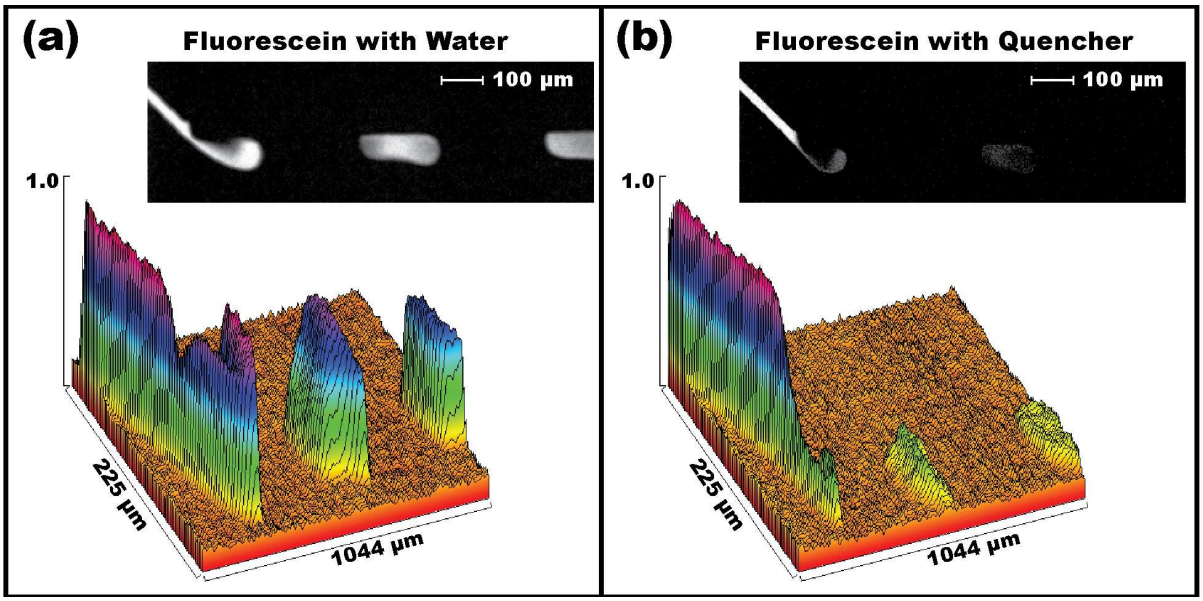


**Figure 5.5 Quenching Results for the Two Phase Droplet Mixers**

(a) and (b) depict the droplet forming process for fluorescein with water and fluorescein with 0.5 M KI quenching solution, respectively. The corresponding surface plot is below each fluorescence image; the intensity of fluorescence is plotted in the z-axis and mapped in false color to more easily discern the differences in intensity.

droplets, and allowing the distance travelled down the channel to be converted to a specific time point. For example, in Figure 5.4b, we will assign the time and position of the droplet being created to both be zero. The second droplet captured in frame 6 has travelled 230 $\mu$m down the channel. Based upon flow rates and the channel geometry, this droplet would have taken 100 ms to travel that distance. This microfluidic architecture is a promising tool, where in combination with vibrational spectroscopy, will provide access to early time reaction kinetics. In addition, the thin-chip microfluidic technology used here allows for experiments to be performed in transmission spectroscopy geometries as opposed to attenuated total reflectance geometries that have been used previously.[58–60] However, droplet generators such as this one are difficult to parallelize in such a way to yield multiplexed measurements.

### 5.3.3 Dual Nozzle Gradient Generation Devices

In the microfluidic community, the success in accomplishing passive fast mixing have made the flow focusing design popular for monitoring kinetic reactions.[17,22] Since the fluid velocity is known and the fluids are in the laminar flow regime, the progression of the reaction is tracked over time by taking measurements at progressive points down the channel. The accessible timescales for these experiments is dependent on how quickly the reactants can be mixed. Previously reported mixing times in flow-focusing devices range from tens of microseconds to millisecond timescales[47,61–65]. We have developed a modified flow-focusing device that not only allows fast mixing of fluids within tens of microseconds, but also has the capability of forming a concentration gradient between the center and outer streams. Altering the flow profile by incorporating a second nozzle into the main channel, the flow characteristics within the device can be tuned to promote the curvature of streamlines. More specifically, the second nozzle creates a contraction/expansion region within the channel. The resulting fluid profile contains a

focused center stream, as found in a traditional flow focusing device, but in addition, a symmetrical concentration gradient of the focused fluid on each side of the center stream. Using time-space mapping, the gradient was determined to form within 2 $\mu$s of passing through the second nozzle, after which the fluid maintains laminar flow. The formation of a stable 75 $\mu$m wide gradient is formed in 1.1 ms.

Utilizing the fast formation of the gradient, chemical kinetic measurements for a model reaction were obtained. Figure 5.6a is an image taken via IR microspectroscopy of a solution of 1.1 M picolinic acid in $D_2O$ being focused by an outer solution of 1.1 M $FeCl_2$. The color map illustrates the concentration of a bound iron-picolinic acid complex. Picolinic acid is a compound of interest due to its importance in increasing uptake and retention of zinc and other metals including iron in human metabolism.[66] More specifically picolinic acid is a bidentate chelating agent for many biologically essential metals like iron; the chelation reaction with iron is described as follows,

$$2Fe^{2+} + \underset{\text{(picolinic acid)}}{C_6H_5NO_2} \leftrightarrow Fe_2C_6H_5NO_2$$

Iron(II) ions binding to picolinic acid upon chelation causes a shift in the vibrational frequency at which picolinic acid absorbs. The concentration was determined using Beers Law calculations from the integrated area under the absorption peak at 1570 $cm^{-1}$, representative of the bound complex. Intensity for this peak appears at the region between the inner and outer fluids after the fluids pass through the second nozzle. At 175 $\mu$m beyond the second nozzle, the gradient maintains a constant width, indicating that diffusion plays a limited roll within the field of view of the image collected. Being in the laminar flow regime assures steady state flow dynamics and affords the ability to observe multiple reaction conditions in the same measurement.

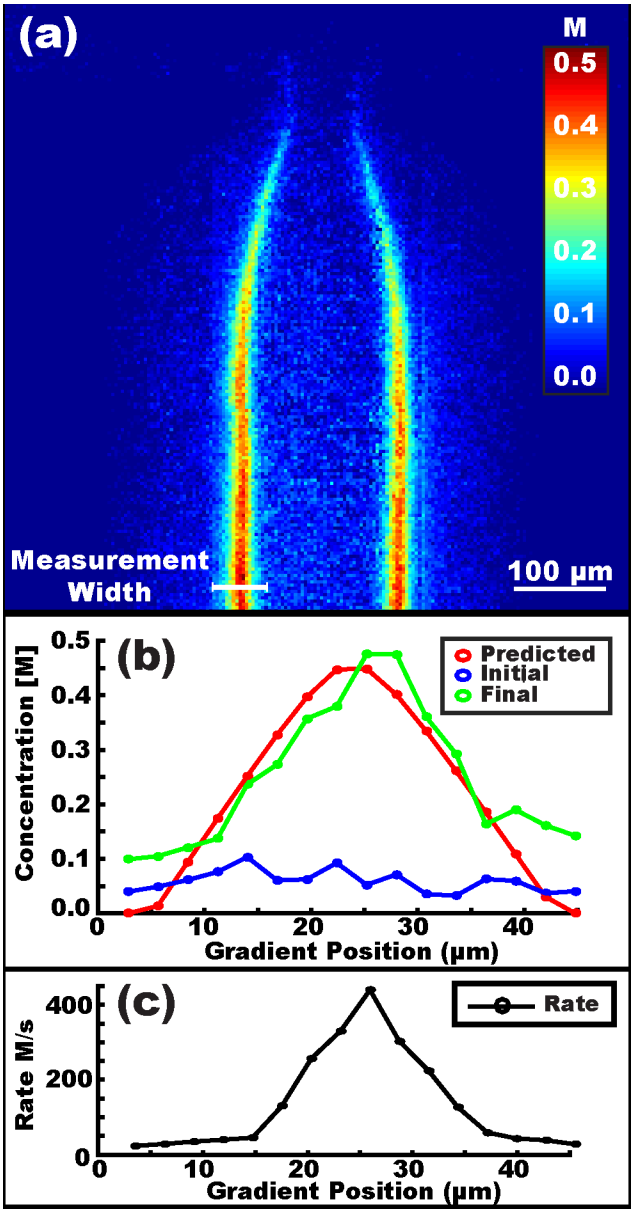


**Figure 5.6 Kinetic Experimental Results for the Dual Nozzle Gradient Generation Geometry**

(a) FTIR microspectroscopy mapping the integrated peak of $Fe^{2+}$ bound to Picolinic Acid. (b) Concentration profiles of reaction products formed across the gradient width indicated in (a) at two different positions: at the nozzle (blue) and the last point down the channel (green). This is compared to the predicted concentration of the reaction product formed at the last point in the channel (red). (c) A graph plotting the measured rate of the products formed at each place across the gradient.

A plot showing individual concentration profiles of the iron-picolinic acid complex is presented in Figure 5.6b. In blue, the concentration of the complex taken at the nozzle is displayed. At such an early point in the gradient formation, both the inner and outer fluids have been mixed. However, insufficient time has been allowed for the complex to be formed. In green, the concentration profile at the last position down the channel captured by the IR acquisition is displayed. The parabolic shape confirms that the formation of the complex has occurred in the travel time since passing through the second nozzle. To determine if the reaction has reached equilibrium, the theoretical concentration of the product was calculated at every pixel. The theoretical concentration of the iron-picolinic acid complex was generated using the concentration ratios provided by the gradient and the binding constant, 54.99 $M^{-1}$, determined from linear IR spectroscopy experiments. The theoretical concentration profile for the last position measured in the IR acquisition is shown in red. The position is 586 $\mu$m past the second nozzle, at which point, the solutions to have been mixed for 2.78 ms. The theoretical profile shown in red, is comparable to the observed profile shown in green, suggesting that at this point in the channel, the equilibrium concentrations have been reached for the chelation reaction.

The rates of the reaction occurring in each streamline were calculated with further data processing and compared. The details of the data processing and analysis required for extracting the rate of reaction for each streamline is described in the supplemental information. Plots of the observed rate of appearance of the bound species for each streamline prior to reaching equilibrium are presented in Figure 5.6c. The center of the gradient, where the concentrations of each reactant are equal, formed the bound product the fastest with an observed rate of reaction of 440 M/s. Similar observations were made at alternative points within the gradient. The symmetry of the reaction rate versus position across the channel suggests a proportional

dependence on concentration in the rate law for each reactant. Therefore, the reaction rate is equal order for both reactants. To our knowledge, this is the first time the rates of chelation of $Fe^{2+}$ by picolinic acid have been measured. Moreover, this work demonstrates the ability to make these measurements in a multiplexed fashion.

## 5.4 Conclusions

A new microfluidic platform that combines IR compatible polymeric microfluidic chips with three specific microfluidic tools for accessing chemical interactions and kinetics with vibrational spectroscopy techniques has been presented in this work. The IR compatible microfluidic chips allow for spectroscopy and microscopy experiments to be performed in transmission geometries often utilized in linear and nonlinear vibrational spectroscopy experiments. The utility of three different devices demonstrated by probing model chemical interactions and chemical reaction kinetics with FTIR microspectroscopy. The entire solvation response profile for NMA in a $D_2O$-DMSO cosolvent gradient was mapped in the single-phase diffusive mixer. The single-phase diffusive mixer was used to form a stable gradient of two solvents; the change in local solvent environments across the channel was reported by the shift of the center frequency of the carbonyl stretching vibrational mode in NMA and is correlated with the solvent composition. The single-phase diffusive mixer is a promising microfluidic tool for probing a wide range of analytes in cosolvent environments in a multiplexed fashion. A droplet generator microfluidic device was used to encapsulate chemical reactants in femtoliter vessels and FTIR microspectroscopy was used to follow the protonation of acetate ion. The chemical reactants mix instantaneously in the drops allowing for a well-characterized time zero for mixing and subsequent reaction monitoring within the droplets with FTIR microspectroscopy. Thus, explicit time points can be recognized further down the channel based on the constant droplet velocity. The fast gradient generator

produced a gradient required for multiplexed measurements of reaction conditions in addition to adding a time axis to the measurements. Thus, the rate of reactions for a range of reactant concentrations could be made on-chip for the first time. This was accomplished with the addition of a second nozzle to a flow-focusing microfluidic device; the fluids undergo contraction/expansion, which results in mixing on the microsecond time scale. Gradient formation simultaneously provides the opportunity to measure chemical kinetics over multiple reaction conditions using the acquisition of a single chemical image. This reinforces the conclusion that the fast gradient generating device design in combination with IR microspectroscopy is an ideal tool for obtaining reaction kinetics on microsecond timescales.

Each of these microfluidic channel designs creates a specific chemical environment previously unavailable to most vibrational spectroscopy techniques including FTIR spectroscopy and 2D IR spectroscopy. Moreover, the materials used in fabricating the devices presented in this work are compatible to optical wavelengths spanning from the ultraviolet to mid-infrared thus creating microfluidic tools that are also compatible with other optical spectroscopy techniques such as femtosecond stimulated raman spectroscopy and 2D electronic spectroscopy. In sum, this work introduces a foundation of microfluidic tools that can be easily interfaced with a multitude of optical spectroscopy techniques in order to probe chemical interactions and kinetics on-chip.

### 5.5 Additional Notes

The authors thank the National Science Foundation (CHE-1255658 to A.T.K) and BP Exploration Operating Company Ltd. for the generous funding for this work.

## References


(1) McCamant, D. W.; Kukura, P.; Mathies, R. A. *J. Phys. Chem. A* **2003**, *107* (40), 8208.

(2) Fuller, F. D.; Pan, J.; Gelzinis, A.; Butkus, V.; Senlik, S. S.; Wilcox, D. E.; Yocum, C. F.; Valkunas, L.; Abramavicius, D.; Ogilvie, J. P. *Nat Chem* **2014**, *6* (8), 706.

(3) Moran, S. D.; Zanni, M. T. *J. Phys. Chem. Lett.* **2014**, *5* (11), 1984.

(4) Sassi, P.; Giugliarelli, A.; Paolantoni, M.; Morresi, A.; Onori, G. *Biophys. Chem.* **2011**, *158* (1), 46.

(5) Kimura, T.; Takahashi, S.; Akiyama, S.; Uzawa, T.; Ishimori, K.; Morishima, I. *J. Am. Chem. Soc.* **2002**, *124* (39), 11596.

(6) Dutta, S.; Cook, R. J.; Houtman, J. C. D.; Kohen, A.; Cheatum, C. M. *Anal. Biochem.* **2010**, *407* (2), 241.

(7) Schleeger, M.; Wagner, C.; Vellekoop, M. J.; Lendl, B.; Heberle, J. *Anal Bioanal Chem* **2009**, *394* (7), 1869.

(8) Mohammed, O. F.; Banerji, N.; Lang, B.; Nibbering, E. T. J.; Vauthey, E. *J Phys Chem A* **2006**, *110* (51), 13676.

(9) King, J. T.; Kubarych, K. J. *J. Am. Chem. Soc.* **2012**, *134* (45), 18705.

(10) Gooding, E. A.; Sharma, S.; Petty, S. A.; Fouts, E. A.; Palmer, C. J.; Nolan, B. E.; Volk, M. *Chem. Phys.* **2013**, *422*, 115.

(11) Anna, J. M.; Baiz, C. R.; Ross, M. R.; McCanne, R.; Kubarych, K. J. *Int. Rev. Phys. Chem.* **2012**, *31* (3), 367.

(12) Bredenbeck, J.; Helbing, J.; Hamm, P. *J. Am. Chem. Soc.* **2004**, *126* (4), 990.

(13) Bredenbeck, J.; Helbing, J.; Behrendt, R.; Renner, C.; Moroder, L.; Wachtveitl, J.; Hamm, P. *J. Phys. Chem. B* **2003**, *107* (33), 8654.

(14) Donten, M. L.; Hamm, P. *Chem. Phys.* **2013**, *422*, 124.

(15) Bleul, R.; Ritzi-Lehnert, M.; Höth, J.; Scharpfenecker, N.; Frese, I.; Düchs, D.; Brunklaus, S.; Hansen-Hagge, T. E.; Meyer-Almes, F.-J.; Drese, K. S. *Anal Bioanal Chem* **2010**, *399* (3), 1117.

(16) Schafer, D.; Gibson, E. A.; Amir, W.; Erikson, R.; Lawrence, J.; Vestad, T.; Squier, J.; Jimenez, R.; Marr, D. W. M. *Opt. Lett.* **2007**, *32* (17), 2568.

(17) Wu, L.; Lapidus, L. J. *Anal. Chem.* **2013**, *85* (10), 4920.

(18) Chen, D. L.; Gerdts, C. J.; Ismagilov, R. F. *J. Am. Chem. Soc.* **2005**, *127* (27), 9672.

(19) Song, H.; Ismagilov, R. F. *J. Am. Chem. Soc.* **2003**, *125* (47), 14613.

(20) Burke, K. S.; Parul, D.; Reddish, M. J.; Dyer, R. B. *Lab Chip* **2013**, *13* (15), 2912.

(21) Gambin, Y.; Simonnet, C.; VanDelinder, V.; Deniz, A.; Groisman, A. *Lab Chip* **2010**, *10* (5), 598.

(22) Zhu, L.; Ghosh, K.; King, M.; Cellmer, T.; Bakajin, O.; Lapidus, L. J. *J. Phys. Chem. B* **2011**, *115* (43), 12632.

(23) Zhu, L.; Kurt, N.; Choi, J.; Lapidus, L. J.; Cavagnero, S. *J. Phys. Chem. B* **2013**, *117* (26), 7868.

(24) Edel, J. B.; Lahoud, P.; Cass, A. E. G.; deMello, A. J. *J. Phys. Chem. B* **2007**, *111* (5), 1129.

(25) Barich, M. V.; Krummel, A. T. *Anal. Chem.* **2013**, *85* (21), 10000.

(26) Mao, H.; Yang, T.; Cremer, P. S. *J. Am. Chem. Soc.* **2002**, *124* (16), 4432.

(27) Dertinger, S. K. W.; Chiu, D. T.; Jeon, N. L.; Whitesides, G. M. *Anal. Chem.* **2001**, *73* (6), 1240.

(28) Lu, Z.; McMahon, J.; Mohamed, H.; Barnard, D.; Shaikh, T. R.; Mannella, C. A.; Wagenknecht, T.; Lu, T.-M. *Sensor. Actuat. B-Chem.* **2010**, *144* (1), 301.

(29) Sudarsan, A. P.; Ugaz, V. M. *PNAS* **2006**, *103* (19), 7228.

(30) Johnson, M.; Kamm, R. *J. Fluid Mech.* **1986**, *172*, 329.

(31) Afzal, A.; Kim, K.-Y. *J. Chem. Eng. Jpn.* **2013**, *46* (3), 230.

(32) Bessoth, F. G.; DeMello, A. J.; Manz, A. *Anal. Commun.* **1999**, *36* (6), 213.

(33) Garstecki, P.; Fuerstman, M. J.; Stone, H. A.; Whitesides, G. M. *Lab Chip* **2006**, *6* (3), 437.

(34) Chen, J.-S.; Jiang, J.-H. *Chinese J. Anal. Chem.* **2012**, *40* (8), 1293.

(35) Baroud, C. N.; Gallaire, F.; Dangla, R. *Lab Chip* **2010**, *10* (16), 2032.

(36) Handique, K.; Burns, M. A. *J. Micromech. Microeng.* **2001**, *11* (5), 548.

(37) Barich, M. V.; Spears, H. M.; Carver, C.; Krummel, A. T. *Anal. Chem.* **2016**, submitted for publication.

(38) Gan, H. Y.; Lam, Y. C.; Nguyen, N. T.; Tam, K. C.; Yang, C. *Microfluid Nanofluid* **2006**, *3* (1), 101.

(39) Gan, H. Y.; Lam, Y. C.; Nguyen, N.-T. *Appl. Phys. Lett.* **2006**, *88* (22), 224103.

(40) Lam, Y. C.; Gan, H. Y.; Nguyen, N. T.; Lie, H. *Biomicrofluidics* **2009**, *3* (1), 014106.

(41) Rodd, L. E.; Scott, T. P.; Boger, D. V.; Cooper-white, J. J.; Mckinley, G. H. *J. Non-Newton. Fluid Mech* **2005**, *129*, 1.

(42) McDonald, J. C.; Duffy, D. C.; Anderson, J. R.; Chiu, D. T.; Wu, H.; Schueller, O. J. A.; Whitesides, G. M. *ELECTROPHORESIS* **2000**, *21* (1), 27.

(43) McDonald, J. C.; Whitesides, G. M. *Acc. Chem. Res.* **2002**, *35* (7), 491.

(44) Miserere, S.; Mottet, G.; Taniga, V.; Descroix, S.; Viovy, J.-L.; Malaquin, L. *Lab Chip* **2012**, *12* (10), 1849.

(45) Hertzog, D. E.; Michalet, X.; Jäger, M.; Kong, X.; Santiago, J. G.; Weiss, S.; Bakajin, O. *Anal Chem* **2004**, *76* (24), 7169.

(46) Abate, A. R.; Poitzsch, A.; Hwang, Y.; Lee, J.; Czerwinska, J.; Weitz, D. A. *Phys. Rev. E* **2009**, *80* (2), 026310.

(47) Burke, K. S.; Parul, D.; Reddish, M. J.; Dyer, R. B. *Lab Chip* **2013**, *13* (15), 2912.

(48) Ham, S.; Kim, J.-H.; Lee, H.; Cho, M. *J. Chem. Phys.* **2003**, *118* (8), 3491.

(49) Eaton, G.; Symons, M. C. R.; Rastogi, P. P. *J. Chem. Soc., Faraday Trans. 1* **1989**, *85* (10), 3257.

(50) Guo, H.; Karplus, M. *J. Phys. Chem.* **1992**, *96* (18), 7273.

(51) Woutersen, S.; Pfister, R.; Hamm, P.; Mu, Y.; Kosov, D. S.; Stock, G. *J. Chem. Phys.* **2002**, *117* (14), 6833.

(52) Woutersen, S.; Mu, Y.; Stock, G.; Hamm, P. *Chem. Phys.* **2001**, *266* (2–3), 137.

(53) Zanni, M. T.; Asplund, M. C.; Hochstrasser, R. M. *J. Chem. Phys.* **2001**, *114* (10), 4579.

(54) Kwac, K.; Cho, M. *J. Raman Spectrosc.* **2005**, *36* (4), 326.

(55) Koenig, J. L.; Wang, S. Q.; Bhargava, R. *Anal. Chem.* **2001**, *73* (13), 360A.

(56) Lewis, E. N.; Treado, P. J.; Reeder, R. C.; Story, G. M.; Dowrey, A. E.; Marcott, C.; Levin, I. W. *Anal. Chem.* **1995**, *67* (19), 3377.

(57) Kaun, N.; Vellekoop, M. J.; Lendl, B. *Appl. Spectrosc.* **2006**, *60* (11), 1273.

(58) Greener, J.; Abbasi, B.; Kumacheva, E. *Lab Chip* **2010**, *10* (12), 1561.

(59) Chan, K. L. A.; Gulati, S.; Edel, J. B.; Mello, A. J. de; Kazarian, S. G. *Lab Chip* **2009**, *9* (20), 2909.

(60) Chan, K. L. A.; Kazarian, S. G. *Anal. Chem.* **2012**, *84* (9), 4052.

(61) Kise, D. P.; Magana, D.; Reddish, M. J.; Dyer, R. B. *Lab Chip* **2013**, *14* (3), 584.

(62) Lee, G.-B.; Chang, C.-C.; Huang, S.-B.; Yang, R.-J. *J. Micromech. Microeng.* **2006**, *16* (5), 1024.

(63) Simonnet, C.; Groisman, A. *Appl. Phys. Lett.* **2005**, *87* (11), 114104.

(64) Knight, J. B.; Vishwanath, A.; Brody, J. P.; Austin, R. H. *Phys. Rev. Lett.* **1998**, *80* (17), 3863.

(65) Hertzog, D. E.; Ivorra, B.; Mohammadi, B.; Bakajin, O.; Santiago, J. G. *Anal. Chem.* **2006**, *78* (13), 4299.

(66) Gary W. Evans. *Life Chemistry Reports* **1982**, *1*, 57.

## Chapter 5 Supplemental Information

### S5.1 Experimental Section

All kinetics information was extracted from linear spectra, a time-space fluorescence map, and an IR microspectroscopy image. The concentration maps of each chemical species present were generated using the molar absorptivity constants extracted from linear spectra taken of a concentration series of the respective chemical species. Figure S5.1 depicts the processing performed on the IR concentration map data. First, a concentration gradient of the product was measured using linear FTIR spectroscopy. Unique absorbance peaks were identified for each chemical species of interest, specifically, the bound and unbound picolinic acid species. Using the molar absorptivity values determined from the linear absorbance spectra, the IR concentration map of the free picolinic acid was obtained via beers law conversion calculations from the integrated absorbance area images. The concentration map was then separated into slices perpendicular to the direction of primary flow in the analysis channel. Each slice was then scanned, identifying the pixel number of a maximum and minimum threshold values defining the gradient region within the chip. The pixel values between the identified locations, including a larger 5 pixel buffer region, were then isolated from the IR concentration map of the product, forming a new matrix. The extracted matrix consists of the streamlines associated with the gradient generated, and was reoriented such that each streamline now travels vertically in a linear fashion. By plotting each streamline versus the slice number, the pixels prior to the product concentration reaching equilibrium were identified. For example, the concentration of the bound complex for the middle position in the gradient rose rapidly as it continued down the channel until plateauing after 1093 $\mu$s. The plateau signals that the reaction has reached equilibrium.

The slope of the pre-equilibrium regions is the initial rate of the appearance of product concentration per $\mu$m.

Similar processing was performed on the time-space image map using the same gradient region identified in the concentration maps. The fluorescence map obtained from the time-space mapping fluorescent microscope consisted of the intensity values of the Europium nanospheres. Intensity values were converted into time values using the decay lifetime of the beads and the decay equation. Using the location of the gradient region boundaries obtained in the concentration map described in the previous paragraph, the time values within the gradient region were isolated. By plotting the time value as a function of distance down the channel, the relationship between time and space was observed for each streamline. The slope of the plot is the average time traveled by the fluid in each streamline per pixel imaged. The general approach to processing the time data is shown in Figure S5.2.

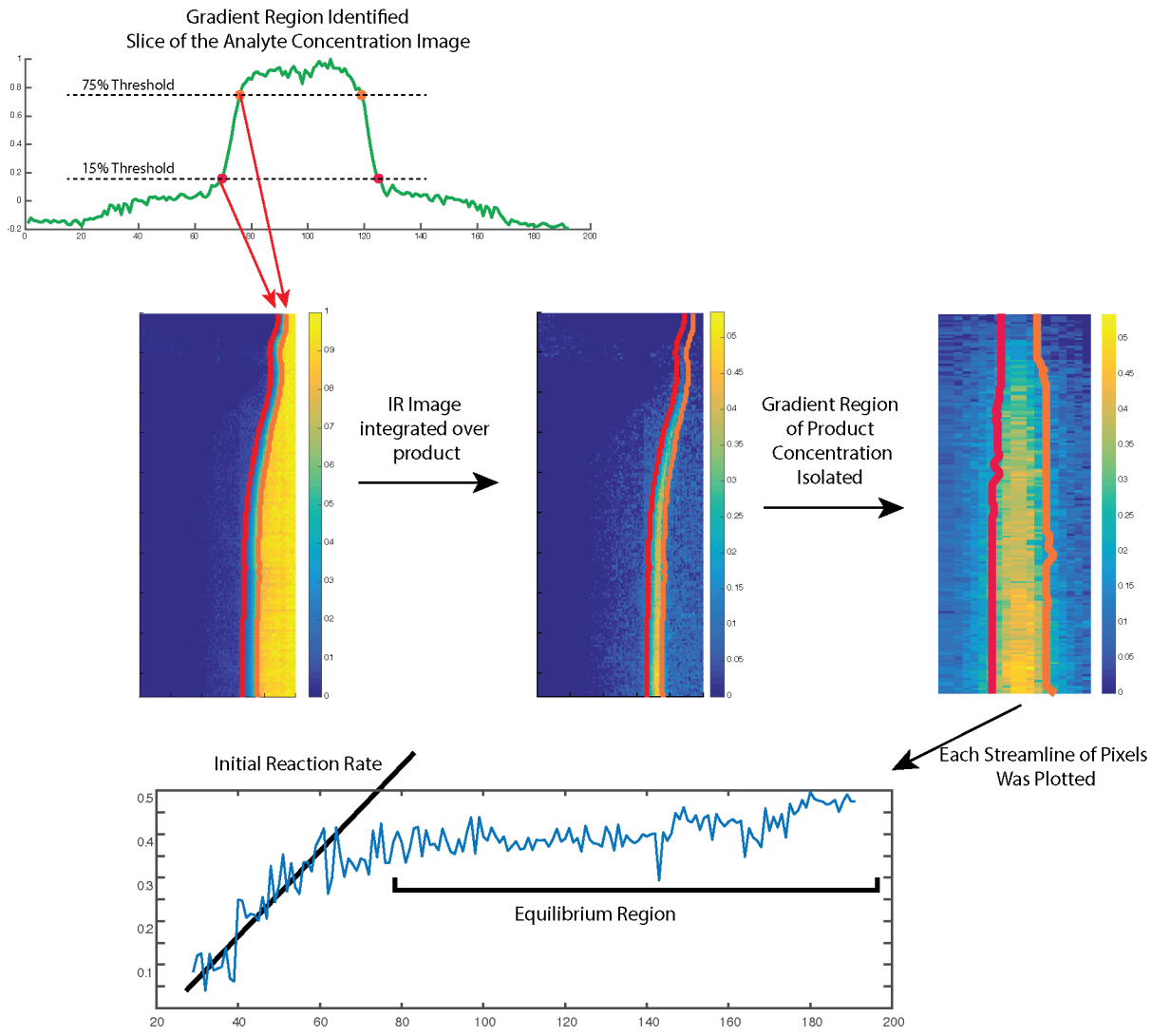


**Figure S5.1 Outline of the Method for Obtaining the Initial Rate of Reaction from the Microspectroscopy Image**

First, the gradient region was identified through identifying threshold values in the concentration of picolinic acid for each row in the IR image. Second, the product concentrations were isolated for the gradient region using the threshold values. Lastly, the slope of the pre-equilibrium region was calculated.

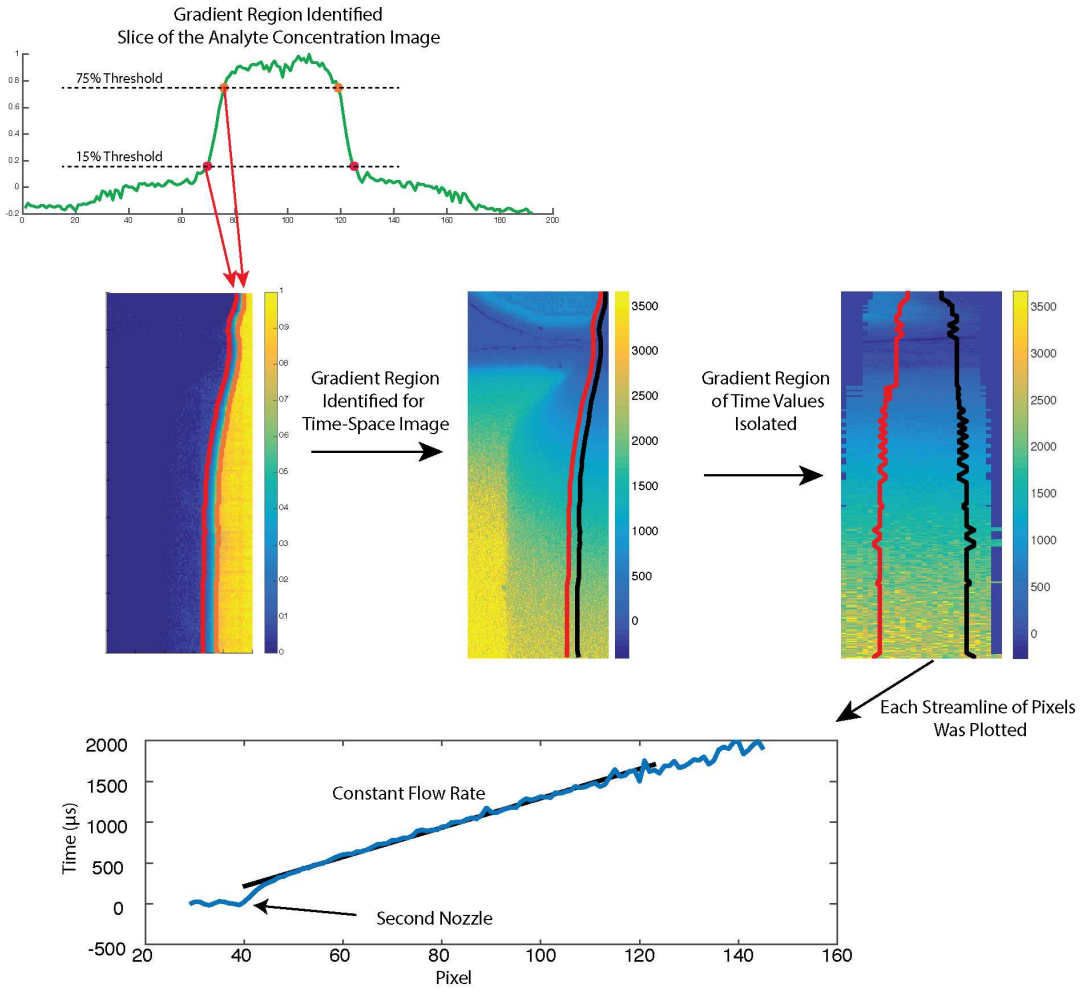


**Figure S5.2 Outlines the Process for Obtaining the Time per Pixel for the Fluids**

First, the gradient region was identified through identifying threshold values in the picolinic acid concentration for each row in the IR image. Second, the time values were isolated for the gradient region using the locations of the threshold values. Lastly, the slope of the time values was calculated from the slope of the time values versus pixel plot.

# Chapter 6

## Probing KOCN in Cosolvent Conditions by Interfacing 2D-IR Spectroscopy with Microfluidic Technology

This chapter is based on a manuscript currently in preparation, performed in cooperation with Kathryn Tracy, focusing on the first successful 2D IR measurements inside microfludic channels. For this work, I fabricated all microfluidic devices and designed the channel geometry to create the co-solvent conditions. The process of interfacing the microfluidic devices with the 2D IR system was accomplished through joint effort between Kathryn and myself.

### 6.1 Introduction

Spectroscopy techniques, such as linear IR absorption spectroscopy and two-dimensional infrared (2D IR) spectroscopy offer chemically specific information about solvent dynamics, reaction kinetics, molecular structure, and conformational dynamics.[1–4] These spectroscopic tools have been used to examine a range of systems including solute-solvent interactions, protein conformational studies, and chemical exchange kinetics. Microfluidic technologies have been applied to numerous chemical applications such as chemical dynamics, reaction kinetics, and reaction monitoring. With recent advances in fabrication technology, there has been a push to utilize microfluidic technology with linear infrared spectroscopy and imaging techniques.[5] Microfluidic technology allows access to chemical conditions previously unattainable through traditional methods.[6] However, microfluidic devices have never been interfaced with nonlinear spectroscopy techniques. The combination of multidimensional spectroscopies and microfluidics would allow chemical information, such as solvent dynamics, kinetics, and molecular structure

to be observed in chemical environments only accessible through the precision sample control of microfluidics. For example, pseudo-halide anions are of particular interest due to their potential as a marker for proteins. They are an ideal molecular probe for the protein folding process because they exhibit long vibrational lifetimes and are sensitive to their local environments.[7–9] Using 2D IR spectroscopy, the local solvation environment around the anion can be determined through monitoring the relaxation rate of the CN stretch.[10–12] However, research on pseudo-halide anions have been centered around their response in pure solvent environments. Co-solvation environments are easily generated in a microfluidic device that was designed to create a solvent gradient. In this work, the CN stretch response to a cosolvation environment is efficiently mapped, using 2D IR measurements performed in a microfluidic device that generates a solvent gradient. Specifically, the sensitivity of the cyanate ion to solvation environment using the anharmonicity of the potential well was quantitatively determined.

### 6.2 IR Response of KOCN

The pseudo-halide anion, cyanate, is a solvatochromic anion that has an absorption highly sensitive to both the solvent and counter ion present in the system. The central frequency of the pseudo halide probe is particularly sensitive to the hydrogen bonding and polarity of the solvent.[11] For example, by observing potassium cyanate (KOCN) in a protic solvent, methanol, a single peak is present at the frequency 2166 $cm^{-1}$ (Figure 6.1a). In an aprotic solvent, N,N-Dimethylformamide (DMF), two features are present, a parent peak with a shoulder, located at frequencies of 2136 $cm^{-1}$ and 2146 $cm^{-1}$, respectively (Figure 6.1b). In this environment, the parent peak is the unbound cyanate ion, while the shoulder is the contact pair of the cyanion ion with the potassium ion. The central frequency of the cyanate peak in methanol is at a higher frequency than in DMF due to the slightly higher polarity associated with methanol as compared

to DMF. By using 2D IR spectroscopy to observe these phenomena, it is possible to identify solvent dynamics associated with the two environments. The sensitivity of the KOCN central absorption wavelength and anharmonicity to changes in solvent environment make cyanate a useful vibrational probe to report on the local environment in more complex systems, such as the protein solvation shell.

### 6.3 Microfluidic Sample Manipulation

Quantifying the spectral response of pseudo-halide anions in mixed solvent environments is of interest due to the different solvation characteristics that drive the protein folding process. In order to measure the response that local solvent environments has on KOCN, microfluidic devices were incorporated into the sample platform for 2D IR spectroscopy. A microfluidic device was used to generate a stable, tunable solvent gradient of methanol and DMF laterally across the channel. The specific geometry, shown in Figure 6.2a, uses a serpentine pattern with a 350 μm wide and 32 μm tall channel to generate small secondary flows, enhancing the diffusive mixing process. The channel then straightens into an observation area, where the gradient is maintained. Within the observation area, the tunable linear solvent gradient of the two incoming fluids can be spatially sampled across the channel. The tunability of the solvent gradient using flow rate is exhibited in Figure 6.2b depicted by plotting the concentration of one fluid at three different flow rates. The gradient affords multiplexed sample prep, reducing the time and chemical usage required to map the chemical interaction as a function of solvent environment.

In this work, a linear gradient of the solvents methanol and DMF, with a constant KOCN concentration was generated from 30 mM KOCN in methanol and 30 mM KOCN in DMF. Characterization of the solvent gradient was performed using FTIR microspectroscopy by chemical mapping of the observation area. The absorption maps were generated by integrating

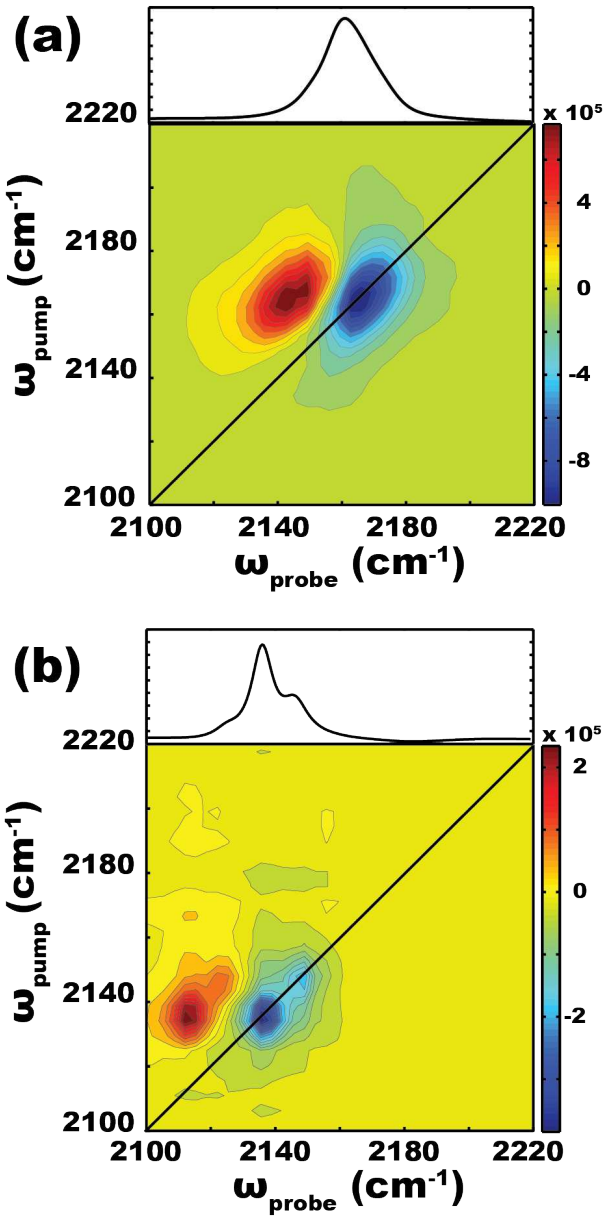


**Figure 6.1 Static IR and 2D IR of KOCN in both Methanol and DMF**

The 2D IR spectra of (a) 30 mM KOCN in methanol and (b) 30 mM KOCN in DMF.

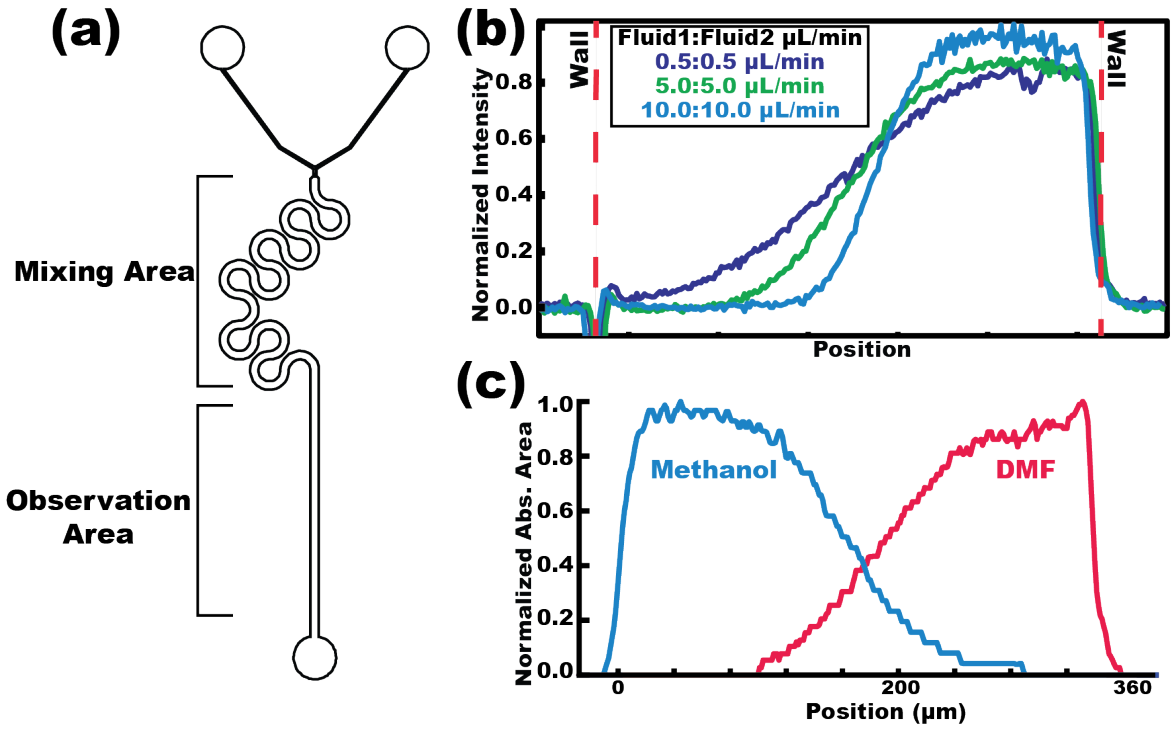


**Figure 6.2 Characteristics of the Microfluidic Device**

(a) The photomask used to create the IR transparent microfluidic devices for gradient generation. (b) The tunability in gradient slope in response to changes in flow rate. (c) The solvent profile used in this work measured within the observation area plotted as solvent percentage is plotted as a function of positions across the microfluidic channel.

under unique absorption peaks for both methanol (3136 to 3189 $cm^{-1}$) and DMF (1720 to 1728 $cm^{-1}$). Figure 6.2c shows the solvent profile for the device extracted from the FTIR microspectroscopy image, confirming the solvent gradient within the channel.

### 6.4 2D IR Measurements in a Microfluidic Device

2D IR spectroscopy was used to observe $OCN^-$ and the $K^+$ $OCN^-$ contact ion pair in the gradient generated by the microfluidic device. Measurements were taken laterally in the microfluidic channel starting at the edge that was 100% methanol and moving in 40 $\mu$m steps towards higher percentages of DMF. The locations at which measurements were taken are indicated in Figure 6.3 next to intensity maps of both methanol and DMF.

The observed 2D IR spectra are displayed in Figure 6.3a. At the edge of the channel scatter is seen and the position of the measurement is confirmed. Measurements taken in methanol had a frequency of 2165 $cm^{-1}$. Moving across the channel to an entirely DMF environment, a shift in peak position to 2150 $cm^{-1}$ is observed. This ability to quantify spectral changes in 40 μm step sizes, which is smaller increments than the beam size of 130 μm, means that the intensity profile of the beam is assisting in the increased spatial resolution across the channel.

The response of KOCN to the different solvent mixtures can be characterized by resolving the 2D IR spectra spatially across the microfluidic devices. To demonstrate this we measured the anharmonicity change associated with the different mixing concentrations. The different solvent environments across the channel will deform the molecular potential energy surface differently depending on force exerted. Modulation of the anharmonicity measured across the channel can be seen in Figure 6.3c. As the solvent gradient changes from mostly DMF to mostly methanol, the anharmonicity decreases from 33 $cm^{-1}$ to 24 $cm^{-1}$.

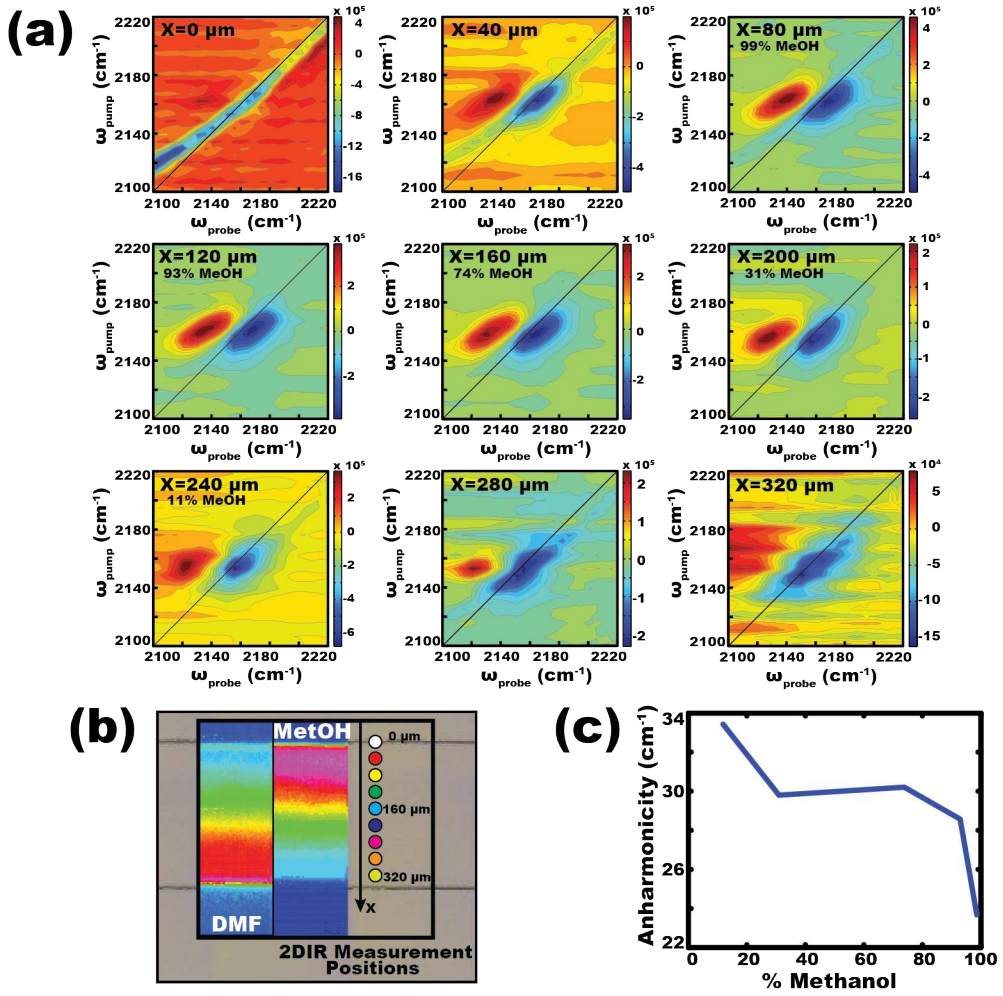


**Figure 6.3 The Measured 2D IR Spectra of KOCN in the Solvent Gradient Formed using a Microfluidic Device**

(a) The 2D IR spectra collected in 40 μm steps across the microfluidic channel moving from higher percentage methanol to DMF. (b) The IR chemical map images integrated from 3136 to 3189 cm-1 for the solvent methanol and 1720 to 1728 cm-1 for the solvent DMF. The dots indicate the locations of 2D IR measurements across the channel. (c) The anharmonicity measured in wavenumbers ($cm^{-1}$) extracted from the 2D IR spectra collected in 40 μm steps across the microfluidic channel plotted as a function of the methanol solvent percentage.

The experiment performed herein shows proof-of-concept that combining 2D IR analysis with microfluidic sample control is possible, expanding the scope of experimentation for both fields. Although the experiments performed in this work utilize a high repetition rate 2D IR spectrometer, microfluidic devices can be interfaced with any type of 2D IR spectrometer as a valuable tool for sample manipulation.

## 6.5 Experimental Methods

The fabrication of the PDMS IR compatible microfluidic device used has been described previously.[5] The devices were fabricated using a standard photolithography technique in Polydimethyl Siloxane (PDMS, Sylgard 184, Dow Corning). Each of the IR transparent microfluidic chips is comprised of four components: a support layer, microchannel layer, adhesion layer, and calcium fluoride backbone. To create the complete microfluidic device, all four components are individually prepared and then assembled by sealing the PDMS with air plasma. Two NE-500 Programmable OEM syringe pumps are used to pump fluid in 10 mL syringes into the microfluidic devices. The flow rates used for this experiment were 6 μL/min for both the outer and inner fluids.

A Bruker Hyperion 3000 FTIR microscope was used to take the infrared microscope images. The FTIR microscope utilizes a 64 x 64 element FPA detector and a 15x objective to give a 2.7 μm spatial resolution. All FTIR microscope images were taken in transmission mode, and were processed using OPUS software (Bruker Optics).

The 2D IR spectroscopy utilized a 100 kHz 2D IR spectrometer that has been described in previous work.[13] This spectrometer is based on optical parametric chirped-pulse amplification (OPCPA) in magnesium doped periodically poled lithium niobate (MgO:PPLN) and difference frequency generation (DFG) in zinc germanium diphosphide (ZGP). The general layout for this

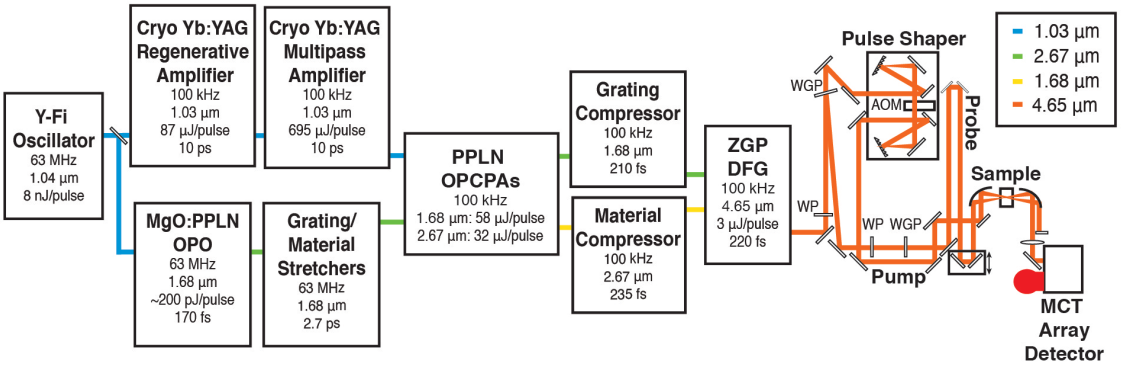


**Figure 6.4 The general layout of the 2D IR spectrometer.**

system can be seen in Figure 6.4. Both the pump and seed beams for the OPCPA stages are generated in an All Normal Dispersion (ANDi)[14] Ytterbium-Fiber (Y-Fi) mode locked oscillator (KM Labs) source. Most of the Y-Fi output is separated and compressed to pump an optical parametric oscillator (OPO) generating 170 fs pulses centered at 1.68 µm light. This is the seed for the OPCPA stages. The remaining uncompressed output centered at 1 µm is amplified in the cryogenically cooled Yb:YAG based regenerative amplifier and the two pass Yb:YAG based amplifier. This is the pump for the OPCPA stages. Three stages of OPCPA amplification in MgO:PPLN crystals are utilized to amplify the stretched 1.68 µm and generate a 2.67 µm idler. The signal and idler are compressed in a transmission grating compressor and a material silicon compressor, respectively. This signal and idler are recombined in a ZGP DFG stage, which generates 3 µJ of 4.65 µm mid-IR idler output with 220 fs pulse lengths. A long pass filter is used to separate and collimate this mid-IR light to be sent to the 2D IR spectrometer. This output is split into two lines, one of which is sent to a mid-IR high speed pulse shaper to generate at 100 kHz the pump pulse pair with a variable delay.[15] The second line is used as the probe pulse. The pump and probe pulses are focused on the sample cell to a spot size of 130 µm

FWHM using a four inch focal length 90° off axis parabolic mirror. The probe beam is then collected by a 100 kHz, 1 x 64 element, mercury cadmium telluride (MCT) mid-IR spectrometer. The 2D spectra are all collected using a four-step phase cycling scheme with a series of 358 pump pulse pairs delayed from 0 to 2.5 ps in 7 fs steps.

The two sample solutions utilized in both the static and microfluidic device experiments were 30 mM KOCN in HPLC grade N,N-Dimethylformamide (DMF) and 30 mM KOCN in ACS grade methanol. The KOCN, DMF, and methanol were all used without purification and were purchased from Sigma Aldrich. All experiments were performed at room temperatures. The FTIR and static 2D IR experiments were performed by placing the sample between two $CaF_2$ plates using a 50-μm-thick Teflon spacer. The samples of KOCN in DMF and methanol had a resulting OD of 0.1 and 0.35, at 2136 $cm^{-1}$ and 2166 $cm^{-1}$ respectively. The microfluidic device experiment was performed by flowing the 30 mM KOCN in DMF and 30 mM KOCN in methanol in the 32-μm-thick channel. The device was centered on the channel by 3D mapping both pump and probe scatter of the channel edges. Translation of the device used a x,y,z translational stage to sample different locations in the channel.

## References


(1) Fayer, M. D. *Annual Review Of Physical Chemistry* **2009**, *60*, 21.

(2) Hochstrasser, R. M. *PNAS* **2007**, *104* (36), 14190.

(3) Zanni, M. T.; Hochstrasser, R. M. *Current Opinion in Structural Biology* **2001**, *11* (5), 516.

(4) Woutersen, S.; Hamm, P. *J. Phys.: Condens. Matter* **2002**, *14* (39), R1035.

(5) Barich, M. V.; Krummel, A. T. *Anal. Chem.* **2013**, *85* (21), 10000.

(6) Barich, M. V.; O'Connell, K.; Carver, C.; Krummel, A. T. *J. Phys. Chem. B* **2016**, submitted for publication.

(7) Son, H.; Jin, H.; Choi, S. R.; Jung, H. W.; Park, S. *J. Phys. Chem. B* **2012**, *116* (30), 9152.

(8) Lenchenkov, V.; She, C.; Lian, T. *J. Phys. Chem. B* **2006**, *110* (40), 19990.

(9) Tucker, M. J.; Gai, X. S.; Fenlon, E. E.; Brewer, S. H.; Hochstrasser, R. M. *Phys. Chem. Chem. Phys.* **2011**, *13* (6), 2237.

(10) Park, K.-H.; Choi, S. R.; Choi, J.-H.; Park, S.; Cho, M. *ChemPhysChem* **2010**, *11* (17), 3632.

(11) Wilderen, L. J. G. W. van; Kern-Michler, D.; Müller-Werkmeister, H. M.; Bredenbeck, J. *Phys. Chem. Chem. Phys.* **2014**, *16* (36), 19643.

(12) Sun, Z.; Zhang, W.; Ji, M.; Hartsock, R.; Gaffney, K. J. *J. Phys. Chem. B* **2013**, *117* (40), 12268.

(13) Luther, B. M.; Tracy, K. M.; Gerrity, M.; Brown, S.; Krummel, A. T. *Opt Express* **2016**, *24* (4), 4117.

(14) Chong, A.; Buckley, J.; Renninger, W.; Wise, F. *Opt Express* **2006**, *14* (21), 10095.

(15) Shim, S.; Zanni, M. T. *Physical Chemistry Chemical Physics* **2009**, *11* (5), 748.

# Chapter 7

## Conclusions/Future Work

### 7.1 Conclusions

This thesis is the first step towards the ability to monitor the protein folding process with atomic structural resolution in real time. In this work, the sample handling capabilities of microfluidic devices are used to expand the experimental range of both infrared (IR) and two dimensional infrared (2D IR) measurement techniques. The IR compatible microfluidic platform developed in this work, affords the advantages of using PDMS microfluidic technology to be performed in transmission geometries often utilized in linear and nonlinear vibrational spectroscopy experiments.

Multiple microfluidic channel geometries were presented in this work. The utility of each device was demonstrated by probing model chemical interactions and chemical reaction kinetics with FTIR microspectroscopy. The single-phase diffusive mixer was used to form a stable gradient of two solvents. The change in local solvent environments across the channel was reported using the shift in the center frequency of the carbonyl stretching vibrational mode in NMA. A droplet generator microfluidic device was used to encapsulate chemical reactants in femtoliter vessels and FTIR microspectroscopy was used to follow the protonation of the acetate ion. The chemical reactants mix instantaneously in the drops allowing for a well-characterized time zero for mixing and subsequent reaction monitoring within the droplets with FTIR microspectroscopy. The dual nozzle gradient generator, a stable gradient useful for incorporating multiplexed measurements of molecular interactions was produced. Moreover, the gradient is established within milliseconds of the fluids passing through the second nozzle in the

device, adding a time axis to the measurements. Using picolinic acid chelating iron (II) as a model system, the rate of binding for a range of reactant concentrations was measured on-chip for the first time. Each of these microfluidic channel designs creates a specific chemical environment previously unavailable to most vibrational spectroscopy techniques including FTIR spectroscopy and 2D IR spectroscopy.

To further prove the effectiveness of the technology developed, a microfluidic gradient was generated to probe the KOCN vibrational lifetimes in cosolvation environments. This was the first time that multidimensional spectroscopy was performed within a microfluidic device. As such, the advances in experimental range of both infrared (IR) and two dimensional infrared (2D IR) measurement techniques was confirmed.

### 7.2 Future Work

As with the protein folding process, there are many pathways with which the work performed in this thesis will continue. Mainly, the techniques developed here will be applied to measure the kinetics of the model system RADA as it is undergoing the self assembly process. The goal of establishing the mechanism with which RADA transforms from primary to secondary, and secondary to higher ordered structures still remains. Both FTIR microspectroscopy and 2D IR spectroscopy analysis techniques on RADA in the single phase gradient generation device as well as the dual nozzle gradient generator would produce valuable evidence towards discovering the mechanism of assembly. Although this work has provided the tools necessary to perform the experiments, much work is still needed.

The technology developed in this work was motivated towards monitoring the protein self-assembly process in real time using vibrational spectroscopy techniques. However, the application is not limited to that specific task. The versatility of microfluidic devices to create

steady state microenvironments provides unlimited avenues to pursue. For example, multiplexed measurements through use of gradients will provide efficiency in further investigation of the solvation response of the pseudo-halide anions and other solvatochromic chemical species. Alternatively, the kinetic rate of surfactin disrupting lipid micelles could be monitored using 2D IR spectroscopy in a dual nozzle gradient generator. These examples represent the broad application of the microfluidic technology developed in this work and reflect the success this work has accomplished in bridging microfluidic capabilities with infrared analysis techniques.

# Appendix I

## MatLab Programs

### A1.1 Linear Processing Code with Basic Analysis

The purpose of this code is to take the linear IR data exported from OPUS and convert it into the raw version of publishable figures. It has the code to perform subtraction of the solvent, normalization, baseline correction, and cropping of the data. Other useful analysis is also included such as determination of the molar absorptivity, or comparison amongst similar specta.

```
clear hold
clc; clear all; %close all;

%% Import
cd('/Users/michaelbarich/Copy/Krummel Group/Research/IR Microscope/2016-03-
14/IR Kinetics')
%%
Dat01 = importdata('2016-03-11_V70-T_D2O_50.0.dpt');
Dat02 = importdata('2016-03-11_V70-T_Device Emittance.0.dpt');
Dat03 = importdata('2016-03-11_V70-T_FeCl2.0.dpt');
Dat04 = importdata('2016-03-11_V70-T_Picolinic Acid +NaCl.0.dpt');
Dat05 = importdata('2016-03-11_V70-T_Picolinic Acid.0.dpt');
Dat06 = importdata('2016-03-14_V70-T_FeCl.0.dpt');
Dat07 = importdata('2016-03-14_V70-T_PicA+NaCl.0.dpt');
Dat08 = importdata('2016-03-14_V70-T_Product.0.dpt');
% Dat09 = importdata('2015-09-28_V70-T_15.0.dpt');
% Dat10 = importdata('2015-09-28_V70-T_Stock.0.dpt');

testplot2 = 1; % Raw data plot for all 5 and D20 blank
testplot3 = 1; % Subtracted data plot
testplot4 = 0; % cropped figure
testplot5a = 1; % shows the basecorrected spectra
testplot5b = 1; % shows the corrected to zero spectra
testplot6 = 1; % normalization plot

lolim = 2000; % set the lower wavelength bound
hilim = 2300; % set the higher wavelength bound
bccore = 0; % should we baseline correct?
norma =0;

in = 8; % how many data files are we looking at?

% DatRD2O = DatRD2O0; % allows to set which blank as the one to use
```

```
%% Initial plot

if testplot2 == 1

    figure(23)
    clf(23)
    hold on

    plot(Dat01(:,1), Dat01(:,2),'b');
    plot(Dat02(:,1), Dat02(:,2),'k');
    plot(Dat03(:,1), Dat03(:,2),'c');
    plot(Dat04(:,1), Dat04(:,2),'m');
    plot(Dat05(:,1), Dat05(:,2),'g');
    %
    plot(Dat06(:,1), Dat06(:,2),'b');
    plot(Dat07(:,1), Dat07(:,2),'k');
    plot(Dat08(:,1), Dat08(:,2),'c');
    %     plot(Dat09(:,1), Dat09(:,2),'m');
    %     plot(Dat10(:,1), Dat10(:,2),'g');

    %     plot(DatRD2O(:,1), DatRD2O(:,2),'r-.');
    %     plot(aDatR(:,1), aDatR(:,2),'k-.');

    title('Raw Data: All')
    %     legend('1','2','3','D2O','Location','NorthWest')
    xlabel('Wavenumber')
    ylabel('Absorbance')
    set(gca,'XDir','reverse')
    %     xlim([lolim-100 hilim+100])

    hold off
end
%%
% NaOH Subtraction

% FNaOH = [0.0255 0.0496 0.0727 0.1011 0.2030 0.0000];
% NaOH = [aDatR(:,1), aDatR(:,2) - DatRD2O(:,2)];

% Subtraction

DatS01 = [Dat01(:,1), Dat01(:,2) - Dat01(:,2)];
DatS02 = [Dat02(:,1), Dat02(:,2) - Dat01(:,2)];
DatS03 = [Dat03(:,1), Dat03(:,2) - Dat01(:,2)];
DatS04 = [Dat04(:,1), Dat04(:,2) - Dat01(:,2)];
DatS05 = [Dat05(:,1), Dat05(:,2) - Dat01(:,2)];
DatS06 = [Dat06(:,1), Dat06(:,2) - Dat01(:,2)];
DatS07 = [Dat07(:,1), Dat07(:,2) - Dat01(:,2)];
DatS08 = [Dat08(:,1), Dat08(:,2) - Dat01(:,2)];
% % DatS09 = [Dat09(:,1), Dat09(:,2) - DatRD2O(:,2) - FNaOH(9,1)*NaOH(:,2)];
% DatS10 = [Dat10(:,1), Dat10(:,2) - DatRD2O(:,2) - FNaOH(10,1)*NaOH(:,2)];

if testplot3 == 1

    figure(33)
    clf(33)
    hold on
```

```
    plot(DatS01(:,1), DatS01(:,2),'b');
    plot(DatS02(:,1), DatS02(:,2),'k');
    plot(DatS03(:,1), DatS03(:,2),'c');
    plot(DatS04(:,1), DatS04(:,2),'m');
    plot(DatS05(:,1), DatS05(:,2),'g');
    %
    %     plot(DatS06(:,1), DatS06(:,2),'b-.');
    %     plot(DatS07(:,1), DatS07(:,2),'k-.');
    %     plot(DatS08(:,1), DatS08(:,2),'c-.');
    %     plot(DatS09(:,1), DatS09(:,2),'m');
    %     plot(DatS10(:,1), DatS10(:,2),'g-.');
%     plot(NaOH(:,1), NaOH(:,2),'k-.');

    title('Blank Subtracted Data: ASP-ASP 5 mM')
    legend('1','2','3','4','5','6','7','8','Stock','Location','NorthWest')
    xlabel('Wavenumber')
    ylabel('Absorbance')
    set(gca,'XDir','reverse')
    %     xlim([1550 1750]) %xlim([lolim-100 hilim+100])

    hold off

end

datasetraw(:,:,1) = Dat01(:,:);
datasetraw(:,:,2) = Dat02(:,:);
datasetraw(:,:,3) = Dat03(:,:);
datasetraw(:,:,4) = Dat04(:,:);
% datasetraw(:,:,5) = Dat05(:,:);
% datasetraw(:,:,6) = Dat06(:,:);
% datasetraw(:,:,7) = Dat07(:,:);
% datasetraw(:,:,8) = Dat08(:,:);
% datasetraw(:,:,9) = Dat09(:,:);
% datasetraw(:,:,10) = Dat10(:,:);

datasetbc(:,:,1) = DatS01(:,:);
datasetbc(:,:,2) = DatS02(:,:);
% datasetbc(:,:,3) = DatS03(:,:);
% datasetbc(:,:,4) = DatS04(:,:);
% datasetbc(:,:,5) = DatS05(:,:);
% datasetbc(:,:,6) = DatS06(:,:);
% datasetbc(:,:,7) = DatS07(:,:);
% datasetbc(:,:,8) = DatS08(:,:);
% datasetbc(:,:,9) = DatS09(:,:);
% datasetbc(:,:,10) = DatS10(:,:);

clear D* FD*

%% Continued processing

i = 1;

p1 = find(datasetbc(:,1,i)>hilim-1 & datasetbc(:,1,i)<hilim+1); p1 =
p1(1,1);% finds the left hand end point
p2 = find(datasetbc(:,1,i)>lolim-1 & datasetbc(:,1,i)<lolim+1); p2 =
p2(1,1);% finds the right hand end point
datasetcrop = zeros(p2-p1+1,2,in);
```

```
% cropping the data set to the set bounds
for i = 1:in

    datasetcrop(:,:,i) = [datasetbc(p1:p2,1,i), datasetbc(p1:p2,2,i)];

    if testplot4 == 1
        hold on
        figure(4)
        clf(4)
        plot(datasetcrop(:,1,i),datasetcrop(:,2,i))
    end

end
hold off

% %% zeroing out the spectra

for i = 1:in

    datasetmin(:,:,i) = [datasetcrop(:,1,i), datasetcrop(:,2,i) -
min(datasetcrop(:,2,i))];

    hold on
    if testplot5b == 1
        figure(6)
        %         clf(6)
        plot(datasetmin(:,1,i), datasetmin(:,2,i),'k')

        legend('Zero to min','Location','NorthWest')
        xlim([lolim-30 hilim+30]) ;
        xlabel('Wavenumber')
        ylabel('Absorbance')
        set(gca,'XDir','reverse')
    end
end
hold off

% %% Baseline correction

if bccore == 1
    p = [1, 1+p2-p1];

    for i = 1:in

        basecor = polyfit(datasetmin(p,1,i), datasetmin(p,2,i),1); %finds the
linear polynomail to fit the data
        basecorefit(:,:,i) = polyval(basecor,datasetmin(:,1,i)); % creates
the baseline data set
        datasetbc2(:,1,i) = datasetmin(:,1,i);
        datasetbc2(:,2,i) = datasetmin(:,2,i)- basecorefit(:,1,i); %
subtracts the baseline

        if testplot5a == 1

            hold on
```

```
            figure(5)

            plot(datasetmin(:,1,i),datasetmin(:,2,i),'r-.')
            plot(datasetbc2(:,1,i),datasetbc2(:,2,i),'b')
            plot(datasetbc2(:,1,i),basecorefit(:,1,i),'c');

            legend('zero to min','base corrected','the polyfit
subtracted','Location','NorthWest')
            xlim([lolim-30 hilim+30]) ; % 'Air',
            xlabel('Wavenumber')
            ylabel('Absorbance')
            set(gca,'XDir','reverse')
        end
    end
    hold off
else
    datasetbc2 = datasetmin;
end

% %% Normalization

if norma == 1;
    datasetnorm = zeros(size(datasetbc2));

    for i = 1:in
        datasetnorm(:,1,i) = datasetbc2(:,1,i);
        datasetnorm(:,2,i) = datasetbc2(:,2,i)./sum(datasetbc2(:,2,i));

        if testplot6 == 1
            hold on
            figure(7)
            clf(7)

            if i == 1
                plotColor = 'k';
            elseif i == 2
                plotColor = 'm';
            elseif i == 3
                plotColor = 'b';
            elseif i == 4
                plotColor = 'c';
            elseif i == 5;
                plotColor = 'g';
            elseif i == 6
                plotColor = 'r';
            end

            plot(datasetnorm(:,1,i),datasetnorm(:,2,i),plotColor)

            legend('1','2','D2O','Location','NorthWest')
            xlim([lolim-30 hilim+30]) ; % 'Air',
            xlabel('Wavenumber')
            ylabel('Absorbance')
            set(gca,'XDir','reverse')
        end
    end
```

```
    hold off
else
    datasetnorm = datasetbc2;
end
hold off

% % %%%%%%%%%%%%%%%%%%%%%%%%%%%%%% output variable is RADAPRO
clc

endpoints = [lolim, hilim]
numspec = in
RADAPRO = datasetnorm;

clear test* p* lo* norm* i* hi* dataset* b* hold

%% summations

p1Lb = 1740; %peak 1 lower bound the 1670ish peak
p1Ub = 1615 ;%peak 1 upper bound
p2Lb = 1615; %peak 2 lower bound the 1614ish peak
p2Ub = 1558; %peak 2 upper bound

x = (RADAPRO(:,1,1));

ap1 = find(x(:,1)>p1Lb-1 & x(:,1)<p1Lb+1); ap1 = ap1(1,1);% finds the left
hand end point
ap2 = find(x(:,1)>p1Ub-1 & x(:,1)<p1Ub+1); ap2 = ap2(1,1);% finds the right
hand end point

aap1 = find(x(:,1)>p2Lb-1 & x(:,1)<p2Lb+1); aap1 = aap1(1,1);% finds the left
hand end point
aap2 = find(x(:,1)>p2Ub-1 & x(:,1)<p2Ub+1); aap2 = aap2(1,1);% finds the
right hand end point

pH = [5.00 4.34 3.25 2.77 1.45 3.02 1.01 1.56 1.38 6.15];

for i = 1:numspec
    SUMat1(1,i) = sum(RADAPRO(ap1:ap2,2,i));
    SUMat2(1,i) = sum(RADAPRO(aap1:aap2,2,i));

end

figure(10)
clf(10)
hold on

plot(pH, SUMat1(1,:),'ro');
plot(pH, SUMat2(1,:),'bo');

title('Fitted Peak Areas')
legend('Peak1- high','Peak2- low','Location','best')
xlabel('Concentration mM')
%     ylabel('')
%     set(gca,'XDir','reverse')
%     xlim([0 7])
```

```
hold off

%% Plotting specific wavelengths
x = (RADAPRO(:,1,1));

p1 = 1580;
p2 = 1677;

PP1 = find(x(:,1)>p1-1 & x(:,1)<p1+1); PP1 = PP1(1,1);% finds the left hand
end point
PP2 = find(x(:,1)>p1-1 & x(:,1)<p2+1); PP2 = PP2(1,1);% finds the right hand
end point
%
figure(15)
clf(15)
hold on

for i = 1:numspec
    plot(pH(1,i),RADAPRO(PP1,2,i)-RADAPRO(1,2,i),'bo');
    plot(pH(1,i),RADAPRO(PP2,2,i)-RADAPRO(1,2,i),'ro');
end

legend('p1','p2','Location','NorthWest')
% xlim([lolim-30 hilim+30]) ; % 'Air',
xlabel('Sample Number')
ylabel('Absorbance')
% set(gca,'XDir','reverse')

hold off

%% difference from the stock
j = 1;

figure(70)
clf(70)

hold on

for i = 1:numspec
    if j == 7
        j = 1;
    end

    if j == 1
        plotColor = 'k';
    elseif j == 2
        plotColor = 'm';
    elseif j == 3
        plotColor = 'b';
    elseif j == 4
        plotColor = 'c';
    elseif j == 5;
        plotColor = 'g';
    elseif j == 6
        plotColor = 'r';
    end
```

```
    plot(RADAPRO(:,1,i),RADAPRO(:,2,i)-RADAPRO(:,2,10),plotColor);

    %     legend('1','2','D2O','Location','NorthWest')
    % xlim([lolim-30 hilim+30]) ; % 'Air',
    xlabel('Wavenumber cm^-^1')
    ylabel('Absorbance')
    set(gca,'XDir','reverse')
    j = j+1;
end

hold off
```

### A1.2 Infrared Image Code with Basic Data Processing

The purpose of this code is to convert the output of the OPUS program into raw versions of publishable figures for the IR images acquired. The code is designed to crop, rearrange, and reorder the data into the IR images. Included is the ability to integrate between two measurement points with or without the use of a baseline in between, and convert the integrated absorbance area into concentrations using a known path length and molar absorptivity. It also contains multiple formats with which to view the images created.

```
clear hold
clc; clear all; close all;

%% Import

cd('/Users/michaelbarich/Krummel Group/Research/IR Microscope/2016-03-14/IR
Kinetics')

IDat01 = importdata('FeO_PicAC_10-10-noz1_DS.0.dpt');
% IDat01 = importdata('FeO_PicAC_10-10-mid1_DS.0.dpt');
chanwidth = 500;
chanheight = 31; %?m

Conc = 1.1112; %M set concentration
% Dat02 = importdata('2016-03-11_V70-T_Device Emittance.0.dpt');

bs = 1;
%% wavelengths
Range1H = 1680;
Range1L = 1635;
```

```
[xx,yy] = size(IDat01);
wavelengths = IDat01(:,1);
%
for  mike = 1
    %% FInd the range bounds
    j = 1;
    k = 0;
    while k == 0;
        if wavelengths(j) <= Range1H
            lefthigh = j;
            k = 1;
        else j = j+1;
        end
    end
    %
    j = xx;
    k = 0;
    while k == 0;
        if wavelengths(j) >= Range1L
            leftlow = j;
            k = 1;
        else j = j-1;
        end
    end

    %% doing the summation integral
    usefuls = zeros(1,yy);
    %%
    for i = 2:yy
        ypoint1 = IDat01(lefthigh,i);
        ypoint2 = IDat01(leftlow,i);
        xpoint1 = wavelengths(lefthigh,1);
        xpoint2 = wavelengths(leftlow,1);
        slope = (ypoint1-ypoint2)/(xpoint1-xpoint2);
        b = ypoint1 - slope*xpoint1;

        %%
        if bs == 1
            for h = 1:(leftlow-lefthigh)
                baselineT(h) = slope*wavelengths(leftlow-(h-1))+b;
            end
            baseline(1,i) = sum(baselineT(:));
        elseif bs == 0
            baseline(1,i) = 0;
        end

        usefuls(1,i-1) = ((sum((IDat01(lefthigh:leftlow,i)))-
baseline(1,i)))*((wavelengths(lefthigh)-wavelengths(leftlow))/(leftlow-
lefthigh));
    end

    clear x* y* slope b baseline* h

    %% reordering the pixels into an image

    imagect(:,:) = reshape(usefuls(1,1:(192*192)),[192,192]);
```

```
    %% puting into the full picture
    OutputimageUR = imagect;

    figure(2)
    image(OutputimageUR,'CDataMapping','scaled')
    title('Absorbance Areas - pixel space')
    colorbar
    %   %%
    %     'draw a line on one of the vertical channel walls'
    %
    %     refI = OutputimageUR;
    %     [x, y] = getline(2);
    %     ang = 90 + atan2d(y(1,1)-y(2,1),x(1,1)-x(2,1));
    %     minF = min(min(refI));
    %     maxF = max(max(refI));
    %%
    Rot = OutputimageUR; %imrotate(refI, ang);
    %%
    %     'box channel width crossing the origin (0,0)'
    figure(101), image(Rot, 'CDataMapping','scaled')
    Rect = getrect(101); % xmin, ymin, width, height
    Iwidth = Rect(1,3);
    Iscale = Iwidth/chanwidth;
    close(101)
    [x,y] = size(Rot);
    clc

    Outputimage = Rot;

    IDat(1,1) = Iscale;
    IDat(2,1:4) = Rect;
    IDat(1,3) = x;
    IDat(1,4) = y;
    %     %
    %     figure(3)
    %     contourf(Outputimage)
    %     colorbar
    %%
    figure(111), image(Outputimage,'CDataMapping','scaled','Xdata',[(0-
Rect(1,1))*1/Iscale,(y-Rect(1,1))*1/Iscale], 'Ydata', [(0-
Rect(1,2))*1/Iscale,(x-Rect(1,2))*1/Iscale]), title('Absorbance Areas - ?m
space')
    xlabel('?m'), ylabel('?m')
    colorbar
end

%% Pull the fit from the profile and excel
%J = max(Outputimage, [], 2);
% Do the excel fitting in between these steps aka replace Fit with the new
data!
Fit = J;
% clear J

%% Pulling Epsi from a spectrum in the image

for i = 1:192
    SprayRegionC(i,:) = SprayRegion(i,:)/Fit(i,:);
```

```
end
%%
X = 99;
Y = 154;

Datapoint(:,2) = IDat01(:,Y+64*3*(X))./Fit(Y,1); % Y then X in the equation
Datapoint(:,1) = IDat01(:,1);

[xx,yy] = size(Datapoint(:,1));

% FInd the range bounds
j = 1;
k = 0;
while k == 0;
    if Datapoint(j,1) <= Range1H
        lefthigh = j;
        k = 1;
    else j = j+1;
    end
end
%
j = xx;
k = 0;
while k == 0;
    if Datapoint(j,1) >= Range1L
        leftlow = j;
        k = 1;
    else j = j-1;
    end
end

% doing the summation integral

ypoint1 = Datapoint(lefthigh,2);
ypoint2 = Datapoint(leftlow,2);
xpoint1 = Datapoint(lefthigh,1);
xpoint2 = Datapoint(leftlow,1);

slope = (ypoint1-ypoint2)/(xpoint1-xpoint2);
b = ypoint1 - slope*xpoint1;

if bs == 1

    for h = 1:(leftlow-lefthigh)
        baselineT(h,1) = Datapoint(leftlow-(h-1),1);
        baselineT(h,2) = slope*Datapoint(leftlow-(h-1),1)+b;
    end

    baseline = sum(baselineT(:,2));

elseif bs == 0

    for h = 1:(leftlow-lefthigh)
        baselineT(h,1) = Datapoint(leftlow-(h-1),1);
        baselineT(h,2) = 0;
    end
```

```
baseline = 0;
end

% Plotting the spectrum at that point
figure(10)
clf(10)
hold on

plot(Datapoint(:,1),Datapoint(:,2))
plot(baselineT(:,1),baselineT(:,2))

xlabel('Wavenumber')
ylabel('Absorbance')
set(gca,'XDir','reverse')

hold off
%
Area = (sum(Datapoint(lefthigh:leftlow,2))-baseline)*((Datapoint(lefthigh,1)-
Datapoint(leftlow,1))/(leftlow-lefthigh));
Epsi = Area/(chanheight*Conc)

clear image* j k l left* useful* xx yy zz i noS mike wave* ans ang maxF minF
Rot Iwidth refI

%% Converting to concentration!
Epsi = 1.3722; % 0.0964 for product - if you have calclated epsi from linear
spectra

OutputimageC = OutputimageF(:,:)./(Epsi*chanheight); %multiplied by
experimentally calculated extinction coefficient and channel height
%% showing concentration map for the wavelengths run prior in this script
figure(112), image(OutputimageC,'CDataMapping','scaled','Xdata',[(0-
IDat(2,1))*1/IDat(1,1),(IDat(1,4)-IDat(2,1))*1/IDat(1,1)], 'Ydata', [(0-
IDat(2,2))*1/IDat(1,1),(IDat(1,3)-IDat(2,2))*1/IDat(1,1)]),
title('Concentration - ?m space')
xlabel('?m'), ylabel('?m')
colorbar

figure(113), image(OutputimageC,'CDataMapping','scaled')
title('Concentration - pixel space')
xlabel('pixel'), ylabel('pixel')
colorbar
%% For the bound and unbound comparison!
figure(112), image(BOutputimageC,'CDataMapping','scaled','Xdata',[(0-
UBIDat(2,1))*1/UBIDat(1,1),(UBIDat(1,4)-UBIDat(2,1))*1/UBIDat(1,1)], 'Ydata',
[(0-UBIDat(2,2))*1/UBIDat(1,1),(UBIDat(1,3)-UBIDat(2,2))*1/UBIDat(1,1)]),
title('Concentration - ?m space')
xlabel('?m'), ylabel('?m')
colorbar

figure(113), image(BOutputimageC,'CDataMapping','scaled')
title('Concentration - pixel space')
xlabel('pixel'), ylabel('pixel')
colorbar
%
figure(114), image(UBOutputimageC,'CDataMapping','scaled','Xdata',[(0-
```

```
UBIDat(2,1))*1/UBIDat(1,1),(UBIDat(1,4)-UBIDat(2,1))*1/UBIDat(1,1)], 'Ydata',
[(0-UBIDat(2,2))*1/UBIDat(1,1),(UBIDat(1,3)-UBIDat(2,2))*1/UBIDat(1,1)]),
title('UB Concentration - ?m space')
xlabel('?m'), ylabel('?m')
colorbar
%%
figure(116), image(OutputimageR,'CDataMapping','scaled')
title('UB Concentration - pixel space')
xlabel('pixel'), ylabel('pixel')
colorbar
```

### A1.3 Extracting Relative Proportions from Gradient IR Data

The purpose of this code is to process the IR images of the gradient collected for Figure 5.2. This includes cropping and reshaping the data, baseline subtraction, and plotting either individual wavelengths or the sum of multiple wavelengths. Other post processing was included to do integration under the individual spectrum collected at each pixel and to plot the IR spectrum vs. position across the gradient in the form of a contour plot.

```
clc; clear all; close all;
 %% Import

RawLong = importdata('Extraction2.0.dpt');

%% extract wavelengths
Wavelengths = [RawLong(:,1);];

Q = size(RawLong);
Raw = RawLong(:,2:(Q(1,2)));

%% Averaging across multiple columns
Cdim = 64
Rdim = 11

AveRaw = [];

for i=1:Q(1,1)
    RawFull = reshape(Raw(i,:),Cdim,Rdim);
    RawT = transpose(RawFull);
    RawAvg = mean(RawT,1);
    AveRaw=[AveRaw; RawAvg];
end

%%  Plot the whole spectra and a single slice at the n position
```

```
figure(99)
hold on
contourf(Wavelengths(:,1), 1:length(AveRaw(1,:)), transpose(AveRaw),25);
xlabel('Position')
ylabel('Wavenumber (cm-1)')
xlim([1450 1800]);
hold off

%%
for n =  40 %:20 %Points(1,2);
    figure(98)
    plot(Wavelengths(:,1),transpose(AveRaw(:,n)),'b');
    xlabel('Wavenumber (cm-1)')
    ylabel('Absorbance (O.D.)')
    xlim([1450 1800]);
end

%% baseline correction

q = 12; %determined baseline position number
p1 = 1184;
p2 = 1099;

ValuesBC = zeros(length(AveRaw(:,1)), length(AveRaw(1,:)));

for k=1:Cdim

    dx = Wavelengths(p2,1)-Wavelengths(p1,1);
    dy = AveRaw(p2,k) - AveRaw(p1,k);
    m = dy/dx;
    b = AveRaw(p2,k) - m*Wavelengths(p2,1);

    testSlicebc(:,1)= AveRaw(:,k)-m*Wavelengths(:,1)-b;
    ValuesBC(:,k) = testSlicebc(:,1);
end

%%  Plot the corrected spectra and a single slice at the n position

figure(88)
hold on
contourf(Wavelengths(:,1), 1:length(ValuesBC(1,:)), transpose(ValuesBC),25);
xlabel('Position')
ylabel('Wavenumber (cm-1)')
xlim([1450 1800]);
hold off

%%
% clf(98)
% clf(89)
for n =  1:64 %:20 %Points(1,2);
    figure(98)
    hold on
    plot(Wavelengths(:,1),transpose(AveRaw(:,n)),'b');
    xlabel('Wavenumber (cm-1)')
    ylabel('Absorbance (O.D.)')
    % xlim([1400 1800]);
```

```
end

for n =  1:64 %:20 %Points(1,2);
    figure(89)
    hold on
    plot(Wavelengths(:,1),transpose(ValuesBC(:,n)),'b');
    xlabel('Wavenumber (cm-1)')
    ylabel('Absorbance (O.D.)')
    % xlim([1400 1800]);
end
%% Shrinking the selection size

Points = size(AveRaw);

LimL = 1114;
LimH = 1172;
A = Wavelengths(LimL(1,1),1)
B = Wavelengths(LimH(1,1),1)

Xt = [Wavelengths(LimL:LimH,1)];
X = transpose(Xt);

Yt = [1:Points(1,2)];
Y = transpose(Yt);

ValuesT = [ValuesBC(LimL:LimH,:)];
Valuest = transpose(ValuesT);

%% plotting the contours for the baseline subtracted section
figure(2)
hold on
contourf(Y,X,ValuesT,25);
xlabel('Position')
ylabel('Wavenumber (cm-1)')
hold off

%% Checking wavelentgh at a specific position

q = 2;

figure(4)
hold on
plot(X,ValuesT(:,q))
xlabel('Position')
ylabel('Absorbance (O.D.)')
hold off

%% plotting the abundance of the parts

figure(50)
hold on

plot(Y,AveRaw(1249,:), 'b')
plot(Y,mean(AveRaw(544:855,:),1), 'k')
plot(Y,ValuesBC(1139,:), 'c')
plot(Y,ValuesBC(1155,:), 'g')
```

```
plot(Y,ValuesBC(1155,:)+ValuesBC(1131,:), 'r')
xlabel('Position')
ylabel('Absorbance (O.D.)')
hold off

%% Normalization of the previous plot

figure(51)
hold on

plot(Y,AveRaw(1251,:)/max(AveRaw(1251,:)), 'b')
plot(Y,mean(AveRaw(544:855,:))/max(mean(AveRaw(544:855,:))), 'k')
plot(Y,ValuesBC(1139,:)/max(ValuesBC(1155,:)+ValuesBC(1139,:)), 'c')
plot(Y,ValuesBC(1155,:)/max(ValuesBC(1155,:)+ValuesBC(1139,:)), 'g')
plot(Y,(ValuesBC(1155,:)+ValuesBC(1139,:))/max(ValuesBC(1155,:)+ValuesBC(1139
,:)), 'r')

legend('D2O','DMSO','1668 cm^-^1','1620 cm^-^1', 'NMA', 'Location','Best')
xlabel('Position')
ylabel('Relative Concentration')
xlim([1 64])
ylim([-0.2 1.01])
hold off

%%
H2OValues(:,1) = Y;
H2OValues(:,2) = mean(AveRaw(544:855,:))/max(mean(AveRaw(544:855,:)));

plot(H2OValues(:,1),H2OValues(:,2))

%%
figure(44)
plot((H2OValues(20:64,2)), BSWave(I(20:yy),1),'k.','MarkerSize', 35)
set(gca,'XDir','reverse')
% legend('D2O','DMSO','1668 cm^-^1','1620 cm^-^1', 'NMA', 'Location','Best')
xlabel('^H2O^X')
ylabel('Lambda Max')

%% %%%%%%%%%%%%%%%%%%%%%%%%%%%%%%%%%%%%%%%%%%%%%%

[xx yy] = size(RawLong);

figure(88)
for i = 2:5:yy
    hold on
    plot(RawLong(:,1),RawLong(:,i))
end
hold off

%%
Range1H = 1700;
Range1L = 1600;

IDat01 = RawLong;

[xx,yy] = size(IDat01);
```

```
wavelengths = IDat01(:,1);

bs = 1;

% FInd the range bounds
j = 1;
k = 0;
while k == 0;
    if wavelengths(j) <= Range1H
        lefthigh = j;
        k = 1;
    else j = j+1;
    end
end
%
j = xx;
k = 0;
while k == 0;
    if wavelengths(j) >= Range1L
        leftlow = j;
        k = 1;
    else j = j-1;
    end
end

% doing the summation integral
usefuls = zeros(1,yy);

for i = 2:yy
    ypoint1 = IDat01(lefthigh,i);
    ypoint2 = IDat01(leftlow,i);
    xpoint1 = wavelengths(lefthigh,1);
    xpoint2 = wavelengths(leftlow,1);
    slope = (ypoint1-ypoint2)/(xpoint1-xpoint2);
    b = ypoint1 - slope*xpoint1;
%%
    if bs == 1
        for h = 1:(leftlow-lefthigh)
            baselineT(h,i) = slope*wavelengths(leftlow-(h-1))+b;
        end

        baseline(1,i) = sum(baselineT(:,i));
    elseif bs == 0
        baseline(1,i) = 0;
    end

    baselineTud = flipud(baselineT);
    BSLong(:,i) = IDat01(lefthigh:leftlow-1,i)-baselineTud(1:h,i);
end
BSWave = IDat01(lefthigh:leftlow-1,1);

clear x* yp* slope bs h b Range* xp* usef* i j k baseline*

[xx yy] = size(BSLong);

RSLong = reshape(BSLong(:,2:yy), xx,64,11);
```

```
for i = 1:xx
    for j = 1:64
        AveLong(i,j) = mean(RSLong(i, j,:));
    end
end

for i = 1:64
    NLong(:,i) = RSLong(:,i);
end

[xx yy] = size(NLong);

figure(89)
clf(89)
for i = 1:4:64
    hold on
    plot(BSWave(:,1),NLong(:,i))
end
hold off

rn = 1
[Y,I] = max(NLong(:,1:yy), [], 1);

figure(55)
clf(55)
hold on
contourf(rn:yy, BSWave(:,1), NLong(:,rn:yy),25)
% plot(rn:yy, BSWave(I(rn:yy),1),'r.','MarkerSize', 35)
```

### A1.4 Compilation Code

This code was designed for processing and spatially calibrating the channel photomask, the 4 visible images, and the time-space data. It also includes basic data analysis on the visible images identifying the gradient.

```
clc; clear all; close all
%% Set the analysis
% this allows you to only use selective parts of this code, if you want to
% use the part that is labeled, make that part equal to 1, if not, leave it
% a 0.
ZPhotomask = 0; %will allow alignment of the photomask file
ZVisRotate = 1; % will perform alignment on the 4 visible images
ZVisParameterFinder = 1; % this section will only work if visrotate is ran
previously
ZTimeFinder = 0; %will perform alignment on the time calibration data

chanwidth = 500;
```

```
Tau = 544; %ms

plot1 = 0; %Correct Coordinates for photomask
plot2 = 1; %Concentration Data: Center Fluid Fluorescence
plot3 = 1; %Concentration Data: Outer Fluid Fluorescence
plot4 = 0; %Time Data: Time Values
plot5 = 0; %Time Data: Intensity Values
plot6 = 0; %Time Data: Brightfield Values

Figures = [plot1, plot2, plot3, plot4, plot5, plot6];
clear plot*

%% import
if ZPhotomask == 1
    cd('/Users/michaelbarich/Copy/Krummel Group/Research/Compilation/Data')
    photomask = imread('plus20spray.tiff');
    photomask1 = im2uint16(photomask(:,:,1));

    'box channel width with upper edge crossing the spot (0,0)'

    [x,y] = size(photomask1);
    figure(101), image(photomask1,'CDataMapping','scaled'), title('photomask
- in pixel space')
    Rect = getrect(101); % xmin, ymin, width, height
    Mwidth = Rect(1,3);
    Mscale =Mwidth/chanwidth;
    MOutput = photomask1;

    close(101)
    %%
    figure(111), image(photomask1,'CDataMapping','scaled','Xdata',[(0-
Rect(1,1))*1/Mscale,(y-Rect(1,1))*1/Mscale], 'Ydata', [(0-
Rect(1,2))*1/Mscale,(x-Rect(1,2))*1/Mscale]), title('photomask - ?m space')
    xlabel('?m'), ylabel('?m')

    MDat(1,1) = Mscale;
    MDat(2,1:4) = Rect;
    MDat(1,3) = x;
    MDat(1,4) = y;

    clear photomask* Rect x y ans Mwidth Mscale
    clc
    close all
end
%% Visible portion %%%%%%%%%%%%%%%%%%%%%%%%%%%%%%%%
if ZVisRotate == 1

    cd('/Users/michaelbarich/Copy/Krummel Group/Research/Compilation/Data/10-
10')  %%%% Choose folder here

    fixed1  = imrotate(imread('VCBF.tif'),270); %brightfield for center
    moving1 = imrotate(imread('VOBF.tif'),270); %brightfield for outer
    fixedFR = imrotate(imread('VCF.tif'),270); %Fluorescence for center
    movingFR = imrotate(imread('VOF.tif'),270); %fluorescence for outer

    %%
```

```
    Min1 = min(min(nonzeros(fixedFR(:,:,1))));
    %     Max1 = max(max(VOutput(:,:,1)));
    Min3 = min(min(nonzeros(movingFR(:,:,1))));
    %     Max3 = max(max(VOutput(:,:,3)));

    fixedF = fixedFR(:,:) - Min1;
    movingF = movingFR(:,:) - Min3;

    %% for matching center to the outer starting with obtaining the edge
files
    fixed2 = edge(fixed1, 'sobel');
    moving2 = edge(moving1, 'sobel');

    % convert to uint16
    fixed = im2uint16(fixed2);
    moving = im2uint16(moving2);

    % View misaligned images
    figure(1), imshowpair(fixed, moving,'Scaling','joint');

    %% Get a configuration suitable for registering images from different
    % sensors.
    [optimizer, metric] = imregconfig('multimodal');

    % Tune the properties of the optimizer to get the problem to converge
    % on a global maxima and to allow for more iterations.
    optimizer.InitialRadius = 0.001;
    optimizer.Epsilon = 1.5e-4;
    optimizer.GrowthFactor = 1.01;
    optimizer.MaximumIterations = 300;

    %% Align the moving image with the fixed image
    tform = imregtform(moving, fixed, 'rigid', optimizer, metric);
    movingRegistered = imwarp(moving, tform, 'OutputView',
imref2d(size(fixed)));
    %% View registered images
    figure(2), imshowpair(fixed, movingRegistered,'Scaling','joint');
    %% find the scale for pixels to microns

    'box the channel width'

    Rect = getrect(2); % xmin, ymin, width, height
    Vwidth = Rect(1,3);
    Vscale = Vwidth/chanwidth;

    close(1)
    close(2)
    %% IDENTIFY CONVERSION

    movingRegistedF = imwarp(movingF, tform, 'OutputView',
imref2d(size(fixed)));
    movingRegistedG = imwarp(moving1, tform, 'OutputView',
imref2d(size(fixed)));
    %%
    %     figure(3), imshowpair(fixedF, movingRegistedF, 'scaling', 'joint');
    figure(4), imshowpair(fixed1, movingRegistedG, 'scaling', 'joint');
```

```
    %% Rotate to vertical
    'draw a line on one of the vertical channel walls'

    refI = fixed1;
    [x, y] = getline(4);
    ang = 90 + atan2d(y(1,1)-y(2,1),x(1,1)-x(2,1));
    minF = min(min(refI));
    maxF = max(max(refI));

    Rot = imrotate(refI, ang);
    %%
    'box channel width crossing the origin (0,0)'
    figure(101), image(Rot, 'CDataMapping','scaled')
    Rect = getrect(101); % xmin, ymin, width, height
    Vwidth = Rect(1,3);
    Vscale = Vwidth/chanwidth;
    close(101)
    %%
    [Vxx Vyy] = size(Rot)
    figure(103), image(Rot,'CDataMapping','scaled','Xdata',[(0-
Rect(1,1))*1/Vscale,(Vyy-Rect(1,1))*1/Vscale], 'Ydata', [(0-
Rect(1,2))*1/Vscale,(Vxx-Rect(1,2))*1/Vscale]), title('photomask - ?m space')
    xlabel('?m'), ylabel('?m')
    close(103)
    %% Transformed images consolidated
    %     [xx,yy] = size(Rot);

    VOutput = zeros(Vxx,Vyy,4);
    VOutput(:,:,1) = imrotate(fixedF(:,:),ang);
    VOutput(:,:,2) = imrotate(fixed1(:,:),ang);
    VOutput(:,:,3) = imrotate(movingRegistedF(:,:),ang);
    VOutput(:,:,4) = imrotate(movingRegistedG(:,:),ang);
    %     ConvV = tform(:,:);
    VDat(1,1) = Vscale;
    VDat(2,1:4) = Rect;
    VDat(1,3) = Vxx;
    VDat(1,4) = Vyy;

    clear Vscale Vwidth Vxx Vyy refI Rect ans
    clear fixed* moving* metric* optimizer* tform x y Rot ang maxF minF
end
%%
close all

%output is Output (1392x1040x2) which is the image with center, then image
%with outer fluids as the fluorescein

%% Vis Value finder...  Image Processing
if ZVisParameterFinder == 1
    plot11 = 0;
    plot12 = 0;
    plot13 = 0;
    [xx yy zz] = size(VOutput);
    ddfound = zeros(xx, yy, 2);
    dtfound = zeros(xx,7);

    threshH = 0.9;
```

```
    threshL = 0.35;

    for k = 1

        slicePositions = [1:1:(length(VOutput(:,:,1)))];
        slices = zeros(length(slicePositions), size(VOutput,2));
        %
        for i = 1:length(slicePositions)
            slices(i,:,1) = VOutput(slicePositions(i),:,1);

            if plot11 == 1
                figure(11)
                clf(11)

                figure(11)
                hold on
                plot(slices(i,:))
                hold off
            end
        end

        %output array: slices (1392x1040x2) which is the image with center,
then image
        %with outer fluids as the fluorescein

        % Normalize the data

        for i = 1:length(slicePositions); %for statement
            clear testSlice
            testSlice = slices(i,:);
            testSlicebc = testSlice;
            testSlicem = testSlicebc-(min(min(testSlicebc(:,:))));
            testSlicep = testSlicem./(max(testSlicem));

            %% Search for the width of the saturated (unmixed) component
            %leftedge
            thresh = threshH;  %%%%%%%%%%%%%%%%%%%%%%%%%%% high threshold
            j = 1;
            k = 0;
            while k == 0;
                if testSlicep(j) >= thresh
                    lefthigh = j;
                    k = 1;
                else j = j+1;
                end
            end
            %
            j = lefthigh;
            k = 0;
            while k == 0;
                if testSlicep(j) < thresh
                    leftlow = j;
                    k = 1;
                else j = j-1;
                end
            end
            % Calculate the slope
```

```
            leftslope = (testSlicep(lefthigh)-testSlicep(leftlow))/(lefthigh-
leftlow);
            b1 = testSlicep(lefthigh)-(leftslope*lefthigh);
            leftMax = (thresh-b1)/leftslope;
            %
            if plot12 == 1
                figure (12)
                hold on
                plot(testSlicep)

plot(leftlow,testSlicep(leftlow),'ro',lefthigh,testSlicep(lefthigh),'bo',left
Max, thresh,'go')
                hold off
            end
            %% same for rightedge
            j = numel(testSlicep);
            k = 0;
            while k == 0;
                if testSlicep(j) >= thresh
                    righthigh = j;
                    k = 1;
                else j = j-1;
                end
            end
            %
            j = righthigh;
            k = 0;
            while k == 0;
                if testSlicep(j) < thresh
                    rightlow = j;
                    k = 1;
                else j = j+1;
                end
            end
            % Calculate the slope
            rightslope = (testSlicep(righthigh)-
testSlicep(rightlow))/(righthigh-rightlow);
            b1 = testSlicep(righthigh)-(rightslope*righthigh);
            rightMax = (thresh-b1)/rightslope;
            %
            if plot12 == 1
                figure (12)
                hold on
                plot(testSlicep)

plot(rightlow,testSlicep(rightlow),'ro',righthigh,testSlicep(righthigh),'bo',
rightMax, thresh,'go')
                hold off
            end
            %% finding the lower threshold

            %leftedge
            thresh = threshL;  %%%%%%%%%%%%%%%%%%%%%%%%%% high threshold
            j = 1;
            k = 0;
            while k == 0;
                if testSlicep(j) >= thresh
                    lefthigh = j;
```

```
                k = 1;
            else j = j+1;
            end
        end
        %
        j = lefthigh;
        k = 0;
        while k == 0;
            if testSlicep(j) < thresh
                leftlow = j;
                k = 1;
            else j = j-1;
            end
        end
        % Calculate the slope
        leftslope = (testSlicep(lefthigh)-testSlicep(leftlow))/(lefthigh-
leftlow);
        b1 = testSlicep(lefthigh)-(leftslope*lefthigh);
        leftMin = (thresh-b1)/leftslope;
        %
        if plot12 == 1
            figure (12)
            hold on
            plot(testSlicep)

plot(leftlow,testSlicep(leftlow),'ro',lefthigh,testSlicep(lefthigh),'bo',left
Min, thresh,'go')
            hold off
        end

        %% same for rightedge
        j = numel(testSlicep);
        k = 0;
        while k == 0;
            if testSlicep(j) >= thresh
                righthigh = j;
                k = 1;
            else j = j-1;
            end
        end
        %
        j = righthigh;
        k = 0;
        while k == 0;
            if testSlicep(j) < thresh
                rightlow = j;
                k = 1;
            else j = j+1;
            end
        end
        % Calculate the slope
        rightslope = (testSlicep(righthigh)-
testSlicep(rightlow))/(righthigh-rightlow);
        b1 = testSlicep(righthigh)-(rightslope*righthigh);
        rightMin = (thresh-b1)/rightslope;
        %%
        if plot12 == 1
            figure (12)
```

```
                hold on
                plot(testSlicep)

plot(rightlow,testSlicep(rightlow),'ro',righthigh,testSlicep(righthigh),'bo',
rightMin, thresh,'go')
                hold off
            end

            %% finding the max point
            threshMax = max(testSlicep(:));
            j = 1;
            k = 0;
            while k == 0;
                if testSlicep(j) == threshMax
                    centerMax = j;
                    k = 1;
                else j = j+1;
                end
            end
            if plot12 == 1
                figure (12)
                hold on
                plot(testSlicep)
                plot(centerMax,threshMax,'ko')
                hold off
            end
            %% calculating the width of the spray

            spraywidthRight = (rightMax - rightMin)/-VDat(1,1);
            spraywidthLeft = (leftMax - leftMin)/VDat(1,1);

            if plot13 == 1
                figure (13)
                hold on
                plot(i,spraywidthRight,'ro',i,spraywidthLeft,'bo')
                hold off
            end
            %% saving these points

            ddfound(i,:,1) = testSlice;
            ddfound(i,:,2) = testSlicep;

            dtfound(i,1) = centerMax;
            dtfound(i,2) = leftMax;
            dtfound(i,3) = rightMax;
            dtfound(i,4) = leftMin;
            dtfound(i,5) = rightMin;
            dtfound(i,6) = spraywidthLeft;
            dtfound(i,7) = spraywidthRight;


        end

        clear left* right* j k b1 center* thresh test* threshMax slice*
    end
end
figure (7)
```

```
hold on
image(ddfound(:,:,2),'CDataMapping','scaled')
plot(dtfound(1:length(dtfound),2),1:length(dtfound),'c','MarkerSize', 20)
plot(dtfound(1:length(dtfound),4),1:length(dtfound),'k','MarkerSize', 20)
plot(dtfound(1:length(dtfound),3),1:length(dtfound),'c','MarkerSize', 20)
plot(dtfound(1:length(dtfound),5),1:length(dtfound),'k','MarkerSize', 20)

hold off

figure (6)
clf(6)
hold on
plot(1:length(dtfound),dtfound(:,6),'ro',1:length(dtfound),
dtfound(:,7),'bo')
% plot(1:length(dtfound),dtfound(:,3),'ro',1:length(dtfound),
dtfound(:,5),'bo')
xlabel('pixels'), ylabel('?m')
hold off

%%%%%%%%%%%%%%%%%%%%%%%%%%%%%%%%%%%%%%%%%%%%%%%%%%%%%%%%%%%%%%%%%%%%%%%%%%%%%%%%
%%%%%%%%%%
%% Time Calibration
if ZTimeFinder == 1
    % DATA IMPORT
    for TPosition = 1:3

        TBlank = imrotate(imread('BLANK.bmp'),270);

        if TPosition==3
            j = 1;
            TFlow = imrotate(imread('TAFF.bmp'),270);
            TNoFlow = imrotate(imread('TA0F.bmp'),270);
            TBF = imrotate(imread('TA0B.bmp'),270);
        elseif TPosition==2
            j = 2;
            TFlow = imrotate(imread('TBFF.bmp'),270);
            TNoFlow = imrotate(imread('TB0F.bmp'),270);
            TBF = imrotate(imread('TB0B.bmp'),270);
        elseif TPosition==1
            j = 3;
            TFlow = imrotate(imread('TCFF.bmp'),270);
            TNoFlow = imrotate(imread('TC0F.bmp'),270);
            TBF = imrotate(imread('TC0B.bmp'),270);
        end

        TFlowBS = TFlow(:,:) - TBlank(:,:);
        TNoFlowBS = TNoFlow(:,:) - TBlank(:,:);
        TBFBS = TBF(:,:) - TBlank(:,:);

        Tinput(:,:,j) = TFlowBS;
        Tinput(:,:,3+j) = TBFBS;
        Tinput(:,:,6+j) = TNoFlowBS;

        clear TBlank TFlow* TNo* TPos* j TBF*
    end
```

```
%% Rotate

'draw a line on one of the vertical channel walls'
refI = Tinput(:,:,4);
figure(14), image(refI,'CDataMapping','scaled');

[x, y] = getline(14);
ang = 90 + atan2d(y(1,1)-y(2,1),x(1,1)-x(2,1));
minF = min(min(refI));
maxF = max(max(refI));

TinputRot = double(imrotate(Tinput(:,:,:), ang));

close(14)

%% Doing the time calibration

TValues = TinputRot(:,:,3);

'box the initial intensity points'

figure(23), image(TValues);
e = imrect;
BW = createMask(e);
I_mean =  mean(TValues(BW));
IntInt = I_mean; %  IntInt = 90;

%%
TOutput = zeros(size(TinputRot));
for j = 1:3

    TOutput(:,:,j) = -Tau*log(TinputRot(:,:,j)./IntInt);
    figure(32+j), image(TOutput(:,:,j),'CDataMapping','scaled');
    TOutput(:,:,3+j) = TinputRot(:,:,j);
    TOutput(:,:,6+j) = TinputRot(:,:,3+j);
end
close(23)

%%
clc
'box the channel width with top edge at (0,0)'
[xxx,yyy] = size(TOutput(:,:,1));

for j = 1:3
    figure(101), image(TOutput(:,:,6+j), 'CDataMapping','scaled')
    Rect = getrect(101); % xmin, ymin, width, height
    Twidth(:,:) = Rect(1,3);
    Tscale = Twidth/chanwidth;
    close(101)

    %%
    TDat(1,1,j) = Tscale;
    TDat(2,1:4,j) = Rect;
    TDat(1,3,j) = xxx;
    TDat(1,4,j) = yyy;
end
```

```
    close all
    clc
    clear j clear ans Tinput* Tscale Twidth
    clear BW e he* I* m* n* Rec* TP* um* x* X* y* Y* TV* TBlank TFlow TNoFlow
TBF
    clear TNoFlowHist TNFHist* FlowTime TFlowBS TNoFlowBS x* y* Rot ang maxF
minF refI
end

%% %%%%%%%%%%%%%%% %% Identifying points within all worked up data
%% This is the scaled photomask figure
if Figures(1,1) == 1
    figure(1000), image(MOutput,'CDataMapping','scaled','Xdata',[(0-
MDat(2,1))*1/MDat(1,1),(MDat(1,4)-MDat(2,1))*1/MDat(1,1)], 'Ydata', [(0-
MDat(2,2))*1/MDat(1,1),(MDat(1,3)-MDat(2,2))*1/MDat(1,1)]), title('Photomask
- ?m space')
    xlabel('?m'), ylabel('?m')
end
%% This is the scaled Visible images of both inner and outer fluorescence
if Figures(1,2) == 1
    figure(1002), image(VOutput(:,:,2),'CDataMapping','scaled','Xdata',[(0-
VDat(2,1))*1/VDat(1,1),(VDat(1,4)-VDat(2,1))*1/VDat(1,1)], 'Ydata', [(0-
VDat(2,2))*1/VDat(1,1),(VDat(1,3)-VDat(2,2))*1/VDat(1,1)]), title('visible -
?m space')
    xlabel('?m'), ylabel('?m')
end
if Figures(1,3) == 1
    figure(1003), image(VOutput(:,:,4),'CDataMapping','scaled','Xdata',[(0-
VDat(2,1))*1/VDat(1,1),(VDat(1,4)-VDat(2,1))*1/VDat(1,1)], 'Ydata', [(0-
VDat(2,2))*1/VDat(1,1),(VDat(1,3)-VDat(2,2))*1/VDat(1,1)]), title('visible -
?m space')
    xlabel('?m'), ylabel('?m')
end
%%
for j = 1:3
    if Figures(1,4) == 1
        figure(1006+j),
image(TOutput(:,:,j),'CDataMapping','scaled','Xdata',[(0-
TDat(2,1,j))*1/TDat(1,1,j),(TDat(1,4,j)-TDat(2,1,j))*1/TDat(1,1,j)], 'Ydata',
[(0-TDat(2,2,j))*1/TDat(1,1,j),(TDat(1,3,j)-
TDat(2,2,j))*1/TDat(1,1,j)]),colorbar,title('Time Values - ?m space')
        xlabel('?m'), ylabel('?m')
    end
    if Figures(1,5) == 1
        figure(1016+j),
image(TOutput(:,:,j+3),'CDataMapping','scaled','Xdata',[(0-
TDat(2,1,j))*1/TDat(1,1,j),(TDat(1,4,j)-TDat(2,1,j))*1/TDat(1,1,j)], 'Ydata',
[(0-TDat(2,2,j))*1/TDat(1,1,j),(TDat(1,3,j)-
TDat(2,2,j))*1/TDat(1,1,j)]),colorbar,title('Time Intensity - ?m space')
        xlabel('?m'), ylabel('?m')
    end

    if Figures(1,6) == 1
        figure(1026+j),
image(TOutput(:,:,j+6),'CDataMapping','scaled','Xdata',[(0-
TDat(2,1,j))*1/TDat(1,1,j),(TDat(1,4,j)-TDat(2,1,j))*1/TDat(1,1,j)], 'Ydata',
[(0-TDat(2,2,j))*1/TDat(1,1,j),(TDat(1,3,j)-
TDat(2,2,j))*1/TDat(1,1,j)]),colorbar,title('Time Intensity - ?m space')
```

```
        xlabel('?m'), ylabel('?m')
    end

end
clear j
%% %%%%%%% Plot profile of concentration gradient

figure(2000), imshowpair(VOutput(:,:,1),VOutput(:,:,3), 'scaling',
'joint','colorchannels', [1,0,2]);
%%
improfile

%%
figure (6)
hold on
plot(1:length(dtfound),dtfound(:,6),'ro',1:length(dtfound),
dtfound(:,7),'bo')
% plot(1:length(dtfound),dtfound(:,3),'ro',1:length(dtfound),
dtfound(:,5),'bo')
hold off
%%
[xx yy] = size(ddfound(:,:,2));
figure (7)
hold on
image(ddfound(:,:,2),'CDataMapping','scaled')
plot(dtfound(1:length(dtfound),2),1:length(dtfound),'r','MarkerSize', 20)
plot(dtfound(1:length(dtfound),4),1:length(dtfound),'b','MarkerSize', 20)
plot(dtfound(1:length(dtfound),3),1:length(dtfound),'r','MarkerSize', 20)
plot(dtfound(1:length(dtfound),5),1:length(dtfound),'b','MarkerSize', 20)
set(gca,'YDir','reverse')
xlim([0 yy])
ylim([0 xx])
hold off
%% This is the Visible images of both inner and outer fluorescence
figure(1012), image(VOutput(:,:,2),'CDataMapping','scaled')
xlabel('pixel'), ylabel('pixel')

figure(1013), image(VOutput(:,:,4),'CDataMapping','scaled')
xlabel('pixel'), ylabel('pixel')
```

### A1.5 Kinetic Analysis Code with Predictive Products

The purpose of this code was to process the IR images collected for the Kinetics extraction. It would process an IR image similar to the previous method, then break down that information to identify the position of the gradient similar to the method for processing the visible images. From here, it would extrapolate the concentration of each of the initial solutions and use them to

predict the concentration of the product of the reaction. This code would also process the raw data to produce a concentration map of the product, and isolate the area such that individual streamlines could be extracted for rate identification in Excel.

```
% clc; clear all; close all
%% Set the analysis
% this allows you to only use selective parts of this code, if you want to
% use the part that is labeled, make that part equal to 1, if not, leave it
% a 0.
ZVisRotate = 1;
ZVisParameterFinder = 1; % this section will only work if visrotate is ran
previously

chanwidth = 500;

plot1 = 0; %Correct Coordinates for photomask
plot2 = 1; %Concentration Data: Center Fluid Fluorescence
plot3 = 1; %Concentration Data: Outer Fluid Fluorescence

Figures = [plot1, plot2, plot3];
clear plot*

%% Transformed images consolidated
[Vxx,Vyy] = size(BOutputimageC);

VOutput = zeros(Vxx,Vyy,2);
VOutput(:,:,1) = BOutputimageC(:,:);
VOutput(:,:,2) = UBOutputimageC;

VDat = BIDat;

%% Vis Value finder...  Image Processing
if ZVisParameterFinder == 1
    plot11 = 0;
    plot12 = 0;
    plot13 = 0;

    [xx yy zz] = size(VOutput);
    ddfound = zeros(xx, yy, 2);
    dtfound = zeros(xx,7);

    threshH = 0.75;
    threshL = 0.16;
    %
    for l = 1

        slicePositions = [1:1:(length(VOutput(:,:,2)))];
        slices = zeros(length(slicePositions), size(VOutput,2));
        %
        for i = 1:length(slicePositions)
```

```
            slices(i,:,1) = VOutput(slicePositions(i),:,2);

            if plot11 == 1
                figure(11)
                %                 clf(11)

                figure(11)
                hold on
                plot(slices(i,:))
                hold off
            end
        end

        %output array: slices (1392x1040x2) which is the image with center,
then image
        %with outer fluids as the fluorescein

        %% Normalize the data

        for i = 1:length(slicePositions); %for statement
            clear testSlice
            testSlice = slices(i,:);
            testSlicebc = testSlice;
            testSlicem = testSlicebc;%-(min(min(testSlicebc(:,:))));
            testSlicep = testSlicem./(max(testSlicem));

            %% Search for the width of the saturated (unmixed) component
            %leftedge
            thresh = threshH;  %%%%%%%%%%%%%%%%%%%%%%%%%%% high threshold
            j = 1;
            k = 0;
            while k == 0;
                if testSlicep(j) >= thresh
                    lefthigh = j;
                    k = 1;
                else j = j+1;
                end
            end
            %%
            j = lefthigh;
            k = 0;
            while k == 0;
                if testSlicep(j) < thresh
                    leftlow = j;
                    k = 1;
                else j = j-1;
                end
            end
            %% Calculate the slope
            leftslope = (testSlicep(lefthigh)-testSlicep(leftlow))/(lefthigh-
            leftlow);
            b1 = testSlicep(lefthigh)-(leftslope*lefthigh);
            leftMax = (thresh-b1)/leftslope;
            %
            if plot12 == 1
                figure (12)
                hold on
```

```
                plot(testSlicep)

plot(leftlow,testSlicep(leftlow),'ro',lefthigh,testSlicep(lefthigh),'bo',left
Max, thresh,'go')
                hold off
            end
            %% same for rightedge
            j = numel(testSlicep);
            k = 0;
            while k == 0;
                if testSlicep(j) >= thresh
                    righthigh = j;
                    k = 1;
                else j = j-1;
                end
            end
            %%
            j = righthigh;
            k = 0;
            while k == 0;
                if testSlicep(j) < thresh
                    rightlow = j;
                    k = 1;
                else j = j+1;
                end
            end
            % Calculate the slope
            rightslope = (testSlicep(righthigh)-testSlicep(rightlow))
/(righthigh-rightlow);
            b1 = testSlicep(righthigh)-(rightslope*righthigh);
            rightMax = (thresh-b1)/rightslope;
            %
            if plot12 == 1
                figure (12)
                hold on
                plot(testSlicep)

plot(rightlow,testSlicep(rightlow),'ro',righthigh,testSlicep(righthigh),'bo',
rightMax, thresh,'go')
                hold off
            end
            %% finding the lower threshold

            %leftedge
            thresh = threshL;  %%%%%%%%%%%%%%%%%%%%%%%%%%%% high threshold
            j = 1;
            k = 0;
            while k == 0;
                if testSlicep(j) >= thresh
                    lefthigh = j;
                    k = 1;
                else j = j+1;
                end
            end
            %
            j = lefthigh;
            k = 0;
            while k == 0;
```

```
                if testSlicep(j) < thresh
                    leftlow = j;
                    k = 1;
                else j = j-1;
                end
            end
            % Calculate the slope
            leftslope = (testSlicep(lefthigh)-testSlicep(leftlow))/(lefthigh-
leftlow);
            b1 = testSlicep(lefthigh)-(leftslope*lefthigh);
            leftMin = (thresh-b1)/leftslope;
            %
            if plot12 == 1
                figure (12)
                hold on
                plot(testSlicep)

plot(leftlow,testSlicep(leftlow),'ro',lefthigh,testSlicep(lefthigh),'bo',left
Min, thresh,'go')
                hold off
            end

            %% same for rightedge
            j = numel(testSlicep);
            k = 0;
            while k == 0;
                if testSlicep(j) >= thresh
                    righthigh = j;
                    k = 1;
                else j = j-1;
                end
            end
            %
            j = righthigh;
            k = 0;
            while k == 0;
                if testSlicep(j) < thresh
                    rightlow = j;
                    k = 1;
                else j = j+1;
                end
            end
            % Calculate the slope
            rightslope = (testSlicep(righthigh)-
testSlicep(rightlow))/(righthigh-rightlow);
            b1 = testSlicep(righthigh)-(rightslope*righthigh);
            rightMin = (thresh-b1)/rightslope;
            %%
            if plot12 == 1
                figure (12)
                hold on
                plot(testSlicep)

plot(rightlow,testSlicep(rightlow),'ro',righthigh,testSlicep(righthigh),'bo',
rightMin, thresh,'go')
                hold off
            end
```

```
            %% finding the max point
            threshMax = max(testSlicep(:));
            j = 1;
            k = 0;
            while k == 0;
                if testSlicep(j) == threshMax
                    centerMax = j;
                    k = 1;
                else j = j+1;
                end
            end
            if plot12 == 1
                figure (12)
                hold on
                plot(testSlicep)
                plot(centerMax,threshMax,'ko')
                hold off
            end
            %% calculating the width of the spray

            spraywidthRight = (rightMax - rightMin)/-VDat(1,1);
            spraywidthLeft = (leftMax - leftMin)/VDat(1,1);

            if plot13 == 1
                figure (13)
                hold on
                plot(i,spraywidthRight,'ro',i,spraywidthLeft,'bo')
                hold off
            end
            %% saving these points

            ddfound(i,:,1) = testSlice;
            ddfound(i,:,2) = testSlicep;

            dtfound(i,1) = centerMax;
            dtfound(i,2) = leftMax;
            dtfound(i,3) = rightMax;
            dtfound(i,4) = leftMin;
            dtfound(i,5) = rightMin;
            dtfound(i,6) = spraywidthLeft;
            dtfound(i,7) = spraywidthRight;


        end

        clear left* right* j k b1 center* thresh test* threshMax slice*
    end
end
%
smoothed(:,1) = smooth(dtfound(:,2),10);
smoothed(:,2) = smooth(dtfound(:,4),10);

%plotting the points found from the spray width onto the product
%concentration map (smoothed)

figure (7)
```

```
hold on
% image(ddfound(:,:,2),'CDataMapping','scaled')
image(VOutput(:,:,1),'CDataMapping','scaled')
plot(smoothed(:,1),1:length(dtfound),'c','MarkerSize', 20)
plot(smoothed(:,2),1:length(dtfound),'k','MarkerSize', 20)
% plot(dtfound(1:length(dtfound),3),1:length(dtfound),'c','MarkerSize', 20)
% plot(dtfound(1:lenset(gca,'YDir','reverse')
xlim([0 yy])
ylim([0 xx])
hold off

%% plotting the spray width
figure (6)
clf(6)
hold on
plot(1:length(dtfound),dtfound(:,6),'ro',1:length(dtfound),
dtfound(:,7),'bo')
% plot(1:length(dtfound),dtfound(:,3),'ro',1:length(dtfound),
dtfound(:,5),'bo')
xlabel('pixels'), ylabel('?m')
hold off

%%

rounded(1:128,1) = round(smoothed(1:128,1));
rounded(1:128,2) = round(smoothed(1:128,2));
rounded(129:192,1) = round(smoothed(129:192,1))-1;
rounded(129:192,2) = round(smoothed(129:192,2))-1;

%% the spray width shown on the product concentration
figure (7)
hold on
% image(ddfound(:,:,2),'CDataMapping','scaled')
image(VOutput(:,:,1),'CDataMapping','scaled')
plot(rounded(:,1),1:length(dtfound),'r','MarkerSize', 20)
plot(rounded(:,2),1:length(dtfound),'b','MarkerSize', 20)
% plot(dtfound(1:length(dtfound),3),1:length(dtfound),'k','MarkerSize', 20)
% plot(dtfound(1:length(dtfound),5),1:length(dtfound),'c','MarkerSize', 20)
set(gca,'YDir','reverse')
xlim([0 yy])
ylim([0 xx])
hold off

%% the spray width shown on the middle concentration
figure (71)
hold on
image(ddfound(:,:,2),'CDataMapping','scaled')
% image(VOutput(:,:,1),'CDataMapping','scaled')
plot(rounded(:,1),1:length(dtfound),'r','MarkerSize', 20)
plot(rounded(:,2),1:length(dtfound),'b','MarkerSize', 20)
% plot(dtfound(1:length(dtfound),3),1:length(dtfound),'k','MarkerSize', 20)
% plot(dtfound(1:length(dtfound),5),1:length(dtfound),'c','MarkerSize', 20)
set(gca,'YDir','reverse')
xlim([0 yy])
ylim([0 xx])
hold off
```

```
%%
SprayRegion = zeros(length(dtfound),10+max(max(rounded(:,1)-rounded(:,2))));

[x y] = size(SprayRegion);

for l = 1:length(dtfound)

    width(l) = rounded(l,1)-rounded(l,2)+10;
    width2(l) = rounded(l,1)-rounded(l,2);
    offset(l) = floor((y - width(l))/2);
    offset2(l) = floor((y - width2(l))/2);
    SprayRegion(l,(1:width(l)+1)+offset(l)) = VOutput(l,(rounded(l,2)-
5):(rounded(l,1)+5),1);
    SprayRegionbound(1,l) = (1+1)+offset2(l);
    SprayRegionbound(2,l) = (width2(l)+1)+offset2(l);

end
%%
figure(8)
hold on
image(SprayRegionC, 'CDataMapping', 'scaled')
plot(smooth(SprayRegionbound(1,:)),1:length(SprayRegionbound),'K','MarkerSize
', 20)
plot(smooth(SprayRegionbound(2,:)),1:length(SprayRegionbound),'k','MarkerSize
', 20)
xlabel('pixels'), ylabel('pixels')
legend('(LEFT) 16%','(RIGHT) 75%','Location','NorthWest')
set(gca,'YDir','reverse')
xlim([1 y])
ylim([29 x])
hold off
%%
figure(16)
clf(16)
hold on

for l = 1:y
    plot(SprayRegionC(:,l))
end
xlabel('pixels'), ylabel('absorbance')
hold off
%%

clear ans chanwidth i l plot1* spraywidth* xx yy ZVis* zz

%% Concentrations of A and B
for l = 1:x

    m(l) = (threshH-threshL)/(width2(l));
    b(l) = threshL-m(l)*SprayRegionbound(1,l);
    %%
    for i = 1:y
        perct(l) = m(l)*i+b(l);

        if perct(l) < 0
            TheoreticalA(l,i) = 0;
```

```
        elseif perct(l) > 1
            TheoreticalA(l,i) = 1;
        else
            TheoreticalA(l,i) = perct(l);
        end
    end
end

TheoreticalB = 1-TheoreticalA;

ConcOuter = 1.0777;
ConcInner = 1.1112;

TheoreticalAC = TheoreticalA*ConcInner;
TheoreticalBC = TheoreticalB*ConcOuter;

% figure(9)
% image(TheoreticalA, 'CDataMapping', 'scaled')
% figure(10)
% image(TheoreticalB, 'CDataMapping', 'scaled')

% Coefficients
for  l = 1:x
    for i = 1:y
        A = 54.9923; % this is the k coefficient 54.9923 for 2; 26.9 for 1
        B(l,i) = -(A*TheoreticalAC(l,i)+A*TheoreticalBC(l,i)+1);
        C(l,i) = A*TheoreticalAC(l,i)*TheoreticalBC(l,i);

        TheoreticalProdC(l,i) = (-B(l,i)-((B(l,i))^2-4*A*C(l,i))^0.5)/(2*A);
        PerctDiff(l,i) = (TheoreticalProdC(l,i)-
SprayRegion(l,i));%/(TheoreticalProdC(l,i)+.000001);
    end
end
%%
figure(11)
hold on
image(TheoreticalProdC, 'CDataMapping', 'scaled')
plot(smooth(SprayRegionbound(1,:)),1:length(SprayRegionbound),'K','MarkerSize
', 20)
plot(smooth(SprayRegionbound(2,:)),1:length(SprayRegionbound),'k','MarkerSize
', 20)
xlabel('pixels'), ylabel('pixels')
legend('(LEFT) 16%','(RIGHT) 75%','Location','NorthWest')
set(gca,'YDir','reverse')
xlim([1 y])
ylim([29 x])
hold off


%%
figure(12)
% clf(12)
hold on

for l = 1:8:x
    %     plot(1:y, TheoreticalProdC(l,:))
```

```
    plot(1:y+1, SprayRegion(l,:))
    %     plot(TheoreticalProdC(:,l))
end

hold off

%% %%%%%%%%%%%%%%%%%%%%%%%%%%%%%%%%%%%%%%%%%%%%%%%%%%%%%%%%%%%%%%%%%%%%%%%%%%%
% Defining the difference
% imshowpair(TheoreticalProdC(:,:), SprayRegion(:,1:18), 'scaling',
'joint','colorchannels', [1,0,2])
%%
% PerctDiff(l,i) = (TheoreticalProdC(l,i)-
SprayRegion(l,i))/(TheoreticalProdC(l,i)+.000001);
figure(13)
image(PerctDiff, 'CDataMapping', 'scaled')
xlabel('pixels'), ylabel('pixels')
legend('(LEFT) 16%','(RIGHT) 75%','Location','NorthWest')
set(gca,'YDir','reverse')
xlim([1 y])
ylim([29 x])
hold off

%%
figure(13)
clf(13)
hold on

plot((1:16)/0.3572, Plots1(1,:),'ro')
plot((1:16)/0.3572, Plots1(2,:),'bo')
plot((1:16)/0.3572, Plots1(3,:),'go')
plot((1:16)/0.3572, Plots1(1,:),'r')
plot((1:16)/0.3572, Plots1(2,:),'b')
plot((1:16)/0.3572, Plots1(3,:),'g')

xlabel('?m across gradient'), ylabel('Concentration [M]')
legend('Predicted','Initial','At the end of the Image')
%%
figure(14)
clf(14)
hold on

plot((1:16)/0.3572, Plots1(4,:),'ko-')
%   plot(1:16, Plots1(2,:),'bo')
%    plot(1:16, Plots1(3,:),'go')
%     plot(1:16, Plots1(1,:),'r')
%   plot(1:16, Plots1(2,:),'b')
%    plot(1:16, Plots1(3,:),'g')

xlabel('?m across gradient'), ylabel('Rate [M]/s')
legend('Observed Rate')
```

### A1.6 Independent Time Processing Code

The purpose of this code is to transform the intensity tiff files that are captured in the time-space mapping fluorescence microscope into raw version of publishable figures depicting the travel time from the second nozzle for the fluid.

```
clc; clear all; close all
%% Set the analysis

chanwidth = 500;
Tau = 544; %ms

plot1 = 0; %Correct Coordinates for photomask
plot2 = 0; %Concentration Data: Center Fluid Fluorescence
plot3 = 0; %Concentration Data: Outer Fluid Fluorescence
plot4 = 1; %Time Data: Time Values
plot5 = 0; %Time Data: Intensity Values
plot6 = 1; %Time Data: Brightfield Values

Figures = [plot1, plot2, plot3, plot4, plot5, plot6];
clear plot*

%%%%%%%%%%%%%%%%%%%%%%%%%%%%%%%%%%%%%%%%%%%%%%%%%%%%%%%%%%%%%%%%%%%%%%%
%% Time Calibration

    cd('/Users/michaelbarich/Copy/Krummel Group/Research/Time Resolved
Fluorescence/2016-03-09/Newest Design/Raw')  %%%% Choose folder here
    TBlank = imrotate(imread('Image_0003.tif'),270);
    TimageR = imrotate(imread('Image_0006.tif'),270);

    Timage = TimageR; % - TBlank;

%     figure(1), image(Timage, 'CDataMapping','scaled')
%     figure(2), image(TimageR, 'CDataMapping','scaled')
%     figure(3), image(TBlank, 'CDataMapping','scaled')

     %% Doing the time calibration

    'box the background intensity '

    figure(23), image(Timage, 'CDataMapping','scaled');

    e = imrect;
    BW = createMask(e);
    I_mean =  mean(Timage(BW));
    BACKGROUND = I_mean; %  IntInt = 90;
    TValues = Timage-BACKGROUND;
    close(23)
```

```
%% Rotate
    'draw a line on one of the vertical channel walls'
    refI = TimageR;
    figure(14), image(refI,'CDataMapping','scaled');

    [x, y] = getline(14);
    ang = 90 + atan2d(y(1,1)-y(2,1),x(1,1)-x(2,1));
    minF = min(min(refI));
    maxF = max(max(refI));

    TValuesBS = double(imrotate(TValues, ang));

    close(14)

    %% Doing the time calibration

    'box the initial intensity points'

    figure(23), image(TValuesBS, 'CDataMapping','scaled');

    e = imrect;
    BW = createMask(e);
    I_mean =  mean(TValuesBS(BW));
    IntInt = I_mean; %  IntInt = 90;

    close(23)

    %%
    TOutput = zeros(size(TValuesBS));

        TOutput(:,:) = -Tau*log(TValuesBS(:,:)./(IntInt));
        figure(32), image(TOutput(:,:),'CDataMapping','scaled');

    %%
    clc
    'box the channel width with top edge at (0,0)'
    [xxx,yyy] = size(TOutput(:,:));


        figure(101), image(TOutput(:,:), 'CDataMapping','scaled')
        Rect = getrect(101); % xmin, ymin, width, height
        Twidth(:,:) = Rect(1,3);
        Tscale = Twidth/chanwidth;
        close(101)

        %
        TDat(1,1) = Tscale;
        TDat(2,1:4) = Rect;
        TDat(1,3) = xxx;
        TDat(1,4) = yyy;
    %%
    close all
    clc
    clear j clear ans Tinput* Tscale Twidth
    clear BW e he* I* m* n* Rec* TP* um* x* X* y* Y* TV* TBlank TFlow TNoFlow
```

```
TBF
    clear TNoFlowHist TNFHist* FlowTime TFlowBS TNoFlowBS x* y* Rot ang maxF
minF refI


%% %%%%%%%%%%%%%% %% Identifying points within all worked up data
%
    if Figures(1,4) == 1
        figure(1006), image(TOutput(:,:),'CDataMapping','scaled','Xdata',[(0-
TDat(2,1))*1/TDat(1,1),(TDat(1,4)-TDat(2,1))*1/TDat(1,1)], 'Ydata', [(0-
TDat(2,2))*1/TDat(1,1),(TDat(1,3)-
TDat(2,2))*1/TDat(1,1)]),colorbar,title('Time Values - ?m space')
        xlabel('?m'), ylabel('?m')
    end

%% %%%%%% Plot profile of concentration gradient

figure(1106)
hold on
image(Subset, 'CDataMapping', 'scaled')
plot(smooth(rounded(:,1)*(456/192)),1:(456/192):length(Subset),'K','MarkerSiz
e', 20)
plot(smooth(rounded(:,2)*(456/192)),1:(456/192):length(Subset),'r','MarkerSiz
e', 20)
%
plot(dtfound(1:length(dtfound),3)*(456/192),1:(456/192):length(Subset),'k','M
arkerSize', 20)
%
plot(dtfound(1:length(dtfound),5)*(456/192),1:(456/192):length(Subset),'c','M
arkerSize', 20)

xlabel('pixels'), ylabel('pixels')
legend('(LEFT) 16%','(RIGHT) 75%','Location','NorthWest')
set(gca,'YDir','reverse')
% xlim([1 y])
% ylim([29 x])
hold off

%%
TimeRound = (456/192)*round(imresize(rounded, [length(Subset) 2]));
TimeRegion = zeros(length(Subset),round(10+max(max(TimeRound(:,1)-
TimeRound(:,2))))+1);

[x y] = size(TimeRegion);
 %
for l = 1:length(Subset)

    width(l) = TimeRound(l,1)-TimeRound(l,2)+10;
    width2(l) = TimeRound(l,1)-TimeRound(l,2);
    offset(l) = floor((y - width(l))/2);
    offset2(l) = floor((y - width2(l))/2);
    TimeRegion(l,(1:(width(l)+1))+offset(l)) = Subset(l,(TimeRound(l,2)-
5):(TimeRound(l,1)+5));
    TimeRegionbound(1,l) = (1+1)+offset2(l);
    TimeRegionbound(2,l) = (width2(l)+1)+offset2(l);
```

```
end
%%
figure(8)
clf(8)
hold on
image(TimeRegion, 'CDataMapping', 'scaled')
plot(smooth(TimeRegionbound(1,:)),1:length(TimeRegionbound),'k','MarkerSize',
20)
plot(smooth(TimeRegionbound(2,:)),1:length(TimeRegionbound),'k','MarkerSize',
20)
xlabel('pixels'), ylabel('pixels')
legend('(LEFT) 16%','(RIGHT) 75%','Location','NorthWest')
set(gca,'YDir','reverse')
xlim([1 y])
ylim([1 x])
hold off

TimeShrank = imresize(TimeRegion, [192 18]);

%%
figure(8)
clf(8)
hold on
image(TimeShrank, 'CDataMapping', 'scaled')
%
plot(smooth(TimeRegionbound(1,:)),1:length(TimeRegionbound),'k','MarkerSize',
20)
%
plot(smooth(TimeRegionbound(2,:)),1:length(TimeRegionbound),'k','MarkerSize',
20)
xlabel('pixels'), ylabel('pixels')
% legend('(LEFT) 16%','(RIGHT) 75%','Location','NorthWest')
set(gca,'YDir','reverse')
% xlim([1 y])
% ylim([1 x])
hold off
```

# Appendix II

## Labview VI's

### A2.1 Syringe Pump Control VI

The following images are of the front panel (GUI) of the labview program that is used to control the syringe pumps. This program uses a state machine to control the commands sent to the pumps during operation. The sheer amount of states and sub-vi's has prohibited the inclusion of the back panel in this appendix. The back panel can be accessed on the operational computer using the password 'begood' or by accessing the identical but unprotected version in the Krummel Lab Dropbox.

This Labview VI was designed to control up to four syringe pumps at a time for microfluidics. It was designed to be leading with aids during the process. No manual tab navigation is required.

Upon initialization, the 'Home' tab will appear.

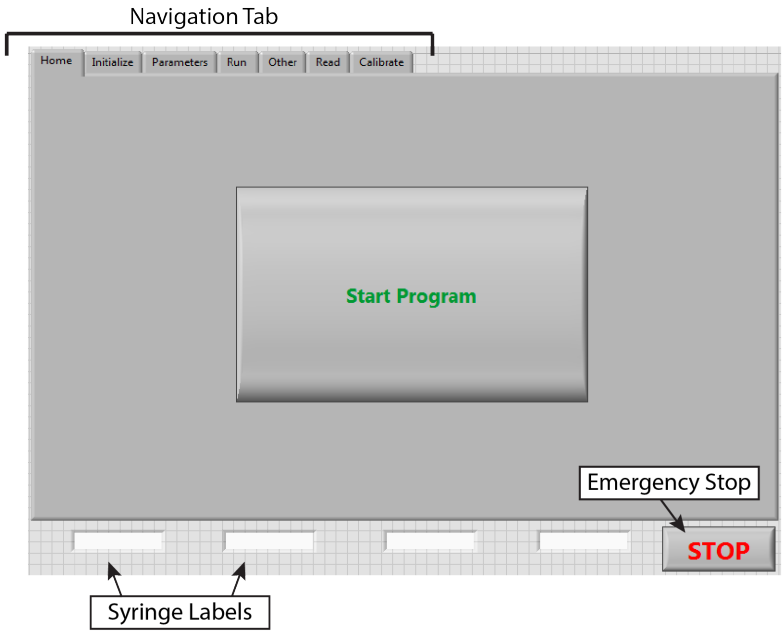

In the second section, each syringe pump must be initialized. Initialization is performed by setting the correct parameters and then clicking on the 'Good!' button. The required parameters are the COM that the pumps are connected through, Baud Rate (always 19200), and pump number.

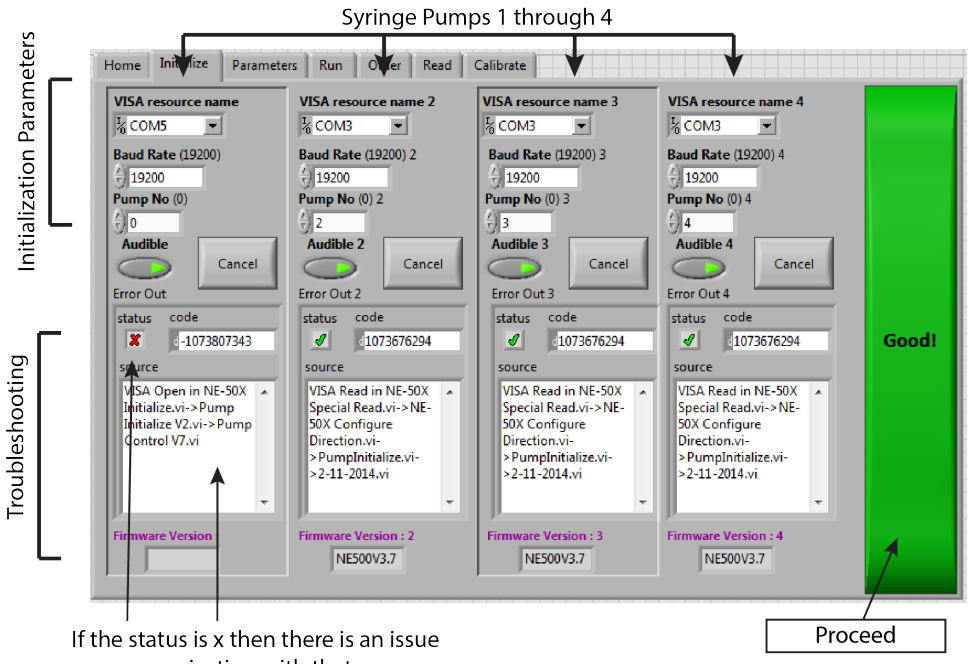


In the Parameters stage, the experimental parameters are set on the pump.
Parameters must be submitted individually to each pump by pressing the 'YES' button.

The available parameters are syringe size, direction of flow, sample volume in the syringe, initial flow rate and units associated, and dispensed volume. Dispensed volume is for experiments where a specific amount of volume is to be dispensed (default is 0).

The 'Run' tab is what controls the experimental parameters such as flow rate and is used to start, stop, and reverse the pumps.


The 'read', 'calibrate', and 'other' navagation tabs are used for the purpose of assigning the pump number to the pump.

Up to 100 syringe pumps can be linked in series and controlled by the same program. This is done by asigning each pump a number between 0 and 99. This number stays with the pump until it is reassigned.

The read tab is to read the number that is assigned to a single pump linked into the program.

The calibrate tab is designed to reset the pump.

The other tab, is designed to combine the read and the calibrate tab and can assign the pump numbers to up to 4 pumps in series.

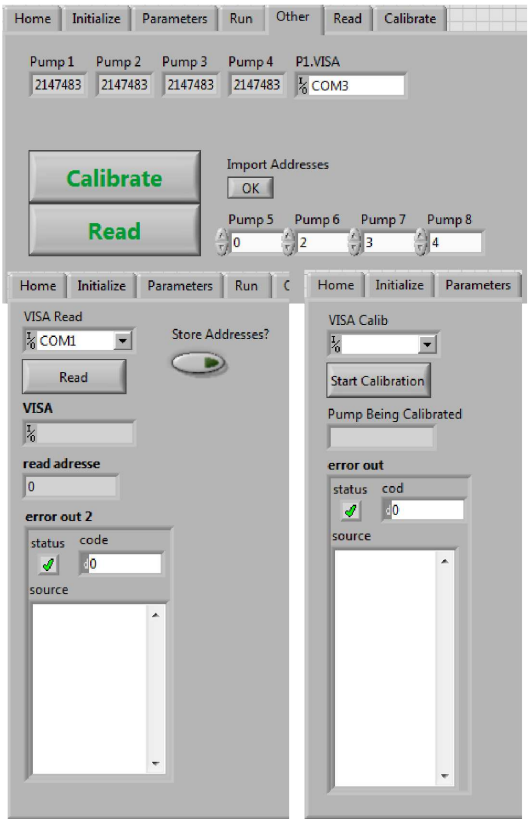

# Appendix III

## Current RADA Data

### A3.1 Linear IR Spectra of RADA and RADA Components

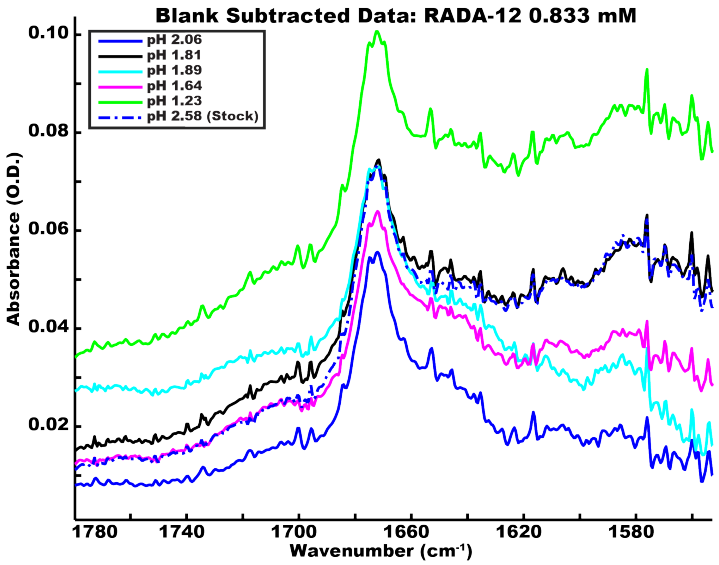


**Figure A3.1 Linear IR Spectra of RADA Under Acidic Conditions**

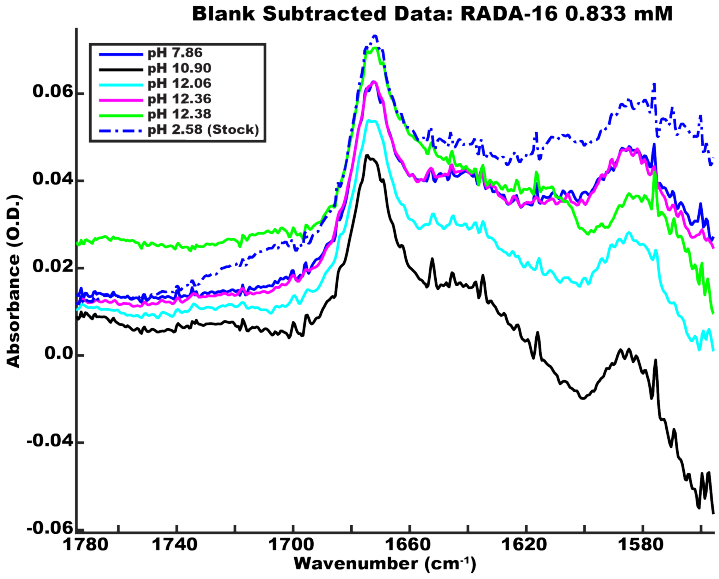


**Figure A3.2 Linear IR Spectra of RADA Under Basic Conditions**

# A3.2 Sample Log for RADA and Amino Acid Standards

| | | | Required | | Added | | (mM) | | Required | | Added | | | | (vol = 250) | M | Fraction of |
|---|---|---|---|---|---|---|---|---|---|---|---|---|---|---|---|---|---|
| SPECIES | MW | esired] mM | olume (mL | Mass (mg) | Mass (g) | olume (mL | Molarity | Equavalent | 1.0 M Acid | 0.1 M Acid | 1.0 M Acid | 0.1 M Acid | *ample Nam* | *pH* | ew Molarit | [Acid] | the |
| ALA | 89.1 | 10 | 4 | 0.3564 | 0.0036 | 4 | 10.10101 | 1/4 | 0 | 6.31 | 0 | 6.31 | *A1* | ***3*** | 9.8523 | 2.4619 | 0.0246 |
| ALA | 89.1 | 10 | 4 | 0.3564 | 0.0036 | 4 | 10.10101 | 1/2 | 1 | 2.62 | 0 | 12.62 | *A2* | ***2.57*** | 9.6156 | 4.8054 | 0.0481 |
| ALA | 89.1 | 10 | 4 | 0.3564 | 0.0036 | 4 | 10.10101 | 3/4 | 1 | 8.94 | 0 | 18.93 | *A3* | ***2.33*** | 9.3900 | 7.0390 | 0.0704 |
| ALA | 89.1 | 10 | 4 | 0.3564 | 0.0036 | 4 | 10.10101 | 1 | 2 | 5.25 | 2 | 5.25 | *A4* | ***2*** | 9.8163 | 9.8154 | 0.0982 |
| ALA | 89.1 | 10 | 4 | 0.3564 | 0.0036 | 4 | 10.10101 | 2 | 5 | 0.5 | 5.05 | 0 | *A5* | ***1.51*** | 9.9010 | 19.8000 | 0.1980 |
| ALA | 89.1 | 10 | 4 | 0.3564 | 0.0036 | 4 | 10.10101 | 0 | 0 | 0 | 0 | 0 | *SA* | ***8.41*** | 10.1010 | 0.0000 | 0.0000 |
| ASP | 133.05 | 10 | 4 | 5.322 | 0.0054 | 4 | 10.146561 | 1/4 | 0 | 8.22 | 0 | 8.22 | *B1* | ***2.42*** | 9.8236 | 3.1833 | 0.0318 |
| ASP | 133.05 | 10 | 4 | 5.322 | 0.0054 | 4 | 10.146561 | 1/2 | 1 | 6.44 | 1 | 6.44 | *B2* | ***2.17*** | 9.8533 | 6.3860 | 0.0639 |
| ASP | 133.05 | 10 | 4 | 5.322 | 0.0054 | 4 | 10.146561 | 3/4 | 2 | 4.66 | 2 | 4.66 | *B3* | ***1.97*** | 9.8833 | 9.6080 | 0.0961 |
| ASP | 133.05 | 10 | 4 | 5.322 | 0.0054 | 4 | 10.146561 | 1 | 3 | 2.88 | 3 | 2.88 | *B4* | ***1.75*** | 9.9134 | 12.8498 | 0.1285 |
| ASP | 133.05 | 10 | 4 | 5.322 | 0.0054 | 4 | 10.146561 | 2 | 6 | 5.76 | 6 | 5.76 | *B5* | ***1.36*** | 9.6907 | 25.1222 | 0.2512 |
| ASP | 133.05 | 10 | 4 | 5.322 | 0.0054 | 4 | 10.146561 | 0 | 0 | 0 | 0 | 0 | *SB* | ***3.06*** | 10.1466 | 0.0000 | 0.0000 |
| ARG | 174.2 | 10 | 4 | 6.968 | 0.007 | 4 | 10.045924 | 1/4 | 0 | 6.27 | 0 | 6.27 | *C1* | ***10.01*** | 9.8001 | 2.4466 | 0.0245 |
| ARG | 174.2 | 10 | 4 | 6.968 | 0.007 | 4 | 10.045924 | 1/2 | 1 | 12.54 | 0 | 12.54 | *C2* | ***9.61*** | 9.5661 | 4.7764 | 0.0478 |
| ARG | 174.2 | 10 | 4 | 6.968 | 0.007 | 4 | 10.045924 | 3/4 | 1 | 18.81 | 0 | 18.81 | *C3* | ***9.15*** | 9.3430 | 6.9975 | 0.0700 |
| ARG | 174.2 | 10 | 4 | 6.968 | 0.007 | 4 | 10.045924 | 1 | 2 | 5.11 | 2 | 5.11 | *C4* | ***3.45*** | 9.7681 | 9.7662 | 0.0977 |
| ARG | 174.2 | 10 | 4 | 6.968 | 0.007 | 4 | 10.045924 | 2 | 5 | 0 | 5.02 | 0 | *C5* | ***1.9*** | 9.8482 | 19.6847 | 0.1968 |
| ARG | 174.2 | 10 | 4 | 6.968 | 0.007 | 4 | 10.045924 | 0 | 0 | 0 | 0 | 0 | *SB* | ***10.9*** | 10.0459 | 0.0000 | 0.0000 |
| ALA-ALA | 160.17 | 5 | 4 | 3.2 | 0.0033 | 4 | 5.1507773 | 1/4 | 0 | 6.44 | 0 | 6.44 | *D1* | ***3.54*** | 5.0214 | 2.5113 | 0.0251 |
| ALA-ALA | 160.17 | 5 | 4 | 3.2 | 0.0033 | 4 | 5.1507773 | 1/2 | 1 | 2.88 | 0 | 12.88 | *D2* | ***2.78*** | 4.8984 | 4.8996 | 0.0490 |
| ALA-ALA | 160.17 | 5 | 4 | 3.2 | 0.0033 | 4 | 5.1507773 | 3/4 | 1 | 9.32 | 0 | 19.32 | *D3* | ***6.39*** | 4.7813 | 7.1736 | 0.0717 |
| ALA-ALA | 160.17 | 5 | 4 | 3.2 | 0.0033 | 4 | 5.1507773 | 1 | 2 | 5.75 | 2 | 5.75 | *D4* | ***1.92*** | 4.9959 | 9.9903 | 0.0999 |
| ALA-ALA | 160.17 | 5 | 4 | 3.2 | 0.0033 | 4 | 5.1507773 | 2 | 5 | 1.5 | 5.2 | 0 | *D5* | ***1.37*** | 5.0458 | 20.3762 | 0.2038 |
| ALA-ALA | 160.17 | 5 | 4 | 3.2 | 0.0033 | 4 | 5.1507773 | 0 | 0 | 0 | 0 | 0 | *SD* | ***6.39*** | 5.1508 | 0.0000 | 0.0000 |
| ASP-ASP | 248.19 | 5 | 4 | 4.96 | 0.005 | 4 | 5.036464 | 1/4 | 0 | 6.3 | 0 | 6.3 | *E1* | ***2.81*** | 4.9127 | 2.4581 | 0.0246 |
| ASP-ASP | 248.19 | 5 | 4 | 4.96 | 0.005 | 4 | 5.036464 | 1/2 | 1 | 2.6 | 0 | 12.6 | *E2* | ***2.32*** | 4.7948 | 4.7982 | 0.0480 |
| ASP-ASP | 248.19 | 5 | 4 | 4.96 | 0.005 | 4 | 5.036464 | 3/4 | 1 | 8.89 | 0 | 18.9 | *E3* | ***2.1*** | 4.6825 | 7.0286 | 0.0703 |
| ASP-ASP | 248.19 | 5 | 4 | 4.96 | 0.005 | 4 | 5.036464 | 1 | 2 | 5.18 | 2 | 5.18 | *E4* | ***1.89*** | 4.8959 | 9.7908 | 0.0979 |
| ASP-ASP | 248.19 | 5 | 4 | 4.96 | 0.005 | 4 | 5.036464 | 2 | 5 | 0.36 | 5.1 | 0 | *E5* | ***1.33*** | 4.9358 | 19.9922 | 0.1999 |
| ASP-ASP | 248.19 | 5 | 4 | 4.96 | 0.005 | 4 | 5.036464 | 0 | 0 | 0 | 0 | 0 | *SE* | ***3.26*** | 5.0365 | 0.0000 | 0.0000 |
| ARG-ARG | 330.39 | 5 | 4 | 6.6 | 0.0069 | 4 | 5.2211023 | 1/4 | 0 | 6.53 | 0 | 6.53 | *F1* | ***5.02*** | 5.0882 | 2.5455 | 0.0255 |
| ARG-ARG | 330.39 | 5 | 4 | 6.6 | 0.0069 | 4 | 5.2211023 | 1/2 | 1 | 3.05 | 0 | 13.06 | *F2* | ***4.39*** | 4.9619 | 4.9646 | 0.0496 |
| ARG-ARG | 330.39 | 5 | 4 | 6.6 | 0.0069 | 4 | 5.2211023 | 3/4 | 1 | 9.58 | 0 | 19.59 | *F3* | ***3.46*** | 4.8417 | 7.2666 | 0.0727 |
| ARG-ARG | 330.39 | 5 | 4 | 6.6 | 0.0069 | 4 | 5.2211023 | 1 | 2 | 6.1 | 2 | 6.1 | *F4* | ***2.6*** | 5.0572 | 10.1124 | 0.1011 |
| ARG-ARG | 330.39 | 5 | 4 | 6.6 | 0.0069 | 4 | 5.2211023 | 2 | 5 | 2.2 | 5 | 2.2 | *F5* | ***1.67*** | 5.0749 | 20.2955 | 0.2030 |
| ARG-ARG | 330.39 | 5 | 4 | 6.6 | 0.0069 | 4 | 5.2211023 | 0 | 0 | 0 | 0 | 0 | *SF* | ***6.02*** | 5.2211 | 0.0000 | 0.0000 |
| ALA | 89.1 | 10 | 4 | 0.3564 | 0.0036 | 4 | 10.10101 | 1/4 | 0 | 6.44 | 0 | 6.44 | *I1* | ***9.15*** | 9.8473 | 2.5113 | 0.0251 |
| ALA | 89.1 | 10 | 4 | 0.3564 | 0.0036 | 4 | 10.10101 | 1/2 | 1 | 2.88 | 0 | 12.88 | *I2* | ***10.25*** | 9.6061 | 4.8996 | 0.0490 |
| ALA | 89.1 | 10 | 4 | 0.3564 | 0.0036 | 4 | 10.10101 | 3/4 | 1 | 9.32 | 0 | 19.32 | *I3* | ***10.66*** | 9.3764 | 7.1736 | 0.0717 |
| ALA | 89.1 | 10 | 4 | 0.3564 | 0.0036 | 4 | 10.10101 | 1 | 2 | 5.75 | 2 | 5.75 | *I4* | ***11.35*** | 9.7973 | 9.9903 | 0.0999 |
| ALA | 89.1 | 10 | 4 | 0.3564 | 0.0036 | 4 | 10.10101 | 2 | 5 | 1.5 | 5.2 | 0 | *I5* | ***12.54*** | 9.8952 | 20.3762 | 0.2038 |
| ALA | 89.1 | 10 | 4 | 0.3564 | 0.0036 | 4 | 10.10101 | 0 | 0 | 0 | 0 | 0 | *SI* | ***7.69*** | 10.1010 | 0.0000 | 0.0000 |
| ASP | 133.05 | 10 | 4 | 5.322 | 0.0054 | 4 | 10.146561 | 1/4 | 0 | 6.3 | 0 | 6.3 | *H1* | ***3.69*** | 9.8972 | 2.4581 | 0.0246 |
| ASP | 133.05 | 10 | 4 | 5.322 | 0.0054 | 4 | 10.146561 | 1/2 | 1 | 2.6 | 0 | 12.6 | *H2* | ***3.94*** | 9.6597 | 4.7982 | 0.0480 |
| ASP | 133.05 | 10 | 4 | 5.322 | 0.0054 | 4 | 10.146561 | 3/4 | 1 | 8.89 | 0 | 18.9 | *H3* | ***4.44*** | 9.4334 | 7.0286 | 0.0703 |
| ASP | 133.05 | 10 | 4 | 5.322 | 0.0054 | 4 | 10.146561 | 1 | 2 | 5.18 | 2 | 5.18 | *H4* | ***5.65*** | 9.8633 | 9.7908 | 0.0979 |
| ASP | 133.05 | 10 | 4 | 5.322 | 0.0054 | 4 | 10.146561 | 2 | 5 | 0.36 | 5.1 | 0 | *H5* | ***11.16*** | 9.9437 | 19.9922 | 0.1999 |
| ASP | 133.05 | 10 | 4 | 5.322 | 0.0054 | 4 | 10.146561 | 0 | 0 | 0 | 0 | 0 | *SH* | ***3.12*** | 10.1466 | 0.0000 | 0.0000 |
| ARG | 174.2 | 10 | 4 | 6.968 | 0.007 | 4 | 10.045924 | 1/4 | 0 | 6.53 | 0 | 6.53 | *G1* | ***11.73*** | 9.7902 | 2.5455 | 0.0255 |
| ARG | 174.2 | 10 | 4 | 6.968 | 0.007 | 4 | 10.045924 | 1/2 | 1 | 3.05 | 0 | 13.06 | *G2* | ***12.23*** | 9.5472 | 4.9646 | 0.0496 |
| ARG | 174.2 | 10 | 4 | 6.968 | 0.007 | 4 | 10.045924 | 3/4 | 1 | 9.58 | 0 | 19.59 | *G3* | ***12.43*** | 9.3159 | 7.2666 | 0.0727 |
| ARG | 174.2 | 10 | 4 | 6.968 | 0.007 | 4 | 10.045924 | 1 | 2 | 6.1 | 2 | 6.1 | *G4* | ***12.62*** | 9.7307 | 10.1124 | 0.1011 |
| ARG | 174.2 | 10 | 4 | 6.968 | 0.007 | 4 | 10.045924 | 2 | 5 | 2.2 | 5 | 2.2 | *G5* | ***12.88*** | 9.7647 | 20.2955 | 0.2030 |
| ARG | 174.2 | 10 | 4 | 6.968 | 0.007 | 4 | 10.045924 | 0 | 0 | 0 | 0 | 0 | *SG* | ***10.54*** | 10.0459 | 0.0000 | 0.0000 |
| ALA-ALA | 160.17 | 5 | 4 | 3.2 | 0.0033 | 4 | 5.1507773 | 1/4 | 0 | 6.44 | 0 | 6.44 | *J1* | ***8.44*** | 5.0214 | 2.5113 | 0.0251 |
| ALA-ALA | 160.17 | 5 | 4 | 3.2 | 0.0033 | 4 | 5.1507773 | 1/2 | 1 | 2.88 | 0 | 12.88 | *J2* | ***9.56*** | 4.8984 | 4.8996 | 0.0490 |
| ALA-ALA | 160.17 | 5 | 4 | 3.2 | 0.0033 | 4 | 5.1507773 | 3/4 | 1 | 9.32 | 0 | 19.32 | *J3* | ***11.84*** | 4.7813 | 7.1736 | 0.0717 |
| ALA-ALA | 160.17 | 5 | 4 | 3.2 | 0.0033 | 4 | 5.1507773 | 1 | 2 | 5.75 | 2 | 5.75 | *J4* | ***12.27*** | 4.9959 | 9.9903 | 0.0999 |
| ALA-ALA | 160.17 | 5 | 4 | 3.2 | 0.0033 | 4 | 5.1507773 | 2 | 5 | 1.5 | 5.2 | 0 | *J5* | ***12.74*** | 5.0458 | 20.3762 | 0.2038 |
| ALA-ALA | 160.17 | 5 | 4 | 3.2 | 0.0033 | 4 | 5.1507773 | 0 | 0 | 0 | 0 | 0 | *SJ* | ***6.94*** | 5.1508 | 0.0000 | 0.0000 |
| ASP-ASP | 248.19 | 5 | 4 | 4.96 | 0.005 | 4 | 5.036464 | 1/4 | 0 | 6.3 | 0 | 6.3 | *K1* | ***3.84*** | 4.9127 | 2.4581 | 0.0246 |
| ASP-ASP | 248.19 | 5 | 4 | 4.96 | 0.005 | 4 | 5.036464 | 1/2 | 1 | 2.6 | 0 | 12.6 | *K2* | ***4.55*** | 4.7948 | 4.7982 | 0.0480 |
| ASP-ASP | 248.19 | 5 | 4 | 4.96 | 0.005 | 4 | 5.036464 | 3/4 | 1 | 8.89 | 0 | 18.9 | *K3* | ***8.29*** | 4.6825 | 7.0286 | 0.0703 |
| ASP-ASP | 248.19 | 5 | 4 | 4.96 | 0.005 | 4 | 5.036464 | 1 | 2 | 5.18 | 2 | 5.18 | *K4* | ***8.63*** | 4.8959 | 9.7908 | 0.0979 |
| ASP-ASP | 248.19 | 5 | 4 | 4.96 | 0.005 | 4 | 5.036464 | 2 | 5 | 0.36 | 5.1 | 0 | *K5* | ***12.28*** | 4.9358 | 19.9922 | 0.1999 |
| ASP-ASP | 248.19 | 5 | 4 | 4.96 | 0.005 | 4 | 5.036464 | 0 | 0 | 0 | 0 | 0 | *SK* | ***3.29*** | 5.0365 | 0.0000 | 0.0000 |
| ARG-ARG | 330.39 | 5 | 4 | 6.6 | 0.0069 | 4 | 5.2211023 | 1/4 | 0 | 6.53 | 0 | 6.53 | *L1* | ***7.78*** | 5.0882 | 2.5455 | 0.0255 |
| ARG-ARG | 330.39 | 5 | 4 | 6.6 | 0.0069 | 4 | 5.2211023 | 1/2 | 1 | 3.05 | 0 | 13.06 | *L2* | ***11.3*** | 4.9619 | 4.9646 | 0.0496 |
| ARG-ARG | 330.39 | 5 | 4 | 6.6 | 0.0069 | 4 | 5.2211023 | 3/4 | 1 | 9.58 | 0 | 19.59 | *L3* | ***12.04*** | 4.8417 | 7.2666 | 0.0727 |
| ARG-ARG | 330.39 | 5 | 4 | 6.6 | 0.0069 | 4 | 5.2211023 | 1 | 2 | 6.1 | 2 | 6.1 | *L4* | ***12.31*** | 5.0572 | 10.1124 | 0.1011 |
| ARG-ARG | 330.39 | 5 | 4 | 6.6 | 0.0069 | 4 | 5.2211023 | 2 | 5 | 2.2 | 5 | 2.2 | *L5* | ***12.77*** | 5.0749 | 20.2955 | 0.2030 |
| ARG-ARG | 330.39 | 5 | 4 | 6.6 | 0.0069 | 4 | 5.2211023 | 0 | 0 | 0 | 0 | 0 | *SL* | ***6.12*** | 5.2211 | 0.0000 | 0.0000 |
| RADA-12 | 1258.33 | 0.8333 | 2 | 2.1 | 0.002 | 2 | 0.7947041 | 1/4 | 0 | 2.38 | 0 | 2.38 | *M1* | ***7.34*** | 0.7872 | 0.9430 | 0.0094 |
| RADA-12 | 1258.33 | 0.8333 | 2 | 2.1 | 0.002 | 2 | 0.7947041 | 1/2 | 0 | 4.76 | 0 | 4.76 | *M2* | ***10.45*** | 0.7799 | 1.8684 | 0.0187 |
| RADA-12 | 1258.33 | 0.8333 | 2 | 2.1 | 0.002 | 2 | 0.7947041 | 3/4 | 0 | 7.14 | 0 | 7.14 | *M3* | ***12.01*** | 0.7726 | 2.7767 | 0.0278 |
| RADA-12 | 1258.33 | 0.8333 | 2 | 2.1 | 0.002 | 2 | 0.7947041 | 1 | 0 | 9.53 | 0 | 9.53 | *M4* | ***12.16*** | 0.7655 | 3.6720 | 0.0367 |
| RADA-12 | 1258.33 | 0.8333 | 2 | 2.1 | 0.002 | 2 | 0.7947041 | 2 | 1.91 | 0 | 1.9 | 0 | *M5* | ***12.38*** | 0.7887 | 7.5427 | 0.0754 |
| RADA-12 | 1258.33 | 0.8333 | 2 | 2.1 | 0.002 | 2 | 0.7947041 | 0 | 0 | 0 | 0 | 0 | *SM* | ***2.99*** | 0.7947 | 0.0000 | 0.0000 |
| RADA-12 | 1258.33 | 0.8333 | 2 | 2.1 | 0.002 | 2 | 0.7947041 | 1/4 | 0 | 2.38 | 0 | 2.38 | *N1* | ***2.56*** | 0.7872 | 0.9430 | 0.0094 |
| RADA-12 | 1258.33 | 0.8333 | 2 | 2.1 | 0.002 | 2 | 0.7947041 | 1/2 | 0 | 4.76 | 0 | 4.76 | *N2* | ***1.85*** | 0.7799 | 1.8684 | 0.0187 |
| RADA-12 | 1258.33 | 0.8333 | 2 | 2.1 | 0.002 | 2 | 0.7947041 | 3/4 | 0 | 7.14 | 0 | 7.14 | *N3* | ***1.88*** | 0.7726 | 2.7767 | 0.0278 |
| RADA-12 | 1258.33 | 0.8333 | 2 | 2.1 | 0.002 | 2 | 0.7947041 | 1 | 0 | 9.53 | 0 | 9.53 | *N4* | ***1.7*** | 0.7655 | 3.6720 | 0.0367 |
| RADA-12 | 1258.33 | 0.8333 | 2 | 2.1 | 0.002 | 2 | 0.7947041 | 2 | 1.91 | 0 | 1.9 | 0 | *N5* | ***1.29*** | 0.7887 | 7.5427 | 0.0754 |
| RADA-16 | 1672.76 | 0.625 | 2 | 2.1 | 0.0024 | 2 | 0.7173773 | 1/4 | 0 | 2.86 | 0 | 2.86 | *O1* | ***7.86*** | 0.7093 | 1.1311 | 0.0113 |
| RADA-16 | 1672.76 | 0.625 | 2 | 2.1 | 0.0024 | 2 | 0.7173773 | 1/2 | 0 | 5.72 | 0 | 5.72 | *O2* | ***10.9*** | 0.7013 | 2.2368 | 0.0224 |
| RADA-16 | 1672.76 | 0.625 | 2 | 2.1 | 0.0024 | 2 | 0.7173773 | 3/4 | 0 | 8.58 | 0 | 8.58 | *O3* | ***12.06*** | 0.6936 | 3.3181 | 0.0332 |
| RADA-16 | 1672.76 | 0.625 | 2 | 2.1 | 0.0024 | 2 | 0.7173773 | 1 | 0 | 11.5 | 1.15 | 0 | *O4* | ***12.36*** | 0.7141 | 4.5789 | 0.0458 |
| RADA-16 | 1672.76 | 0.625 | 2 | 2.1 | 0.0024 | 2 | 0.7173773 | 2 | 2.29 | 0 | 2.29 | 0 | *O5* | ***12.38*** | 0.7109 | 9.0769 | 0.0908 |
| RADA-16 | 1672.76 | 0.625 | 2 | 2.1 | 0.0024 | 2 | 0.7173773 | 0 | 0 | 0 | 0 | 0 | *SO* | ***2.58*** | 0.7174 | 0.0000 | 0.0000 |
| RADA-16 | 1672.76 | 0.625 | 2 | 2.1 | 0.0024 | 2 | 0.7173773 | 1/4 | 0 | 2.86 | 0 | 2.86 | *P1* | ***2.06*** | 0.7093 | 1.1311 | 0.0113 |
| RADA-16 | 1672.76 | 0.625 | 2 | 2.1 | 0.0024 | 2 | 0.7173773 | 1/2 | 0 | 5.72 | 0 | 5.72 | *P2* | ***1.81*** | 0.7013 | 2.2368 | 0.0224 |
| RADA-16 | 1672.76 | 0.625 | 2 | 2.1 | 0.0024 | 2 | 0.7173773 | 3/4 | 0 | 8.58 | 0 | 8.58 | *P3* | ***1.89*** | 0.6936 | 3.3181 | 0.0332 |
| RADA-16 | 1672.76 | 0.625 | 2 | 2.1 | 0.0024 | 2 | 0.7173773 | 1 | 0 | 11.5 | 1.15 | 0 | *P4* | ***1.64*** | 0.7141 | 4.5789 | 0.0458 |
| RADA-16 | 1672.76 | 0.625 | 2 | 2.1 | 0.0024 | 2 | 0.7173773 | 2 | 2.29 | 0 | 2.29 | 0 | *P5* | ***1.23*** | 0.7109 | 9.0769 | 0.0908 |

# A3.3 Fitting Parameters for the Adding Acid and Adding Base to Components of RADA

| ALA | 3 | 2.57 | 2.33 | 2 | 1.51 | 8.41 |
|---|---|---|---|---|---|---|
| 1 | 1612 | 1612.5 | 1612.5 | 1612.5 | 1612.5 | 1612.5 |
| 2 | 1728 | 1728 | 1728 | 1728 | 1728 | 1728 |
| 3 | 0 | 0 | 0 | 0 | 0 | 0 |
| 4 | 0 | 0 | 0 | 0 | 0 | 0 |
| 5 | 0 | 0 | 0 | 0 | 0 | 0 |
| 6 | 0 | 0 | 0 | 0 | 0 | 0 |
| 7 | 0 | 0 | 0 | 0 | 0 | 0 |
| 8 | 0 | 0 | 0 | 0 | 0 | 0 |
| 9 | 0 | 0 | 0 | 0 | 0 | 0 |
| 10 | 23 | 23 | 23 | 23 | 23 | 23.5 |
| 11 | 30 | 30 | 33 | 33 | 33 | 33 |
| 12 | 0 | 0 | 0 | 0 | 0 | 0 |
| 13 | 0 | 0 | 0 | 0 | 0 | 0 |
| 14 | 0 | 0 | 0 | 0 | 0 | 0 |
| 15 | 0 | 0 | 0 | 0 | 0 | 0 |
| 16 | 0 | 0 | 0 | 0 | 0 | 0 |
| 17 | 0 | 0 | 0 | 0 | 0 | 0 |
| 18 | 0 | 0 | 0 | 0 | 0 | 0 |
| 19 | 1.75 | 1.55 | 1.17 | 0.55 | 0.2 | 2.56 |
| 20 | 0.2 | 0.26 | 0.39 | 0.62 | 0.62 | 0 |
| 21 | 0 | 0 | 0 | 0 | 0 | 0 |
| 22 | 0 | 0 | 0 | 0 | 0 | 0 |
| 23 | 0 | 0 | 0 | 0 | 0 | 0 |
| 24 | 0 | 0 | 0 | 0 | 0 | 0 |
| 25 | 0 | 0 | 0 | 0 | 0 | 0 |
| 26 | 0 | 0 | 0 | 0 | 0 | 0 |
| 27 | 0 | 0 | 0 | 0 | 0 | 0 |
| 28 | 0 | 0 | 0 | 0 | 0 | 0 |

| ASP | 2.42 | 2.17 | 1.97 | 1.75 | 1.36 | 3.06 |
|---|---|---|---|---|---|---|
| 1 | 0 | 0 | 0 | 0 | 0 | 0 |
| 2 | 0 | 0 | 0 | 0 | 0 | 0 |
| 3 | 1623 | 1622.75 | 1622.75 | 1622.75 | 1622.5 | 1623 |
| 4 | 1715.8 | 1719 | 1722 | 1720 | 1721 | 1711 |
| 5 | 0 | 0 | 0 | 0 | 0 | 0 |
| 6 | 0 | 0 | 0 | 0 | 0 | 0 |
| 7 | 0 | 0 | 0 | 0 | 0 | 0 |
| 8 | 0 | 0 | 0 | 0 | 0 | 0 |
| 9 | 0 | 0 | 0 | 0 | 0 | 0 |
| 10 | 0 | 0 | 0 | 0 | 0 | 0 |
| 11 | 0 | 0 | 0 | 0 | 0 | 0 |
| 12 | 22 | 24 | 24 | 23 | 23 | 22 |
| 13 | 42 | 42 | 46 | 47 | 49 | 42 |
| 14 | 0 | 0 | 0 | 0 | 0 | 0 |
| 15 | 0 | 0 | 0 | 0 | 0 | 0 |
| 16 | 0 | 0 | 0 | 0 | 0 | 0 |
| 17 | 0 | 0 | 0 | 0 | 0 | 0 |
| 18 | 0 | 0 | 0 | 0 | 0 | 0 |
| 19 | 0 | 0 | 0 | 0 | 0 | 0 |
| 20 | 0 | 0 | 0 | 0 | 0 | 0 |
| 21 | 1.74 | 1.3 | 0.73 | 0.95 | 0.36 | 1.74 |
| 22 | 0.85 | 1 | 1.2 | 1.04 | 1.2 | 0.83 |
| 23 | 0 | 0 | 0 | 0 | 0 | 0 |
| 24 | 0 | 0 | 0 | 0 | 0 | 0 |
| 25 | 0 | 0 | 0 | 0 | 0 | 0 |
| 26 | 0 | 0 | 0 | 0 | 0 | 0 |
| 27 | 0 | 0 | 0 | 0 | 0 | 0 |
| 28 | 0 | 0 | 0 | 0 | 0 | 0 |

| ARG | 10.01 | 9.61 | 9.15 | 3.45 | 1.9 | 10.9 |
|---|---|---|---|---|---|---|
| 1 | 0 | 0 | 0 | 0 | 0 | 0 |
| 2 | 0 | 0 | 0 | 0 | 0 | 0 |
| 3 | 0 | 0 | 0 | 0 | 0 | 0 |
| 4 | 0 | 0 | 0 | 0 | 0 | 0 |
| 5 | 1612 | 1612.5 | 1613 | 1612.5 | 1612 | 1611 |
| 6 | 1582 | 1584.5 | 1585.5 | 1584.5 | 1586 | 1577.5 |
| 7 | 0 | 0 | 0 | 0 | 0 | 0 |
| 8 | 0 | 0 | 0 | 0 | 0 | 0 |
| 9 | 0 | 0 | 0 | 0 | 0 | 0 |
| 10 | 0 | 0 | 0 | 0 | 0 | 0 |
| 11 | 0 | 0 | 0 | 0 | 0 | 0 |
| 12 | 0 | 0 | 0 | 0 | 0 | 0 |
| 13 | 0 | 0 | 0 | 0 | 0 | 0 |
| 14 | 25 | 26.5 | 26.5 | 26.5 | 26.5 | 22 |
| 15 | 25 | 19 | 18.5 | 18.5 | 18.5 | 32.5 |
| 16 | 0 | 0 | 0 | 0 | 0 | 0 |
| 17 | 0 | 0 | 0 | 0 | 0 | 0 |
| 18 | 0 | 0 | 0 | 0 | 0 | 0 |
| 19 | 0 | 0 | 0 | 0 | 0 | 0 |
| 20 | 0 | 0 | 0 | 0 | 0 | 0 |
| 21 | 0 | 0 | 0 | 0 | 0 | 0 |
| 22 | 0 | 0 | 0 | 0 | 0 | 0 |
| 23 | 2.7 | 3.45 | 3.45 | 3.45 | 3.255 | 2 |
| 24 | 2.7 | 1.8 | 1.6 | 2 | 1.65 | 3.05 |
| 25 | 0 | 0 | 0 | 0 | 0 | 0 |
| 26 | 0 | 0 | 0 | 0 | 0 | 0 |
| 27 | 0 | 0 | 0 | 0 | 0 | 0 |
| 28 | 0 | 0 | 0 | 0 | 0 | 0 |

| ALA-ALA | 3.54 | 2.78 | 6.39 | 1.92 | 1.37 | 6.39 |
|---|---|---|---|---|---|---|
| 1 | 1589 | 1589 | 1589 | 1589 | 1589 | 1590 |
| 2 | 1716 | 1716 | 1716 | 1716 | 1715.5 | 1715.5 |
| 3 | 0 | 0 | 0 | 0 | 0 | 0 |
| 4 | 0 | 0 | 0 | 0 | 0 | 0 |
| 5 | 0 | 0 | 0 | 0 | 0 | 0 |
| 6 | 0 | 0 | 0 | 0 | 0 | 0 |
| 7 | 0 | 0 | 0 | 0 | 0 | 0 |
| 8 | 1665 | 1667 | 1665 | 1668 | 1668.5 | 1663 |
| 9 | 0 | 0 | 0 | 0 | 0 | 0 |
| 10 | 34.5 | 34.5 | 27 | 27 | 27 | 28 |
| 11 | 33 | 33 | 27 | 39 | 39 | 39 |
| 12 | 0 | 0 | 0 | 0 | 0 | 0 |
| 13 | 0 | 0 | 0 | 0 | 0 | 0 |
| 14 | 0 | 0 | 0 | 0 | 0 | 0 |
| 15 | 0 | 0 | 0 | 0 | 0 | 0 |
| 16 | 0 | 0 | 0 | 0 | 0 | 0 |
| 17 | 28 | 28 | 28 | 28 | 28 | 28 |
| 18 | 0 | 0 | 0 | 0 | 0 | 0 |
| 19 | 0.75 | 0.3 | 1.15 | 0 | 0 | 1.35 |
| 20 | 0.1 | 0.3 | 0 | 0.35 | 0.38 | 0 |
| 21 | 0 | 0 | 0 | 0 | 0 | 0 |
| 22 | 0 | 0 | 0 | 0 | 0 | 0 |
| 23 | 0 | 0 | 0 | 0 | 0 | 0 |
| 24 | 0 | 0 | 0 | 0 | 0 | 0 |
| 25 | 0 | 0 | 0 | 0 | 0 | 0 |
| 26 | 0.7 | 0.7 | 0.75 | 0.75 | 0.8 | 0.675 |
| 27 | 0 | 0 | 0 | 0 | 0 | 0 |
| 28 | 0 | 0 | 0 | 0 | 0 | 0 |

| ASP-ASP | 2.81 | 2.32 | 2.1 | 1.89 | 1.33 | 3.26 |
|---|---|---|---|---|---|---|
| 1 | 0 | 0 | 0 | 0 | 0 | 0 |
| 2 | 0 | 0 | 0 | 0 | 0 | 0 |
| 3 | 1595 | 1595 | 1595 | 1595 | 1595 | 1595 |
| 4 | 1714 | 1715 | 1715.5 | 1715.5 | 1715.5 | 1714.5 |
| 5 | 0 | 0 | 0 | 0 | 0 | 0 |
| 6 | 0 | 0 | 0 | 0 | 0 | 0 |
| 7 | 0 | 0 | 0 | 0 | 0 | 0 |
| 8 | 1674 | 1674 | 1675 | 1676 | 1676 | 1673.5 |
| 9 | 0 | 0 | 0 | 0 | 0 | 0 |
| 10 | 0 | 0 | 0 | 0 | 0 | 0 |
| 11 | 0 | 0 | 0 | 0 | 0 | 0 |
| 12 | 39 | 39 | 39 | 39 | 39 | 35 |
| 13 | 42 | 44 | 43 | 43 | 43 | 40.5 |
| 14 | 0 | 0 | 0 | 0 | 0 | 0 |
| 15 | 0 | 0 | 0 | 0 | 0 | 0 |
| 16 | 0 | 0 | 0 | 0 | 0 | 0 |
| 17 | 30 | 29 | 31 | 30 | 30 | 30 |
| 18 | 0 | 0 | 0 | 0 | 0 | 0 |
| 19 | 0 | 0 | 0 | 0 | 0 | 0 |
| 20 | 0 | 0 | 0 | 0 | 0 | 0 |
| 21 | 0.8 | 0.5 | 0.2 | 0.08 | 0.08 | 1.08 |
| 22 | 0.9 | 1 | 1.1 | 1.16 | 1.16 | 0.76 |
| 23 | 0 | 0 | 0 | 0 | 0 | 0 |
| 24 | 0 | 0 | 0 | 0 | 0 | 0 |
| 25 | 0 | 0 | 0 | 0 | 0 | 0 |
| 26 | 0.68 | 0.68 | 0.664 | 0.67 | 0.67 | 0.7 |
| 27 | 0 | 0 | 0 | 0 | 0 | 0 |
| 28 | 0 | 0 | 0 | 0 | 0 | 0 |

| ARG-ARG | 5.02 | 4.39 | 3.46 | 2.6 | 1.67 | 6.02 |
|---|---|---|---|---|---|---|
| 1 | 0 | 0 | 0 | 0 | 0 | 0 |
| 2 | 0 | 0 | 0 | 0 | 0 | 0 |
| 3 | 0 | 0 | 0 | 0 | 0 | 0 |
| 4 | 0 | 0 | 0 | 0 | 0 | 0 |
| 5 | 1607.5 | 1609 | 1608.5 | 1609 | 1609 | 1609 |
| 6 | 1585 | 1587 | 1587 | 1587.5 | 1586.5 | 1586.5 |
| 7 | 0 | 1709.5 | 1709.5 | 1712 | 1712 | 0 |
| 8 | 1664 | 1668 | 1669 | 1672.5 | 1672.8 | 1664 |
| 9 | 0 | 0 | 0 | 0 | 0 | 0 |
| 10 | 0 | 0 | 0 | 0 | 0 | 0 |
| 11 | 0 | 0 | 0 | 0 | 0 | 0 |
| 12 | 0 | 0 | 0 | 0 | 0 | 0 |
| 13 | 0 | 0 | 0 | 0 | 0 | 0 |
| 14 | 25 | 24 | 23 | 20 | 20.8 | 22.8 |
| 15 | 25 | 25 | 24 | 22 | 20.8 | 24.8 |
| 16 | 0 | 29 | 31 | 31.5 | 33.5 | 0 |
| 17 | 30 | 31 | 33 | 33 | 33 | 26 |
| 18 | 0 | 0 | 0 | 0 | 0 | 0 |
| 19 | 0 | 0 | 0 | 0 | 0 | 0 |
| 20 | 0 | 0 | 0 | 0 | 0 | 0 |
| 21 | 0 | 0 | 0 | 0 | 0 | 0 |
| 22 | 0 | 0 | 0 | 0 | 0 | 0 |
| 23 | 1.55 | 1.35 | 1.45 | 1.25 | 1.48 | 1.48 |
| 24 | 2 | 1.63 | 1.7 | 1.28 | 1.38 | 2.1 |
| 25 | 0 | 0.4 | 0.55 | 0.77 | 0.86 | 0 |
| 26 | 0.45 | 0.6 | 0.6 | 0.65 | 0.77 | 0.4 |
| 27 | 0 | 0 | 0 | 0 | 0 | 0 |
| 28 | 0 | 0 | 0 | 0 | 0 | 0 |

| ALA | ALA | ALA | ALA | ALA | ALA |
|---|---|---|---|---|---|
| 9.15 | 10.25 | 10.66 | 11.35 | 12.54 | 7.69 |
| 1612.7 | 1612.7 | 1612.7 | 1612.7 | 1612.7 | 1612.5 |
| 0 | 0 | 0 | 0 | 0 | 0 |
| 0 | 0 | 0 | 0 | 0 | 0 |
| 0 | 0 | 0 | 0 | 0 | 0 |
| 0 | 0 | 0 | 0 | 0 | 0 |
| 0 | 0 | 0 | 0 | 0 | 0 |
| 0 | 0 | 0 | 0 | 0 | 0 |
| 0 | 0 | 0 | 0 | 0 | 0 |
| 23.5 | 23.5 | 23.5 | 23.5 | 23.5 | 25 |
| 0 | 0 | 0 | 0 | 0 | 0 |
| 0 | 0 | 0 | 0 | 0 | 0 |
| 0 | 0 | 0 | 0 | 0 | 0 |
| 0 | 0 | 0 | 0 | 0 | 0 |
| 0 | 0 | 0 | 0 | 0 | 0 |
| 0 | 0 | 0 | 0 | 0 | 0 |
| 0 | 0 | 0 | 0 | 0 | 0 |
| 1.85 | 1.33 | 0.63 | 0.13 | 0.13 | 2.78 |
| 0 | 0 | 0 | 0 | 0 | 0 |
| 0 | 0 | 0 | 0 | 0 | 0 |
| 0 | 0 | 0 | 0 | 0 | 0 |
| 0 | 0 | 0 | 0 | 0 | 0 |
| 0 | 0 | 0 | 0 | 0 | 0 |
| 0 | 0 | 0 | 0 | 0 | 0 |
| 0 | 0 | 0 | 0 | 0 | 0 |

| ASP | ASP | ASP | ASP | ASP | ASP |
|---|---|---|---|---|---|
| 3.69 | 3.94 | 4.44 | 5.65 | 11.16 | 3.12 |
| 0 | 0 | 0 | 0 | 0 | 0 |
| 0 | 0 | 0 | 0 | 0 | 0 |
| 1621 | 1619.5 | 1617.5 | 1616 | 1616 | 1622.6 |
| 1713.5 | 1713.5 | 1713.5 | 1713.5 | 1713.5 | 1713.5 |
| 0 | 0 | 0 | 0 | 0 | 0 |
| 0 | 0 | 0 | 0 | 0 | 0 |
| 0 | 0 | 0 | 0 | 0 | 0 |
| 0 | 0 | 0 | 0 | 0 | 0 |
| 0 | 0 | 0 | 0 | 0 | 0 |
| 0 | 0 | 0 | 0 | 0 | 0 |
| 24.5 | 24.8 | 26 | 24.5 | 24.5 | 23.6 |
| 39 | 39 | 39 | 39 | 39 | 39 |
| 0 | 0 | 0 | 0 | 0 | 0 |
| 0 | 0 | 0 | 0 | 0 | 0 |
| 0 | 0 | 0 | 0 | 0 | 0 |
| 0 | 0 | 0 | 0 | 0 | 0 |
| 0 | 0 | 0 | 0 | 0 | 0 |
| 0 | 0 | 0 | 0 | 0 | 0 |
| 0 | 0 | 0 | 0 | 0 | 0 |
| 0 | 0 | 0 | 0 | 0 | 0 |
| 2.4 | 2.45 | 2.7 | 3.18 | 0.25 | 2.25 |
| 0.55 | 0.35 | 0.2 | 0 | 0 | 0.75 |
| 0 | 0 | 0 | 0 | 0 | 0 |
| 0 | 0 | 0 | 0 | 0 | 0 |
| 0 | 0 | 0 | 0 | 0 | 0 |
| 0 | 0 | 0 | 0 | 0 | 0 |
| 0 | 0 | 0 | 0 | 0 | 0 |
| 0 | 0 | 0 | 0 | 0 | 0 |

| ARG | ARG | ARG | ARG | ARG | ARG |
|---|---|---|---|---|---|
| 11.73 | 12.23 | 12.43 | 12.62 | 12.88 | 10.54 |
| 0 | 0 | 0 | 0 | 0 | 0 |
| 0 | 0 | 0 | 0 | 0 | 0 |
| 0 | 0 | 0 | 0 | 0 | 0 |
| 0 | 0 | 0 | 0 | 0 | 0 |
| 1610.5 | 1610 | 1610 | 1610 | 1610 | 1610.5 |
| 1581.5 | 1581 | 1581 | 1581 | 1581 | 1581.5 |
| 0 | 0 | 0 | 0 | 0 | 0 |
| 0 | 0 | 0 | 0 | 0 | 0 |
| 0 | 0 | 0 | 0 | 0 | 0 |
| 0 | 0 | 0 | 0 | 0 | 0 |
| 0 | 0 | 0 | 0 | 0 | 0 |
| 0 | 0 | 0 | 0 | 0 | 0 |
| 22 | 22.5 | 22.5 | 22.5 | 22.5 | 22.5 |
| 24 | 24 | 24 | 24 | 24 | 24 |
| 0 | 0 | 0 | 0 | 0 | 0 |
| 0 | 0 | 0 | 0 | 0 | 0 |
| 0 | 0 | 0 | 0 | 0 | 0 |
| 0 | 0 | 0 | 0 | 0 | 0 |
| 0 | 0 | 0 | 0 | 0 | 0 |
| 0 | 0 | 0 | 0 | 0 | 0 |
| 0 | 0 | 0 | 0 | 0 | 0 |
| 0 | 0 | 0 | 0 | 0 | 0 |
| 1.85 | 1.75 | 1.75 | 1.75 | 1.85 | 2.05 |
| 3.27 | 3.1 | 3.1 | 3.1 | 3.3 | 3.15 |
| 0 | 0 | 0 | 0 | 0 | 0 |
| 0 | 0 | 0 | 0 | 0 | 0 |
| 0 | 0 | 0 | 0 | 0 | 0 |
| 0 | 0 | 0 | 0 | 0 | 0 |

| ALA-ALA | ALA-ALA | ALA-ALA | ALA-ALA | ALA-ALA | ALA-ALA |
|---|---|---|---|---|---|
| 8.44 | 9.56 | 11.84 | 12.27 | 12.74 | 6.94 |
| 1589 | 1589 | 1589 | 1589 | 1588.7 | 1591 |
| 0 | 0 | 0 | 0 | 0 | 0 |
| 0 | 0 | 0 | 0 | 0 | 0 |
| 0 | 0 | 0 | 0 | 0 | 0 |
| 0 | 0 | 0 | 0 | 0 | 0 |
| 0 | 0 | 0 | 0 | 0 | 0 |
| 0 | 0 | 0 | 0 | 0 | 0 |
| 1665 | 1628 | 1628 | 1628 | 1628 | 1664 |
| 0 | 0 | 0 | 0 | 0 | 0 |
| 23 | 25.5 | 26.8 | 26.8 | 27.5 | 25 |
| 0 | 0 | 0 | 0 | 0 | 0 |
| 0 | 0 | 0 | 0 | 0 | 0 |
| 0 | 0 | 0 | 0 | 0 | 0 |
| 0 | 0 | 0 | 0 | 0 | 0 |
| 0 | 0 | 0 | 0 | 0 | 0 |
| 0 | 0 | 0 | 0 | 0 | 0 |
| 0 | 0 | 0 | 0 | 0 | 0 |
| 0.98 | 1.26 | 1.26 | 1.33 | 1.33 | 1.3 |
| 0 | 0 | 0 | 0 | 0 | 0 |
| 0 | 0 | 0 | 0 | 0 | 0 |
| 0 | 0 | 0 | 0 | 0 | 0 |
| 0 | 0 | 0 | 0 | 0 | 0 |
| 0 | 0 | 0 | 0 | 0 | 0 |
| 0 | 0 | 0 | 0 | 0 | 0 |
| 0.26 | 0.68 | 0.68 | 0.68 | 0.68 | 0.71 |
| 0 | 0 | 0 | 0 | 0 | 0 |
| 0 | 0 | 0 | 0 | 0 | 0 |

| ASP-ASP | ASP-ASP | ASP-ASP | ASP-ASP | ASP-ASP | ASP-ASP |
|---|---|---|---|---|---|
| 3.84 | 4.55 | 8.29 | 8.63 | 12.28 | 3.29 |
| 0 | 0 | 0 | 0 | 0 | 0 |
| 0 | 0 | 0 | 0 | 0 | 0 |
| 1594.5 | 1593 | 1585.5 | 1583.5 | 1581 | 1595.6 |
| 1714.5 | 1714.5 | 1714.5 | 1714.5 | 1714.5 | 1714.5 |
| 0 | 0 | 0 | 0 | 0 | 0 |
| 0 | 0 | 0 | 0 | 0 | 0 |
| 0 | 0 | 0 | 0 | 0 | 0 |
| 1672.5 | 1670.5 | 1668.5 | 1668.5 | 1635.5 | 1675 |
| 0 | 0 | 0 | 0 | 0 | 0 |
| 0 | 0 | 0 | 0 | 0 | 0 |
| 0 | 0 | 0 | 0 | 0 | 0 |
| 33 | 33 | 40 | 40 | 41 | 29 |
| 39.8 | 39.8 | 38.8 | 38.8 | 38.8 | 39.5 |
| 0 | 0 | 0 | 0 | 0 | 0 |
| 0 | 0 | 0 | 0 | 0 | 0 |
| 0 | 0 | 0 | 0 | 0 | 0 |
| 28.8 | 31 | 27 | 24 | 27 | 28.8 |
| 0 | 0 | 0 | 0 | 0 | 0 |
| 0 | 0 | 0 | 0 | 0 | 0 |
| 0 | 0 | 0 | 0 | 0 | 0 |
| 1.46 | 1.79 | 2.05 | 2.2 | 2.5 | 0.96 |
| 0.53 | 0.33 | 0 | 0 | 0 | 0.76 |
| 0 | 0 | 0 | 0 | 0 | 0 |
| 0 | 0 | 0 | 0 | 0 | 0 |
| 0 | 0 | 0 | 0 | 0 | 0 |
| 0.65 | 0.64 | 0.35 | 0.28 | 0.53 | 0.65 |
| 0 | 0 | 0 | 0 | 0 | 0 |
| 0 | 0 | 0 | 0 | 0 | 0 |

| ARG-ARG | ARG-ARG | ARG-ARG | ARG-ARG | ARG-ARG | ARG-ARG |
|---|---|---|---|---|---|
| 7.78 | 11.3 | 12.04 | 12.31 | 12.77 | 6.12 |
| 0 | 0 | 0 | 0 | 0 | 0 |
| 0 | 0 | 0 | 0 | 0 | 0 |
| 0 | 0 | 0 | 0 | 0 | 0 |
| 0 | 0 | 0 | 0 | 0 | 0 |
| 1608.5 | 1608.5 | 1608.5 | 1608.5 | 1608.5 | 1608.5 |
| 1586.5 | 1586.5 | 1586.5 | 1586.5 | 1586.5 | 1586.5 |
| 1665 | 1665 | 1665 | 1665 | 1665 | 1712 |
| 1629 | 1630.5 | 1630 | 1631 | 1631 | 1665 |
| 0 | 0 | 0 | 0 | 0 | 0 |
| 0 | 0 | 0 | 0 | 0 | 0 |
| 0 | 0 | 0 | 0 | 0 | 0 |
| 0 | 0 | 0 | 0 | 0 | 0 |
| 20.8 | 20.8 | 20.8 | 20.8 | 20.8 | 20.8 |
| 24.8 | 24.8 | 24.8 | 24.8 | 24.8 | 24.8 |
| 33.5 | 33.5 | 33.5 | 33.5 | 33.5 | 33.5 |
| 28 | 30 | 30 | 33 | 33 | 24 |
| 0 | 0 | 0 | 0 | 0 | 0 |
| 0 | 0 | 0 | 0 | 0 | 0 |
| 0 | 0 | 0 | 0 | 0 | 0 |
| 0 | 0 | 0 | 0 | 0 | 0 |
| 0 | 0 | 0 | 0 | 0 | 0 |
| 1.3 | 1.25 | 1.25 | 1.15 | 1.05 | 1.3 |
| 2 | 1.95 | 1.9 | 1.55 | 1.8 | 2 |
| 0.2 | 0 | 0 | 0 | 0 | 0 |
| 0.5 | 0.6 | 0.57 | 0.47 | 0.55 | 0.4 |
| 0 | 0 | 0 | 0 | 0 | 0 |
| 0 | 0 | 0 | 0 | 0 | 0 |

# A3.4 Compilation of Fitting Parameters and Peak Behavior for RADA Components

| *ALA* | Wavelength | |
|---|---|---|
| ***pH*** | **1612.00** | **1728.00** |
| *3.00* | 0.18 | 0.02 |
| *2.57* | 0.16 | 0.03 |
| *2.33* | 0.12 | 0.04 |
| *2.00* | 0.06 | 0.06 |
| *1.51* | 0.02 | 0.06 |
| *8.41* | 0.25 | 0.00 |
| 9.15 | 0.19 | 0.00 |
| 10.25 | 0.14 | 0.00 |
| 10.66 | 0.06 | 0.00 |
| 11.35 | 0.01 | 0.00 |
| 12.54 | 0.01 | 0.00 |
| 7.69 | 0.28 | 0.00 |

| *ASP* | Wavelength | |
|---|---|---|
| ***pH*** | **1623.00** | **1715.80** |
| *2.42* | 0.18 | 0.09 |
| *2.17* | 0.13 | 0.10 |
| *1.97* | 0.07 | 0.12 |
| *1.75* | 0.10 | 0.10 |
| *1.36* | 0.04 | 0.12 |
| *3.06* | 0.17 | 0.08 |
| 3.69 | 0.24 | 0.06 |
| 3.94 | 0.25 | 0.04 |
| 4.44 | 0.29 | 0.02 |
| 5.65 | 0.32 | 0.00 |
| 11.16 | 0.03 | 0.00 |
| 3.12 | 0.22 | 0.07 |

| *ARG* | Wavelength | |
|---|---|---|
| ***pH*** | **1612.00** | **1582.00** |
| *10.01* | 0.28 | 0.28 |
| *9.61* | 0.36 | 0.19 |
| *9.15* | 0.37 | 0.17 |
| *3.45* | 0.35 | 0.20 |
| *1.90* | 0.33 | 0.17 |
| *10.90* | 0.20 | 0.30 |
| 11.73 | 0.19 | 0.33 |
| 12.23 | 0.18 | 0.32 |
| 12.43 | 0.19 | 0.33 |
| 12.62 | 0.18 | 0.32 |
| 12.88 | 0.19 | 0.34 |
| 10.54 | 0.20 | 0.31 |

| *ALA-ALA* | Wavelength | | | |
|---|---|---|---|---|
| ***pH*** | **1589.00** | **1716.00** | **1665.00** | **1628.00** |
| *3.54* | 0.07 | 0.01 | 0.07 | 0.00 |
| *2.78* | 0.03 | 0.03 | 0.07 | 0.00 |
| *6.39* | 0.12 | 0.00 | 0.08 | 0.00 |
| *1.92* | 0.00 | 0.04 | 0.08 | 0.00 |
| *1.37* | 0.00 | 0.04 | 0.08 | 0.00 |
| *6.39* | 0.13 | 0.00 | 0.07 | 0.00 |
| *8.44* | 0.10 | 0.00 | 0.03 | 0.00 |
| *9.56* | 0.13 | 0.00 | 0.00 | 0.07 |
| *11.84* | 0.13 | 0.00 | 0.00 | 0.07 |
| *12.27* | 0.13 | 0.00 | 0.00 | 0.07 |
| *12.74* | 0.13 | 0.00 | 0.00 | 0.07 |
| *6.94* | 0.13 | 0.00 | 0.07 | 0.00 |

| *ASP-ASP* | Wavelength | | |
|---|---|---|---|
| ***pH*** | **1595.00** | **1714.00** | **1674.00** |
| *2.81* | 0.08 | 0.09 | 0.07 |
| *2.32* | 0.05 | 0.10 | 0.07 |
| *2.10* | 0.02 | 0.12 | 0.07 |
| *1.89* | 0.01 | 0.12 | 0.07 |
| *1.33* | 0.01 | 0.12 | 0.07 |
| *3.26* | 0.11 | 0.08 | 0.07 |
| *3.84* | 0.15 | 0.05 | 0.07 |
| *4.55* | 0.19 | 0.03 | 0.07 |
| *8.29* | 0.22 | 0.00 | 0.04 |
| *8.63* | 0.22 | 0.00 | 0.03 |
| *12.28* | 0.25 | 0.00 | 0.05 |
| *3.29* | 0.10 | 0.08 | 0.06 |

| *ARG-ARG* | Wavelength | | | | |
|---|---|---|---|---|---|
| ***pH*** | **1607.50** | **1585.00** | **1709.50** | **1664.00** | **1630.00** |
| *5.02* | 0.15 | 0.20 | 0.00 | 0.04 | 0.00 |
| *4.39* | 0.14 | 0.16 | 0.04 | 0.06 | 0.00 |
| *3.46* | 0.15 | 0.18 | 0.06 | 0.06 | 0.00 |
| *2.60* | 0.12 | 0.13 | 0.08 | 0.06 | 0.00 |
| *1.67* | 0.15 | 0.14 | 0.08 | 0.08 | 0.00 |
| *6.02* | 0.14 | 0.20 | 0.00 | 0.04 | 0.00 |
| *7.78* | 0.13 | 0.20 | 0.00 | 0.02 | 0.05 |
| *11.30* | 0.13 | 0.20 | 0.00 | 0.00 | 0.06 |
| *12.04* | 0.13 | 0.20 | 0.00 | 0.00 | 0.06 |
| *12.31* | 0.11 | 0.15 | 0.00 | 0.00 | 0.05 |
| *12.77* | 0.10 | 0.18 | 0.00 | 0.00 | 0.05 |
| *6.12* | 0.12 | 0.19 | 0.00 | 0.04 | 0.00 |

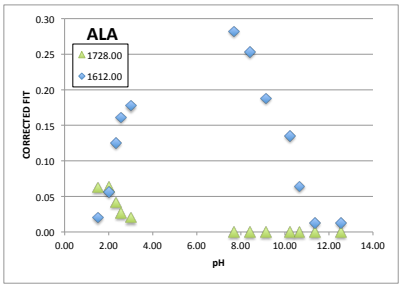


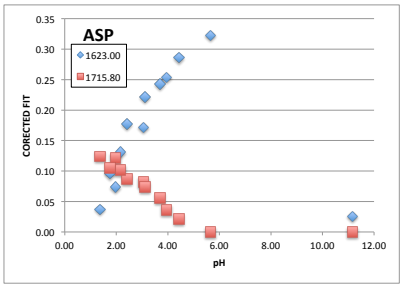


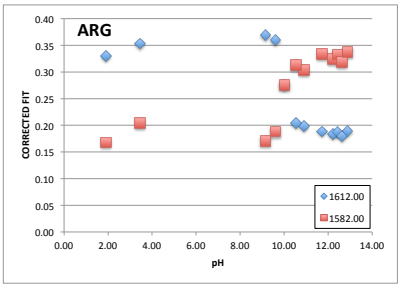


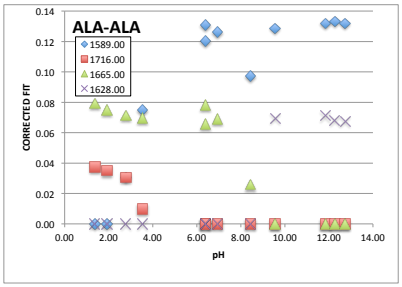


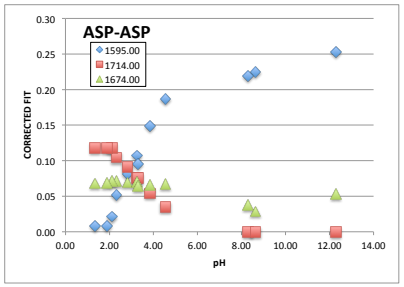


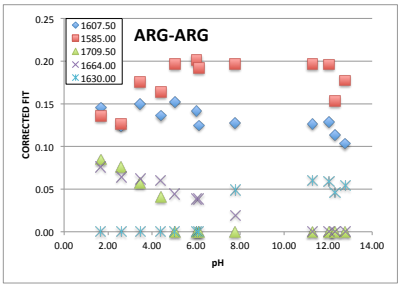

## List of Abbreviations

| Abbreviations | Full Name |
|---|---|
| 2D IR | Two dimensional infrared spectroscopy |
| AFM | Atomic force microscopy |
| ATR | Attenuated total reflectance |
| $CaF_2$ | Calcium fluoride |
| CD | Circular dichroism |
| COC | Cyclic olefin copolymer |
| COP | Cyclic olefin polymer |
| DMF | Dimethylformamide |
| DMSO | Dimethyl Sulfoxide |
| FTIR | Fourier transform infrared |
| HMDS | Hexamethyldisilazame |
| IR | Infrared (spectroscopy) |
| KOCN | Potassium cyanate |
| NMA | N-methylacetamide |
| NMR | Nuclear magnetic resonance |
| OPCPA | Optical parametric chirped pulse amplification |
| WAXD | Wide angle X-ray diffraction |